Magnetohydrodynamical Mechanisms for Outflows from Hot Jupiters
巨大灼熱惑星の磁気流体力学的質量放出機構

Yuki A. Tanaka

Laboratory for Theoretical Astronomy & Astrophysics (Ta-Lab)
Department of Physics, Nagoya University
Furo-cho, Chikusa-ku, Nagoya, Aichi, 464-8602, Japan

February 26, 2016

Abstract

A huge number of exoplanets have been discovered so far, and a substantial number of planets that have Jupiter-like masses and extremely small semi-major axes also have been detected. These exoplanets, so-called "hot Jupiters", undergo a significant amount of atmospheric escape, and the signature of it have been observed by the transit observations of the exoplanets in the ultraviolet wavelength. Several observations suggested that the hydrodynamic escape occurs at hot Jupiters, because the radial velocity of the atmosphere exceeds the sound speed, and not only the hydrogen atoms, but also heavier elements are detected in the escaping atmosphere. A number of theoretical works suggested that the heating of the upper atmosphere by the strong X-ray and extreme ultraviolet radiation from the host star can drive the hydrodynamic escape, and can explain the estimated mass-loss rates. However, effects of the magnetic fields of hot Jupiters on the atmospheric escape have not been investigated in detail so far. If hot Jupiters have the strong magnetic fields, and there is atmospheric turbulence, magnetohydrodynamic (MHD) waves are excited at the surface of the planets. The MHD waves propagate upward along the magnetic field lines, and dissipate to heat up the atmosphere and drive the outflows. We test this scenario by performing one-dimensional MHD simulations in the atmosphere of hot Jupiters, and we find that a large amount of atmospheric escape that is consistent with the observed values is obtained, and the velocity of the escaping atmosphere reaches $\sim 100\,\mathrm{km\,s^{-1}}$. Next we examine effects of ohmic dissipation of the MHD waves in weakly-ionized atmospheres, and show non-ideal effects strongly affect the atmospheric structure and escape. Complicated natures of the propagation, reflection, and dissipation of the waves in the atmosphere are also investigated. Furthermore, we improve the treatment of the radiative cooling and heating rates by solving the radiative transfer in the atmosphere, and we find that the mass-loss rates and atmospheric structure are affected by the detailed treatment of the radiative cooling and heating rates. We also treat several physical properties as parameters of the simulations, and find that the mass-loss rate strongly depends on the velocity dispersion at the planetary surface, and the pressure scale height of the atmosphere. Finally, we apply our model of the atmospheric escape to a hot Neptune GJ 436b, and successfully explain the mass-loss rate and radial velocity that are needed to explain the observed features. Our mechanism of the atmospheric escape, the magnetically driven outflows, would be important to understand the natures of the mass loss from planets, and may also be essential for long-term evolution of planets.

Contents

Chapter 1

Introduction

1.1 Discoveries of Exoplanets

Recently, a huge number of exoplanets have been found by various detection methods. The first exoplanet that orbiting around a solar-type star was discovered by the radial velocity method in 1995 (Mayor and Queloz, 1995). This exoplanet, 51 Peg b, is a gaseous planet with a very small orbital distance. This discovery was surprising because gaseous planets were thought to exist far from their central star as in the solar system. After the discovery of 51 Peg b, a lot of exoplanets were detected through the radial velocity method, and most of them were gaseous planets with very small semi-major axes.

The first detection of the transit of an exoplanet was HD 209458b (Charbonneau et al., 2000; Henry et al., 2000). HD 209458b is also a gaseous planet with the very small semi-major axis. After this discovery, a number of exoplanets discovered by the transit method also started to increase. In particular, *Kepler* have been discovered thousands of exoplanets and exoplanet candidates (e.g., Borucki et al., 2010). Other detection methods, such as the direct imaging, gravitational microlensing, and transit timing variations are also important to discover the exoplanets.

A large number of the discoveries of the exoplanets tell us that the exoplanets are very rich in diversity. For example, some of them have very small semi-major axes and masses that are similar to Jupiter. These exoplanets are known as hot Jupiters. 51 Peg b and HD 209458b are the famous and typical examples of hot Jupiters.

Figure 1.1 shows the plots of the discovered exoplanets so far. The hot Jupiters are located in the upper left region of Figure 1.1. Their semi-major axes are smaller than ~ 0.1 AU, and rich in diversity in the mass and radius. Since the incident fluxes from the central stars are

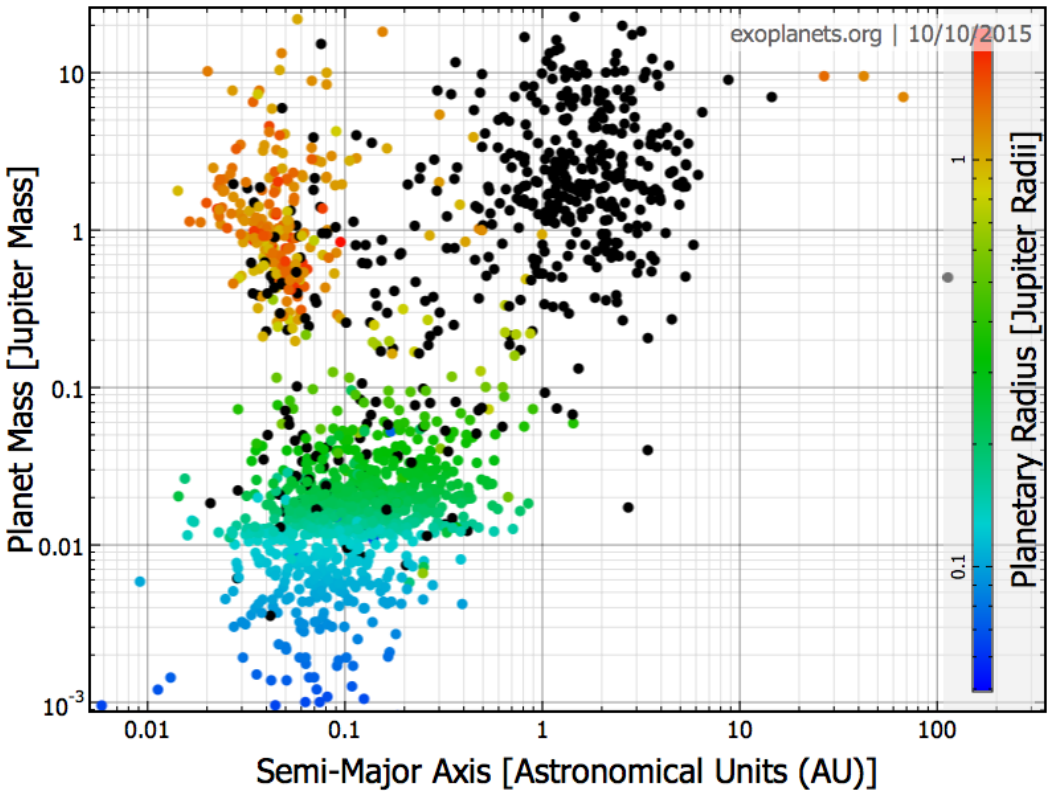

Figure 1.1: The relation between the semi-major axis and mass of the discovered exoplanets. The figure is taken from exoplanets.org (http://exoplanets.org) (Wright et al., 2011). The horizontal axis is the semi-major axis in unist of AU, and the vertical axis is the mass of the planets that is normalized by Jupiter's mass. Color corresponds to the radius of the planets normalized by Jupiter's radius. The radius is available if the planets are discovered through the transit method, and the direct imaging. Since the radii the planets which are discovered by other methods such as the radial velocity and gravitational microlensing are unknown, they are showed in the black dots.

significant, the typical surface temperatures of the hot Jupiters become $\sim$ 1000 K or higher.

Additionally, some groups of the confirmed exoplanets can be seen in Figure 1.1. Around the semi-major axis is 1 AU, numbers of Jupiter-like exoplanets are detected. These planets are mostly discovered by the radial velocity method. Furthermore, smaller exoplanets have been discovered recently. Neptune-like planets with the very small semi-major axis, so-called hot Neptunes, and planets slightly larger than Earth, so-called super-Earths, are also discovered.

1.2 Observations of Atmospheres of Exoplanets

1.2.1 Observation in the Optical and Infrared

The transit observation is a very useful method to know the radius of planets and their orbital period. In addition, it is also important to observe and characterize the properties of the atmosphere. For example, spectroscopy in the optical and infrared wavelength during the primary transit and secondary eclipse give us the information of the atmospheric structure and composition. The transmission spectrum of the atmosphere during the primary transit and the reflection spectrum during the secondary eclipse are important to reveal the atmospheric structure.

Strong emission lines have been detected during the secondary eclipses of several hot Jupiters, and these observations suggest the existence of a thermal inversion layer in the atmosphere of the hot Jupiters(Hubeny et al., 2003; Burrows et al., 2007). The detections of the thermal inversion layer are reported in several hot Jupiters such as HD 149026b (Harrington et al., 2007), HD 209458b (Burrows et al., 2007; Knutson et al., 2008), and XO-1b (Machalek et al., 2008). It is thought that some sort of absorbers in the atmosphere, such as TiO and VO create the thermal inversion layer (Hubeny et al., 2003), but details are still unclear. Additionally, recent observations and analyses suggest that the strong thermal inversion layer may not exist (e.g., Stevenson et al., 2012; Diamond-Lowe et al., 2014; Schwarz et al., 2015), so the existence of the thermal inversion layer and structure of the atmosphere are still an open question.

Various elements and molecules such as Na, Ca, H_2O, CH_4, CO, and CO_2 have been detected in the atmosphere of exoplanets through transit spectroscopic observations in the optical and infrared (e.g., Charbonneau et al., 2002; Tinetti et al., 2007; Snellen et al., 2008; Swain et al., 2008, 2009). Transmission and reflection spectra are easier to obtain in hot Jupiters because of larger radii and atmospheric scale heights, and are harder in smaller planets, However, recent observations enable us to investigate the atmospheric composition and structure of the smaller planets such as hot Neptunes and super Earths (e.g., Bean et al., 2010).

Transmission and reflection spectra in the optical and infrared wavelength correspond to the lower atmosphere and surface of the planets. Therefore, these features of the spectra reflect the properties of the atmosphere of the lower region and the surface of the planets.

1.2.2 Observation in the Ultraviolet

In the meanwhile, transit observations in the UV band provide interesting physical properties of the upper atmosphere. The transit in the UV band gives us properties of the exosphere, and existence of an extended upper atmosphere, and atmospheric escape from hot Jupiters. For example, absorption in the H Lyα has been confirmed in some hot Jupiters, such as HD 209458b (Vidal-Madjar et al., 2003), HD 189733b (Lecavelier des Etangs et al., 2010), and 55 Cnc b (Ehrenreich et al., 2012). A transit depth corresponds to the apparent radius of the planet. While the transit depth of HD 209458b in the optical wavelength is $\sim$ 1.5%, which corresponds to $\sim$ 1.38 R_J (Jupiter's radius), the transit depth in the H Lyα is $\sim$ 15%, which corresponds to $\sim$ 4.3 R_J (Vidal-Madjar et al., 2003). Similar phenomena are reported for HD 189733b (Lecavelier des Etangs et al., 2010), and hot Neptune GJ 436b (Kulow et al., 2014; Ehrenreich et al., 2015). Similar to this, the transit depth in the visible band at HD 189733b is $\sim$ 2.4%, (Pont et al., 2007), and $\sim$ 5.1% in the H Lyα (Lecavelier des Etangs et al., 2010). The typical surface temperature of hot Jupiters is assumed to be approximately 1000 K, but the pressure scale height at this temperature cannot explain the observed larger apparent radii in the H Lyα. Therefore, these observations suggest that the existence of the extended exosphere that is filled up with the high-temperature atomic hydrogen gas. Interestingly, although 55 Cnc b is not a transiting planet in the optical wavelength, the observation in the H Lyα suggests that the extended upper atmosphere of the planet occults the central star (Ehrenreich et al., 2012). In addition, a transit observation in the X-ray band of HD 189733b has been done recently, and the result also suggests that the apparent radius in the X-ray is a few times larger than the radius in the visible band (Poppenhaeger et al., 2013).

Moreover, transit observations in the UV band strongly suggest the existence of mass loss from hot Jupiters. The observed apparent radius in the H Lyα of HD 209458b is $\sim$ 4.3 R_J, and the radius of the Roche lobe of the planet is $\sim$ 3.6 R_J (Vidal-Madjar et al., 2003). Since the high temperature atmosphere extends beyond the Roche lobe, the outer region of the extended atmosphere is not bounded by the gravity of the planet. This suggests the mass loss from the upper atmosphere should occur.

1.3 Atmospheric Escape from Gaseous Planets

1.3.1 Observations of the Atmospheric Escape from Hot Jupiters

A lot of properties of the atmospheric escape from hot Jupiters have been revealed by many observations, mainly done by the UV band. For example, shape of the transit light curves in the UV band strongly suggests the existence of the escaping atmosphere. The transit light curves in the optical and infrared wavelength generally show symmetric shape. In the UV band, however, shape of the light curves is different compared with the optical and infrared: the ingress of the transit is slightly earlier, and the egress is much later, so the resultant shape of the light curves becomes asymmetry as in Figure 1.2 (e.g., Vidal-Madjar et al., 2003). This bizarre shape of

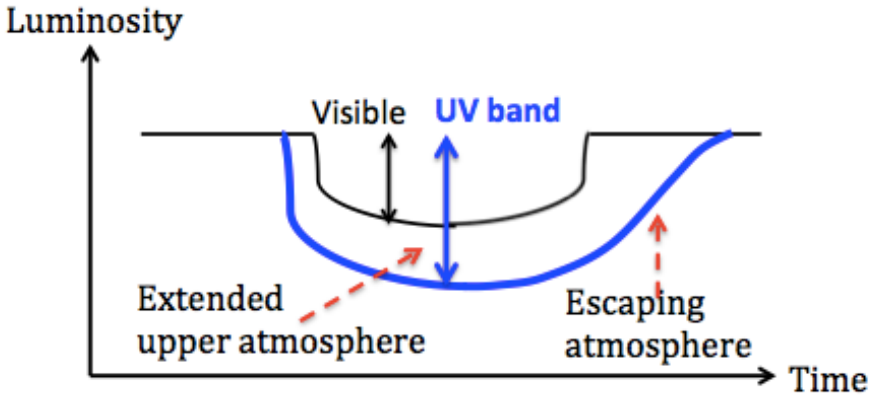

Figure 1.2: This figure is a schematic picture of the comparison between the light curve in the optical and UV wavelength. The black line is the light curve in the optical wavelength, which shows almost symmetric shape. The blue line is the light curve in the UV wavelength, which shows the deeper transit depth due to the extended upper atmosphere, and asymmetric shape due to the atmospheric escape.

the light curve can be explained by the escaping atmosphere. The escaped atmosphere which consist from high temperature hydrogen atoms makes a cometary-tail-like structure due to the effect of the radiation of the central star, then this structure absorbs the UV radiation from the central star. This cometary-tail-like structure by the escaping atmosphere around hot Jupiters is predicted by Schneider et al. (1998). Consequently, dimming of the central star in the UV band continues even after the transit in the other band ends.

The velocity of the escaping atmosphere is also observed by the transit in the UV band. It is known that the H Lyα line is shifted because the escaping atmosphere has the large radial velocity. According to the blue shift of the H Lyα absorption, the maximum radial velocity of

the escaping atmosphere at HD 209458b is as fast as $\sim 100\,\mathrm{km\,s^{-1}}$, which is much faster the sound speed (Vidal-Madjar et al., 2003). The radial velocity of the escaping atmosphere is also measured at HD 189733b, and the obtained value is much faster, $\sim 230\,\mathrm{km\,s^{-1}}$ (Lecavelier des Etangs et al., 2012). These values are too large to be explained by the thermal velocities in the atmosphere of the planets, therefore strong acceleration mechanisms are needed for these supersonic velocity. Thus, it can be said that the atmospheres are escaping hydrodynamically, not hydrostatically.

Not only the hydrogen atoms, but also heavier elements have been detected in the extended and escaping atmospheres. For example, $\mathrm{O_I}$, $\mathrm{C_{II}}$, $\mathrm{Si_{III}}$ (Vidal-Madjar et al., 2004; Linsky et al., 2010; Ben-Jaffel and Sona Hosseini, 2010), $\mathrm{Si_{IV}}$ (Schlawin et al., 2010), and $\mathrm{Mg_I}$ (Vidal-Madjar et al., 2013) are detected at HD 209458b. Similarly, $\mathrm{O_I}$, and possibly $\mathrm{C_{II}}$ are detected at HD 189733b (Ben-Jaffel and Ballester, 2013), and $\mathrm{Mg_{II}}$ is detected at WASP-12b (Fossati et al., 2010b; Haswell et al., 2012). Although not yet detected, neutral magnesium atoms, other heavier elements and their ions such as $\mathrm{Mn_I}$, $\mathrm{Mn_{II}}$, $\mathrm{Fe_I}$, and $\mathrm{Fe_{II}}$ are expected to be detected through the UV observations (Bourrier et al., 2015). These detections of the heavier elements in the extended upper atmosphere and escaping atmosphere also strongly suggest that the hydrodynamic escape takes place. If the atmospheric escape occurs in a hydrostatic manner, the heavier elements cannot escape from the planets.

The mass-loss rate from these planets are estimated from the observations, but their values vary largely by estimation methods. For instance, Vidal-Madjar et al. (2003) estimated the mass-loss rate by using a particle simulation that combined with their observation, and gave a lower limit of the mass-loss rate of $\dot{M} \geq 10^{10}\,\mathrm{g\,s^{-1}}$ at HD 209458b. Because of saturation of the absorption of the H Lyα line, they only gave the lower limit of the mass-loss rate. Linsky et al. (2010) used a theoretical calculation and gave the value of $\dot{M} = (8 - 40) \times 10^{10}\,\mathrm{g\,s^{-1}}$. For other hot Jupiters, Lecavelier des Etangs et al. (2010) estimated that the mass-loss rate to be $\sim 10^{10}\,\mathrm{g\,s^{-1}}$ at HD 189733b by the combination with the observed data and fitting of their simulations. Other estimations from the observations of the mass-loss rates also suggest that the mass-loss rates at the hot Jupiters are around $10^{10}\,\mathrm{g\,s^{-1}}$ or an order of magnitude larger (e.g., Lecavelier des Etangs et al., 2010).

As for the existence of the extended upper atmosphere and a large amount of the atmospheric escape, a temporal variation is detected. Lecavelier des Etangs et al. (2012) reported that no detection of the transit in H Lyα in April 2010, and the total dimming rate during the transit in H Lyα is 2.9%, which is comparable to the transit depth in the near-infrared and optical

(Désert et al., 2009, 2011; Sing et al., 2011). However, in the later observation in September 2011, the deep transit in H Lyα is detected and the transit depth became 5.0% which is deeper than the infrared and optical. They estimated that the mass-loss rate of $\sim 10^9\,\mathrm{g\,s^{-1}}$ during the later phase, but they also noted that this value is a lower limit for the net mass-loss rate because this value does not include ionized hydrogen. They inferred that this large time-variability can be caused by the variation of the X-ray radiation from the central star, because the central star HD 189733 has X-ray variability, and a strong stellar flare was also detected.

1.3.2 Theoretical Works on the Atmospheric Escape from Hot Jupiters

Although the detailed mechanisms of the strong mass loss from hot Jupiters are still unclear, various theoretical models have been developed to explain such a large amount of the mass-loss rate from hot Jupiters. A leading example of them is that energy-limited escape by the X-ray and extreme ultraviolet (XUV) radiation from a central star (Lammer et al., 2003). In this mechanism, certain amounts of the energy of the XUV from the central star heats up the upper atmosphere through photodissociation and photoionization, then the hydrodynamic escape is driven. This is so-called XUV-driven escape, and the mass-loss rate from HD 209458b is calculated as $\sim 10^{12}\,\mathrm{g\,s^{-1}}$ (Lammer et al., 2003).

Several previous works derived a analytic formula of the mass-loss rate that is driven by the XUV radiation (Erkaev et al., 2007; Lopez et al., 2012). The formula is follow;

$$\dot{M} = \frac{\epsilon \pi F_{\mathrm{XUV}} R_{\mathrm{XUV}}^3}{G M_{\mathrm{p}} K_{\mathrm{tide}}}, \tag{1.1}$$

$$K_{\mathrm{tide}} = \frac{(\xi - 1)^2 (2\xi + 1)}{2\xi^3}, \tag{1.2}$$

$$\xi = \frac{R_{\mathrm{Roche}}}{R_{\mathrm{p}}} = \left(\frac{M_{\mathrm{p}}}{3M_\star}\right)^{1/3} \frac{a}{R_{\mathrm{p}}}. \tag{1.3}$$

In these equations, F_{XUV} is the flux of the XUV radiation from the central star, and R_{XUV} is the radius at which the optical depth for the XUV becomes unity. G is the gravitational constant, R_{p} is the radius of the planet, and M_{p} is the mass of the planet. Equation (1.2) is a reduction factor of the potential energy due to the tidal effect by the central star. Equation (1.3) is the ratio of the radius of the Roche lobe R_{Roche} to the radius of the planet, and the Roche radius can be written by M_{p}, mass of the central star $M_\star$, and semi-major axis a. In the equation (1.1), ϵ is heating efficiency that denotes the fraction of the absorbed energy of the XUV radiation that is used to drive the atmospheric escape. The heating efficiency is the

important parameter for calculation of the mass-loss rate driven by the XUV radiation, but it is not easy to estimate the value of it. Therefore, the heating efficiency is often treated as a free parameter. For example, previous works of early date assumed that the heating efficiency is 100% (e.g., Lammer et al., 2003; Baraffe et al., 2004; Lecavelier des Etangs et al., 2004). The value of the heating efficiency can vary, and wide range of the value within $\sim 10 - 100\%$ has been assumed in a lot of several works (Shematovich et al., 2014, and references therein). The heating efficiency should be determined by realistic calculations of the atmosphere. Several studies suggested that the heating efficiency becomes $\sim 30\%$ (e.g., Yelle, 2004), but a recent simulation that includes the effects of electron-impact and suprathermal photoelectrons showed that the heating efficiency does not become higher than 20%, so several works that assuming the values higher than 20% may overestimated the mass-loss rates (Shematovich et al., 2014).

After the work by Lammer et al. (2003), theoretical models for the XUV-driven escape have been developed by many previous works. For example, an one-dimensional calculation that includes chemical reactions was investigated by Yelle (2004). They showed that since the cooling by H_3^+ from the atmosphere is efficient, and a portion of the absorbed XUV energy is used for hydrogen ionization, a resultant mass-loss rate becomes smaller than the result of Lammer et al. (2003), $\dot{M} = 4.7 \times 10^{10}\,\mathrm{g\,s^{-1}}$ (Yelle, 2004, 2006). However, they obtained that the radial velocity of the escaping atmosphere becomes subsonic, $\sim 1\,\mathrm{km\,s^{-1}}$, which is much smaller than the observed value at HD 209458b (Vidal-Madjar et al., 2003) and HD 189733b (Lecavelier des Etangs et al., 2012).

Tian et al. (2005) and García Muñoz (2007) demonstrated one-dimensional atmospheric calculations and showed that the velocity of the escaping atmosphere can exceed the sound speed, which possibly explains the observed features. In particular, García Muñoz (2007) showed that the escaping atmosphere can be both supersonic and subsonic flow with various conditions. Both works obtained the mass-loss rates of $\geq 10^{10}\,\mathrm{g\,s^{-1}}$.

According to the model of Lecavelier des Etangs et al. (2012), stellar radiation pressure can accelerate the escaping atmosphere up to $\sim 120\,\mathrm{km\,s^{-1}}$, therefore the observed feature in HD 209458b can be explained ($\sim 100\,\mathrm{km\,s^{-1}}$), but in HD 189733b is difficult to explain. So, another acceleration mechanisms might be needed. Several theoretical works suggested that the effects of the radiation pressure on the escaping atmosphere and the charge exchange between the particles in the escaping atmosphere and protons in the hot stellar wind are also important to explain the observed feature (Holmström et al., 2008; Ekenbäck et al., 2010; Bourrier and Lecavelier des Etangs, 2013; Tremblin and Chiang, 2013).

1.3.3 Atmospheric Escape from Other Types of Planets

The atmospheric escape occurs not only at hot Jupiters, but also at other types of planets. Recently, signatures of the atmospheric escape are observed at GJ 436b, a warm Neptune-sized planet (Kulow et al., 2014; Ehrenreich et al., 2015). The transit depth of GJ 436b in the optical wavelength is very shallow $\sim 0.6\%$ due to the small size of the planet (Gillon et al., 2007; Bean et al., 2008). The transit depth in the infrared wavelength is almost similar to the optical (Deming et al., 2007). Ehrenreich et al. (2015) reported, however, surprisingly deep transit in H Lyα, $\sim 56\%$, along with the peculiar asymmetric light curve. They observed the ingress of the transit in the UV band about two hours earlier, and the egress more than three hours later compared to the optical transit. They concluded that GJ 436b has an extremely large comet-like neutral hydrogen cloud whose radius larger than the central star ($\sim 0.44 R_\odot$) and the radius of the planetary Roche lobe. The estimated value of the mass-loss rate from GJ 436b is $\sim 5 \times 10^8\,\mathrm{g\,s^{-1}}$.

Additionally, it is suggested that the XUV-driven escape can occur at gaseous planets that have moderate surface temperatures. Chadney et al. (2015) demonstrated that the hydrodynamic escape driven by the XUV at gaseous planets that orbit around an active and low-mass star by using an one-dimensional upper atmospheric model that includes photochemical reactions. According to their calculation, because the strong XUV insolation from the active star destroys molecules and radiation cooling by the molecules is suppressed, the hydrodynamic escape from the upper atmosphere can be driven even if the case for gaseous planets that orbit beyond 1 AU from the central star in some cases.

Also, several observations have been hinted the existence of a comet-tail like structure of the escaping material from a super-Mercury planet KIC 12557548b (Rappaport et al., 2012; Budaj, 2013). The transit light curves with asymmetric shape and variable depth are reported in the optical wavelength, so it is assumed that the comet-tail-like structure contains a large amount of dust.

Therefore, large amounts of the atmospheric escape can occur in the hot/warm Neptunes, relatively cooler gaseous planets, and even rocky planets.

1.3.4 Impacts of the Atmospheric Escape

Mass loss from planets is important to understand the evolution and population of the exoplanets. If the mass-loss rates are larger and/or the initial masses are small, gaseous planets may

lose most of their envelope masses and will disappear, or remain only their solid cores (e.g., Lammer et al., 2003). Since the stellar XUV flux is especially strong during an early phase of stars, the XUV-driven escape from hot Jupiters can lead to lose their envelopes drastically and can affect to the population of the close-in planets (e.g., Kurokawa and Nakamoto, 2014). A detailed work on the population of the exoplanets and size distribution that includes the effect of the atmospheric escape was recently investigated by Jin et al. (2014).

A large amount of the mass-loss can also changes the semi-major axis and the rotational period because the escaping atmosphere can remove the angular momentum of the planet. Several previous works argued that the migration of the close-in planets can be driven by the strong atmospheric escape (Gu et al., 2003; Chang et al., 2010). By including this effect, it is theoretically examined that some mini-Neptunes orbiting around a M-drarf can turn into habitable super-Earths by losing their entire envelopes because of the XUV-driven escape (Luger et al., 2015).

1.4 Magnetic Fields of Exoplanets

1.4.1 Theoretical Works on Magnetic Fields

Physical properties and phenomena related to magnetic fields of the exoplanets have been investigated in more detail by both theoretical and observational studies. For the theoretical works, for example, several authors pointed out possible effects on the radii and internal structures of hot Jupiters by ohmic dissipation in the atmosphere and interior (Ben-Jaffel and Sona Hosseini, 2010; Perna et al., 2010; Batygin et al., 2011). In the condition of the atmosphere of hot Jupiters, alkali metals are ionized, and strong atmospheric circulation (e.g., Showman et al., 2008) generates the electric current in the atmosphere. Then, the interaction between the planetary magnetic fields and the current in the atmosphere induces the current inside of the planet, energy is deposited to the interior of the planet through the ohmic dissipation of the induced current. Therefore, since the ohmic dissipation serves as an extra heat source inside of the planet, the radius of the planet can be inflated, or halted against contraction associated with the thermal evolution. The effects and validity of ohmic dissipation are studied in more detail (e.g., Huang and Cumming, 2012; Menou, 2012; Wu and Lithwick, 2013; Rogers and Showman, 2014).

Magnetic fields of gaseous planets are thought to also be important for the mass-loss rate and the structure of the atmosphere. Outflows from the upper atmosphere of the gaseous planets

that are driven by the XUV irradiation will be magnetically-controlled, therefore the outflows cannot be spherically symmetry and will be limited to escape through open regions of the magnetic fields, and the mass-loss rate can be about an order of magnitude smaller (Adams, 2011; Owen and Adams, 2014). Also, models of the upper atmosphere with the planetary magnetic fields are proposed and the effects on the transit depth and the loss of the angular momentum by the planetary magnetic fields are discussed (Trammell et al., 2011, 2014).

1.4.2 Observational Aspects of Magnetic Fields

From a viewpoint of observations, information on the properties of the planetary magnetic fields and the magnetic activities, such as the strength of the magnetic fields and the interaction between a magnetosphere of the planets and the stellar winds have been suggested. For instance, observations of the secondary eclipse at numerous exoplanets at 150 MHz have been suggested that the radio emission at this wavelength is weak and an upper limit of the magnetic fields is given (Lecavelier Des Etangs et al., 2011; Sirothia et al., 2014). Lecavelier Des Etangs et al. (2011) observed the secondary eclipse of two exoplanets at 150 MHz and implied that no emission was detected from HD 209458b and a weak signal from the direction of HD 189733b, which is not confirmed that is associated with the planet. They suggested that the planetary magnetic fields are not so strong to be bright at 150 MHz, and they gave the upper limit ~ 50 G for these planets. The subsequent radio observations during the secondary eclipses of many exoplanets also suggested the same results in most cases (Sirothia et al., 2014).

The magnetic moment of HD 209458b was estimated by the H Lyα observations combined with the calculation of the atmospheric escape, and a resultant magnetic moment is around 10% of the value of Jupiter, $\sim 1.6 \times 10^{26}\,\mathrm{A\,m^2}$ (Kislyakova et al., 2014). These observation implies the weaker magnetic fields than Jupiter, and it was suggested by several theoretical works that assumed tidally-locked close-in condition, or a model of the atmosphere of the hot Jupiters, or an empirical relation of the magnetic fields (Grießmeier et al., 2004; Sánchez-Lavega, 2004; Durand-Manterola, 2009; Koskinen et al., 2010) (but see also (Christensen et al., 2009; Reiners and Christensen, 2010)).

Magnetic activities and interactions between stellar winds and the exosphere of hot Jupiters are also investigated. For example, Vidotto et al. (2010) showed that the bow shock can be created due to the interaction with the stellar wind and the exosphere of the planets, and the bow shock can explain the early ingress of transit in the near UV in WASP-12b (Fossati et al., 2010a). They also gave an upper limit of the strength of the magnetic field of WASP-12b is

< 24 G.

1.4.3 Effects of Magnetic Activity on the Atmospheric Escape

Numerous works have been showed that the magnetic activities are quite important for the structure of the atmosphere and atmospheric escape. However, the acceleration of gas flow and resultant mass loss from the gaseous planets that are caused by the magnetic activities have not been studied before. If a gaseous planet has the magnetic fields and its atmosphere is ionized, magnetohydrodynamic (MHD) waves such as Alfvén waves can be excited by turbulence at the surface. Since the MHD waves transport the energy upward and they will dissipate in the upper atmosphere, the gas will be heated up and the gas flow will also be accelerated. Typical examples of the mass loss that is driven by this mechanism are stellar winds from intermediate- and low-mass stars, such as the solar wind. We calculate the mass loss driven by the MHD waves from the gaseous planets, especially from hot Jupiters, by one-dimensional MHD simulations and analyze the dependence of the mass-loss rates and the atmospheric structure on various properties of the gaseous planets.

Chapter 2

Magnetically Driven Wind from Gaseous Planets

In this chapter, we denote our concept of simulations of the atmospheric escape driven by the MHD waves, and show our main results briefly. Main results in this chapter are published in Tanaka et al. (2014).

2.1 Numerical Method

2.1.1 Concept of the Model

Here we extend a numerical simulation code for the solar wind (Suzuki and Inutsuka, 2005, 2006) to calculate atmospheric escape from gaseous planets. This simulation code is generally applicable to stars with a surface convective layer. This code have also been applied to winds from red giants (Suzuki, 2007) and young active solar-type stars (Suzuki et al., 2013). First, we introduce briefly general properties of stellar winds from stars with the surface convection, and our simulation code.

In stars with the surface-convective layer, magnetic fields are generated by dynamo action (e.g., Choudhuri et al., 1995), and various types of MHD waves are excited at the surface (Matsumoto and Suzuki, 2012, 2014). In that condition, Alfvén waves can transport the energy in the surface convection region to the upper atmosphere through various dissipation processes and heat up the upper atmosphere to make a corona and drive the stellar winds (Goldstein, 1978; Heyvaerts and Priest, 1983; Terasawa et al., 1986; Kudoh and Shibata, 1999; Matthaeus et al., 1999).

Figure 2.1 shows a schematic picture of this model. We assume the turbulence at the surface that is generated by some sort of reasons. The magnetic fields are perturbed by the turbulence

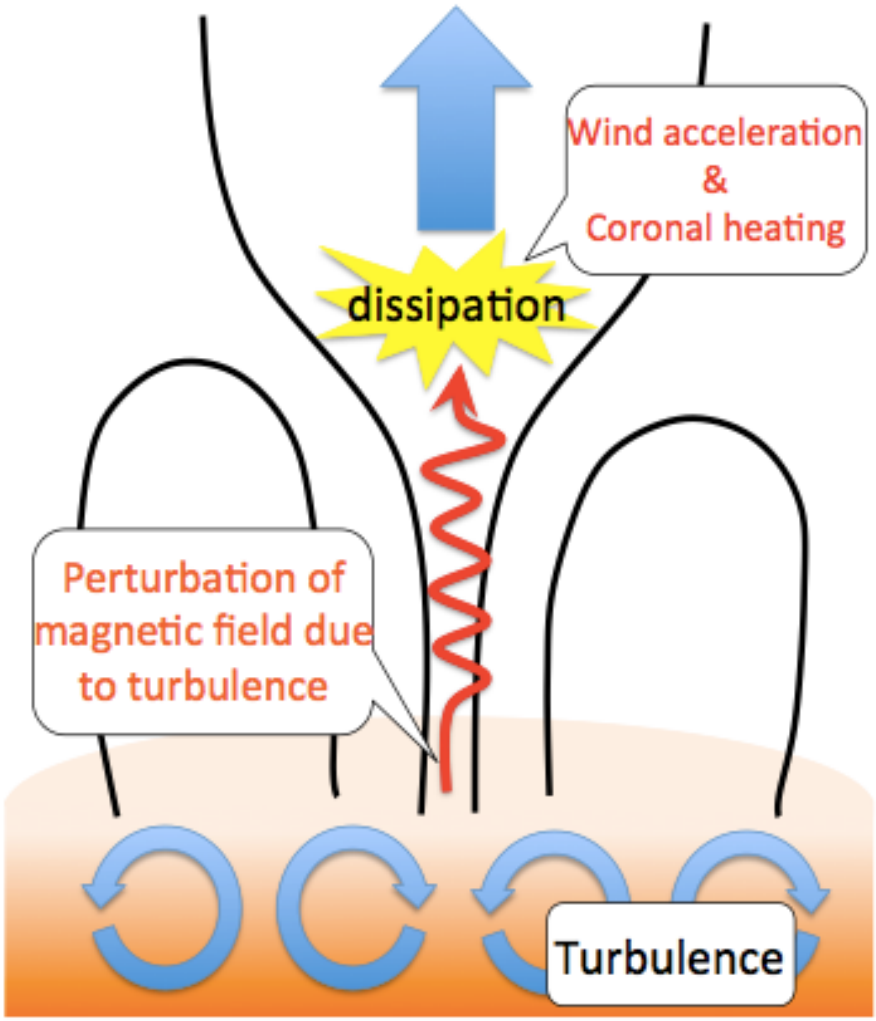

Figure 2.1: A schematic picture of a single open flux tube. The black lines correspond to the magnetic fields.

and the MHD waves are generated. The MHD waves propagate upward along with the magnetic fields, and dissipate in the upper atmosphere. Therefore, the upper atmosphere is heated up and gas flow can be accelerated. Although details are uncertain, hot Jupiters are expected to have their own magnetic fields as described in Section 1.4, so this mechanism is applicable to hot Jupiters.

2.1.2 Basic Equations for MHD

We time-dependently solve the propagation and dissipation of MHD waves and consequent heating of the gas in a single open flux tube. We consider super-radially open magnetic flux

tubes as in Figure 2.1. For the conservation of the magnetic flux, we use the following equation;

$$B_r r^2 f(r) = B_{r,0} r_{r,0}^2 f_0, \tag{2.1}$$

where B_r is the radial magnetic field strength. In Equation 2.1, $f(r)$ is an areal filling factor of the open magnetic flux tubes at radial distance r, and the subscript 0 represents the values at the surface. We use an equation for $f(r)$ as follows;

$$f(r) = \frac{\exp\left(\frac{r-r_0-h1}{h_1}\right) + f_0 - (1-f_0)/e}{\exp\left(\frac{r-r_0-f_1}{h_1}\right) + 1}, \tag{2.2}$$

where h_1 denotes the typical height of closed magnetic loops. This factor is essentially same as a super-radial expansion form of the magnetic flux tubes which was introduced by Kopp and Holzer (1976).

We solve following MHD equations for an one-dimensional open flux tube that include radiative cooling and thermal conduction,

$$\frac{d\rho}{dt} + \frac{\rho}{r^2 f}\frac{\partial}{\partial r}\left(r^2 f v_r\right) = 0, \tag{2.3}$$

$$\rho\frac{dv_r}{dt} = -\frac{\partial p}{\partial r} - \frac{1}{8\pi r^2 f}\frac{\partial}{\partial r}\left(r^2 f B_\perp^2\right) + \frac{\rho v_\perp^2}{2r^2 f}\frac{\partial}{\partial r}\left(r^2 f\right) - \rho\frac{GM_\mathrm{p}}{r^2}, \tag{2.4}$$

$$\rho\frac{d}{dt}\left(r\sqrt{f}v_\perp - \frac{GM_\mathrm{p}}{r}\right) = \frac{B_r}{4\pi}\frac{\partial}{\partial r}\left(r\sqrt{f}B_\perp\right). \tag{2.5}$$

$$\rho\frac{d}{dt}\left(e + \frac{v^2}{2} + \frac{B^2}{8\pi\rho}\right) + \frac{1}{r^2 f}\frac{\partial}{\partial r}\left[r^2 f\left\{\left(p + \frac{B^2}{8\pi}\right)v_r - \frac{B_r}{4\pi}\left(\mathbf{B}\cdot\mathbf{v}\right)\right\}\right] + \frac{1}{r^2 f}\frac{\partial}{\partial r}\left(r^2 f F_\mathrm{c}\right) + q_\mathrm{R} = 0, \tag{2.6}$$

$$\frac{\partial B_\perp}{\partial t} = \frac{1}{r\sqrt{f}}\frac{\partial}{\partial r}\left[r\sqrt{f}\left(v_\perp B_r - v_r B_\perp\right)\right], \tag{2.7}$$

where ρ, $\mathbf{v}$, p, e, and $\mathbf{B}$ are the density, velocity, pressure, specific energy, and magnetic field strength, respectively. The subscripts r and $\perp$ denote the radial and perpendicular components of each variables. And d/dt and $\partial/\partial t$ denote the Lagrangian and Eulerian derivatives, respectively. F_c is the thermal conductive flux, and q_R is the radiative cooling term. For the thermal conductive flux we assume Coulomb collision that is described as follow;

$$F_\mathrm{c} = \kappa_0 T^{5/2}\left(\frac{dT}{dr}\right), \tag{2.8}$$

where T is the gas temperature, and $\kappa_0 \approx 10^{-6}$ in cgs unit. The effect of the super-radial expansion of the magnetic flux tubes is appeared as the factor $r\sqrt{f}$. We use a second-order Godunov scheme for MHD with the Method of Characteristics for Alfvén waves and Constrained Transport (MOC-CT; Sano et al., 1999). We note that we assume the ideal MHD condition in this chapter; the effects of magnetic diffusion is ignored here.

2.1.3 Boundary Conditions and Setups

In the simulations for the solar and stellar winds (Suzuki and Inutsuka, 2005, 2006; Suzuki, 2007; Suzuki et al., 2013), the photosphere was chosen as the inner boundary. In our calculations, we set the inner boundary at the position that gives $p_0 = 10^5\,\mathrm{dyn\,cm^{-2}}$ ($= 0.1\,\mathrm{bar}$). We fix the temperature at the inner boundary to the given surface temperature, T_0, which can be treated as a free parameter. The density at the inner boundary is determined to give p_0 with the corresponding temperature. The outer boundary radius is set to 360 planetary radii, and total number of grids is 6000. At the innermost region, dr is fixed to 0.0001 planetary radii, and dr increases gradually as the distance from the surface.

Since the strength and the configuration of the magnetic fields of hot Jupiters have large uncertainties, we set up an open magnetic flux tube referring to the observation of the Sun. Recent observations by the *HINODE* satellite showed that the footprints of open flux tubes in polar region are anchored to so-called lH patches (Tsuneta et al., 2008; Ito et al., 2010; Shiota et al., 2012). The strength of the magnetic fields is approximately the equipartition to the internal energy of the gas. The magnetic field lines are super-radially open as the distance from the surface, and the cross section is typically expand with a factor of 1000, which represent that the filling factor of the open magnetic flux tubes at the photosphere is on the order of 1/1000. Therefore, the typical strengths of the magnetic fields in the corona are on the order of 1 G. From these properties of the magnetic fields, we assume that the magnetic pressure which is determined by the strength of the radial magnetic field strength is comparable to the gas pressure at the surface. In other words, we assume that plasma β

$$\beta = \frac{8\pi p}{B^2} \tag{2.9}$$

becomes unity at the inner boundary (Cranmer and Saar, 2011). In out setups, the boundary condition for the strength of the radial magnetic field is $B_{r,0} = 1.59\,\mathrm{kG}$. The filling factor at the inner boundary is set to be $f_0 = 1/1600$ to satisfy that the average field strength contributed from the open magnetic flux tube regions is ≈ 1 G.

For the boundary condition of the temperature, we use the typical surface temperature of the hot Jupiter, $T_0 = 1000\,\mathrm{K}$ as the standard case for our calculations. Of course this value changes if we consider another surface temperature of gaseous planets, for example, hotter/cooler gaseous planets. We inject velocity perturbations at the planetary surface with amplitude $\delta v_0 = 0.2 c_{\mathrm{s},0}$ for the standard case, where δv_0 is the velocity dispersion at the surface,

and $c_{s,0}$ is the sound speed at the surface. Here we assume a broadband spectrum of δv_0 in proportion to $1/\nu$, where ν denotes frequency of the perturbations.

For the standard case of our setups, we used the height of the magnetic loop, $h_1 = 0.5r_0$. This value corresponds to the height where the open magnetic flux tubes open most rapidly (see schematic picture of Figure 2.1). This height changes with the parameters. We assume that this height is controlled by the pressure scale height of the atmosphere, so if we change the surface temperature T_0, h_1 also changes in proportion to T_0.

2.1.4 Origin of the Velocity Dispersion

The origin of the velocity dispersion at the photosphere of the Sun is considered to be the turbulence because of the surface-convective layer. The velocity dispersion caused by the turbulence at the photosphere of the Sun is $\sim 20-30\%$ of the sound speed(Matsumoto and Kitai, 2010). However, the value of the velocity dispersion at the surface of exoplanets is unknown. In addition, the radiative-convective boundary in atmosphere of hot Jupiters locates in a deep interior region ($\geq$1 bar; Burrows et al., 2003; Fortney et al., 2007) because of the strong irradiation from the central star. The irradiation pushes down the radiative-convective boundary, so the typical hot Jupiters are thought to have a thick outer radiative layer.

However, convective overshoot and propagating waves from the convective region may be one of the source of the δv in out setups. Moreover, there can be turbulence at the planetary surface that is caused by the mechanism differ from convection. One example is the strong atmospheric flow or circulation at the surface of gaseous planets. Recently, three-dimensional models of the global atmospheric circulation in the gaseous planets have been developed, and these works have been suggested that some hot Jupiters have the strong atmospheric circulation, and speed of the equatorial winds can reach $2-5\,\mathrm{km\,s^{-1}}$ (e.g., Showman and Guillot, 2002; Cooper and Showman, 2005; Dobbs-Dixon and Lin, 2008). These results suggest that the supersonic atmospheric circulation can be driven on the surface of the hot Jupiters; therefore, the turbulence may be generated by the strong circulation.

2.1.5 A Radiative Cooling Term

We assumed that the composition of the atmosphere of hot Jupiters is same as the solar metallically gas, and the radiative cooling term (q_{R} in Equation (2.6)) from the solar abundance gas. In the simulations for the solar and stellar winds (Suzuki and Inutsuka, 2005, 2006;

Suzuki, 2007; Suzuki et al., 2013), the optically thin radiative cooling for the solar coronal plasma (Landini and Monsignori Fossi, 1990; Sutherland and Dopita, 1993), and the empirical radiative cooling function for the chromospheric gas that takes into account optically thick effects based on observations of the solar chromosphere (Anderson and Athay, 1989a) are used.

However, the typical surface and atmospheric temperatures of hot Jupiters are lower than the solar chromosphere, so we have to prescribe the radiative cooling for the gas with lower temperature down to $\sim$ 1000 K. Here we adopt a simple treatment by extrapolating the empirical cooling rate of the solar chromosphere (Anderson and Athay, 1989a). We extrapolate the cooling rate as follows; it is proportional to the gas density, $4.5 \times 10^9 \rho$ ($\mathrm{erg\,cm^{-3}\,s^{-1}}$). We switch off the cooling when the gas temperature becomes lower than the surface temperature T_0. This treatment of the radiative cooling is probably too simplified as describe in Tanaka et al. (2014), so we improve this part in a later section.

2.2 Dependence on the Velocity Dispersion

First, we show the relation between the velocity dispersion of the magnetic field at the surface of planets and the mass-loss rate from gaseous planets as well as the atmospheric structure.

2.2.1 Dependence of the Mass-Loss Rate

The relation between the velocity dispersion at the surface of planets and the mass-loss rate is appeared in Figure 2.2. As seen in Figure 2.2, the mass-loss rate increases with an increase of the velocity dispersion at the surface, because the larger velocity dispersion means that the larger energy is deposited to the magnetic fields. In the low-velocity dispersion region below $\sim 0.3 c_\mathrm{s}$, the mass-loss rate increases very rapidly with δv, but in the high-velocity dispersion region above $\sim 0.3 c_\mathrm{s}$, the increase of the mass-loss rate seems to saturate. This result suggests that there may be an upper limit of the mass-loss rate that is driven by the MHD waves.

Several observations suggest that the mass-loss rates of some hot Jupiters are around orders of $10^{10}\,\mathrm{g\,s^{-1}}$, therefore our results are consistent with the observations when the value of the velocity dispersion is larger than $\sim 0.2 c_\mathrm{s}$. Additionally, many previous works on the XUV-driven escape from hot Jupiters also suggest that the similar amount of the mass-loss rates. Therefore, the resultant mass-loss rate that is driven by the MHD waves can be comparable to that is driven by the XUV irradiation.

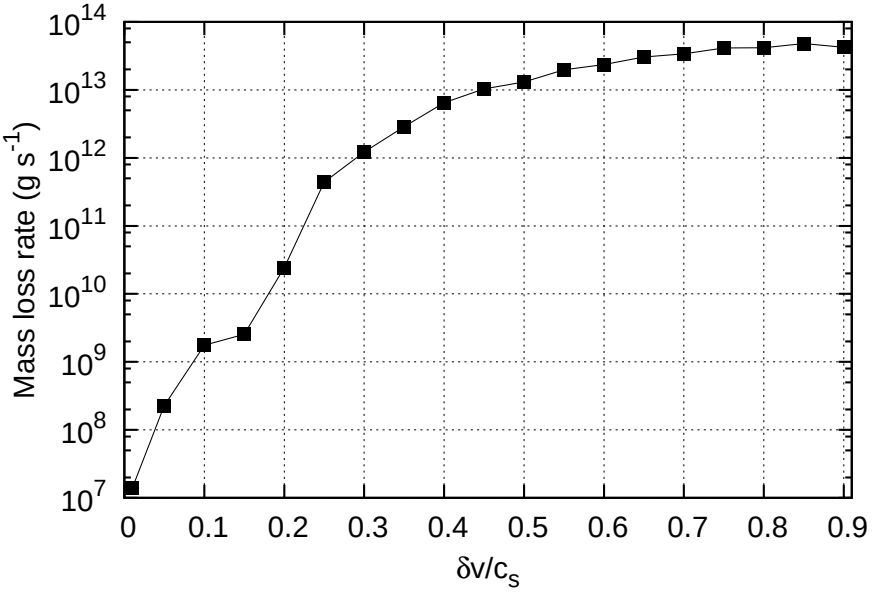

Figure 2.2: Relation between the value of the velocity dispersion at the surface of planets and the mass-loss rate from the planets. The horizontal axis is the velocity dispersion that is normalized by the sound speed at the surface. The vertical axis is the mass-loss rate in units of $\mathrm{g\,s^{-1}}$. In these calculations we assumed that the radius and mass of the planet is same as Jupiter, and the surface temperature is fixed to 1000 K.

2.2.2 Atmospheric Structures

The structures of the temperature, density, and radial velocity of the atmosphere are shown in Figure 2.3. The temperature in the lower atmosphere is almost constant, and the value is same as the surface temperature. In the upper atmosphere, the temperature increases rapidly and reaches $\sim$ 10,000 K, thus a corona-like region is created in the upper atmosphere because of the dissipation of the MHD waves, whereas the temperature is much lower than the temperature of the solar corona ($\sim 10^6$ K). The density profiles in the lower atmosphere are almost same in each values of the velocity dispersion because the dissipation of the MHD waves is insufficient in that region where the gas pressure is dominant. The density profiles change in the upper atmosphere where the temperature rises rapidly. When the velocity dispersion is larger, much amount of gas can be uplifted.

2.2.3 Saturation of the Mass-Loss Rate

As shown in Section 2.2.1, the mass-loss rate seems to saturate in the high-velocity dispersion region. The mass-loss rate is obtained from product of the gas density and radial velocity at

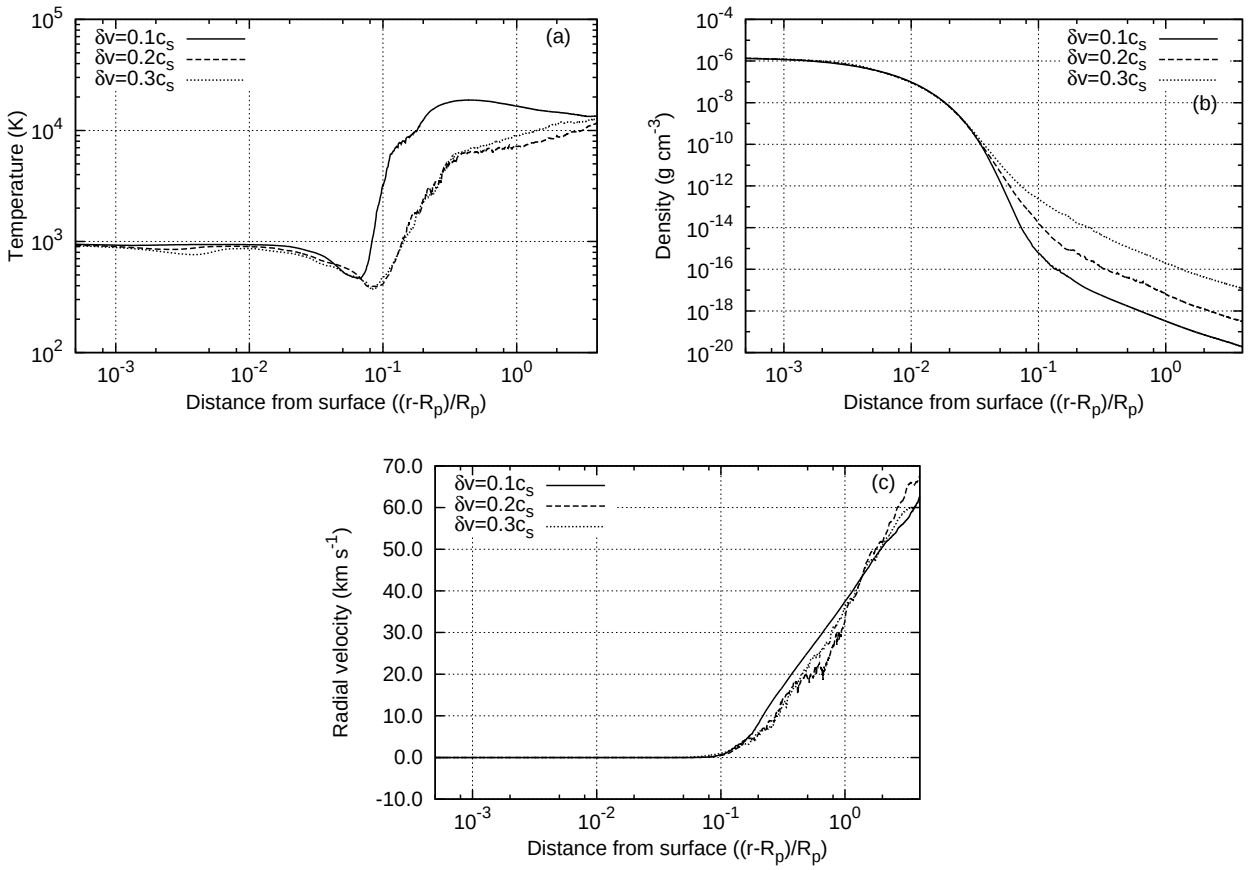

Figure 2.3: Velocity dispersion dependence of the atmospheric structures. (a) is the temperature structure, (b) is the density profile, and (c) is the radial velocity profile. The horizontal axes denote the distance from the surface of the planet that is normalized by the radius of the planet. The solid, dashed, and dotted lines correspond to the values of the velocity dispersion, $0.1c_{\rm s}$, $0.2c_{\rm s}$, and $0.3c_{\rm s}$, respectively.

some radius. It means that the mass-loss rate increases when the gas density in the upper atmosphere becomes larger and/or the radial velocity in the upper atmosphere becomes faster. When the value of the velocity dispersion is relatively small, the density in the upper atmosphere increases with the increase of the velocity dispersion, and the radial velocity profiles are almost same as shown in Figure 2.3. Subsequently, the increase of the mass-loss rate is determined by the increase of the density in the upper atmosphere, and the mass-loss rate increases rapidly in the low-velocity dispersion region.

However, things are changed in the high-velocity dispersion region. Figure 2.4 shows the density profile and radial velocity profile in many cases of the values of the velocity dispersion. The increase of the density in the upper atmosphere becomes gradual in the larger velocity dispersion cases. Additionally, the radial velocity in the upper atmosphere decreases as the

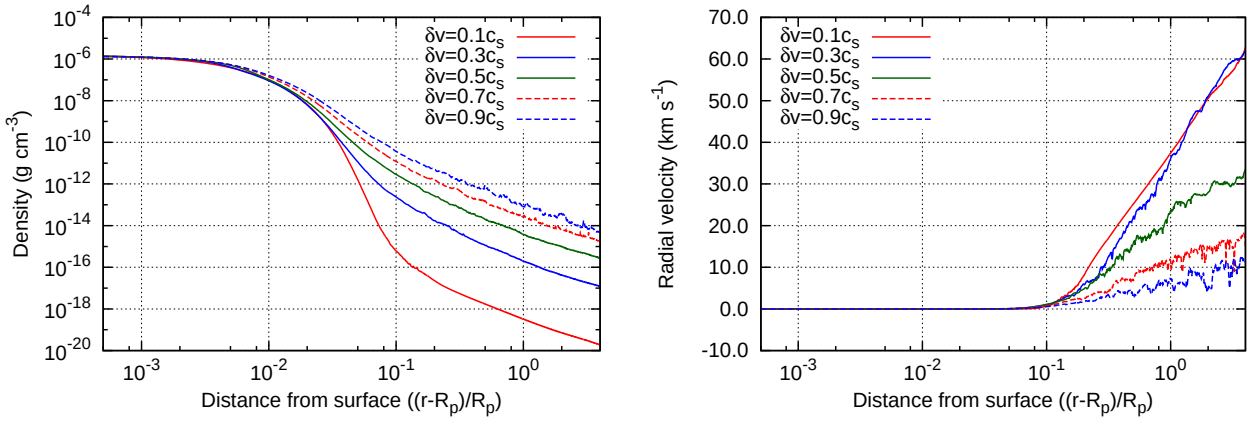

Figure 2.4: Velocity dispersion dependence of the density profile (left) and radial velocity profile (right) in many values of the velocity dispersion. The horizontal axes are same as Figure 2.3. The red solid, blue solid, green solid, red dashed, and blue dashed lines correspond to the value of the velocity dispersion, $0.1c_{\rm s}$, $0.3c_{\rm s}$, $0.5c_{\rm s}$, $0.7c_{\rm s}$, and $0.9c_{\rm s}$, respectively.

velocity dispersion becomes larger. These aspects cause the saturation of the mass-loss rate in the Figure 2.2.

Although the increase of the density of the upper atmosphere causes the increase of the mass-loss rate, it also enhances the radiative cooling from the upper atmosphere because the cooling rate is proportion to ρ^2 in the optically thin limit. Hence, a larger fraction of the injected energy is lost by the radiative cooling rather than transferred to the kinetic energy of the escaping atmosphere (Suzuki et al., 2013). In fact, efficient radiative cooling from the upper atmosphere due to higher density suppresses the increase of the mass-loss rate.

2.2.4 Time Variability of the Mass-Loss Rate

In our calculations, the physical properties in the upper atmosphere such as the density, temperature, radial velocity have large time variation. Therefore, the atmospheric escape that is driven by the MHD waves is a dynamical phenomena, and the mass-loss rate also has large time variation.

Figure 2.5 shows the time variability of the mass-loss rate and its dependence on the velocity dispersion. When the velocity dispersion is $0.2c_{\rm s}$, the time-averaged mass-loss rate is $\sim 2.4 \times 10^{10}\,{\rm g\,s^{-1}}$. However, the mass-loss rate varies in several orders of magnitude as shown in Figure 2.5. The minimum mass-loss rate is $\sim 10^{9}\,{\rm g\,s^{-1}}$, and the maximum is $\sim 10^{11}\,{\rm g\,s^{-1}}$ when the velocity dispersion is $0.2c_{\rm s}$. If the velocity dispersion is larger, although the time-variability is seen, its range of variation becomes smaller (the blue and green lines in the figure). These results

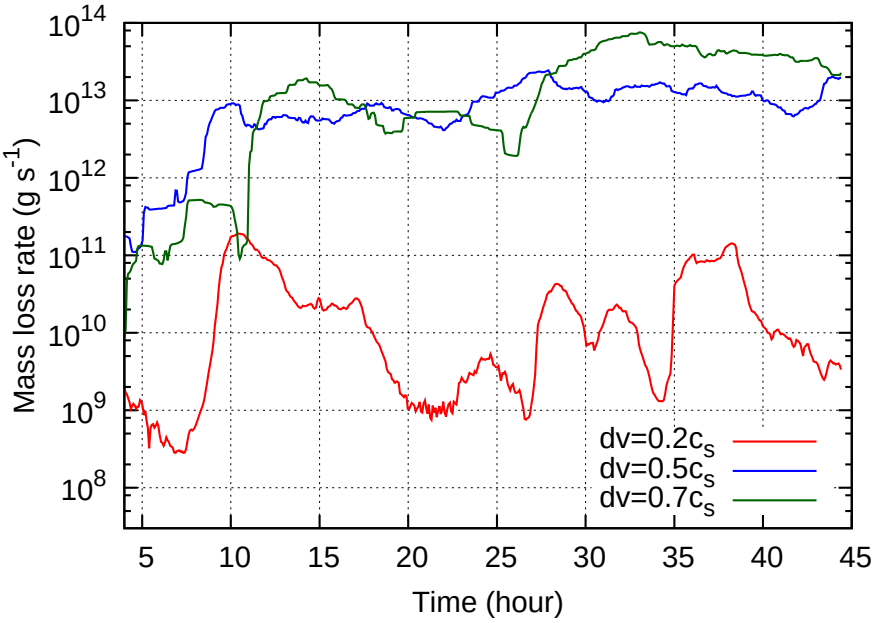

Figure 2.5: Time variability of the mass-loss rate. The horizontal axis is time in units of hour, and the vertical axis is the mass-loss rate in units of $\mathrm{g\,s^{-1}}$. The red, blue, and green lines correspond to the value of the velocity dispersion, $0.2c_\mathrm{s}$, $0.5c_\mathrm{s}$, and $0.7c_\mathrm{s}$, respectively. For all cases, the radius and mass are set to the values same as Jupiter, and the surface temperature is set to 1000 K.

suggest that the atmospheric escape that is driven by the MHD waves have large fluctuation whose timescale is several hours.

In addition, the results also predict the existence of the variability of the mass-loss rate that is not correlated with XUV activities of the host star. If the dominant driving mechanism of the mass loss is the XUV-driven escape, the mass-loss rate is mainly determined by the strength of the XUV irradiation from the central star. Therefore, when the central star is magnetically active and has large time-variation in the X-ray and extreme ultraviolet radiation, heating by the XUV radiation also varies, and a resultant mass-loss rate should have time-variability. Good examples of that kind of variation are strong X-ray emission from stellar corona, and/or transient emission events such as stellar flares. Thus, if the time-variability of the mass-loss rate and upper atmospheric structure are correlated with the stellar activities which can be observed in the optical, UV, and X-ray, the variability may be caused by the stellar activities. However, if the correlation is weak or not seen, the variability may be caused by magnetic activities of the planet itself; magnetically driven escape.

2.3 Dependence on the Radius and Mass

Next we show the dependence of the mass-loss rate and atmospheric structure on the radius and mass of the planets. As shown in Figure 1.1, the radius and mass of the exoplanets are rich in diversity. Of course this trend is same for hot Jupiters, thus we treat them as parameters. We change the radius of hot Jupiters from $0.8R_{\rm J}$ to $2R_{\rm J}$, and the mass from $0.3M_{\rm J}$ to $1.5M_{\rm J}$.

2.3.1 Radius Dependence of the Atmospheric Structures

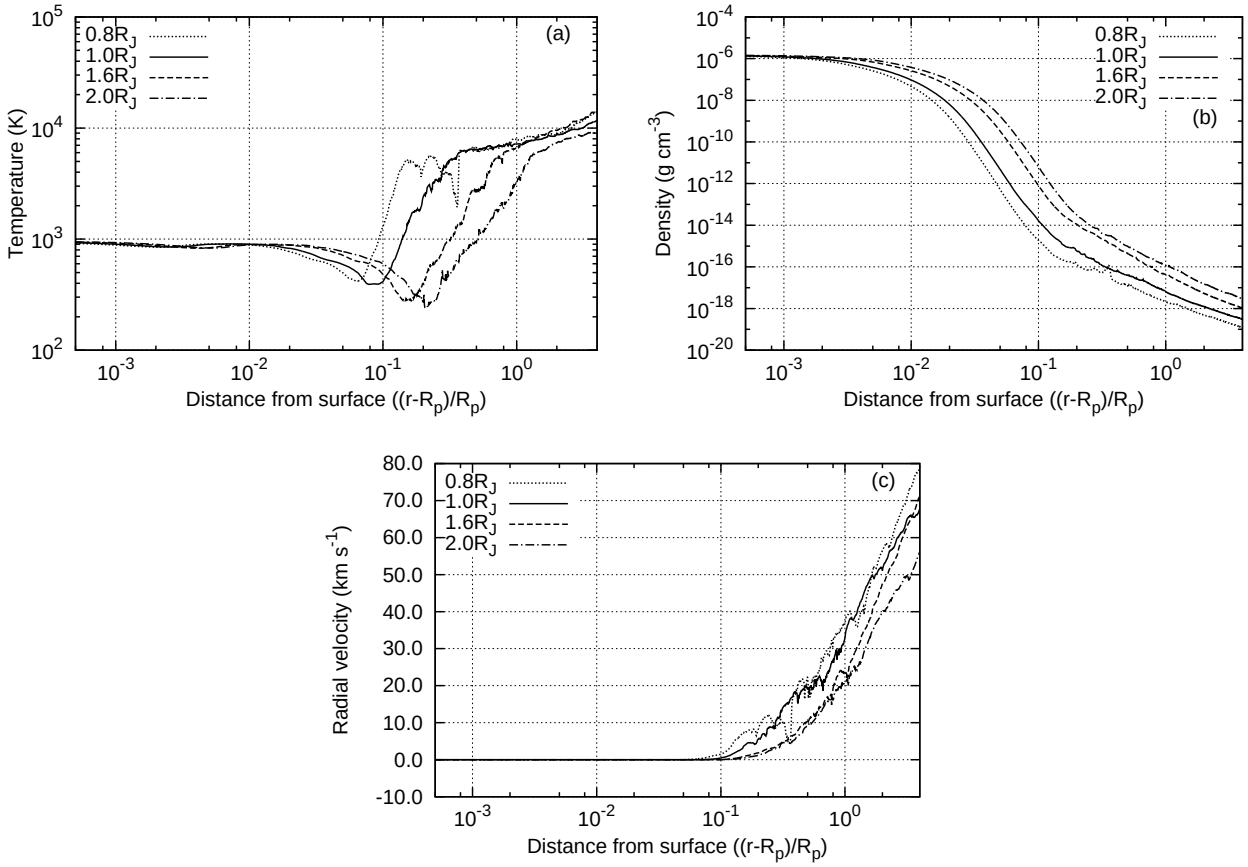

Figure 2.6: Planetary radius dependence of the atmospheric structures. (a) is the temperature structure, (b) is the density profile, and (c) is the radial velocity profile. The horizontal axes denote the distance from the surface of the planet that is normalized by the radius of the planet. The dotted, solid, dashed, and dot-dashed lines correspond to the radii of planets, $0.8R_{\rm J}$, $1R_{\rm J}$, $1.6R_{\rm J}$, and $2.0R_{\rm J}$, respectively. The surface temperature is set to 1000 K.

Figure 2.6 shows the relations between the atmospheric structures and the radius of the planets. The temperatures of the upper atmosphere become $\sim 10^4$ K in all cases, but heating starts at a lower altitude when the radius is smaller. The density profiles show similar shapes,

but the density in the upper atmosphere is higher when the radius become larger. Similarly, the radial velocity profiles also indicate similar trend in each cases, but become slightly faster in the cases when the radius is smaller, because the escape velocity that is determined by the surface gravity changes.

2.3.2 Mass Dependence of the Atmospheric Structures

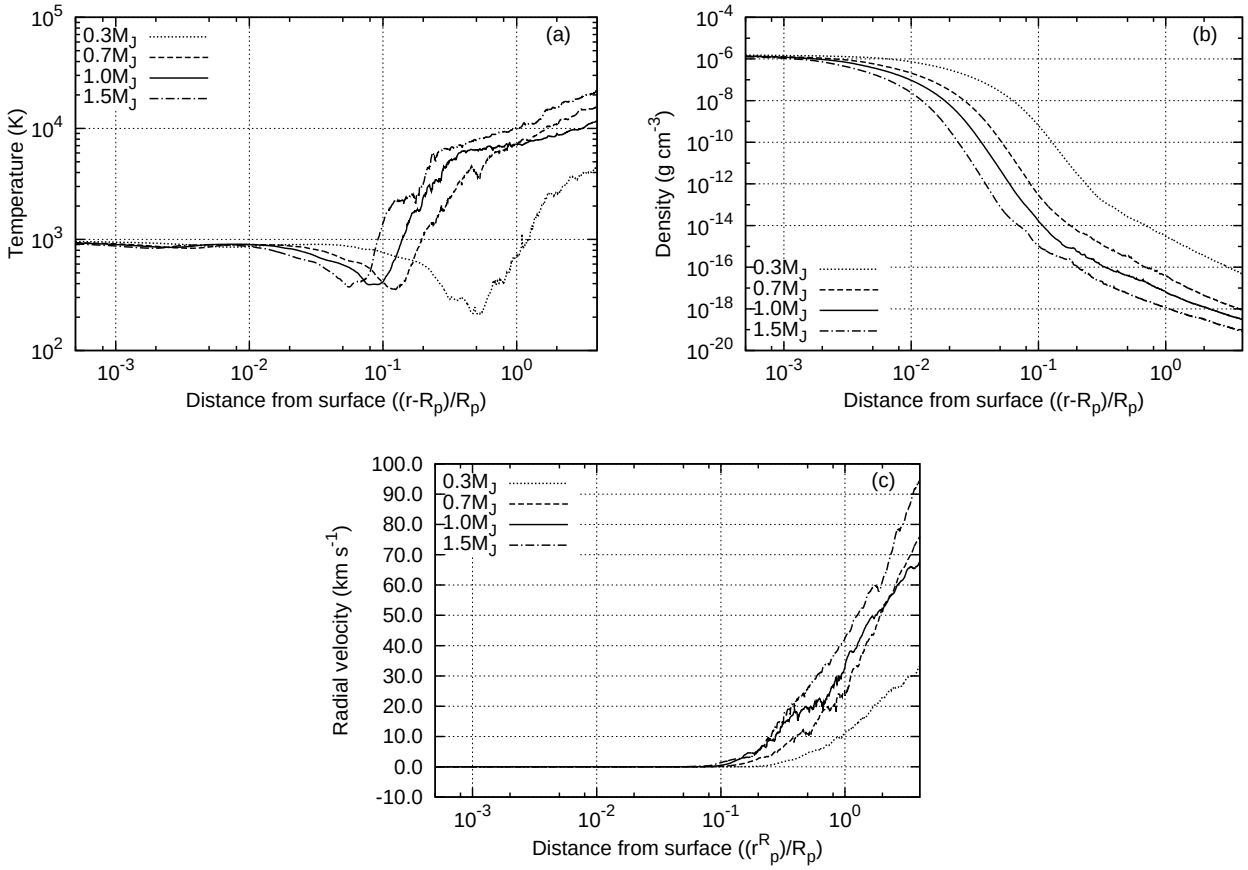

Figure 2.7: Planetary mass dependence of the atmospheric structures. (a) is the temperature structure, (b) is the density profile, and (c) is the radial velocity profile. The horizontal axes denote the distance from the surface of the planet that is normalized by the radius of the planet. The dotted, dashed, solid, and dot-dashed lines correspond to the masses of planets, $0.3M_{\rm J}$, $0.7M_{\rm J}$, $1.0M_{\rm J}$, and $1.5M_{\rm J}$, respectively. The surface temperature is set to 1000 K.

Figure 2.7 shows the relation between the atmospheric structures and the mass of the planets. General trends are similar to Figure 2.6. For example, the radial velocity in the case of $0.3M_{\rm J}$ is particularly slow compared with the other cases. This is because the radial velocity is roughly scaled by the escape velocity $\propto \sqrt{M_{\rm p}/R_{\rm p}}$.

In addition, the density in the upper atmosphere becomes very high in the $0.3M_{\rm J}$ case, and the temperature in the upper atmosphere becomes significantly lower. Since the surface gravity is smaller in the $0.3M_{\rm J}$ case, a large amount of the gas can be lifted up by the dissipation of the MHD waves. However, denser gas is more difficult to heat up, and the radiative cooling from the denser gas becomes efficient, thus these trends in Figure 2.7 appear.

2.3.3 Dependence of the Mass-Loss Rate

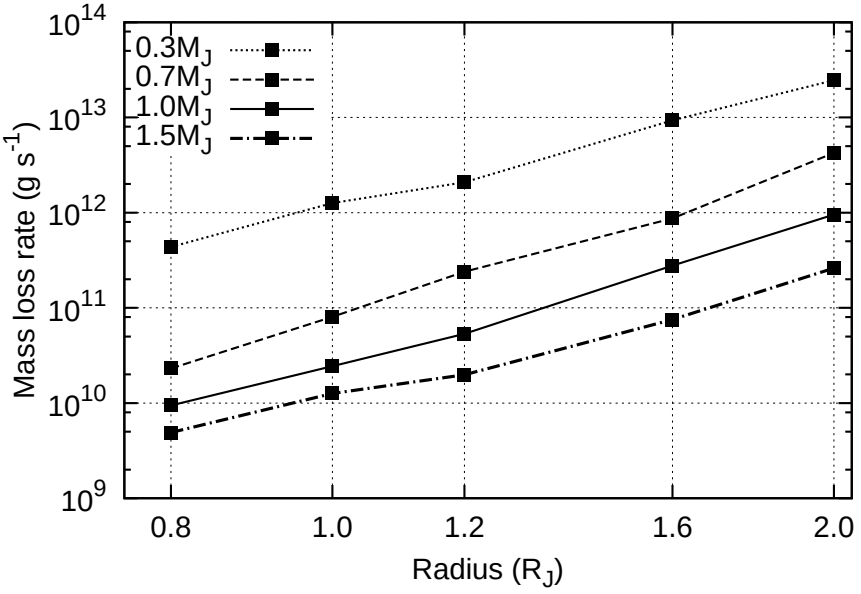

Figure 2.8: Dependence of the mass-loss rate on the radius and mass of the planets. The horizontal axis is the radius of the planets that is normalized by the radius of Jupiter, and the vertical axis is the mass-loss rate in the units of $\mathrm{g\,s^{-1}}$. Note that both axes are logarithmic scale. The dotted, dashed, solid, and dot-dashed lines correspond to the masses of the planets, $0.3M_{\rm J}$, $0.7M_{\rm J}$, $1.0M_{\rm J}$, and $1.5M_{\rm J}$, respectively. The surface temperature is set to 1000 K in all cases.

Figure 2.8 shows the dependence of the mass-loss rate on the radius and mass of the planets. When the radius of the planet is small, the mass-loss rate becomes smaller, and when the radius is large, the mass-loss rate becomes larger. The mass-loss rate increases by an order of magnitude when the radius is doubled. The mass-loss rate also changes drastically with the mass; in the case of a lighter planet, it becomes a very large value. As shown in Figure 2.7, the radial velocity becomes quite slower and the density in the upper atmosphere becomes larger in the lighter planet. Therefore, it can be said that slow and dense planetary wind blows out from a lighter planet, and fast and low-density wind blows out from a heavier planet.

2.3.4 Parameter Dependence of the Mass-Loss Rate

The mass-loss rate seems to be related to the scale height of the atmosphere. Here we derive a parameter dependence of the mass-loss rate from the atmospheric structure and the injected energy. In out model, atmosphere is heated up rapidly due to the dissipation of the MHD waves, and then the atmospheric escape is driven. The mass-loss rate seems to depend on the density of the region where the atmospheric gas is accelerated, and its density varies with the scale height of the atmosphere.

The mass-loss rate and other parameters are expected to be related by the following equiation

$$\frac{1}{2}\dot{M}v_{\rm esc}^2 \propto 4\pi R^2 \rho(r_{\rm c})\, v_{\rm w}\langle \delta v^2 \rangle, \tag{2.10}$$

where $v_{\rm esc}$, $v_{\rm w}$, and δv are the escape velocity at the surface, Alfvén velocity, and velocity dispersion, respectively. The left-hand side denotes the kinetic energy transported by the planetary wind per unit time. The right-hand side is the energy flux at the transonic point where the radial wind velocity equals to the sound speed. The escape velocity is written as

$$v_{\rm esc} = \sqrt{\frac{2GM_{\rm p}}{R_{\rm p}}}. \tag{2.11}$$

To derive the parameter dependence of the mass-loss rate, first we assume that the atmosphere is in almost hydrodynamic equilibrium. Although the upper atmosphere is far from the hydrostatic equilibrium because of the dissipation of the MHD wave energy and the atmospheric escape, the hydrostatic density profile is still reasonable approximation below the region where the acceleration and heating occur. The density profile of the atmosphere in hydrostatic equilibrium determines the density at the acceleration region, and it controls the mass-loss rate. The hydrostatic equilibrium is denoted as

$$\frac{1}{\rho}\frac{dp}{dr} + \frac{GM_{\rm p}}{r^2} = 0. \tag{2.12}$$

By assuming isothermal flow, Equation (2.11) can be solved as follows;

$$\rho(r) = \rho_0 \exp\left(-\frac{r - R_{\rm p}}{H_0}\frac{R_{\rm p}}{r}\right), \tag{2.13}$$

where ρ_0 is the density at the surface, and H_0 is the pressure scale height of the atmosphere that denoted as

$$H_0 = \frac{k_{\rm B}T_0}{mg}, \tag{2.14}$$

where $k_{\rm B}$ is the Boltzmann constant, m is the mean molecular weight, and g is the gravitational acceleration at the surface. Combining this with Equation (2.10), we obtain

$$\dot{M} \propto \frac{R_{\rm p}^3}{M_{\rm p}} \exp\left(-\frac{G}{c_{\rm s}^2}\frac{r_{\rm c}-R_{\rm p}}{r_{\rm c}}\frac{M_{\rm p}}{R_{\rm p}}\right). \tag{2.15}$$

This is a semi-analytical description of the parameter dependence of the mass-loss rate. Since the acceleration point of the atmosphere $r_{\rm c}$ is around twice as large as the radius of the planet, $(r_{\rm c}-R)/r_{\rm c}$ is an order of unity. In addition, $c_{\rm s}$ is constant when we assume same surface temperature. Therefore, $(G/c_{\rm s}^2)(r_{\rm c}-R)/r_{\rm c}$ can be treated as a constant for simplification.

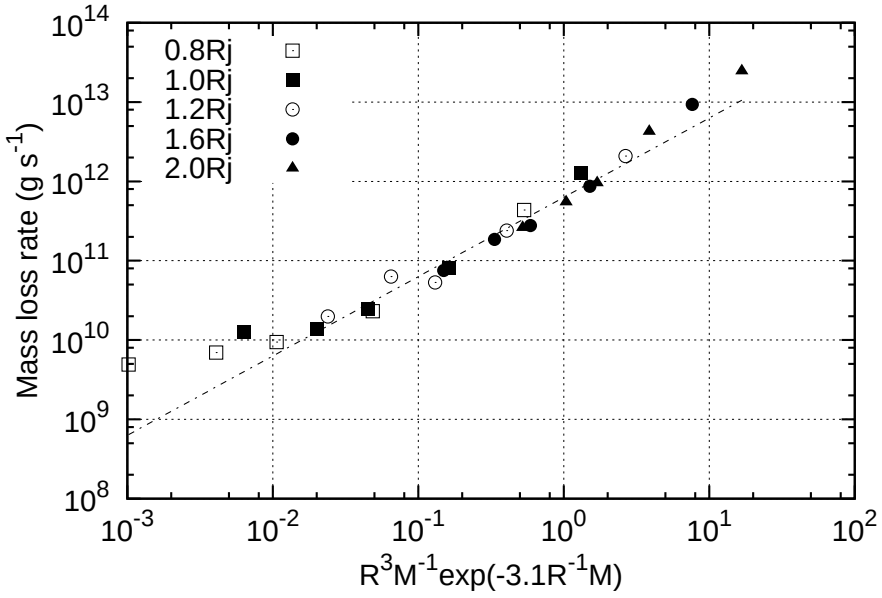

Figure 2.9: Comparison between the semi-analytical expression and the numerical simulations of the mass-loss rates. The horizontal axis is the semi-analytical form $R_{\rm p}^3 M_{\rm p}^{-1}\exp\left(-3.1R_{\rm p}^{-1}M\right)$, where the factor -3.1 is determined by fitting. The vertical axis is the mass-loss rate in units of $\mathrm{g\,s^{-1}}$. The dot-dashed line corresponds to $\dot{M} = R_{\rm p}^3 M_{\rm p}^{-1}\exp\left(-3.1R_{\rm p}^{-1}M\right)$.

This semi-analytically derived parameter dependence of the mass-loss rate on the radius and mass is shown in Figure 2.9. In these calculations, the velocity dispersion at the surface is fixed to 20% of the sound speed, and the surface temperature is set to 1000 K. The numerical results are basically consistent with the semi-analytical formula. At the leftmost region, difference between the semi-analytical expression and the numerical results become larger. This may be caused by the approximative treatment in the derivation.

2.4 Dependence on the Surface Temperature

In this section, we change the surface temperature of the planet. As we mentioned in the Introduction chapter, the discovered exoplanets and systems are very rich in diversity, for example the semi-major axis, and types of host stars. Therefore, the surface temperature of exoplanets is also rich in diversity, and it will be an important parameter for the atmospheric escape. Generally speaking, it is difficult to measure the surface temperature directly, but we can estimate the equilibrium temperature of exoplanets by using the separation between host stars and planets, and the effective temperature of the host stars.

The equilibrium temperature can be estimated by simple calculation of the energy balance of a planet. The total energy that a planet receives from the host star $E_{\rm in}$ is

$$E_{\rm in} = S_{\rm p}\pi R_{\rm p}^2 \left(1 - A_{\rm B}\right), \tag{2.16}$$

where $S_{\rm p}$ is the stellar flux at the distance of the orbit of the planet, $R_{\rm p}$ is the radius of the planet, and $A_{\rm B}$ is the Bond albedo. The right-hand side means that the energy that the planet receives which is written as the product of the stellar flux at the orbit, the cross section of the planet, and the fraction of the energy that the planet can receive. $S_{\rm p}$ is expressed by using the semi-major axis a and the luminosity of the star L_* as follows,

$$S_{\rm p} = \frac{L_*}{4\pi a^2}. \tag{2.17}$$

In addition, assuming the black body radiation from the surface of the star, the luminosity can be written as

$$L_* = 4\pi R_*^2 \sigma_{\rm SB} T_{\rm eff}^4. \tag{2.18}$$

where R_* is the radius of the star, $\sigma_{\rm SB}$ is the Stefan-Boltzmann constant, and $T_{\rm Jeff}$ is the effective temperature of the star, respectively. By substituting Equation (2.17) and (2.18) to (2.16), the equation becomes

$$E_{\rm in} = \left(\frac{R_*}{a}\right)^2 \pi R_{\rm p}^2 \left(1 - A_{\rm B}\right) \sigma_{\rm SB} T_{\rm eff}^4. \tag{2.19}$$

Next we consider the energy which is lost from the planet by radiation. Assuming the blackbody radiation and effective heat redistribution in the planetary atmosphere, the energy loss from the planet $E_{\rm out}$ can be denoted as follows;

$$E_{\rm out} = 4\pi R_{\rm p}^2 \sigma_{\rm SB} T_{\rm eq}^4, \tag{2.20}$$

where $T_{\rm eq}$ is the equilibrium temperature of the planet. The right-hand side of the equation means the product of the surface area and energy emitted from the surface in the unit area and the unit time with the temperature $T_{\rm eq}$. In the equilibrium state, $E_{\rm in}$ and $E_{\rm out}$ should be same. Therefore, from Equation (2.19) and (2.20), the equilibrium temperature of the planet can be derived as follows;

$$T_{\rm eq} = \left(\frac{R_{\rm p}}{a}\right)^{1/2} \left(\frac{1-A_{\rm B}}{4}\right)^{1/4} T_{\rm eff}. \tag{2.21}$$

We note that this derivation of the equilibrium temperature ignores the internal heat flux such as the contraction heat of gaseous planets. Although the internal heat flux is important for cold gaseous planets for example Jupiter and Saturn, it can be ignored in the condition of close-in planets because the irradiation is significantly strong. Therefore, the equilibrium temperature of the planet can be written by the radius and effective temperature of the host star, semi-major axis, and Bond albedo of the planet. If we assume typical values for hot Jupiters for the equation, it can be rewritten as follows,

$$T_{\rm eq} \simeq 1200\,{\rm K} \left(\frac{R_*}{R_\odot}\right)^{1/2} \left(\frac{a}{0.05\,{\rm AU}}\right)^{-1/2} (1-A_{\rm B})^{1/4} \left(\frac{T_{\rm eff}}{5500\,{\rm K}}\right), \tag{2.22}$$

where $R_\odot$ is the solar radius. Therefore, if assuming zero albedo, the equilibrium temperature of hot Jupiters becomes ~ 1200 K.

The stellar radius, effective temperature, and semi-major axis can be obtain from observations. However, the Bond albedo is difficult to observe. The Bond albedo of Jupiter is ~ 0.343 (Hanel et al., 1981), but it should differ in hot Jupiters because of presence of clouds with different composition, or lack of clouds in the atmosphere. Several theoretical works on the clouds and haze in the atmosphere of exoplanets and their albedo have been done (e.g., Sudarsky et al., 2000). Sudarsky et al. (2000) examined the impacts of the composition and altitude of clouds in gaseous planets with several ranges of the equilibrium temperatures, and showed the Bond albedo varies largely depending on the equilibrium temperature. In the case of cold gaseous planets such as Jupiter, NH_3 clouds contribute to the reflection, and the Bond albedo becomes $A_{\rm B} \sim 0.4 - 0.65$. In relatively cooler gaseous planets whose temperature is ~ 250 K, H_2O clouds strongly reflect the incident flux and albedo becomes much high, $A_{\rm B} \sim 0.9$. However, in the warm gaseous planets and hot Jupiter-type gaseous planets, Bond albedo becomes significantly low. In the warm and hot atmosphere, NH_3 and H_2O clouds cannot be created, and silicate clouds exist only in the deep region of the atmosphere, so they cannot contribute to the reflection. Additionally, because absorption of the alkali metals becomes strong

absorbers, the Bond albedo becomes significantly low, ~ 0.01. In the higher temperature, $\gtrsim$ 1500 K, however, the Bond albedo becomes higher again due to the presence of the silicate cloud in the high altitude, and the albedo is ~ 0.5 or higher. Therefore, according to the work by (Sudarsky et al., 2000), the Bond albedo of hot Jupiters can be both high and low depending on their temperatures. The significantly low albedo of hot Jupiters is also suggested by the observation of TrES-2 (Kipping and Spiegel, 2011). Although the dependence of the

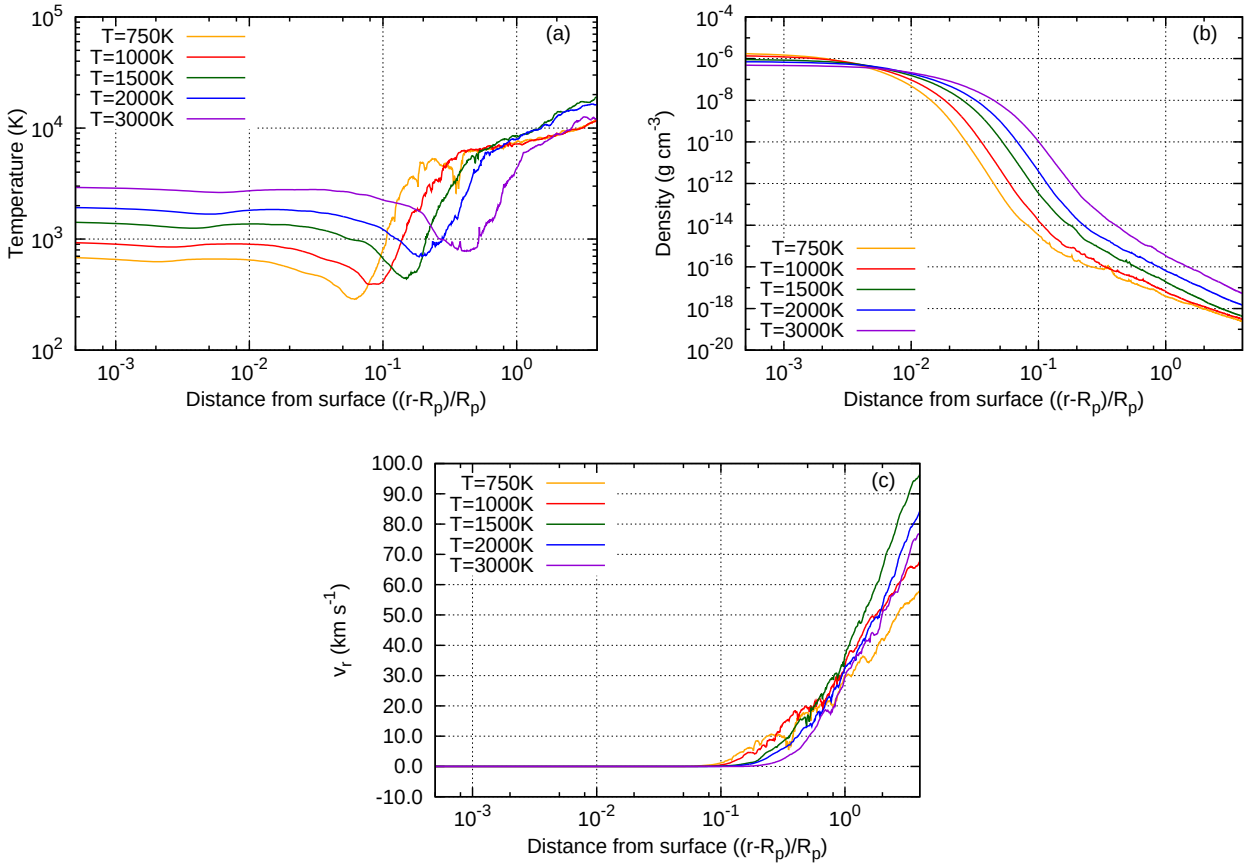

Figure 2.10: Surface temperature dependence of the atmospheric structures. (a) Temperature structure, (b) density profile, and (c) radial velocity profile, respectively. The horizontal axes denote the distance from the surface of the planet that is normalized by the planetary radius. The orange, red, green, blue, and violet lines correspond to the surface temperature, 750 K, 1000 K, 1500 K. 2000 K, 3000 K, respectively. The radius and mass are set to Jupiter's values, and the velocity dispersion is fixed to 20% of the sound speed at the surface..

equilibrium temperature on the Bond albedo is weak as shown in Equation (2.22), the surface temperature changes with the albedo because of the possible wide range of the Bond albedo as denoted in Sudarsky et al. (2000). In addition to this, properties of host stars and semi-major axis are also differ largely. For example, the equilibrium temperature of HD 209458b is

calculated to be $\sim$ 1200 K, HD 189733b is $\sim$ 1000 K, and WASP-103b is $\sim$ 2100 K by using Equation (2.22) and assuming $A_{\rm B} = 0.5$. If we assume $A_{\rm B} = 0$ for these planets (and it is not a bad assumption according to Sudarsky et al. (2000)), the equilibrium temperatures become $\sim$ 1500 K, $\sim$ 1200 K, and $\sim$ 2500 K, respectively. Therefore, simulations with a wide range of the surface temperature are necessary to investigate nature of the atmospheric escape from hot Jupiters. Here we change the surface temperature from 300 K to 3000 K.

Figure 2.10 shows the surface temperature dependence of the atmospheric structure. We show the cases for the surface temperature is 750 K , 1000 K, 1500 K, 2000 K, and 3000 K in the figure. As shown in the figure, the temperature is almost isothermal in the lower atmosphere in the all cases. In the upper atmosphere, since the heating by the dissipation of the MHD waves becomes important, temperature rises rapidly to $\sim 10^4$ K, same as the other simulations in Section 2.2 and 2.3. The altitude where the temperature rises rapidly is different in each case, and the altitude increases with the surface temperature. This trend is caused by the pressure scale height of the atmosphere. In these simulations, the value of the velocity dispersion at the planetary surface is fixed, and the radius and mass of the planet are also fixed. Thus the pressure scale height is the function of only the surface temperature. The pressure scale height is small when the surface temperature is low, so the density in the upper atmosphere becomes low. And then, the altitude where the heating by the dissipation is important becomes lower compared to the higher surface temperature cases. The difference of the pressure scale hight with the surface temperature is seen in Figure 2.10(b). For the cases of the lower surface temperature, the density decreases faster than the cases of the higher surface temperature. In all the cases, the radial velocity of the escaping atmosphere becomes fast, $\gtrsim 50\,{\rm km\,s^{-1}}$ in the upper atmosphere.

Figure 2.11 shows the dependence of the mass-loss rate on the surface temperature. As a general trend, the mass-loss rate is a increasing function of the surface temperature. This is natural because the amount of the energy injected to the magnetic fields increases with the surface temperature since we assumed that the value of the velocity dispersion at the planetary surface is 20% of the sound speed, and the sound speed is proportional to the square root of the temperature. When the surface temperature is high, more amount of the atmospheric gas is uplifted and the density in the upper atmosphere is enhanced, as shown in Figure 2.10(b), because the energy injection is large. The mass-loss rate of the $T_0 = 2000$ K case is about an orders of magnitude larger than that of the $T_0 = 1000$ K case. Therefore, the difference of the surface temperature is also important to evaluate the mass-loss rate and the atmospheric

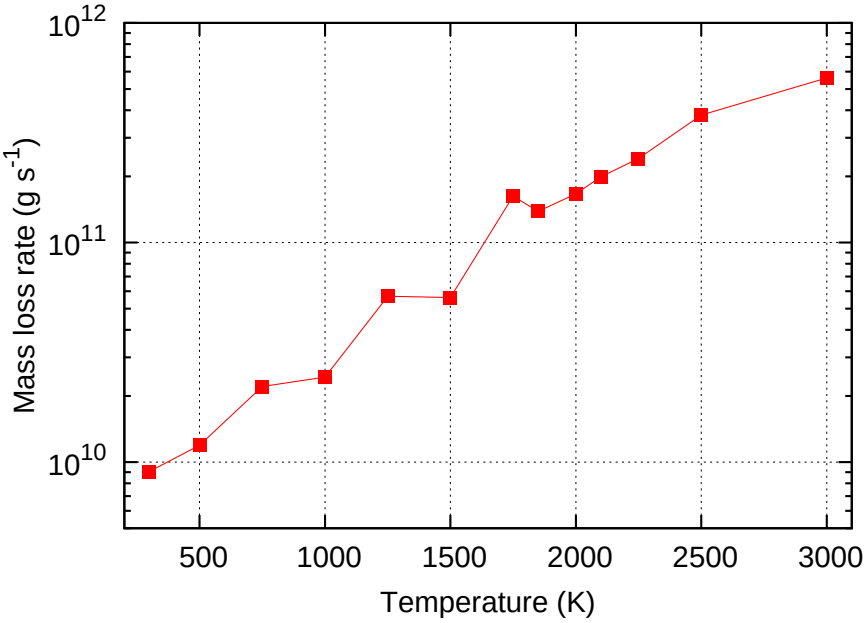

Figure 2.11: Dependence of the mass-loss rate on the surface temperature. The horizontal axis denotes the surface temperature, and the vertical axis denotes the mass-loss rate in units of $\mathrm{g\,s^{-1}}$.

structure.

In Figure 2.11, the dependence in the lower temperature down to 300 K is shown. In these calculations, even in the gaseous planets which cannot be called "hot Jupiters" the outflow is driven by the dissipation of the MHD waves. Therefore, these results suggest that this mechanism can occur not only in hot Jupiters, but also in warm Jupiters and cool Jupiters. However, the mass-loss rate in the case of the lower surface temperature may be overestimated, because in that range of the temperature, ideal MHD approximation are thought to be invalid. Non-ideal effects such as the ohmic dissipation will be significant and diffusion of the injected MHD waves will become large. Therefore, careful treatment of the ionization degree and magnetic resistivity is needed for more realistic calculation for the cases of the low surface temperature.

2.5 Dependence on the Magnetic Field Strength

In the previous sections we fixed the strength of the magnetic fields as described in Section 2.1. In this setups, the average field strength is almost same as that of Jupiter. Although several observations indicate the existence of the magnetic fields of some hot Jupiters, the strength of

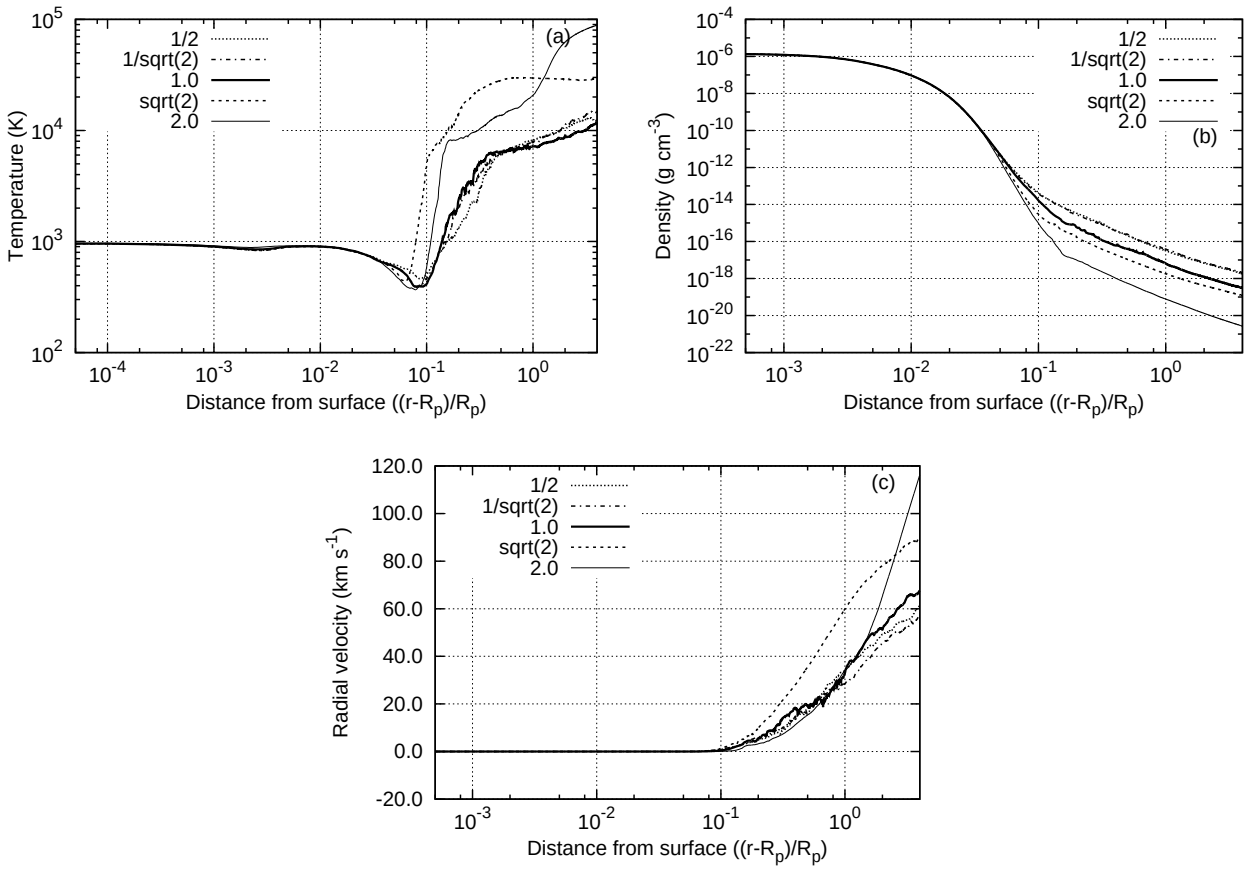

Figure 2.12: Dependence of the atmospheric structures on the strength of the planetary magnetic field. (a) Temperature structure, (b) density profile, and (c) radial velocity profile, respectively. The thick solid line denotes the structure in the standard case. The dotted, dot-dashed, dashed, and thin solid lines correspond to the strength of the magnetic fields that are 1/2, $1/\sqrt{2}$, $\sqrt{2}$, and 2 times that of the standard case. The surface temperature is set to 1000 K in all cases, the radius and mass are set to Jupiter's values, and the velocity dispersion is fixed to 20% of the sound speed.

the magnetic fields of hot Jupiters are still unknown, and it can be both stronger or weaker than Jupiter. Figure 2.12 shows the dependence of the atmospheric structures on the strength of the magnetic fields, and Figure 2.13 shows the dependence of the mass-loss rate on the strength of the magnetic fields.

As mentioned in Section 1.4.2, the observations and the several theoretical works of the hot Jupiter suggest that the magnetic fields might be weaker compared to Jupiter (Grießmeier et al., 2004; Sánchez-Lavega, 2004; Durand-Manterola, 2009; Koskinen et al., 2010; Kislyakova et al., 2014). Interestingly, our model suggests that the mass-loss rate can be large even if the strength of the magnetic fields is weaker than Jupiter. Thus, weak magnetic fields of hot

Jupiters may enhance the atmospheric escape. The density in the upper atmosphere decreases

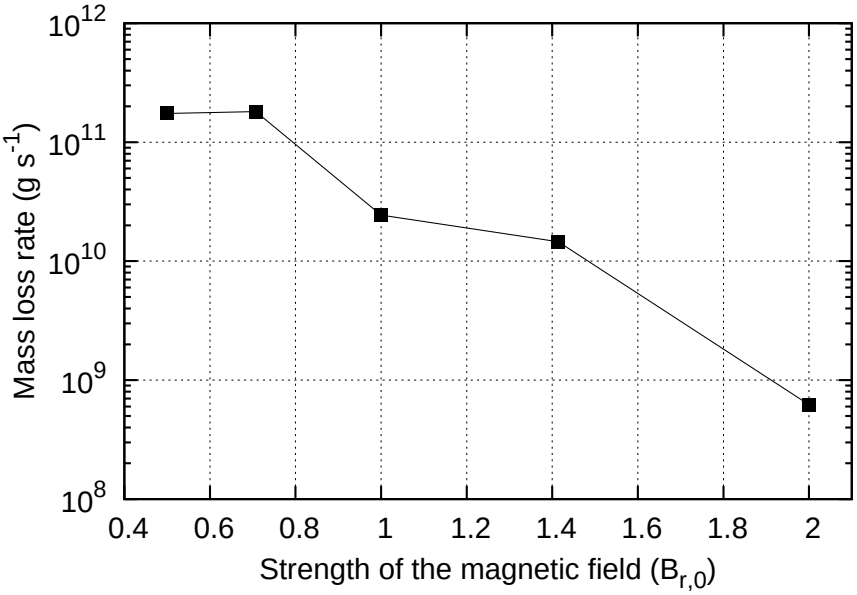

Figure 2.13: Dependence of the mass-loss rate on the strength of the magnetic fields. The horizontal axis shows the strength of the magnetic field that is normalized by the value at the surface of the planet that is described in Section 2.1.

with the increase of the strength of the magnetic field, and the radial velocity does not change substantially, therefore the mass-loss rate decreases with the strength of the magnetic fields. For the weaker magnetic filed case, the MHD waves are easy to dissipate in the upper atmosphere, and since the reflection of the waves in the atmosphere is suppressed because of the gradual decrease of the density, energy can be transported to the acceleration region of the planetary winds. This may cause the larger mass-loss rates in the weaker magnetic fields case, and the smaller in the stronger magnetic fields.

Chapter 3

Effects of Magnetic Diffusion in the Weakly-Ionized Atmosphere

In this chapter, we describe the non-ideal MHD calculation of the magnetically driven atmospheric escape and the atmospheric structures. The ideal MHD condition is assumed in the previous chapter, but the atmospheres of hot Jupiters are thought to be weakly-ionized condition because of their low temperature. Some parts in this chapter are previously published in Tanaka et al. (2014) and Tanaka et al. (2015).

3.1 Applicability of the Ideal MHD

In Chapter 2, we assumed the ideal MHD condition that requires good coupling between gas and magnetic fields. To fulfill this condition, sufficient amount of electrons are needed to couple field lines and weakly ionized gas, although required ionization degree can be as small as $10^{-10} - 10^{-5}$, whereas the actual value depends on the density. Since the typical surface temperature of hot Jupiters $\sim$ 1000 K is not so high, it is not clear whether or not the ideal MHD approximation is applicable for the calculation of the atmosphere of hot Jupiters. For this reason, here we look at the applicability of the ideal MHD approximation.

An induction equation is expressed as follows:

$$\frac{\partial \mathbf{B}}{\partial t} = \nabla \times (\mathbf{v} \times \mathbf{B}) - \nabla \times \eta (\nabla \times \mathbf{B}), \tag{3.1}$$

where η is magnetic resistivity. In this equation, $\eta = 0$ corresponds to the ideal MHD approximation because there is no diffusion of the magnetic fields. If the second term of the right-hand side dominates over the first term, the magnetic fields diffuse out, and the ideal MHD approximation is no longer valid. The most dominant source of the magnetic resistivity

in the atmosphere of hot Jupiters is thought to be the collision between electrons and neutral particles. The magnetic resistivity depends on temperature and an ionization degree, and it can be expressed as

$$\eta \approx 234 \frac{\sqrt{T\ (\mathrm{K})}}{x_\mathrm{e}}\ \left(\mathrm{cm^2\,s^{-1}}\right) \tag{3.2}$$

(e.g., Blaes and Balbus, 1994). It is useful to introduce a magnetic Reynolds number to estimate the applicability of the ideal MHD condition, and it is determined as

$$R_\mathrm{m} = \frac{vL}{\eta}, \tag{3.3}$$

where L is a typical length of a system. When the magnetic Reynolds number is quite a bit larger then unity, the ideal MHD approximation is applicable to the system. For the typical length of the system, we assume the typical wavelength of the Alfvén wave that we are injecting as a perturbation,

$$L \sim v_\mathrm{A}\tau \sim c_\mathrm{s}\tau. \tag{3.4}$$

In this equation, v_A is the Alfvén velocity and almost same as the sound speed c_s, because we assumed the equipartition of the gas pressure and the magnetic pressure for the magnetic flux tubes in out setups. Typical timescale τ is given approximately by the pressure scale height of the atmosphere divided by the sound speed at the surface. By assuming the properties of typical hot Jupiters, the typical timescale can be denoted as

$$L \sim 270\,\mathrm{km} \left(\frac{c_\mathrm{s}}{2.6\,\mathrm{km\,s^{-1}}}\right)\left(\frac{\tau}{100\,\mathrm{s}}\right). \tag{3.5}$$

From these equations, the magnetic Reynolds number is estimated as follows;

$$R_\mathrm{m} = 2.2 \left(\frac{v}{0.5\,\mathrm{km\,s^{-1}}}\right)\left(\frac{\tau}{100\,\mathrm{s}}\right)\left(\frac{x_\mathrm{e}}{10^{-8}}\right), \tag{3.6}$$

where v is normalized by the value of the velocity dispersion that we are using, $\delta v = 0.2 c_\mathrm{s}$. According to this magnetic Reynolds number, the ideal MHD approximation is not so bad in the atmosphere of hot Jupiters. In addition, the requirement for the ideal MHD approximation becomes more mild in the upper atmosphere, because the amplitude of Alfvén waves becomes larger due to the density decreases and the temperature becomes higher.

However, to evaluate non-ideal effects in the weakly-ionized atmosphere more detail, non-ideal MHD calculations are needed. Therefore, we perform numerical simulations that contain the effects of magnetic diffusion.

3.2 Model Description

3.2.1 Basic Equations for Non-Ideal MHD

As for our non-ideal MHD calculations, we basically follow the description in Chapter 2 and in Tanaka et al. (2014), except that we consider magnetic diffusion. In the basic equations of MHD (Equation (2.3 - 2.6)), the effects of the magnetic resistivity explicitly appear in the energy equation (Equation (2.6)) and induction equation (Equation (2.7)). In the non-ideal MHD condition, these two equations become as follows;

$$\rho\frac{d}{dt}\left(e+\frac{v^2}{2}+\frac{B^2}{8\pi\rho}-\frac{GM_{\rm p}}{r}\right)+\frac{1}{r^2 f}\frac{\partial}{\partial r}\left\{r^2 f\left[\left(p+\frac{B^2}{8\pi}\right)v_{\rm r}-\frac{b_{\rm r}}{4\pi}\left(\mathbf{B}\cdot\mathbf{v}\right)\right.\right.$$
$$\left.\left.-\frac{\eta}{4\pi}\frac{B_\perp}{r\sqrt{f}}\frac{\partial}{\partial r}\left(r\sqrt{f}B_\perp\right)\right\}\right]+\frac{1}{r^2 f}\frac{\partial}{\partial r}\left(r^2 f F_{\rm c}\right)+q_{\rm R}, \tag{3.7}$$

$$\frac{\partial B_\perp}{\partial t}=\frac{1}{r\sqrt{f}}\frac{\partial}{\partial r}\left[r\sqrt{f}\left(v_\perp B_r-v_r B_\perp\right)+\eta\frac{\partial}{\partial r}\left(r\sqrt{f}B_\perp\right)\right]. \tag{3.8}$$

The meanings of each characters are same as Equation 2.3 - 2.7. Note that the term with η in the Equation (3.7) indicates ohmic heating and the term with η in Equation (3.8) indicates diffusion of magnetic fields.

The magnetic resistivity can be calculated by Equation (3.2). Ionization degrees are determined by a method that is originally developed for Betelgeuse by Hartmann and Avrett (1984) (see also Harper et al., 2009). In this method, the ionization and recombination of H, C, Na, Mg, Al, Si, S, Ca, Fe, and K in the gas phase are calculated, and we adopt the solar abundance gas (Anders and Grevesse, 1989). Since the typical surface temperature of hot Jupiters is $\sim$ 1000 K and it is too low to ionize hydrogen, elements whose ionization energies are relatively low, such as Na and K, are the dominant ionizing sources in the lower atmosphere.

3.2.2 Poynting Flux

The behavior of the Alfvén waves in the atmosphere, such as propagation, reflection, and dissipation is a key to understand the atmospheric structure. In the ideal MHD simulations the dissipation of the Alfvén waves is done by nonlinear mode conversion. The fluctuations of the magnetic pressure associated with the Alfvén waves excite compressive waves. These waves eventually steepen to shocklets, which finally dissipate and heat the atmosphere (Tanaka et al., 2014). This process has been theoretically examined in terms of the heating of the solar corona and acceleration of the solar wind (Hollweg, 1982; Kudoh and Shibata, 1999; Suzuki

and Inutsuka, 2005). Recently, a radio observation by JAXA's spacecraft *Akatsuki* actually revealed that radial distribution of compressive waves in the solar corona, which supports this scenario (Miyamoto et al., 2014).

In the resistive MHD case, the magnetic diffusion also contributes to the dissipation of MHD waves. When the surface temperature is lower, the dissipation of the waves in the lower atmosphere where the magnetic resistivity is high affects the structure of the atmosphere. Therefore, an energetics argument of propagating MHD waves in the non-ideal MHD condition is important for understanding the properties of the atmospheric structures and resultant mass loss.

To evaluate the propagation, reflection, and dissipation of the Alfvén wave energy in the atmosphere, it is convenient to introduce Poynting flux which carried by the Alfvén waves. The net Poynting flux arising from magnetic tension, which represents the energy flux of the Alfvén waves measured from the comoving frame, can be written as follows:

$$F_{\rm P} = -B_{\rm r}\frac{v_\perp B_\perp}{4\pi} \tag{3.9}$$

The Poynting flux can be divided into an outward (parallel with $B_{\rm r}$) part and an inward (antiparallel with $B_{\rm r}$) part (Jacques, 1977; Cranmer et al., 2007; Suzuki et al., 2013). In order to evaluate the inward and outward Poynting flux, we introduce Elsässer variables,

$$z_\pm = v_\perp \mp \frac{B_\perp}{\sqrt{4\pi\rho}}. \tag{3.10}$$

By using the Elsässer variables, the net Poynting flux can be written as

$$F_{\rm P} = \frac{1}{4}\rho\left(z_+^2 - z_-^2\right)v_{\rm A}. \tag{3.11}$$

In this equation, $\rho z_+^2 v_{\rm A}/4$ and $\rho z_-^2 v_{\rm A}/4$ correspond to the outward and inward components of the Poynting flux, respectively. Although in our simulations we inject only the outward component of Alfvén waves from the surface, reflection in the atmosphere eventually generates the inward component.

3.3 Role of Ohmic Dissipation

In resistive MHD simulations, the propagation and dissipation of MHD waves are affected by the magnetic diffusivity, and accordingly the atmospheric structures would be modified. We

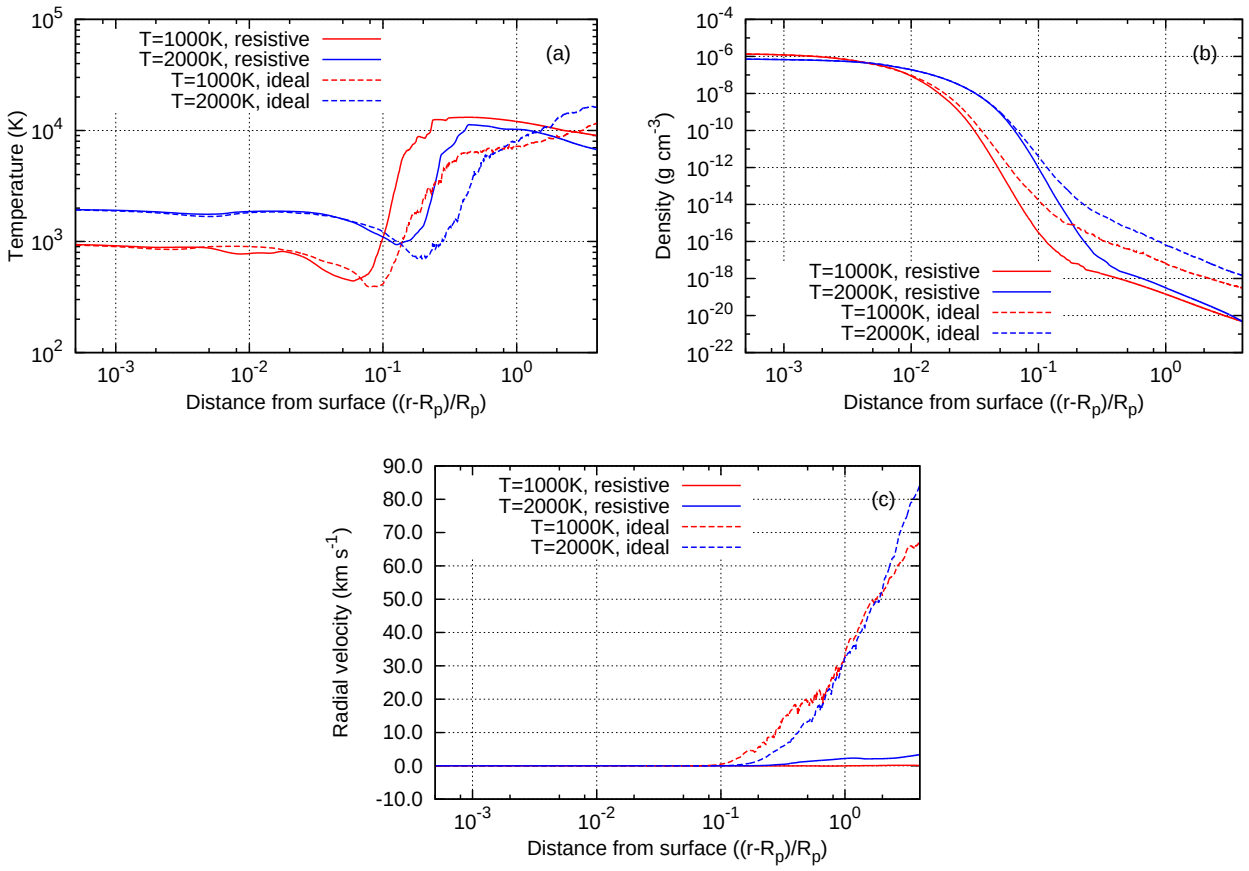

Figure 3.1: Comparison of the atmospheric structures between ideal and resistive MHD calculations. (a) Temperature structure, (b) density profile, and (c) radial velocity profile. The horizontal axes are distance from the planetary surface that is normalized by the planetary radius. The solid and dashed lines correspond to resistive and ideal MHD cases, respectively. The red and blue colors correspond to the surface temperature, T_0 = 1000 K, and 2000 K, respectively.

compare the ideal MHD and resistive MHD calculations and investigate how the magnetic diffusion affects the structures of planetary atmospheres and outflows.

Figure 3.1 compares the time-averaged atmospheric structures of resistive MHD cases with that of ideal MHD cases. In these figures, the radius and mass are fixed to the same value of Jupiter, and the velocity dispersion at the surface is set to 20% of the sound speed. The gas density in the upper atmosphere decreases more gradually in the ideal MHD cases (the dashed lines in (b)) because a larger amount of energy of the Alfvén waves can reach the upper atmosphere and lifts up the gas by the magnetic pressure associated with the waves. On the other hand, however, in the resistive MHD cases the Alfvén waves are damped in the cool atmosphere at low altitudes because of the high resistivity, and then the gas density sharply

drops without the support from the magnetic pressure. The Alfvén waves that enter the upper atmosphere can contribute to the acceleration of outflows from gaseous planets. The wind speeds are quite low in the resistive MHD cases, while the winds are accelerated to several tens of kilometers per second in the ideal MHD cases.

As a result, the mass-loss rates in the resistive MHD cases are much smaller than those in the ideal MHD cases, because the density in the upper atmosphere is around two orders of magnitude less than that of the ideal MHD cases, and the radial velocity is also much smaller. If a planet is isolated or has large distance from the central star, the planetary wind does not stream out in the resistive MHD condition except for intermittently driven outflows observed in the simulations because the average velocity is smaller than the escape velocity. However, if a planet is a hot Jupiter having small semi-major axis, the gas easily outflows from the small Roche lobe and will be blown away by the stellar wind from the central star.

In contrast to the large difference in the density and radial velocity profiles, the temperature structure of the resistive and ideal MHD cases are not so different from each other. Although the locations of the temperature inversion are slightly different, the upper atmospheres are heated up to $\sim 10^4$ K in both ideal and resistive MHD cases. The small difference in the altitudes of the temperature inversion is caused by the rapid decrease of the density in the resistive cases. Since the upper atmosphere becomes more less dense in the cases of resistive MHD calculations, the upper atmosphere slightly becomes easy to heat up by the MHD wave energy. Therefore, the heating by the dissipation of the MHD waves is still important in the atmosphere of the resistive cases, in particular for the upper atmosphere.

3.4 Dependence on the Surface Temperature

Here we show the relation between the surface temperature, T_0, of gaseous planets and the atmospheric structures, and then we discuss the dependence of the mass-loss rate. We fix the radius to Jupiter's radius, mass to Jupiter's mass, and the amplitude of the velocity dispersion to 20% of the sound speed at the surface. Therefore, larger T_0 corresponds to larger MHD wave energy that is deposited to the magnetic flux tube. The surface temperatures are thought to be mainly determined by the irradiation from the central star, more specifically, determined by the combination of the effective temperature of the central star and the semi-major axis of the planet. This implies that, in the framework of the MHD wave-driven planetary winds, when we take a planetary system that have a similar central star. properties of the mass loss from hot

Jupiters strongly depend on the distance from a central star. In fact, the surface temperature of gaseous planets also depends on the albedo and properties of the heat distribution in the atmosphere, such as day-night atmospheric flow or super rotation of the atmosphere.

3.4.1 Atmospheric Structures

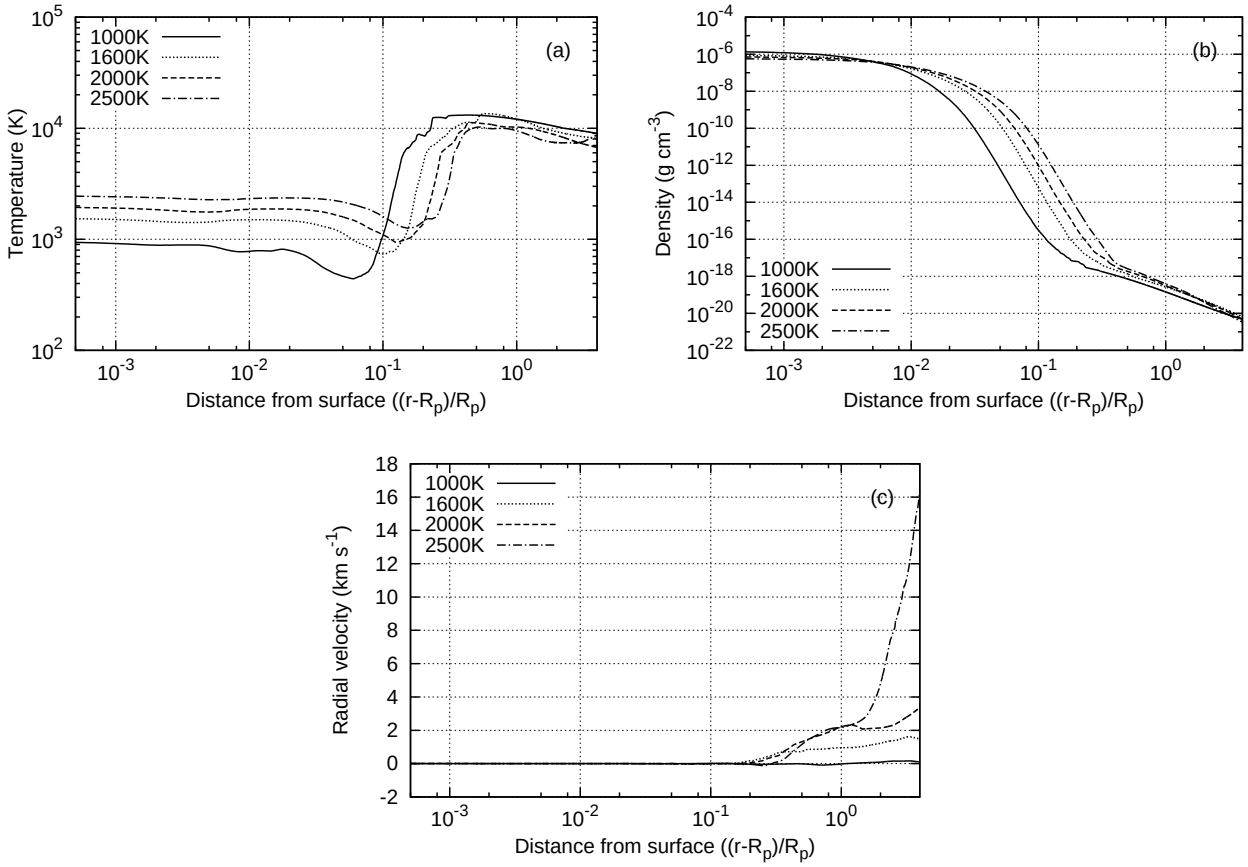

Figure 3.2: Surface temperature dependence of the atmospheric structures. (a) Temperature structure, (b) density profile, and (c) radial velocity profile. The horizontal axes denote the distance from the surface that is normalized by the planetary radius. The solid, dotted, dashed, dot-dashed lines correspond to $T_0 = 1000$, 1600, 2000, and 2500 K, respectively.

Figure 3.2 shows the dependence of the atmospheric structures on the surface temperatures. In all cases, the gas temperature in the lower atmosphere are almost isothermal, and they rise rapidly in the upper atmosphere because of the dissipation of the Alfvén waves. The dissipation of the energy in the upper atmosphere makes a high-temperature ($\sim$ 10,000 K) corona-like region around the hot Jupiters. In all the cases, a low-temperature region forms just below the location of the temperature inversion because of the adiabatic expansion of the gas. As

shown in Figure 3.2(a), the altitude of the temperature inversion is higher for higher T_0. This is mainly caused by the difference of the density in the upper atmosphere which depends on the scale height of the atmosphere. In cases with higher T_0, the density in the upper atmosphere is higher because of the larger scale height; the density decreases more gradually with altitude (Equation (2.13)). Since larger heating is generally required to heat up the denser gas, the temperature inversion is located at a higher altitude in cases with larger T_0.

While the temperature and density panels in Figure 3.2 show more or less similar profiles, there is a large difference in the radial velocity profiles. The cases with low surface temperature $T_0 \leq 2000$ K yield quite low wind velocities $< 3\,\mathrm{km\,s^{-1}}$. In contrast, in the case with high T_0 of 2500 K, gas is largely accelerated to attain a much faster velocity, $\approx 10\,\mathrm{km\,s^{-1}}$, than the other three cases. These results of the velocity and density profiles suggest that the wind structure can be categorized into two regimes: while slow and weak planetary winds stream out from cooler gaseous planets, fast and strong planetary winds are accelerated from hotter gaseous planets. We discuss this difference in the two regimes in later, Section 3.4.2.

Next, we examine the ionization degree that determines the magnetic resistivity in the atmosphere by Equation (3.2). To evaluate the non-ideal effects in the weakly-ionized atmosphere, we also compare the magnetic Reynolds number, that is described in Equation (3.3). For evaluation of the magnetic Reynolds number, we use the pressure scale height (Equation (2.14)) for a typical length of the system L, and the velocity dispersion at the surface for a typical velocity of the system, v.

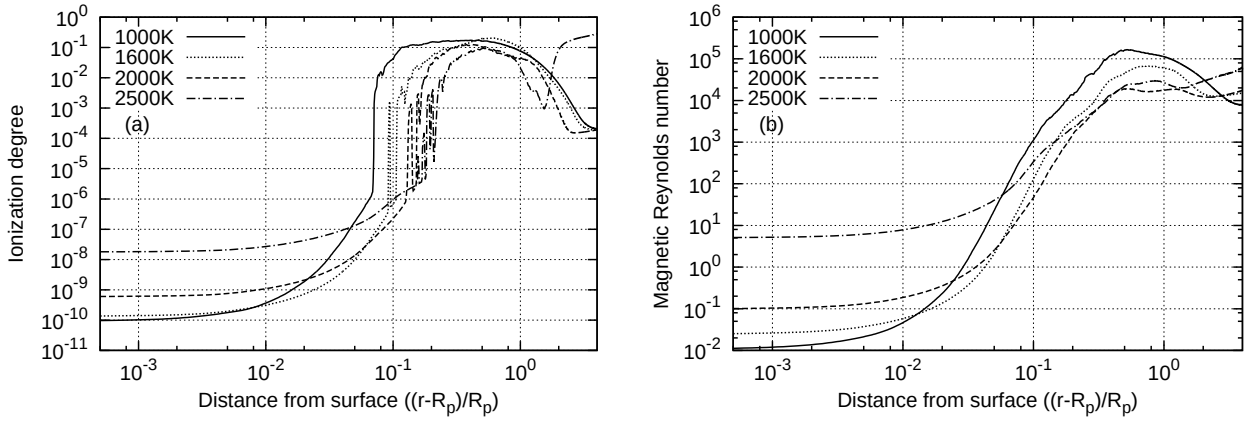

Figure 3.3: Surface temperature dependence of the atmospheric structures. (a) Ionization degree, and (b) magnetic Reynolds number in the atmosphere. The horizontal axes denote the distance from the surface that is normalized by the planetary radius. The solid, dotted, dashed, dot-dashed lines correspond to $T_0 = 1000$, 1600, 2000, and 2500 K, respectively.

Figure 3.3 shows the surface temperature dependence of the ionization degree, x_e and the magnetic Reynolds number. Since the typical value of T_0 is too low to ionize hydrogen atoms, the ionization degree is very low in the lower atmosphere. For example, $x_e \sim 10^{-10}$ in the cases with $T_0 = 1000$ and 1600 K, and x_e is still $\sim 10^{-8}$ even for $T_0 = 2500$ K. In this range of the temperature, the ionization degree is supported by the ionization of alkali metals such as sodium and potassium, that have relatively low ionization potential. This low ionization degree leads to high magnetic resistivity and small magnetic Reynolds number. As a result, the magnetic Reynolds number in the lower atmosphere is very small, $R_m \sim 10^{-2}$ in the cases with $T_0 = 1000$ and 1600 K, ant still $R_m \sim 1$ for T_0= 2500 K, although it is ≈ 100 times larger owing to the higher x_e.

The resultant low R_m means that the non-ideal effects are important in the lower atmosphere. In the upper atmosphere, however, high gas temperature and low gas density cause a sudden surge of the ionization degree. It increases gradually in the region below the temperature inversion as the density decreases with altitude, because the recombination rate drops with the decrease of the density. The ionization degree is very high above the temperature inversion region because the temperature rises high enough to ionize the hydrogen atoms.

3.4.2 Two Regimes of the Poynting Flux

As described in the previous section, the structure of the winds can be devided into two regimes. In order to investigate differences between the two regimes, we take a look at the Poynting flux in the atmosphere. Figure 3.4 shows the net Poynting flux in the atmosphere for cases with different surface temperatures. The net outgoing Poynting flux decreases rapidly with an increase of the altitude in the lower atmosphere because of both reflection and dissipation, and it becomes almost constant in the upper atmosphere. The Poynting flux injected at the surface increases monotonically with T_0, but its behavior in the atmosphere is not simple; the net Poynting flux in the upper atmosphere is smaller for higher T_0 when $T_0 \leq 1600$ K (Figure 3.4(a)), but is is larger for higher T_0 when $T_0 \geq 1600$ K (Figure 3.4(b)). The Alfvénic waves are damped in the lower atmosphere, where the magnetic resistivity is high. The scale height of the atmosphere plays a key role in the resistive dissipation of the Alfvénic waves.

When T_0 is higher, the scale height becomes larger and then it gives the large density in the upper atmosphere. It leads to a larger amount of mass loss, but on the other hand, it gives a negative effect on the wind though the enhancement of the resistive dissipation of the Alfvénic waves. The ionization degree is lower in the higher-density gas because of the

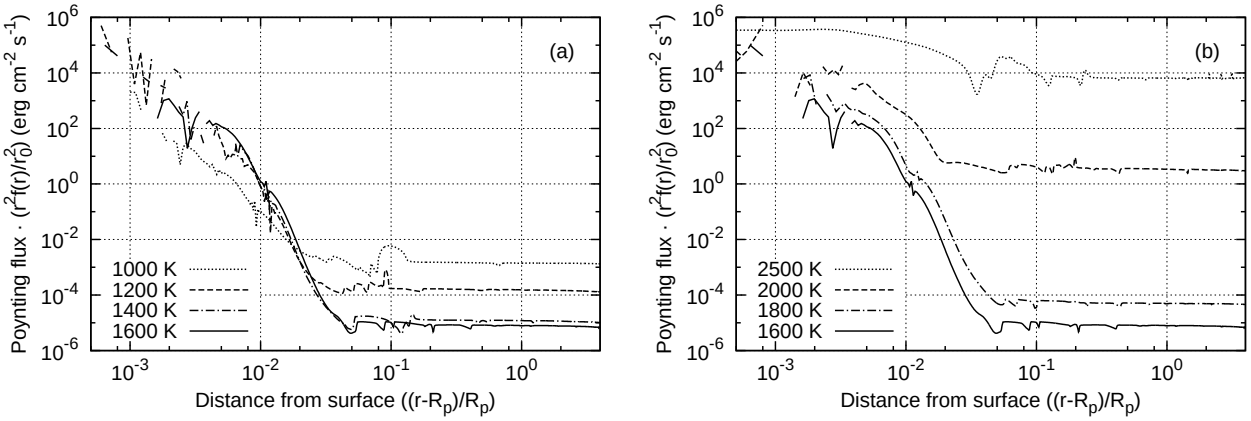

Figure 3.4: Net outgoing Poynting flux as a function of the distance from the surface for different T_0 cases. The left panel (a) presents cases with lower surface temperature, $T_0 \leq 1600$ K, and the right panel (b) presents cases with $T_0 \geq 1600$ K. The solid lines in both panels correspond to $T_0 = 1600$ K. In (a), the dotted, dashed, and dot-dashed lines correspond to $T_0 = 1000$, 1200, and 1400 K, respectively, and in (b), they correspond to 2500, 2000, and 1800 K, respectively. The net Poynting flux is multiplied by $r^2 f(r) / r_0^2$ to separate the effect of the adiabatic expansion of the flux tube, where $f(r)$ is described in Equation (2.2).

efficient recombination, and consequently the magnetic resistivity becomes relatively higher. In Figure 3.3(b), the magnetic Reynolds number of the case with $T_0 = 1000$ K is low in the lower atmosphere. In the case with $T_0 = 1600$ K, it is as low as the case with $T_0 = 1000$ K in the lower atmosphere, but it increases more slowly than the case with $T_0 = 1000$ K. Therefore, the magnetic Reynolds number remains relatively lower in almost the entire region than in the $T_0 = 1000$ K case. Because of the larger resistivity and larger scale height, a smaller fraction of the injected wave energy reaches the upper atmosphere in the $T_0 = 1600$ K case, compared to the $T_0 = 1000$ K case. This is the main reason why the transmitted Poynting flux shows the negative tendency on the surface temperature for $T_0 < 1600$ K. However, for $T_0 > 1600$ K, the Poynting flux exhibits a positive correlation with T_0 because the magnetic resistivity is lower for higher T_0.

Figure 3.5 compares the outward and inward energy flux by the Alfvénic waves, which is described in Equation (3.11). Here we show three cases with the surface temperature of 1000 K, 1600 K, and 2000 K. Every case shows that the inward energy flux tracks the outward energy flux with a slightly smaller level in almost the entire region of the atmosphere. The net outgoing Poynting flux in the Figure 3.4 is considerably smaller than the outward energy flux in Figure 3.5. These results indicate that the most injected outgoing Alfvén waves are reflected back downward through the propagation in the atmosphere. A tiny fraction of the injected

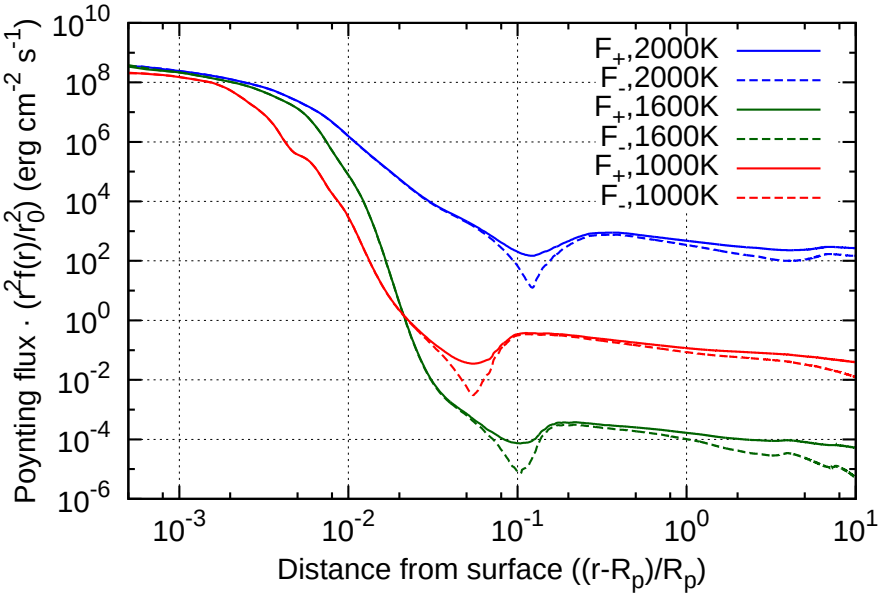

Figure 3.5: Comparison of the inward and outward Poynting flux versus distance from the surface for the cases with $T_0 = 1000$ K (red), 1600 K (green), and 2000 K (blue). The solid lines are the outward Poynting flux F_+, and the dashed lines are the inward Poynting flux F_-, respectively. The Poynting fluxes are multiplied by $r^2 f(r)\,/r_0^2$ to separate the effect of the adiabatic expansion of the flux tube, where $f(r)$ is described in Equation (2.2).

Alfvén waves can reach the upper atmosphere, which contributes to the heating and the acceleration of the gas. In general, a small fraction of the injected Poynting flux by the Alfvén waves is transmitted to the upper atmosphere because they suffer dissipation and reflection, whereas the resistivity is one of the keys that controls the dissipation of the waves. The fraction that enters the upper atmosphere determines the properties of the wind. For instance, if a large amount of the MHD wave energy reaches the upper atmosphere, it will increase the density of there, and drive more amounts of outflows.

The effect of the resistive dissipation of the Alfvénic waves is also seen in Figure 3.5. Both dissipation and reflection of the waves decrease the Poynting flux. The Poynting flux in the case with $T_0 = 1000$ K (red lines) decreases much faster than that of the case with $T_0 = 2000$ K (blue lines), which is caused by both resistive dissipation and reflection. The higher magnetic resistivity in the 1000 K case make the Alfvénic waves dissipate faster, and the steeper density gradient results in strong reflection. In the 1600 K case (green lines), the Poynting flux also drops quickly, but much faster than in the other two cases. For the $T_0 = 1600$ K case, since the scale height is larger than that of the $T_0 = 1000$ K case, the reflection of the Alfvénic waves

is suppressed due to more gradual decrease of the density. In this case, as mentioned above, the resistive dissipation of the Alfvénic waves is the primary reason for the rapid drop of the Poynting flux, and the amount of energy that can reach the upper atmosphere becomes quite small.

3.4.3 Time Variability of the Mass-Loss Rate

Our simulations show large time variabilities of the atmospheric structures and mass-loss rates. Figure 3.6 shows the mass-loss rates for different T_0 cases with time. One can see that in the

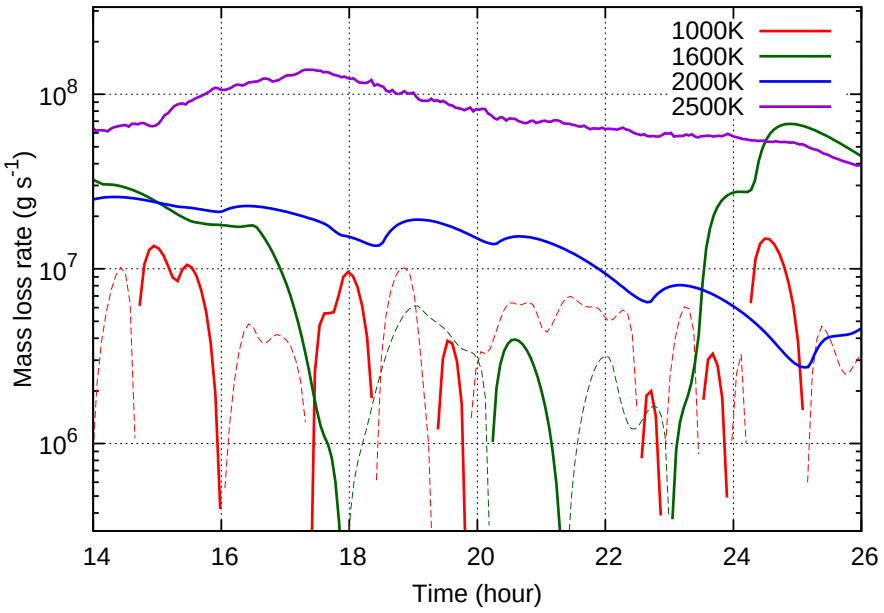

Figure 3.6: Time evolution of the mass-loss rates for the cases with $T_0 = 1000$ K (red lines), 1600 K (green lines), 2000 K (blue lines), and 2500 K (violet lines). Thick solid lines show the outflow rate, and dashed lines show the infall rates. The vertical axis is the mass-loss rate in units of gram per second, and the horizontal axis denotes time, where zero corresponds to the start of the calculations.

cases with lower surface temperatures $T_0 \leq 1600$ K the outflow is not time steady, but the atmospheric material inflows during certain periods, which is shown as the dashed lines in the figure. For example, in the case with $T_0 = 1000$ K, the outflowing phases are relatively shorter and they are comparable to the total duration of the infall phases. In the case with $T_0 = 1600$ K, the integrated duration of the outflowing phases is longer than that of the infall phases, and the infall phase disappears for the higher temperature, $T_0 \geq 2000$ K.

These results suggest that in the cases with the low surface temperature $T_0 \leq 1600$ K the

atmosphere is almost hydrostatic because the damping of the Alfvénic waves is too severe to drive steady winds, and the outflow can occur only intermittently. For higher T_0 the intermittency of the outflow disappears, and more steady outflows are obtained. Therefore, for the lower T_0 cases, there might be an "active" phase and "inactive" phase for the outflow.

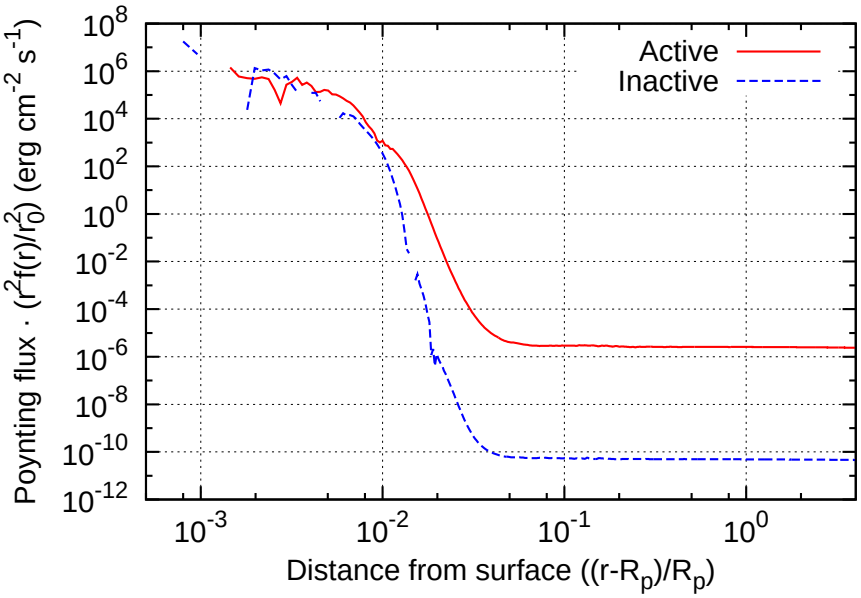

Figure 3.7: Comparison of the Poynting flux in the active (outflow) phase and inactive (infall) phase for the case with $T_0 = 1600$ K. The red solid, and blue dashed lines correspond to the active and inactive phases, respectively. The Poynting fluxes are multiplied by $r^2 f(r)/r_0^2$ to separate the effect of the adiabatic expansion of the flux tube, where $f(r)$ is described in Equation (2.2).

In Figure 3.7 we compare the Poynting flux by the Alfvén waves in the active phase during 23.6 - 31.6 hour and that in the infall phase during 17.8 - 20.2 hour in Figure 3.6. In the active phase, a larger amount of the Poynting flux is carried by the Alfvén waves into the upper atmosphere, while in the inactive phase, the Poynting flux in the upper atmosphere is strongly reduced by around four orders of magnitude. This results imply that the transmission of the Poynting flux into the upper layer controls the on-off nature of the atmospheric escape for the lower T_0 cases. However, we would like to note that the case with $T_0 = 1000$ K (not shown) shows more complicated behavior; the Poynting flux during an active phase does not always exceed the Poynting flux during inactive phases because of the rapid temporal variations in the atmospheric structures.

3.5 Dependence on the Planet Radius

Here we describe the dependence of the atmospheric structure and the mass-loss rate on the radius of gaseous planets $R_{\rm p}$ by treating it as a parameter. The mass-loss rate is very small for low surface temperature; therefore, we set $T_0 = 2000$ K in this section. We also fix the amplitude of the velocity dispersion at the surface to 20% of the sound speed, and the mass to Jupiter's mass.

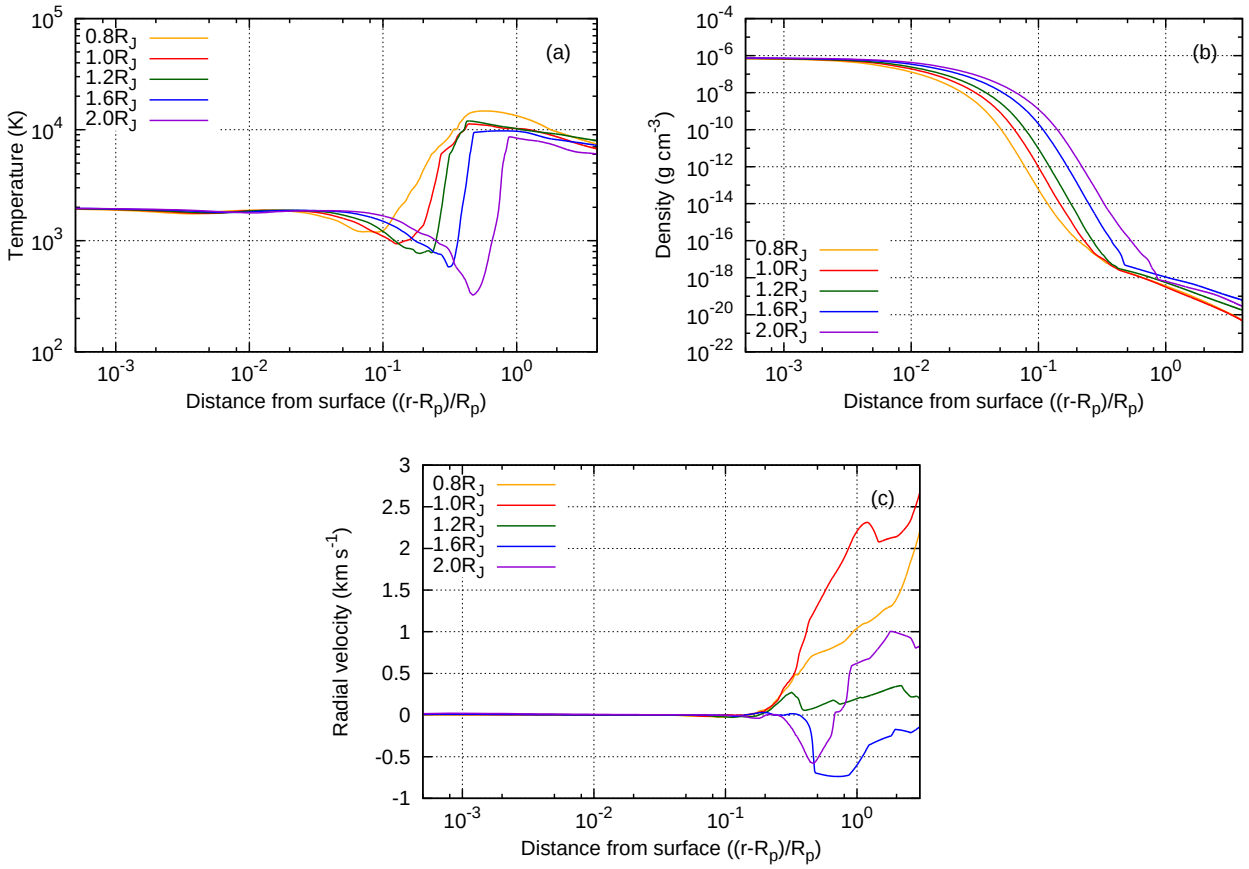

Figure 3.8: Dependence of the atmospheric structures on the planetary radius. (a) Temperature structure, (b) density profile, and (c) radial velocity profile. The horizontal axes denote the distance from the surface that is normalized by the planetary radius. The orange, red, green, blue, and violet lines correspond to $R_{\rm p} = 0.8R_{\rm J}$, $1.0R_{\rm J}$, $1.2R_{\rm J}$, $1.6R_{\rm J}$, and $2.0R_{\rm J}$, respectively.

Figure 3.8 shows the dependence of the atmospheric structures on $R_{\rm p}$. At low altitudes the temperature is almost constant and approximately same as the surface temperature in all the cases. It decreases initially but rises eventually by the heating owing to the dissipation of the MHD waves. The temperature inversion is located at higher altitude for larger $R_{\rm p}$, because the pressure scale height is larger; the slow decrease of the density leads to higher

density in the upper atmosphere (Figure 3.8(b)), which is not heated up to high temperatures. Accordingly the bending location of the density gradient, which corresponds to the location of the temperature inversion, is systematically higher for larger $R_{\rm p}$ for the same reason.

In all the cases, the temperature of the upper atmosphere is elevated to $\sim 10^4$ K, by the dissipation of the MHD waves. However, the wind velocity is quite slow. Particularly in the cases with large $R_{\rm p} \geq 1.2R_{\rm J}$, the gas in the atmosphere is almost static or even inflows partly, whereas the cases with the smaller radius show outflows with a few $\mathrm{km\,s^{-1}}$. We would like to note that intermittent mass loss do occur in every case, but in the time-averaged radial velocity profile becomes negative in some cases.

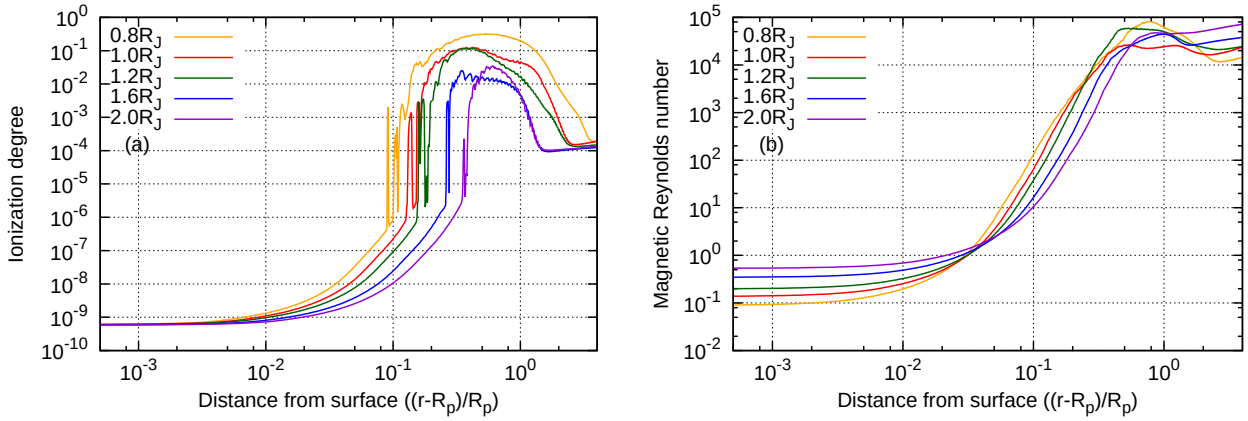

Figure 3.9: Dependence of the atmospheric structures on the planetary radius. (a) Ionization degree, and (b) magnetic Reynolds number. The horizontal axes denote the distance from the surface that is normalized by the planetary radius. The orange, red, green, blue, and violet lines correspond to $R_{\rm p} = 0.8R_{\rm J}$, $1.0R_{\rm J}$, $1.2R_{\rm J}$, $1.6R_{\rm J}$, and $2.0R_{\rm J}$, respectively.

Figure 3.9 shows the $R_{\rm p}$ dependence of the ionization degree and magnetic Reynolds number in the atmosphere. The ionization degree is quite low in the lower atmosphere because of the low temperature of there (≈ 2000 K) in all the cases. The dominant ion sources in the lower atmosphere are the alkali metals. In contrast, the ionization degree increases to $10^{-4} - 10^{-1}$ in the upper atmosphere in all the cases. In the smaller $R_{\rm p}$ cases, the ionization degree starts to increase from a lower altitude and the final value is also higher in the upper atmosphere, because the recombination is slower in there owing to the lower density.

Resultant mass-loss rates remain very small in these cases. The case with $R_{\rm p} = 1.0R_{\rm J}$ gives the mass-loss rate of $\sim 1.7 \times 10^7\,\mathrm{g\,s^{-1}}$, and the case with $0.8R_{\rm J}$ gives $\sim 1.4 \times 10^7\,\mathrm{g\,s^{-1}}$, respectively. In the ideal MHD calculations, a mass-loss rate in the case with $R_{\rm p} = 1.0R_{\rm J}$ and $T_0 = 2000$ K is $\sim 1.9 \times 10^{10}\,\mathrm{g\,s^{-1}}$. Our results show that the large resistivity as a result of the

low ionization degree in the lower atmosphere significantly surpasses the mass loss from hot Jupiters. However, we would like to note that the wind shows large fluctuations. The possibility remains that the planetary wind streams out in an intermittent manner. Also, the Roche lobe of hot Jupiters is generally small, several planetary radii, because of the small separation from the central star. Then, once slow gas material overflows the Roche lobe, it will be blown away by the stellar wind from the central stars, or accelerated by some mechanisms such as the charge exchange between high energy particles in the stellar wind and radiation pressure.

3.6 Dependence on the Velocity Dispersion

The amplitude of the velocity dispersion at the surface, δv, is also an important parameter that controls the structure of the atmosphere and the mass-loss rate. Here we show the dependence of several physical properties on the velocity dispersion.

In Figure 3.10, we show the atmospheric structures of the cases with different δv. The cases with different δv give quite similar density and temperature profiles. Only a partial region shows the different profile in the upper atmosphere around the distance from the surface $\sim 0.2R_{\rm p} - 1.0R_{\rm p}$ in both the density profile and temperature structure. On the other hand, larger δv gives faster radial velocity. Because of the similarity of the profiles of the density and temperature, which affect the ionization degree, the ionization degree and the resultant magnetic resistivity also have the similar profiles in all the cases (Figure 3.11).

The ionization degree have the same value in the lower atmosphere because the temperatures around there are same, $\sim$ 2000 K in all the cases. The heating by the dissipation of the MHD waves is significantly weak in the lower atmosphere, because the gas pressure dominates over the magnetic pressure in the lower atmosphere. The magnetic Reynolds number is also almost similar, but slightly differ with the velocity dispersion. This is because the magnetic Reynolds number is determined by Equation (3.3), and we assume that the typical velocity of the system as the velocity dispersion at the planetary surface, and other values, the typical length of the system and the magnetic resistivity that is determined by the ionization degree and temperature, are almost same in all the cases. Thus, the resultant magnetic Reynolds number slightly differs in the lower atmosphere. In spite of the difference in the magnetic Reynolds number in the lower atmosphere, it is quite low even in the cases when the velocity dispersion is larger, so the MHD waves are significantly damped in all the cases. Only a tiny amount of the MHD wave energy can reach the upper atmosphere, and the small difference in

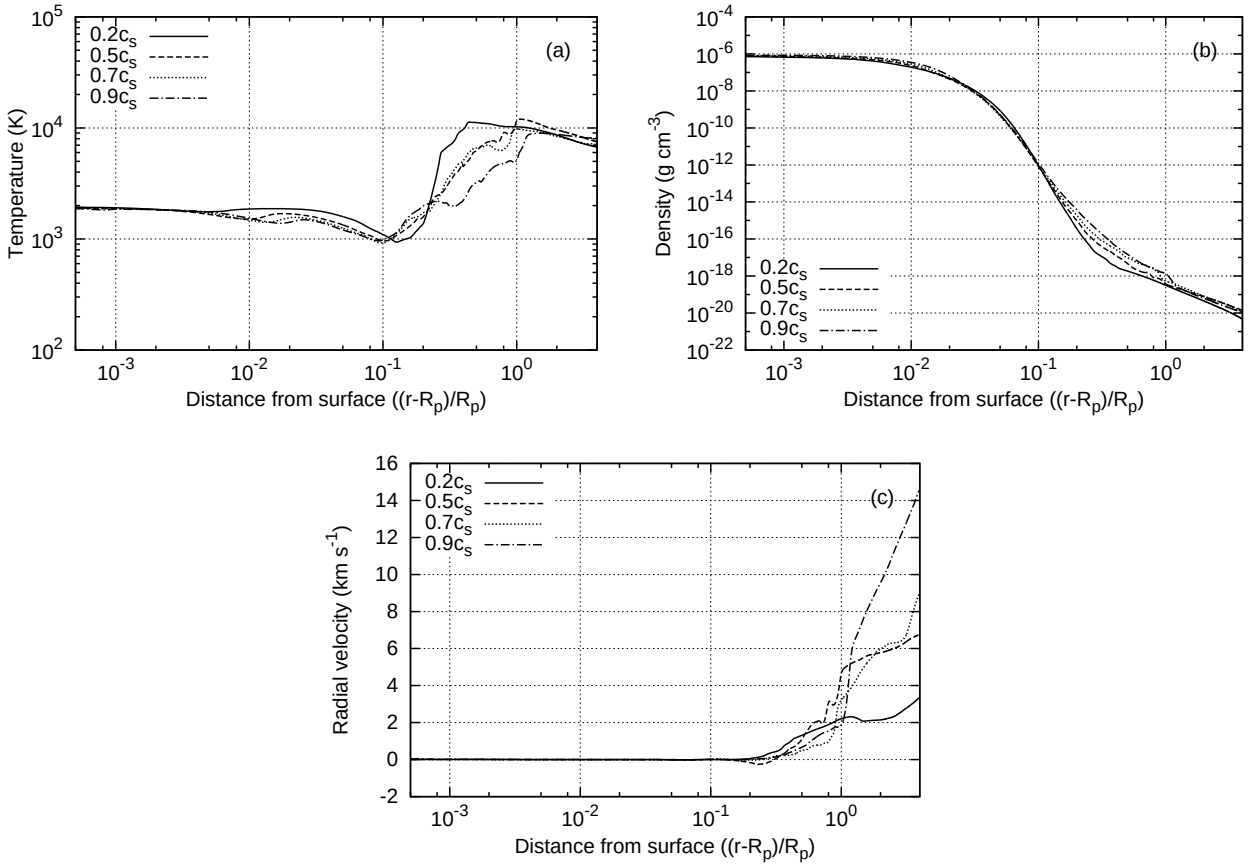

Figure 3.10: Dependence of the atmospheric structures on the velocity dispersion at the surface. (a) Temperature structure, (b) density profile, and (c) radial velocity profile. The horizontal axes denote the distance from the surface that is normalized by the planetary radius. The solid, dashed, dotted, dot-dashed lines correspond to $\delta v = 0.2c_{\rm s}$, $0.5c_{\rm s}$, $0.7c_{\rm s}$, and $0.9c_{\rm s}$, respectively. In all cases, $R_{\rm p} = 1.0R_{\rm J}$, $M_{\rm p} = 1.0M_{\rm J}$, and the surface temperature is fixed to 2000 K.

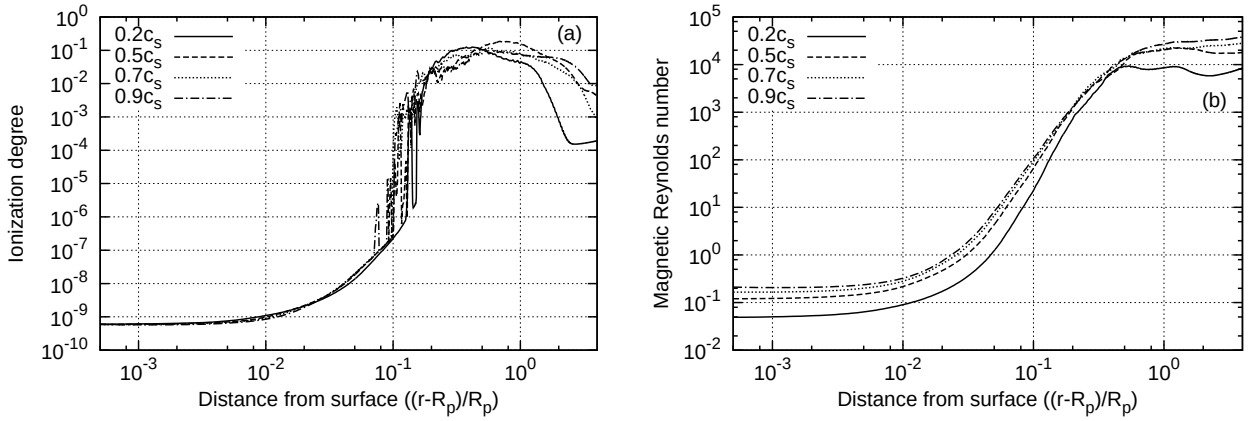

Figure 3.11: Dependence of the atmospheric structures on the planetary radius. (a) Ionization degree, and (b) magnetic Reynolds number. Lines and setups are same as Figure 3.10.

the amount of the energy that can reach there appears as the difference in the radial velocity profiles. Therefore, it can be said that the difference of the velocity dispersion at the surface has a small effect on the structure of the atmosphere except for the radial velocity.

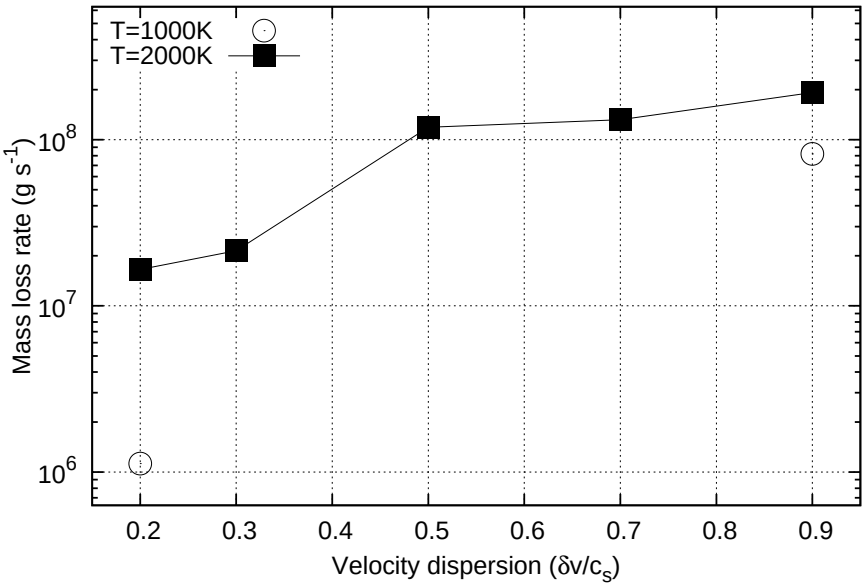

Figure 3.12: Relation between the velocity dispersion at the surface and the mass-loss rate for $T_0 = 1000$ K (circle) and 2000 K (filled square). The mass-loss rate is shown in units of gram per second. The horizontal axis denotes the amplitude the velocity dispersion that is normalized by the sound speed at the surface.

Although the difference of the density in the upper atmosphere is very small, the wind velocity is faster for the larger velocity dispersion, and it causes the increase of the mass-loss rate. Figure 3.12 shows the dependence of the mass-loss rate on the velocity dispersion for cases with $T_0 = 1000$ K and 2000 K.

Increase of the mass-loss rate with the velocity dispersion is more gradual compared with the ideal MHD case in Figure 2.2. In the ideal MHD approximation, decrease of the energy that is transported by the Alfvénic waves only caused by the reflection and dissipation, and the dissipated wave energy was converted to the heat energy and the kinetic energy of the planetary wind. In the non-ideal MHD condition, however, decrease of the energy is also caused by the resistive dissipation, and its effect is relatively strong. The dependence of the mass-loss rate on the velocity dispersion therefore does not show the clear dependence like the case of the ideal MHD condition appeared in Figure 2.2.

3.7 Effect of Ohmic Heating in a Planetary Atmosphere

We have investigated the effects of the magnetic diffusion on the dissipation of the Alfvénic waves, which stresses the planetary winds, so far. On the other hand, the resistive dissipation also heat up the surrounding gas via ohmic heating (Joule heating), which may play a positive role in driving outflows. In this section, we examine the role of the ohmic heating in a quantitative manner.

Current density can be written as follows;

$$\mathbf{j} = \frac{c}{4\pi} \left(\nabla \times \mathbf{B} \right), \tag{3.12}$$

where c is the speed of light. Electric conductivity σ is related to the magnetic resistivity η by

$$\frac{1}{\sigma} = \frac{4\pi}{c^2} \eta. \tag{3.13}$$

Since ohmic heating rate per unit volume is

$$Q_{\rm ohm} = \frac{\mathrm{j}^2}{\sigma}, \tag{3.14}$$

this term can be written by η and $\mathbf{B}$ as follows;

$$Q_{\rm ohm} = \frac{\eta}{4\pi} \left(\nabla \times \mathbf{B} \right)^2. \tag{3.15}$$

Figure 3.13 shows the ohmic heating rate in comparison with the ideal MHD heating (red solid line) and cooling (blue dashed line) rates of the gas. The ideal MHD heating includes shock heating in addition to adiabatic heating. In the lower atmosphere, the ohmic heating dominates over, or is comparable to, the ideal MHD heating because of the large resistivity. However, since the Alfvénic waves dissipate very rapidly, the ohmic heating rate decreases drastically as the altitude increases.

The magnetic resistivity depends sensitively on the temperature. Figure 3.14 compares the ohmic heating rates for cases with different surface temperatures. The high T_0 cases have smaller ohmic heating rates in the lower atmosphere, but this reverses in the upper atmosphere, because the dissipation of the Alfvénic waves is more gentle at low altitude in these cases and a larger amount of the wave energy reaches the upper atmosphere. In addition, as shown in Figure 3.3, the magnetic Reynolds number is relatively smaller in the upper atmosphere for higher T_0, which further increases the resistive heating.

However, the ohmic heating rate is quite small in comparison to the shock heating except for the region close to the surface (Figure 3.13), so this effect is negligible in the upper atmosphere

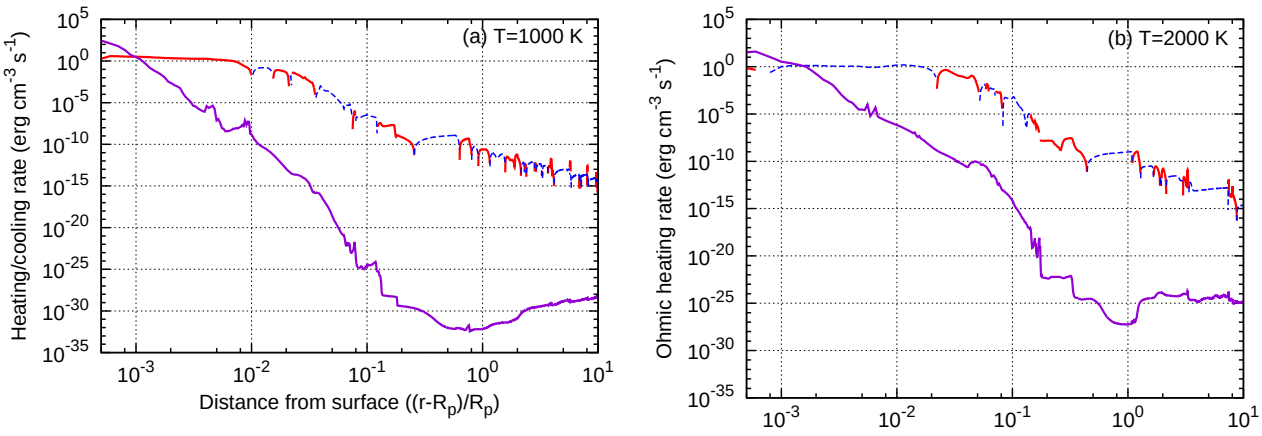

Figure 3.13: Comparison of ideal MHD heating rate (red solid), cooling rate (blue dashed), and ohmic heating rate (violet solid) per unit volume respectively for cases with (a) $T_0 = 1000$ K and (b) 2000 K. The vertical axes denote the heating and cooling rates in units of erg cm^{-3} s^{-1}. The horizontal axes denote the distance from the surface that is normalized by the planetary radius. We set $\delta v = 20\%$ of the sound speed, $M_{\rm p} = M_{\rm J}$, and $R_{\rm p} = R_{\rm J}$.

and gives little contribution to the atmospheric escape. Even in low atmosphere where the ohmic heating is large, it does not play a primary role. The comparison between the ideal and non-ideal calculations in the Figure 3.1(a) shows that the temperature structures in the lower atmosphere are almost the same. In fact, the temperature in the lower atmosphere in the resistive cases are barely higher than the ideal cases, and the difference is only several tens of kelvin. In summary, the ohmic heating does not play an important role in the entire structure of the atmosphere and atmospheric escape.

3.8 A Possibility for Bipolar Outflows

In this work (Tanaka et al., 2015) and the previous work (Tanaka et al., 2014), we have fixed the shape of the open magnetic flux tubes that is described in Section 2.1. We presume that the overall structure of magnetic field lines of gaseous planets is similar to that of the Sun. The Sun has a multipole magnetic field, and the properties of the open magnetic flux tubes are observed in detail (e.g., Tsuneta et al., 2008; Ito et al., 2010). However, actual structures of the magnetic fields in exoplanets are unknown at the moment, and only several glimpses of the existence of the magnetic fields have been observed. The overall structure of the planetary magnetic fields affect the shape of the open magnetic flux tubes.

The most critically affected parameter in our modeling is the filling factor $f(r)$ that is

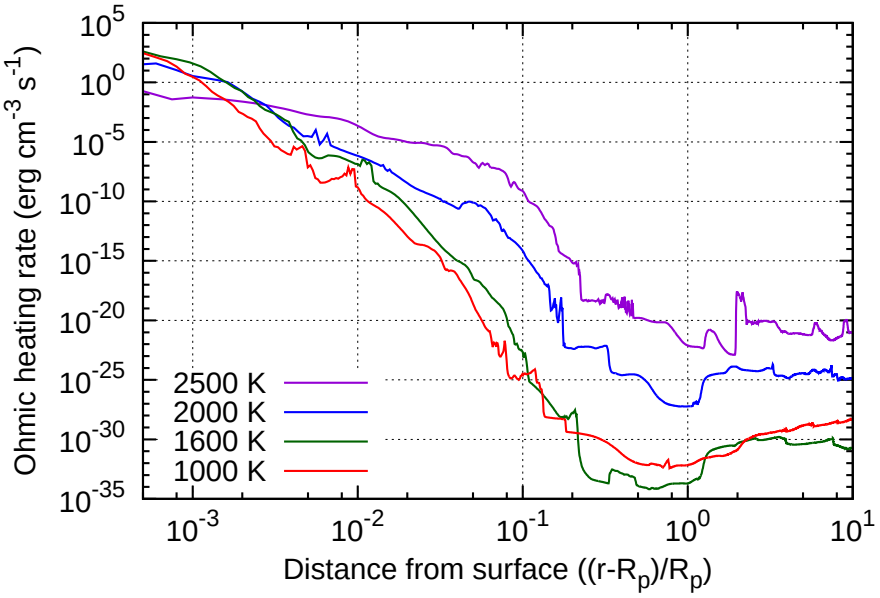

Figure 3.14: Dependence of the ohmic heating rate per unit volume on the surface temperature. The red, blue, green, and violet lines correspond to T_0 = 1000 K, 1600 K, 2000 K, and 2500 K, respectively. The vertical axes denote the heating and cooling rates in units of erg $\mathrm{cm}^{-3}\,\mathrm{s}^{-1}$. The horizontal axes denote the distance from the surface that is normalized by the planetary radius.

described by Equation (2.2). If the planetary magnetic field has a simple dipole structures open magnetic flux tubes appear in the magnetic polar regions. In this case, heating in the upper atmosphere and the acceleration of gas flow by the MHD wave energy occur only in the polar regions. Therefore, the actual appearance of flow is expected to be bipolar, like polar winds. In the simple dipole case of the magnetic field, the degree of super-radial expansion of the open magnetic flux tube should be smaller, and thus the mass-loss rate is expected to be smaller because the reflection of the energy flux is thought to be enhanced. To investigate this more quantitatively, a three-dimensional calculation is required, which remains difficult at present. On the other hand, the observation of the bipolar outflow from an exoplanet is, in principle, possible in the detailed analysis of the differential spectroscopy for transiting hot Jupiters, unless the magnetic dipole axis is perpendicular to both the orbital plane of the exoplanet and the line of sight. This is because a blue shifted outflow before ingress and a redshirted outflow after the egress, or vise versa, can be seen in this case. Once the mass flux of the bipolar outflow from the exoplanet is observed, we will possibly constrain the properties of the magnetic field of the exoplanet by assuming the driving mechanism of the atmospheric escape as described in our work.

3.9 Comparison with the XUV Heating

As we mentioned in Section 1.3.2, high-energy radiation such as the X-ray and extreme ultraviolet from a central star is important for the heating of the upper atmosphere and atmospheric escape from hot Jupiters. Here we compare the height where the heating by the MHD waves is important and the penetration depth of stellar XUV radiation. It is useful to introduce $R_{\rm XUV}$, the radius at which XUV radiation is absorbed and the heating by the absorption of the XUV radiation becomes important. $R_{\rm XUV}$ means that the optical depth for the XUV radiation reaches unity at that radius, and it corresponds to the radius where the column density of hydrogen becomes $\sim 5 \times 10^{17}\,{\rm cm}^{-2}$ (e.g., Murray-Clay et al., 2009; Rogers et al., 2011). We calculate $R_{\rm XUV}$ in each calculation and compare it with the region where the heating by the dissipation of the MHD waves become important.

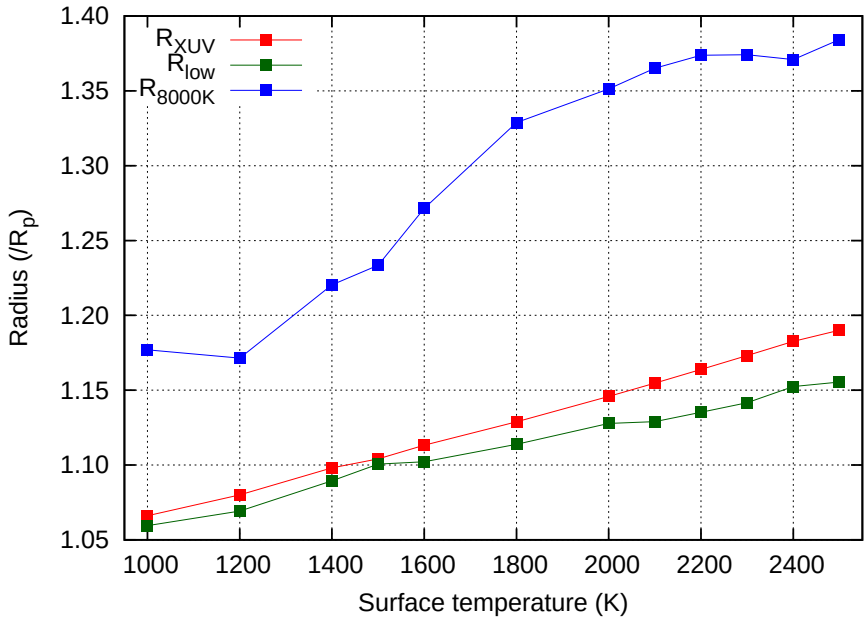

Figure 3.15: Dependence of $R_{\rm XUV}$, $R_{\rm low}$ and $R_{\rm 8000K}$ on the surface temperature. The red squares correspond to $R_{\rm XUV}$, and the green and blue squares correspond to $R_{\rm low}$ and $R_{\rm 8000K}$, respectively. The horizontal axis denotes the surface temperature, and the vertical axis denotes the radius that is measured from the center of the object.

Figure 3.15 shows the surface temperature dependence of $R_{\rm XUV}$ and comparison with other considerable radii. As shown in Figure 3.2(a), the gas temperature slightly drops with the altitude owing to the adiabatic expansion, and then gas is heated drastically to $\sim 10^4$ K. Here we introduce R_{low}, which is the radius at which the temperature becomes lowest and heating by the MHD waves start to become important. Additionally, we also introduce $R_{\rm 8000K}$, which

is the radius at which the temperature becomes higher then 8000 K. In this range of the surface temperature, $R_{\rm XUV}$ is always located only slightly above $R_{\rm low}$, and the value varies between $1.05R_{\rm p}$ and $1.20R_{\rm p}$. This result is consistent with previous works on the XUV heating in the atmosphere of hot gaseous planets (e.g., Murray-Clay et al., 2009). In addition, we find $R_{8000\rm K}$ always lies at a much higher altitude then $R_{\rm XUV}$.

These results suggest that the region heated up to $\sim 10^4$ K by the dissipation of the MHD waves is optically thin to the XUV photons, and the XUV photons can reach the altitude at which the temperature becomes lowest in our model. Photoionization, cooling from metal lines, and H Lyα play important roles in the upper atmosphere of hot Jupiters. At this stage, our model does not include the effects of stellar XUV irradiation, the inclusion of which should improve our model. In the present modeling, the results cannot explain the observational results of the mass-loss rates adequately, since the mass-loss rates are largely reduced when we take into account the effects of the magnetic resistivity. This seems to indicate that the resulting mass-loss rate strongly depends on the details of the input physics. More realistic treatment, for example improvement of the radiative cooling term in the atmosphere, is critically needed.

Chapter 4

Radiative Transfer in the MHD Calculation for the Atmosphere of Gaseous Planets I

4.1 Radiative Cooling in the Previous Calculations

As described in Section 2.1.5, we have used the cooling functions for the solar condition for the radiation cooling term, $q_{\rm R}$, in the energy equation (Equation (2.6) and (3.7)). The cooling functions used in our calculations are, the optically thin radiative cooling for the coronal plasma (Landini and Monsignori Fossi, 1990; Sutherland and Dopita, 1993), and empirical radiative cooling for the solar chromospheric gas with the optically thick effect that is based on the observation of the solar chromosphere (Anderson and Athay, 1989a). In addition, we extrapolated the latter cooling function for lower gas temperature of gaseous planets down to ~ 1000 K, by using the relation, $q_{\rm R} = 4.5 \times 10^9 \rho$ (erg cm^{-3} s^{-1}). We also switch off the cooling when the gas temperature becomes lower than the surface temperature.

This approximated treatment might be crude, particularly for gas with $T < 10^4$ K. For gas of the solar chromospheric condition, 4000 K $\lesssim T \lesssim 10^4$ K, in which the main coolants are H I, Mg II, Ca II, and Fe II (Vernazza et al., 1981). The cooling rates for these species are smaller for gas with lower temperature (Anderson and Athay, 1989b). On the other hand, molecules such as CO, SiO, CS, OH, and H_2O, supersede them as dominant coolants (Tsuji, 1967, 1973). Although the cooling rates of these molecules seem roughly comparable to that of the main coolants foe the solar chromosphere (e.g., Muchmore et al., 1987, for SiO), the precise cooling rate depends on the actual structure of an atmosphere (Muchmore et al., 1987). To know that whether the approximated treatment of the radiative cooling function in our calculation

is overestimation or underestimation, we need to improve treatment of the radiative cooling by calculating radiative transfer in the atmosphere in a self-consistent manner. In this chapter, we focus on our improvements on the radiative transfer in the atmosphere and incorporating it into our MHD simulations.

4.2 Radiative Cooling and Heating Rates

Cooling or heating rate by radiation can be written as follows;

$$Q_{\rm rad} = 4\pi \int_0^\infty \kappa_\nu J_\nu d\nu - 4\pi \int_0^\infty \epsilon_\nu d\nu, \tag{4.1}$$

where $Q_{\rm rad}$ is radiative cooling or heating rate per unit mass, κ_ν is frequency-dependent absorption cross section per unit mass, or simply opacity, J_ν is frequency-dependent mean intensity, and ϵ_ν is frequency-dependent emissivity per unit mass, respectively, and ν denote frequency of radiation. The first term in the right-hand side denotes the gain of the energy of material from radiation, and the second term denotes the radiative loss from the material. When the first term dominates over the second term, $Q_{\rm rad}$ become positive and the material is heated, and vice versa. Here we assume the local thermodynamic equilibrium (LTE) condition for atmospheres. In the LTE condition,

$$\epsilon_\nu = \kappa_\nu B(T_{\rm gas}) \tag{4.2}$$

is achieved, where $T_{\rm gas}$ is gas temperature, and $B_\nu(T_{\rm gas})$ is the Planck function. By substituting Equation (4.2) to (4.1), we obtain

$$Q_{\rm rad} = 4\pi \int_0^\infty \kappa_\nu J_\nu - 4\pi \int_0^\infty \kappa_\nu B_\nu(T_{\rm gas})\, d\nu. \tag{4.3}$$

Here we introduce following mean opacities, absorption mean opacity

$$\kappa_J \equiv \frac{\int_0^\infty \kappa_\nu J_\nu d\nu}{\int_0^\infty J_\nu d\nu} \tag{4.4}$$

and Planck mean opacity

$$\kappa_B \equiv \frac{\int_0^\infty \kappa_\nu B_\nu(T_{\rm gas})\, d\nu}{\int_0^\infty B_\nu(T_{\rm gas})\, d\nu}. \tag{4.5}$$

From these opacities and Equation (4.3),

$$Q_{\rm rad} = 4\pi\kappa_J \int_0^\infty J_\nu - 4\pi\kappa_B \int_0^\infty B_\nu(T_{\rm gas})\, d\nu \tag{4.6}$$

is obtained. Integrals can be written as follows;

$$\int_0^\infty J_\nu d\nu = \frac{\sigma_{\rm SB}}{\pi} T_{\rm rad}^4 \tag{4.7}$$

$$\int_0^\infty B_\nu(T_{\rm gas})\, d\nu = \frac{\sigma_{\rm SB}}{\pi} T_{\rm gas}^4, \tag{4.8}$$

where $\sigma_{\rm SB}$ is Stefan-Boltzmann constant, and $T_{\rm rad}$ is radiation temperature. Therefore, Equation (4.6) can be described as

$$Q_{\rm rad} = 4\sigma_{\rm SB}\left(\kappa_J T_{\rm rad}^4 - \kappa_{\rm B} T_{\rm gas}^4\right). \tag{4.9}$$

Since temperature of the gas is calculated in our MHD simulations, it is necessary to calculate the radiation temperature in the atmosphere to derive the radiative cooling/heating rate. If we obtain the radiation temperature in each point by some kind of method, then we can calculate the radiative cooling or heating from comparison between the radiation temperature and the gas temperature by using Equation 4.9.

4.3 Modified Unno-Kondo Method for Radiative Transfer

In order to calculate the radiation temperature in the planetary atmosphere, we need to treat the radiative transfer. Firstly, we use the modified Unno-Kondo method to derive the radiation temperature. This is one of the method to treat the radiative transfer in the one-dimensional spherical symmetric coordinate by assuming two-stream approximation, and developed mainly for envelopes of asymptotic giant branch (AGB) stars. This method is firstly introduced by Unno and Kondo (1976), then developed by Unno (1989), and further modification was done by Hashimoto (1995). Here we introduce the modified Unno-Kondo method to derive the radiation temperature in the atmosphere.

4.3.1 Radiative Transfer Equation in the Spherical Coordinate

The general form of the time-independent radiative transfer equation is denoted as follows;

$$\frac{\partial I_\nu}{\partial s} = -\alpha_\nu I_\nu + j_\nu \tag{4.10}$$

where I_ν is specific intensity, s is direction of a ray, α_ν is absorption coefficient, and j_ν is an emissivity. The subscripts ν means that the frequency-dependence of the quantities.

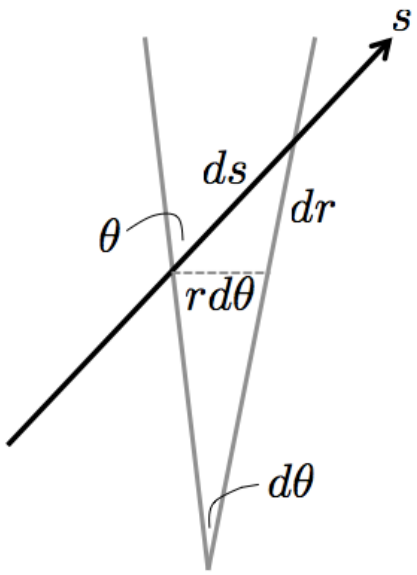

Figure 4.1: A schematic picture of a ray in the spherical symmetric coordinate.

In the spherical symmetric coordinate, relation between the direction s and the radial coordinate r is expressed as the schematic picture Figure 4.1. Here, θ is the angle between the radial direction and the direction of the ray. In this geometry, they can be written as $dr = \cos\theta ds$, and $rd\theta = -\sin\theta ds$. By using these relation and the cosine of the angle $\mu = \cos\theta$, the left-hand side of the Equation (4.10) can be modified as follows,

$$\begin{aligned}\frac{\partial I_\nu}{\partial s} &= \frac{\partial r}{\partial s}\frac{\partial I_\nu}{\partial r} + \frac{\partial \theta}{\partial s}\frac{\partial I_\nu}{\partial \theta} \\ &= \mu\frac{\partial I_\nu}{\partial r} - \frac{\sin\theta}{r}\left(-\sin\theta\frac{\partial I_\nu}{\partial \mu}\right) \\ &= \mu\frac{\partial I_\nu}{\partial r} + \frac{1-\mu^2}{r}\frac{\partial I_\nu}{\partial \mu}. \end{aligned} \tag{4.11}$$

Therefore, Equation (4.10) is denoted as

$$\mu\frac{\partial I_\nu}{\partial r} + \frac{1-\mu^2}{r}\frac{\partial I_\nu}{\partial \mu} = -\alpha_\nu I_\nu + j_\nu \tag{4.12}$$

in the spherical symmetric coordinate.

If we assume absorption, emission, and scattering in the LTE condition, the time-independent radiative transfer equation can be denoted as follows;

$$\begin{aligned}\mu\frac{\partial I_\nu(r,\mu)}{\partial r} + \frac{1-\mu^2}{r}\frac{\partial I_\nu(r,\mu)}{\partial \mu} &= -\left[\alpha_\nu(r) + \sigma_\nu(r)\right] I_\nu(r,\mu) + \alpha_\nu(r)\, B_\nu[T(r)] \\ &\quad + \frac{1}{2}\sigma_\nu(r)\int_{-1}^{1} R_\nu(\mu,\mu')\, I_\nu(r,\mu')\, d\mu' \end{aligned} \tag{4.13}$$

where α_ν is an absorption coefficient, σ_ν is a scattering coefficient. $R(\mu, \mu')$ is scattering phase function. The first, second, and third terms in the left-hand side of the Equation(4.13) denote the extinction of the intensity due to the absorption and scattering, increase due to the emission, and increase due to the scattering from other directions, respectively (Hashimoto, 1995). Hereafter, we omit the subscript ν and arguments μ and r, for simplicity.

4.3.2 Three-Zone Approximation

Here we describe three-zone approximation, or modified two-stream generalized Eddington approximation that is introduced by Unno (1989). In this approximation, the intensity I is divided into following three components by the value of μ,

$$I(r,\mu) = \begin{cases} I_+(r) & (\mu_1 < \mu \leq 1) \\ I_0(r) & (\mu_2 < \mu \leq \mu_1) \\ I_-(r) & (-1 \leq \mu \leq \mu_2) \end{cases} . \tag{4.14}$$

In this equation, μ_1 and μ_2 are function of r and ν.

The zeroth to fourth order moments of the radiation field are described as

$$J = \frac{1}{2}\int_{-1}^{1} I d\mu, \tag{4.15}$$

$$\frac{F}{4} = \frac{1}{2}\int_{-1}^{1} \mu I d\mu = H, \tag{4.16}$$

$$K = \frac{1}{2}\int_{-1}^{1} \mu^2 I d\mu, \tag{4.17}$$

$$\frac{L}{4} = \frac{1}{2}\int_{-1}^{1} \mu^3 I d\mu, \tag{4.18}$$

$$M = \frac{1}{2}\int_{-1}^{1} \mu^4 I d\mu, \tag{4.19}$$

respectively. By substituting Equation (4.14) to (4.15), then

$$J = \frac{1}{2}\left[(I_+ + I_-) - \mu_1 (I_+ - I_0) - \mu_2 (I_0 - I_-)\right] \tag{4.20}$$

is obtained. Similarly, by substituting Equation (4.14) to (4.16), we obtain

$$F = \left(1 - \mu_1^2\right)(I_+ - I_0) + \left(1 - \mu_2^2\right)(I_0 - I_-) . \tag{4.21}$$

Here we define

$$S = I_+ + I_-, \tag{4.22}$$

$$D = \left(1 - \mu_1^2\right)(I_+ - I_0) - \left(1 - \mu_2^2\right)(I_0 - I_-) , \tag{4.23}$$

then using these variables, J is written as the following form,

$$J = \frac{1}{4}\left[2S - \left(\frac{\mu_1}{1-\mu_1^2} + \frac{\mu_2}{1-\mu_2^2}\right) F - \left(\frac{\mu_1}{1-\mu_1^2} - \frac{\mu_2}{1-\mu_2^2}\right) D\right]. \tag{4.24}$$

Similarly, the other moments can be written as follows;

$$K = \frac{1}{12}\left[2S - \left(\frac{\mu_1^3}{1-\mu_1^2} + \frac{\mu_2^3}{1-\mu_2^2}\right) F - \left(\frac{\mu_1^3}{1-\mu_1^2} - \frac{\mu_2^3}{1-\mu_2^2}\right) D\right], \tag{4.25}$$

$$L = \frac{1}{4}\left[\left(2+\mu_1^4+\mu_2^4\right) F + \left(\mu_1^4-\mu_2^4\right) D\right], \tag{4.26}$$

$$M = \frac{1}{20}\left[2S - \left(\frac{\mu_1^5}{1-\mu_1^2} + \frac{\mu_2^5}{1-\mu_2^2}\right) F - \left(\frac{\mu_1^5}{1-\mu_1^2} - \frac{\mu_2^5}{1-\mu_2^2}\right) D\right]. \tag{4.27}$$

Now we assume that $D = 0$ (Unno, 1989; Hashimoto, 1995), that is corresponding to

$$I_0 = \frac{(1-\mu_1^2)\, I_+ + (1-\mu_2^2)\, I_-}{(1-\mu_1^2) - (1-\mu_2^2)}. \tag{4.28}$$

Substituting $D = 0$ into the moments of the radiation, then eliminating S from the equations, we obtain the relations between each moment of the radiation field as follows,

$$3K - J = \frac{1}{4}\left(\mu_1 + \mu_2\right) F, \tag{4.29}$$

$$2L - F = \frac{1}{2}\left(\mu_1^2 + \mu_2^2\right) F, \tag{4.30}$$

$$5M - 3K = \frac{1}{4}\left(\mu_1^3 + \mu_2^3\right) F. \tag{4.31}$$

If one assume $\mu_1 = \mu_2 = \mu_r$, which is denoted as an one peaking angle theory in Unno (1989), these relations become follows,

$$3K - J = \frac{1}{2}\mu_r F, \tag{4.32}$$

$$2L - F = \mu_r^2 F, \tag{4.33}$$

$$5M - 3K = \frac{1}{2}\mu_r^3 F. \tag{4.34}$$

4.3.3 Moments of the Radiative Transfer Equation

Here we calculate zeroth to third moments of the radiative transfer equation (4.13). We assume the scattering phase function

$$R(\mu, \mu') = \sum_{l=0}^{\infty} a^{(l)} P_l(\mu)\, P_l(\mu')\,, \tag{4.35}$$

same as Hashimoto (1995), and P_l is the Legendre polynomial. Hereafter we neglect the terms larger than third order in the scattering phase function, and $a^{(0)} = 1$.

Integrating Equation (4.13) by μ, we obtain the zeroth moment of the radiative transfer equation,

$$\frac{1}{r^2}\frac{d}{dr}\left(r^2F\right) = -4\alpha\left(J - B\right), \tag{4.36}$$

or using Equation (4.16) it becomes,

$$\frac{1}{r^2}\frac{d}{dr}\left(r^2H\right) = -\alpha\left(J - B\right). \tag{4.37}$$

Multiplying μ and integrating it, we get

$$\frac{dK}{dr} + \frac{1}{r}\left(3K - J\right) = -\frac{1}{4}\left(\alpha + \sigma\right)F + \frac{1}{12}\sigma a^{(1)}F. \tag{4.38}$$

Here we define

$$k = \alpha + \sigma, \tag{4.39}$$

and substituting Equation (4.32), this equation can be modifies as

$$\frac{dJ}{dr} + \frac{1}{2}\frac{1}{r^3}\frac{d}{dr}\left(r^3\mu_r F\right) = -\frac{3}{4}k\left(1 - \frac{1}{3}\frac{\sigma}{k}a^{(1)}\right)F. \tag{4.40}$$

If we use H, this equation becomes

$$\frac{dJ}{dr} + \frac{2}{r^3}\frac{d}{dr}\left(r^3\mu_r H\right) = -3k\left(1 - \frac{1}{3}\frac{\sigma}{k}a^{(1)}\right)H. \tag{4.41}$$

This is the first moment of the radiative transfer equation (4.13).

Similarly, the second moment is calculated by multiplying Equation (4.13) by μ^2 and integrating it.

$$\frac{d\mu_r}{dr} = \frac{1 - \mu_r^2}{r\mu_r} - \frac{2}{3}\left[k - \frac{1}{5}\sigma a^{(2)} + \frac{1 + 3\mu_r^3}{4\mu_r}\frac{1}{r^2F}\frac{d}{dr}\left(r^2F\right)\right] \tag{4.42}$$

is the second moment, and it can be written by using H as follows,

$$\frac{d\mu_r}{dr} = \frac{1 - \mu_r^2}{r\mu_r} - \frac{2}{3}\left[k - \frac{1}{5}\sigma a^{(2)} + \frac{1 + 3\mu_r^3}{4\mu_r}\frac{1}{r^2H}\frac{d}{dr}\left(r^2H\right)\right]. \tag{4.43}$$

We can obtain the differential equation for μ_r from the second moment of the radiative transfer equation in this manner.

The third moment of the radiative transfer equation is written as

$$\frac{d\mu_r^3}{dr} = \frac{1}{4}k + \frac{3}{r}\mu_r - \frac{5}{4}k\mu_r^2 - \frac{5}{r}\mu_r^3 - \mu_r^3\frac{1}{F}\frac{dF}{dr}, \tag{4.44}$$

or

$$\frac{d\mu_r^3}{dr} = \frac{1}{4}k + \frac{3}{r}\mu_r - \frac{5}{4}k\mu_r^2 - \frac{5}{r}\mu_r^3 - \mu_r^3\frac{1}{H}\frac{dH}{dr}. \tag{4.45}$$

Therefore, we obtain the differential equation for μ_r^3 from the third moment of the radiative transfer equation.

As pointed out in Unno (1989), Equation (4.43) which gives the differential equation for μ_r, has a singularity at $\mu_r = 0$, thus this term will cause numerical instability around $\mu_r = 0$. If one use Equation (4.45) which gives the equation for μ_r^3 instead of Equation (4.43), one can avoid the numerical instability.

4.3.4 Radiation Temperature

When the thermal equilibrium is achieved, the relation

$$\int_0^\infty \kappa_\nu J_\nu d\nu = \int_0^\infty \kappa_\nu B(T)\, d\nu \tag{4.46}$$

is satisfied. From this equation, we obtain $J - B = 0$ where J and B is integrated by all frequency. Then the zeroth moment of the radiative transfer equation becomes

$$\frac{1}{r^2}\frac{d}{dr}\left(r^2 F\right) = 0, \tag{4.47}$$

which describes the conservation of flux. By using this, the third moment can be written as

$$\frac{d\mu_r^3}{dr} = \frac{1}{4}k\left(1 - 5\mu_r^2\right) + \frac{3}{r}\mu_r\left(1 - \mu_r^2\right). \tag{4.48}$$

Equation (4.47) can be solved as

$$F(r) = \frac{r_0^2 F_0}{r^2}, \tag{4.49}$$

where r_0 is the inner boundary (or sometimes surface of an object), and F_0 is the flux in the inner boundary, $F(r_0)$. Now Equation (4.40) can be written as

$$\frac{dJ}{dr} = -r_0^2 F_0\left[\frac{1}{2}\frac{d}{dr}\left(\frac{\mu_r}{r^2}\right) + \frac{3}{2}\frac{\mu_r}{r^3} + \frac{3}{4}k\left(1 - \frac{1}{3}\frac{\sigma}{k}a^{(1)}\right)\frac{1}{r^2}\right]. \tag{4.50}$$

We can integrate this from r to the outer boundary R, then we obtain

$$J(R) - J(r) = -r_0^2 F_0\left[\frac{\mu_R}{R^2} - \frac{\mu_r}{r^2} + \int_r^R \left\{\frac{3}{4}k\left(1 - \frac{1}{3}\frac{\sigma}{k}a^{(1)}\right) + \frac{3}{2}\frac{\mu_{r'}}{r'}\right\}\frac{dr'}{r'^2}\right], \tag{4.51}$$

where μ_R is the value of μ at the outer boundary.

Here we assume that incoming intensity at the outer boundary is zero, and isotropic scattering $a^{(l)} = 0$ for simplicity. In addition, using the relation

$$T_{\rm rad}^4(r) = \frac{\pi}{\sigma_{\rm SB}} J(r)\,, \tag{4.52}$$

now we can derive the equation for the radiation temperature,

$$T_{\rm rad}^4(r) = \frac{r_0^2 F_0}{2\sigma_{\rm SB}} \left\{ \frac{1}{R^2\left(1+\mu_R\right)} + \frac{\mu_R}{R^2} - \frac{\mu_r}{r^2} + \frac{3}{2}\int_r^R \left[k(r') + \frac{2\mu_{r'}}{r'} \right] \frac{dr'}{r'^2} \right\}. \tag{4.53}$$

Finally, here we ignore the effect of scattering for simplification, then we obtain following equations on the radiative temperature,

$$T_{\rm rad}^4(r) = \frac{r_0^2 F_0}{2\sigma_{\rm SB}} \left\{ \frac{1}{R^2\left(1+\mu_R\right)} + \frac{\mu_R}{R^2} + \frac{\mu_r}{r^2} + \frac{3}{2}\int_r^R \left[\alpha(r') + \frac{2\mu_{r'}}{r'} \right] \frac{dr'}{r'^2} \right\}, \tag{4.54}$$

$$\frac{d\mu_r^3}{dr} = \frac{\alpha(r)}{4}\left(1-5\mu_r^2\right) + \frac{3\mu_r}{r}\left(1-\mu_r^2\right). \tag{4.55}$$

If one knows the extinction coefficient α at each position in the atmosphere and an appropriate boundary condition, μ_r can be obtained by integrating Equation (4.55). Subsequently, the radiation temperature in the atmosphere is calculated from Equation (4.54). These equations to derive the radiation temperature are sometimes used for dynamical models for the envelopes of AGB stars (e.g., Winters et al., 1997; Schirrmacher et al., 2003).

4.3.5 Test Calculations

Here we demonstrate test calculations of the derivation of the radiation temperature that described in the previous section. First, we calculate μ in a model atmosphere, that is a time-averaged density profile and a temperature structure which are calculated by the ideal MHD simulation in Chapter 2. Figure 4.2 shows the density profile and temperature structure of the model atmosphere that we use for the test calculation. The parameters for the calculation are follows; the radius and mass are same as Jupiter, the surface temperature is 1000 K, and the velocity dispersion at the surface is 20% of the sound speed.

To calculate Equation (4.54) and (4.55), the absorption coefficient is needed. Here we use an opacity table that is given by Helling and Lucas (2009) to calculate the value of the absorption coefficient in each point. The absorption coefficient is calculated as follows,

$$\alpha = \kappa\rho \tag{4.56}$$

where ρ is the density of the gas, and κ is a mean opacity that depends on the pressure and temperature of the material, and it is obtained from the opacity table. Here we use the table

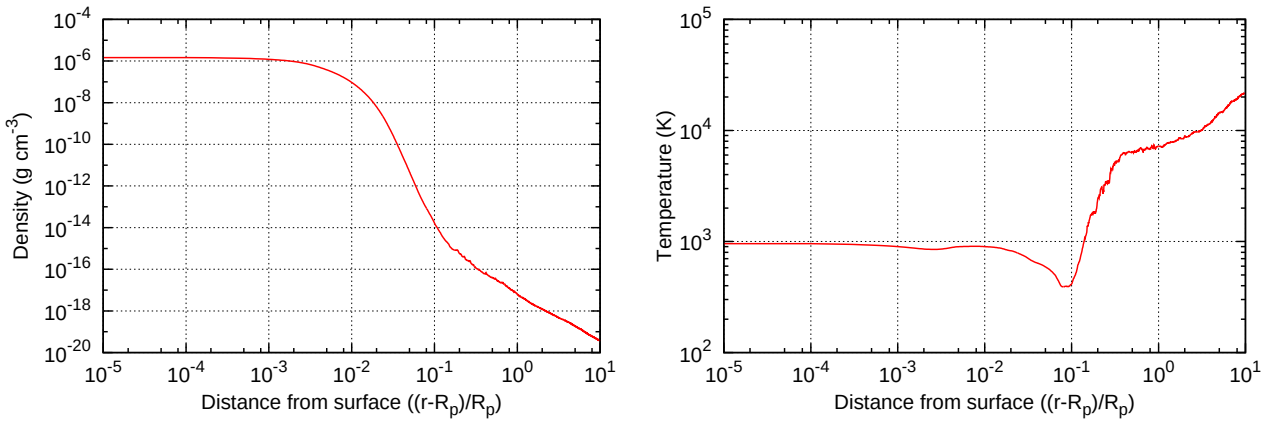

Figure 4.2: The model atmosphere for the test calculation of μ and the radiation temperature. The left panel shows the time-averaged density structure, and the right panel shows the time-averaged temperature structure. The horizontal axes denote the distance from the planetary surface that is normalized by the planetary radius.

of Rosseland mean opacity in solar compositional gas. Here we assume the inner boundary condition for μ that is $\mu = 0$ at the surface.

Figure 4.3 shows the result of the integration of Equation (4.55) in the model atmosphere. Both panel show the same plot, but the left panel shows the wider range of the distance from the surface, and both axes are logarithmic scale. The right panel shows the μ in the lower atmosphere, and both axes are linear scale. As shown in the figure, μ rapidly increases as the altitude, and asymptotically approach unity in the upper atmosphere.

Now we obtain the value of μ, then we can calculate the radiation temperature by Equation (4.54). Here we assume that the flux at the inner boundary is determined by the black-body radiation at the surface temperature (in this case, it is 1000 K). The result is shown in Figure 4.4. In the figure we compare the gas temperature that calculated by the MHD simulation (red line), and the radiation temperature we derived here (blue line). The radiation temperature almost same as the gas temperature in the lower atmosphere. However, while the gas temperature increases because of the heating by the MHD waves, the radiation temperature simply drops as the altitude, therefore difference becomes very large in the upper atmosphere. Interestingly, the radiation temperature exceeds the gas temperature around $(r - R_{\rm p})/R_{\rm p} \sim 10^{-1}$, because the gas temperature around there decreases due to the adiabatic expansion that is caused by the strong acceleration of the planetary wind at the region above there.

Since we get the profile of the radiation temperature, now we can calculate the cooling or heating rate in the atmosphere by using Equation (4.9). Here we use an approximation that

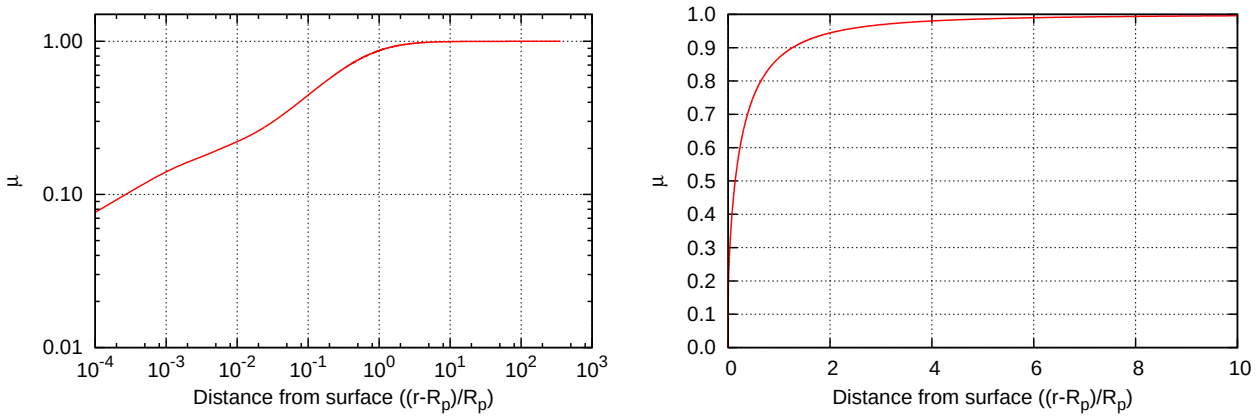

Figure 4.3: Test calculation of μ in the model atmosphere. Both panels show same results, but ranges and scale are different.

the opacities are Rosseland mean opacity given in Helling and Lucas (2009) for simplicity. The result is shown in Figure 4.5. For comparison, we plot two sets of the radiative cooling/heating rate. One set is the cooling and heating rate that calculated by the opacity from the opacity table of Helling and Lucas (2009), and another set is the cooling and heating rate that calculated by a constant opacity and absorption coefficient, where $\kappa = 2.0 \times 10^{-4}\,\mathrm{cm^2\,g^{-1}}$, and $\alpha = 2.0 \times 10^{-4}\rho\,\mathrm{cm^{-1}}$. The blue lines denote the radiative cooling, and red lines denote the radiative heating, respectively, and solid lines correspond to the rates calculated with the opacity from the opacity table, and dashed lines correspond to that with the constant opacity. In each case general trend is similar; the radiative cooling rates are almost constant in the lower atmosphere because the density and temperature do not change significantly, and the radiation temperature also do not change in that region. However, in the upper atmosphere the cooling rates become much larger because of the large difference between the gas temperature and radiation temperature which shown in Figure 4.4. In addition, around the region where $(r - R_\mathrm{p})/R_\mathrm{p} \sim 10^{-1}$, heating by radiation occur, because the radiation temperature exceeds the gas temperature around that region, as described above.

In addition, as shown in Figure 4.5, the constant opacity case largely differ in the upper atmosphere from the case which the opacity table is used. This result shows that the approximation of the simple constant opacity in the atmosphere is not so bad in the lower atmosphere, but it gives significantly wrong value in the less dense, and high temperature condition in the upper atmosphere.

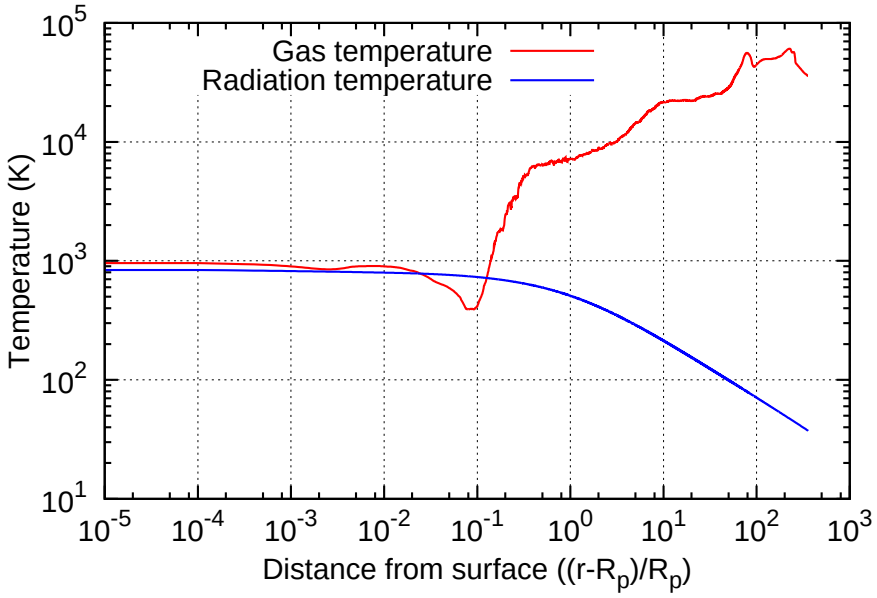

Figure 4.4: Comparison of the (time-averaged) gas temperature calculated by the ideal MHD simulation and the radiation temperature calculated by Equation (4.54). The red, and blue lines are the gas temperature, and radiation temperature, respectively, and the horizontal axis denotes the distance from the surface that is normalized by the planetary radius.

4.3.6 Incorporating into the MHD Simulations

In the previous section we show the test calculation of μ, the radiation temperature, and the resultant radiative cooling and heating rates in the model atmosphere. In order to combine this radiative transfer method to our MHD simulation, we should solve them in each time step in the MHD simulation. We incorporate the radiative transfer method that we describe above as follows. First, MHD part is solved to determine the atmospheric structure that is necessary to solve the radiative cooling and heating. Next, Equation (4.54) and (4.55) are solved by using the density and temperature that determined by the MHD calculation, and the mean opacity table by Helling and Lucas (2009). Subsequently, the radiative cooling and heating rates are calculated by Equation (4.9). Since $Q_{\rm rad}$ denotes the radiative cooling or heating rate per unit mass, we multiply the density of the gas to it and obtain the radiative cooling or heating rate per unit volume. Then we substitute it to the radiative cooling or heating term $q_{\rm R}$, in the energy equation, Equation (2.6). From the next time step, the MHD part is solved with the new radiative cooling and heating rate.

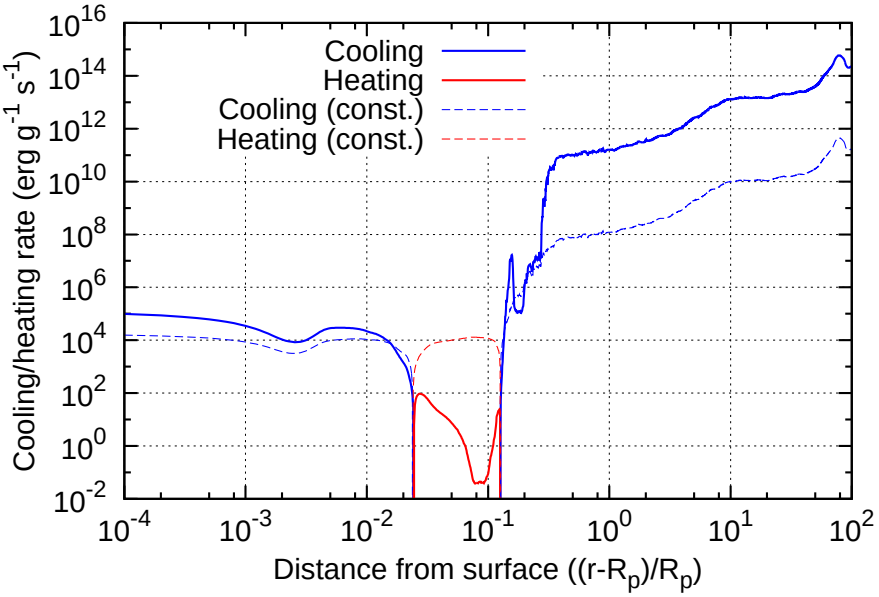

Figure 4.5: Cooling and heating rates in the atmosphere that is calculated by Equation (4.9). The blue and red lines are cooling rate, and heating rate per unit mass, respectively, and shown in units of erg g^{-1} s^{-1}. We also show the cooling and heating rates which are calculated with a constant opacity for comparison, and they are shown by dashed lines.

4.4 Comparison of New Results with the Previous Results

From here we show results of the new calculations that include the new radiative cooling and heating function calculated through the modified Unno-Kondo method (Unno and Kondo, 1976; Unno, 1989; Hashimoto, 1995). First we compare new results and the previous results whose radiative cooling rate is calculated by the solar chromospheric and coronal cooling rates.

4.4.1 Atmospheric Structures and Mass-Loss Rate

Fiigure 4.6 shows the comparison of the atmospheric structures between the new and previous calculations. In these calculations, we assume the ideal MHD condition for the planetary atmosphere, and the parameters for the planet are follows; the radius and mass are same as Jupiter, the surface temperature is 1000 K, and the value of the velocity dispersion is 20% of the sound speed at the surface. The red lines show the result with the new cooling function which based on the modified Unno-Kondo method described in Section 4.3, and the blue lines show the previous result that is same calculation in Section 2.

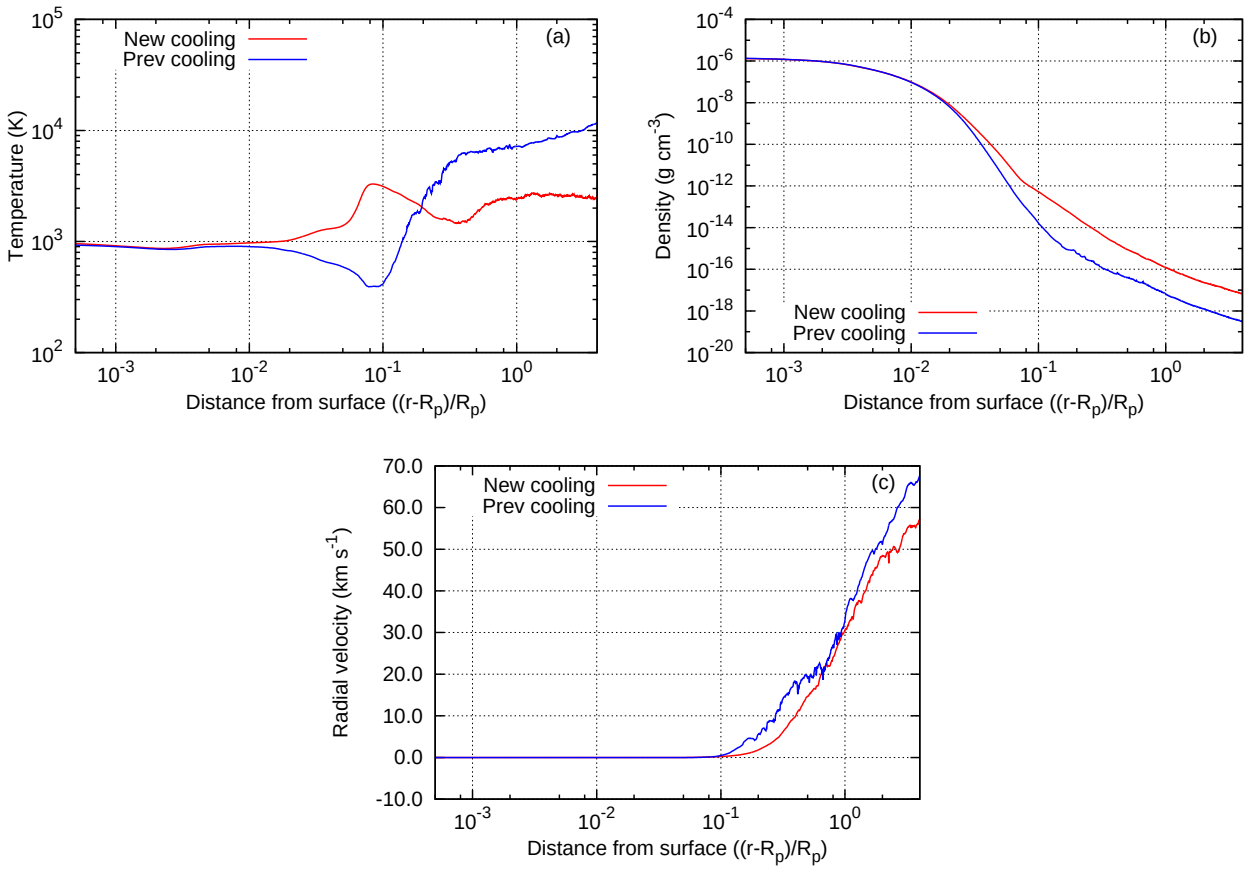

Figure 4.6: Comparison of the atmospheric structures between the previous and new calculations. (a) Temperature structure, (b) density profile, and (c) radial velocity profile. The red lines correspond to the new calculation, and the blue lines correspond to the previous calculation.

As shown in the figures, the atmospheric structure is changed due to the improvement of the radiative cooling term. Most significant difference appears in the temperature structure. In the previous calculation, temperature decreases around $(r - R_{\rm p})/R_{\rm p} \sim 10^{-1}$ to form the temperature inversion region because of the adiabatic expansion caused by the planetary wind. Then, temperature increases rapidly and the high temperature corona-like region is created. In the new calculation, however, the decrease of the temperature that appeared in the previous calculation disappears, and temperature in the upper atmosphere becomes much lower compared to the previous results.

In the density profile, general trend is almost similar; the atmospheric gas is uplifted by the dissipation of the MHD wave energy in the upper atmosphere, so the profiles become gradual around there. However, much more amount of gas is uplifted in the new calculation, therefore

the gas density in the upper atmosphere becomes higher around an order of magnitude than the previous calculation. The radial velocity profile also show the similar trend in both cases. Although the velocity in the upper atmosphere in the new calculation is slightly slower than the previous calculation, the difference is so small. In addition, the acceleration of the atmospheric gas is very efficient, so the radial velocity of the escaping atmosphere can exceed the sound speed in the upper atmosphere; the supersonic outflow is produced.

According to the new calculation, a resultant mass-loss rate becomes larger than the previous because the gas density in the upper atmosphere is enhanced and the radial velocity is not changed significantly. In this calculation, we obtain the mass-loss rate of $\dot{M} = 5.83 \times 10^{11}\,\mathrm{g\,s^{-1}}$, which is about 24 times larger than the previous calculation.

4.4.2 Radiative Cooling Rate

Despite we only changed the radiative cooing term q_{R} in the energy equation (Equation (2.6)), the atmospheric structure are modified in particular the temperature structure, and the mass-loss rate becomes larger. Therefore, the improvement of the radiative cooling and heating rate in the atmosphere has the large effect to the results of the MHD calculation. In order to check

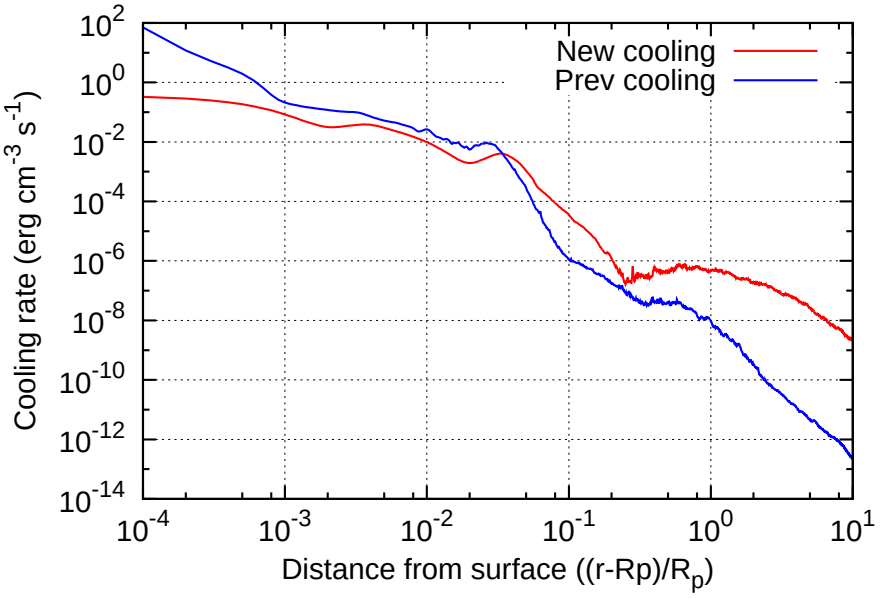

Figure 4.7: Comparison of the cooling rate in the planetary atmosphere. The red and blue lines correspond to the new and previous cooling rates, respectively. The horizontal axis denotes the distance from the surface that is normalized by the planetary radius, and the vertical axis denotes the radiative cooling rate per unit volume in the units of $\mathrm{erg\,cm^{-3}\,s^{-1}}$.

the effects of the modification of the radiative cooling term, we compare the radiative cooling rate per unit volume of the new and previous calculations in Figure 4.7.

As shown in the figure, two profiles of the radiative cooling rate in the atmosphere is different. Large differences appear in the lower and upper parts of the atmosphere. In the lower atmosphere, the new cooling rate is smaller than the previous case. In particular, in the lowest region in this calculation, the new cooling rate is two orders of magnitude lower than the previous case. This reduced radiative cooling rate causes the enhancement of the uplifting of the atmospheric gas in the upper atmosphere. In contrast with the lower atmosphere, the radiative cooling rate becomes around two to four orders of magnitude larger in the upper atmosphere. This strong radiative loss in the upper atmosphere causes the temperature that is cooler than the previous calculation, as shown in Figure 4.6(a).

In summary, it can be said that the radiative cooling function in the previous calculation overestimated the cooling rate in the lower atmosphere, and underestimated it in the upper atmosphere. These differences cause the enhancement of the density in the upper atmosphere and the larger mass-loss rate, and different shape of the temperature structure.

4.5 Dependence on the Velocity Dispersion

As with the previous chapters, we perform the MHD simulations with the various parameters. Here we describe the dependence of the atmospheric structures and mass-loss rates on the value of the velocity dispersion at the planetary surface.

4.5.1 Dependence of the Mass-Loss Rate

As described in Section 2.2, the value of the velocity dispersion at the planetary surface is one of the important parameter to determine the atmospheric structures and the mass-loss rate. Here we show the dependence of the mass-loss rate on the velocity dispersion. Figure 4.8 is the relation between the velocity dispersion and the mass-loss rate. The red line and plots show the mass-loss rates calculated by the new simulation. The dependence of the mass-loss rate calculated with the previous cooling function that is shown in Figure 2.2 is also shown in the grey line for comparison.

The mass-loss rate is smaller when the velocity dispersion is small, which is similar trend with the previous result. When the value of the velocity dispersion is 10% - 20% of the sound speed, the mass-loss rates become $10^{10} - 10^{12}\,\mathrm{g\,s^{-1}}$, so it can be said that if the velocity

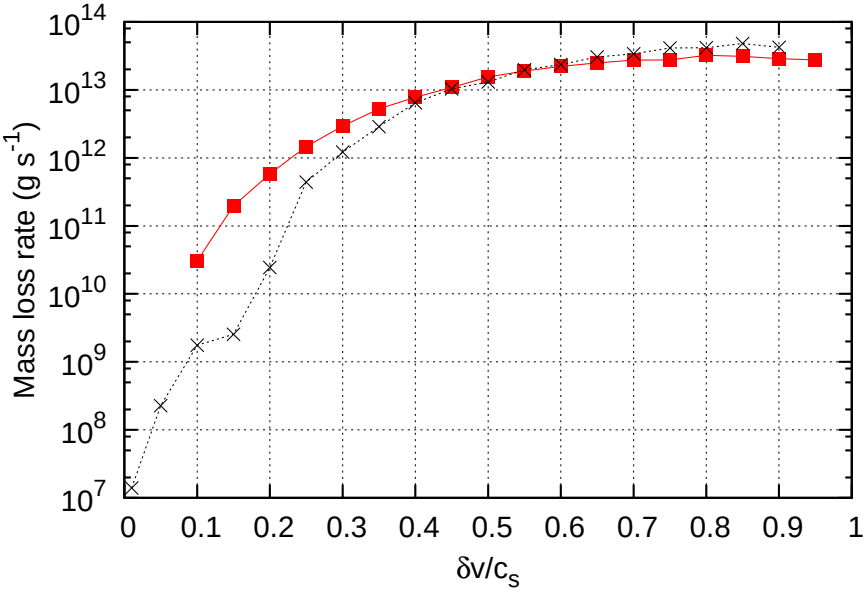

Figure 4.8: Relation between the value of the velocity dispersion at the surface of the planet and the mass-loss rate from the planet. The horizontal axis denotes the velocity dispersion that is normalized by the sound speed at the surface, and the vertical axis denotes the mass-loss rate in units of $\mathrm{g\,s^{-1}}$. In these calculations we assumed that the radius and mass of the planet are same as Jupiter, and the surface temperature is fixed to 1000 K. The mass-loss rate by previous calculation (same as in Figure 2.2) is also shown in the grey dotted line for comparison.

dispersion is not so large and the perturbation of the magnetic fields is small, a huge amount of the gas can escape from the planet. The values of the mass-loss rates which are suggested by several observations are $\sim 10^{10} - 10^{12}\,\mathrm{g\,s^{-1}}$, therefore our calculation can sufficiently explain the observations even if the velocity dispersion is small. In addition, since the dependence is steeper when the velocity dispersion is small, the mass-loss rate strongly depends on the change of the velocity dispersion in the low velocity dispersion cases.

On the other hand, increase of the mass-loss rate becomes gradual or almost constant when the velocity dispersion is large. This trend is also appeared in the previous result. It is thought that the acceleration of the gas becomes more inefficient when the velocity dispersion is larger, because of the larger density and enhanced radiative cooling in the upper atmosphere. We show them more detail later.

Compared with the previous result, the mass-loss rate is one to two orders of magnitude larger when the velocity dispersion is small. When $\delta v \sim 0.5 c_{\mathrm{s}}$, the mass-loss rates are almost same, and inverses very slightly in the larger velocity dispersion cases.

4.5.2 Atmospheric Structures

Next we show the atmospheric structures. Figure 4.9 is the dependence of the atmospheric structures on the value of the velocity dispersion at the planetary surface. In these calculations, the parameters for the planet are follows; the radius and mass are same as Jupiter, and the surface temperature is 1000 K. Similar to the previous calculations, temperature in the lower

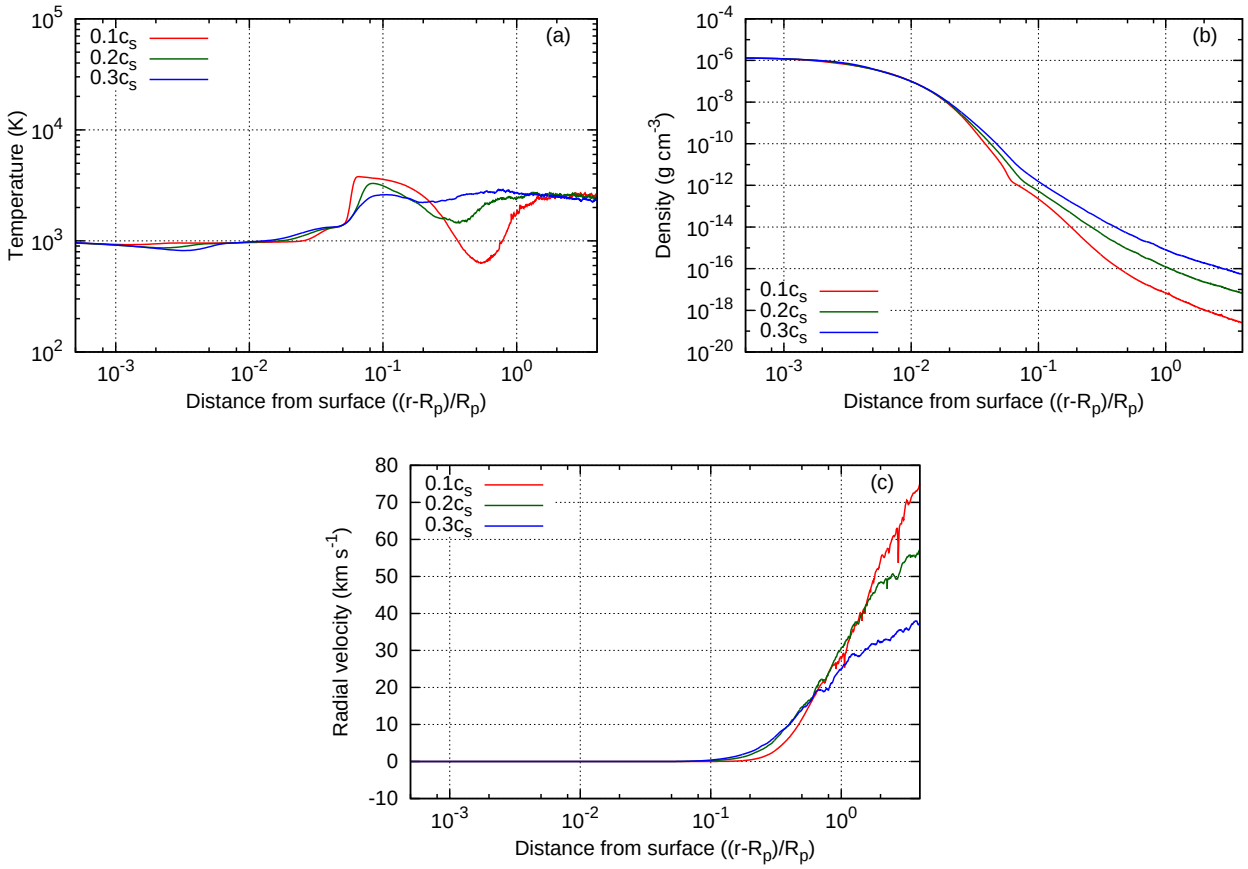

Figure 4.9: Velocity dispersion dependence of the atmospheric structures. (a) Temperature structure, (b) density profile, and (c) radial velocity profile. The horizontal axes denote the distance from the surface that is normalized by the planetary radius. The red, green, and blue lines correspond to the values of the velocity dispersion, $0.1c_{\rm s}$, $0.2c_{\rm s}$, and $0.3c_{\rm s}$, respectively.

atmosphere is almost constant, and its value is almost same as the surface temperature. Then the temperature increases due to the dissipation of the MHD wave energy, but it does not exceed $\sim 10^4$ in this time-averaged temperature profile. This is caused by the larger radiative cooling rate in the upper atmosphere that is mentioned in the Section 4.4.

The density in the upper atmosphere increases with the increase of the velocity dispersion. The larger velocity dispersion corresponds to the larger injection of the energy into the magnetic

fields, therefore more amounts of the gas can be uplifted. This effect also enhances the mass-loss rate. The radial velocity exceeds the sound speed in the upper atmosphere in the all cases; supersonic outflow is driven by the dissipation of the MHD wave energy. In this calculation, similar to the previous results, the radial velocity in the upper atmosphere gradually decreases with the increase of the velocity dispersion. The acceleration of the gas becomes slightly weaker because the density in the upper atmosphere is enhanced by the larger injection energy, and the radiative cooling rate is also enhanced by the larger gas density.

4.5.3 Radiative Cooling Rate

As described in Section 4.4.2 and shown in Figure 4.7, difference of the radiative cooling rate in the atmosphere strongly affects the resultant atmospheric structure and the mass-loss rate. Here we show the dependence of the radiative cooling rate in the atmosphere on the velocity dispersion to understand the behavior of the atmospheric structure and the mass-loss rate dependence on the velocity dispersion. Figure 4.10 shows the dependence of the radiative

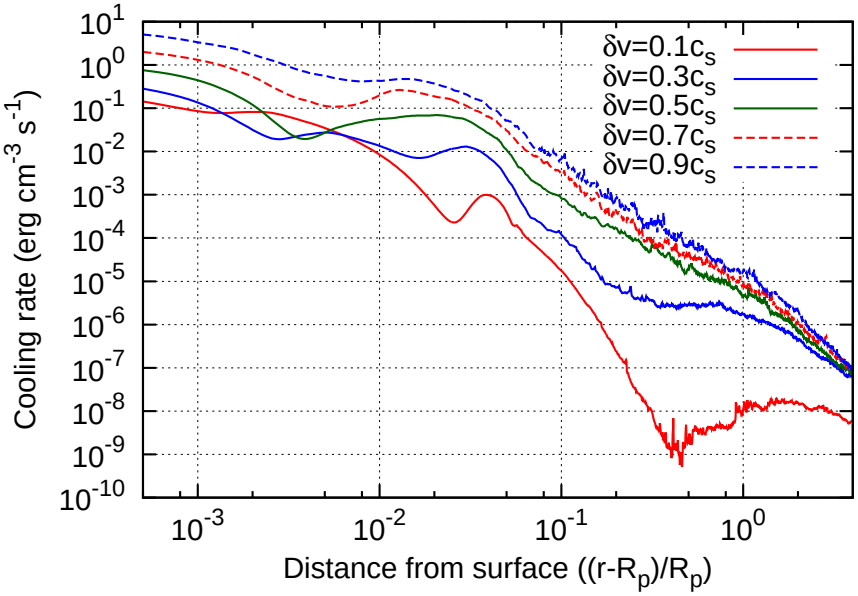

Figure 4.10: The radiative cooling rates in the atmosphere as a function of the altitude. The horizontal axis denotes the distance from the surface that is normalized by the planetary radius, and the vertical axis denotes the radiative cooling rate per unit volume in units of erg cm^{-3} s^{-1}. The red solid, blue solid, green solid, red dashed, and blue dashed lines correspond to the values of the velocity dispersion, $0.1c_s$, $0.3c_s$, $0.5c_s$, $0.7c_s$, and $0.9c_s$, respectively.

cooling rate per unit volume as a function of the altitude. In the almost all region in the

atmosphere, the radiative cooling rate increases with the increase of the velocity dispersion. In particular, the radiative cooling rate differs largely in the upper atmosphere. This strong enhancement of the radiative cooling rate in the entire region of the atmosphere when the velocity dispersion become larger significantly affect the structure of the atmosphere. Figure

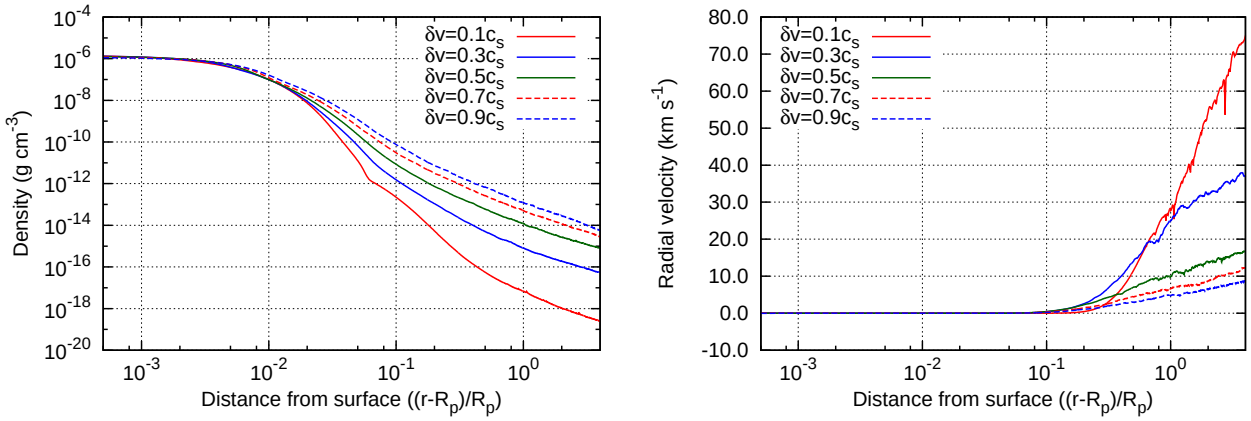

Figure 4.11: Velocity dispersion dependence of the density profile (left) and radial velocity profile (right) in several values of the velocity dispersion. The horizontal axes denote the distance from the surface that is normalized by the planetary radius. The red solid, blue solid, green solid, red dashed, and blue dashed lines correspond to the value of the velocity dispersion, $0.1c_{\rm s}$, $0.3c_{\rm s}$, $0.5c_{\rm s}$, $0.7c_{\rm s}$, and $0.9c_{\rm s}$, respectively.

4.11 shows the density profile and radial velocity profile in several cases of the values of the velocity dispersion. The density in the upper atmosphere increases with the increase of the velocity dispersion, but the increase rate on the velocity dispersion becomes small when the velocity dispersion becomes larger. In addition, the radial velocity in the upper atmosphere significantly slows down in the larger velocity dispersion cases.

This phenomena can be understood by the effect of the enhanced radiative cooling rate. When the velocity dispersion is large, more amounts of the energy are injected to the magnetic fields as the MHD waves and more amounts of the energy dissipate in the atmosphere to uplift the atmospheric gas. Thus the density in the upper atmosphere increases. However, since this means that the upper atmosphere become heavier, it becomes difficult to accelerate the upper atmospheric gas, so the radial velocity becomes slower in the larger velocity dispersion cases. In addition to this, the radiative cooling rate also becomes larger because of the denser upper atmosphere. In this condition, the MHD wave energy that dissipated in the upper atmosphere is lost by the radiative cooling rather than converted into the kinetic energy of the escaping atmosphere.

These two elements, the inefficient acceleration of the denser upper atmosphere, and the enhanced radiative loss in the denser atmosphere, cause the slowing in the increase of the density in the upper atmosphere and the radial velocity. Therefore, the saturation of the increase of the mass-loss rate that shown in Figure 4.8 occurs.

4.5.4 Time Variability of the Mass-Loss Rate

In the all cases, there are large time-variability in the upper atmosphere. In particular, fluctuation of the density and radial velocity in the upper atmosphere cause the time-variation of the mass-loss rate. Here we show how the mass-loss rates vary with the time.

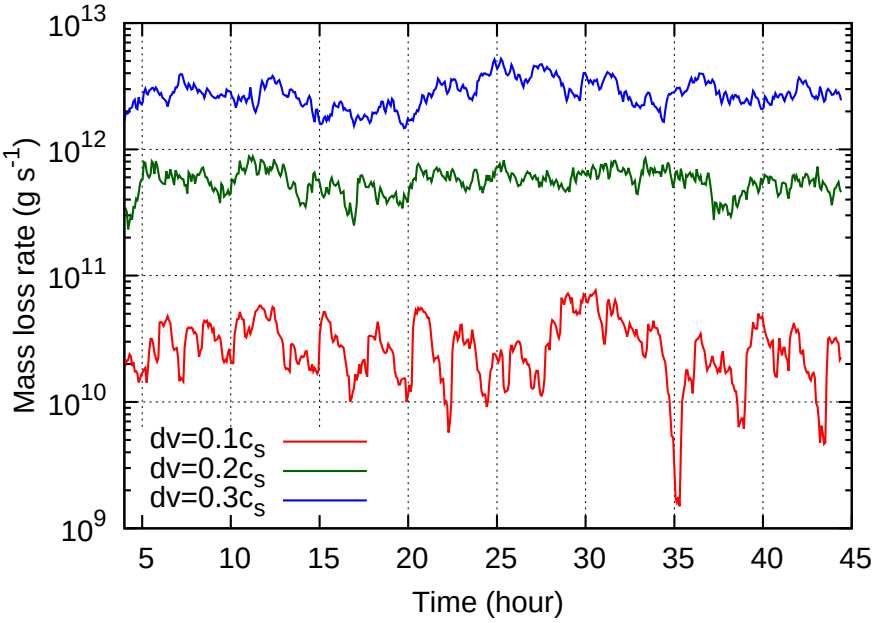

Figure 4.12: Time variability of the mass-loss rate. The horizontal axis is time in units of hour, and the vertical axis is the mass-loss rate in units of $\mathrm{g\,s^{-1}}$. The red, blue, and green lines correspond to the value of the velocity dispersion, $0.1c_\mathrm{s}$, $0.2c_\mathrm{s}$, and $0.3c_\mathrm{s}$, respectively. For all cases, the radius and mass are set to the value same as Jupiter, and the surface temperature is set to 1000 K.

Figure 4.12 shows the time variability of the mass-loss rate in three cases of the velocity dispersion. When the velocity dispersion is 10% of the sound speed (red line), the mass-loss rate has variations with the period of several hours. In addition, the magnitude of the variation sometimes exceed an order of magnitude. For the larger velocity dispersion cases, while the mass-loss rates become larger, the amplitude of the time-variation becomes smaller. But the variability itself still can be seen, and small jitter of the mass-loss late with short periods

also exist. Figure 4.13 also shows the time-variability of the mass-loss rate of the different

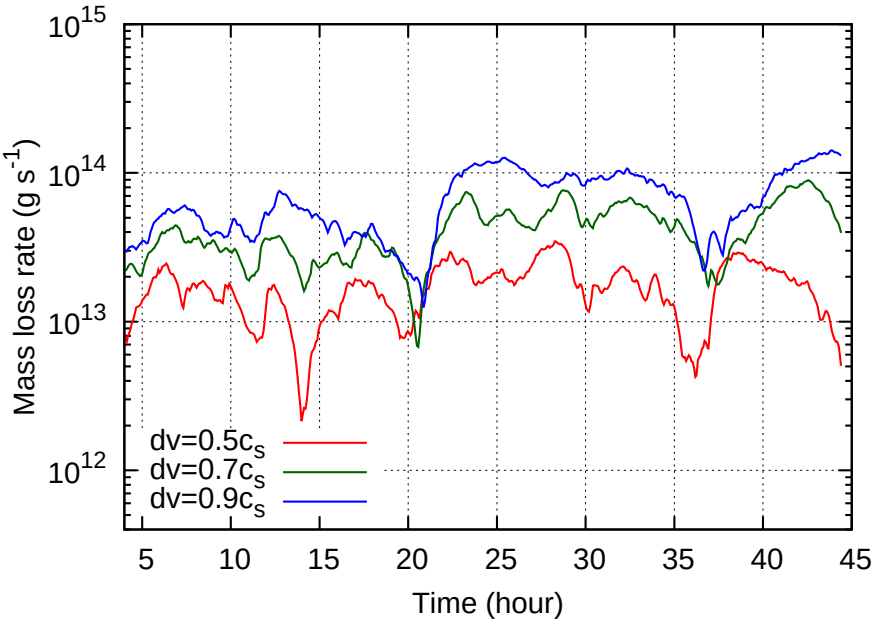

Figure 4.13: Time variability of the mass-loss rate. The horizontal axis is time in units of hour, and the vertical axis is the mass-loss rate in units of $\mathrm{g\,s^{-1}}$. The red, blue, and green lines correspond to the value of the velocity dispersion, $0.5c_\mathrm{s}$, $0.7c_\mathrm{s}$, and $0.9c_\mathrm{s}$, respectively. For all cases, the radius and mass are set to the value same as Jupiter, and the surface temperature is set to 1000 K. Note that the range of the vertical axis is different from Figure 4.12.

cases of the velocity dispersion. The time-variation of the mass-loss rate also appears in the larger velocity dispersion cases, and the amplitude of the variation is around an order of the magnitude. Therefore, it can be said that although the amplitude and duration differ depending on the value of the velocity dispersion, the variation of the mass-loss rate exist in all the cases. This time-variation of the mass loss and atmospheric structure is one of the aspect of the magnetically driven atmospheric escape.

4.6 Dependence on the Radius and Mass

Next we show the dependence of the mass-loss rate and atmospheric structures on the radius and mass of the planet. We change the radius of hot Jupiters from $0.8R_\mathrm{J}$ to $2R_\mathrm{J}$, and the mass from $0.3M_\mathrm{J}$ to $1.2M_\mathrm{J}$.

4.6.1 Radius Dependence of the Atmospheric Structures

Figure 4.14 shows the relations between the atmospheric structures and the radius of the planets. Temperature in the upper atmosphere is heated up by the dissipation of the MHD wave

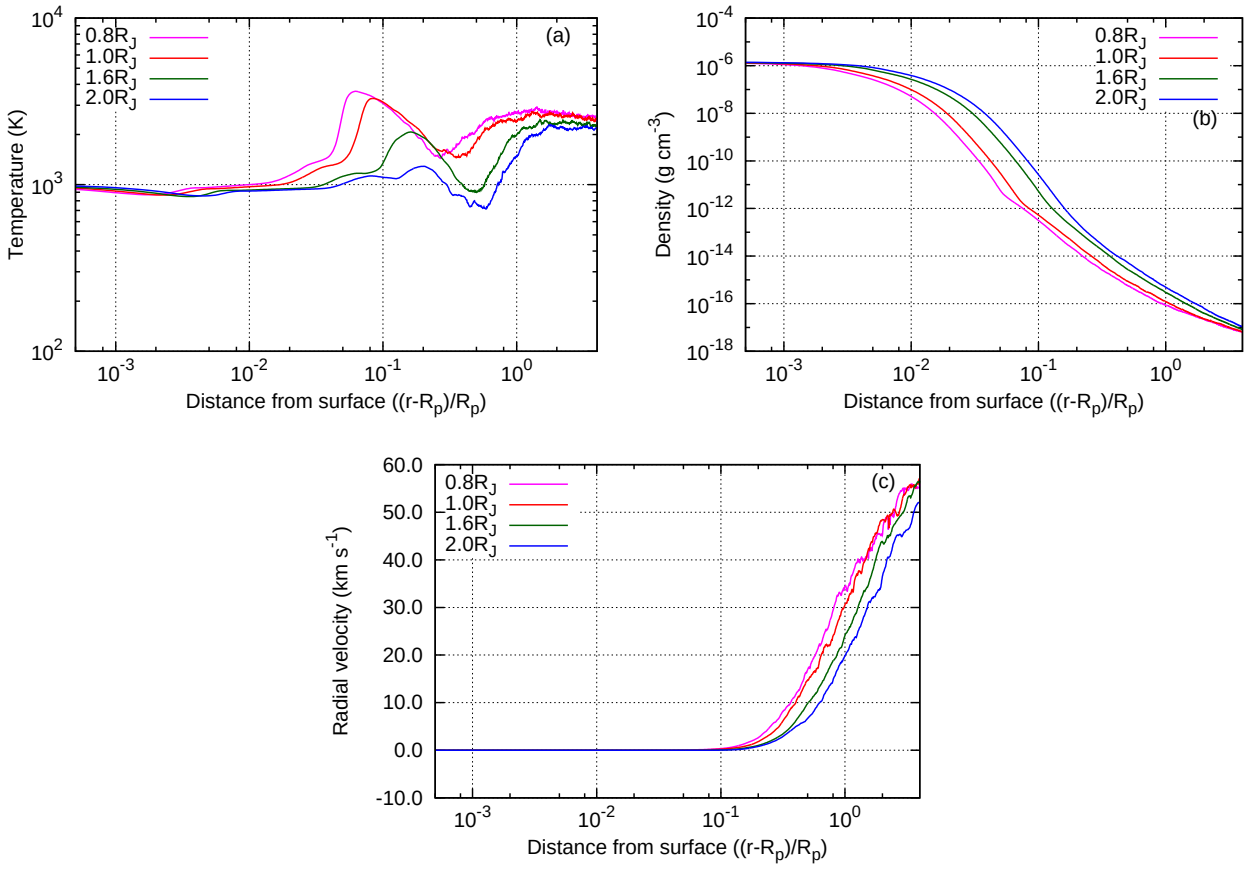

Figure 4.14: Planetary radius dependence of the atmospheric structures. (a) Temperature structure, (b) density profile, and (c) radial velocity profile. The horizontal axes denote the distance from the surface of the planet that is normalized by the radius of the planet. The magenta, red, green, and blue lines correspond to radii of planets, $0.8R_{\rm J}$, $1R_{\rm J}$, $1.6R_{\rm J}$, and $2.0R_{\rm J}$, respectively. The surface temperature is set to 1000 K, and the velocity dispersion is 20% of the sound speed in the all cases.

energy, but the altitude where the heating becomes important is different in each cases (Figure 4.14(a)). This fact corresponds to the scale height of the atmosphere; when the radius of the planet is smaller, the pressure scale height becomes smaller because the surface temperature and mass of the planet are fixed in this simulation. Therefore, the gas density in the upper atmosphere becomes smaller, which is easier to be heated up by the dissipation of the MHD wave energy. In contrast to this, when the radius is larger, the scale height becomes larger, that means the upper atmosphere is relatively dense and becomes harder to heat up by the same amount

of the injected energy. The effect of the scale height is shown in Figure 4.14(b); the density in the upper atmosphere increases as the increase of the radius. The radial velocity profiles are almost similar in all the cases, but they become faster in the cases of the larder radius. These trends therefore cause the larger mass-loss rate for the cases of the larder planetary radius.

4.6.2 Mass Dependence of the Atmospheric Structures

Here we show the dependence of the atmospheric structures on the mass of the planet. Figure 4.15 is the relation between the atmospheric structures and the mass of the planets. In these calculations, the radius of the planet is fixed to Jupiter's radius, the surface temperature is 1000 K, and the velocity dispersion is 20% of the sound speed. The temperature in the upper

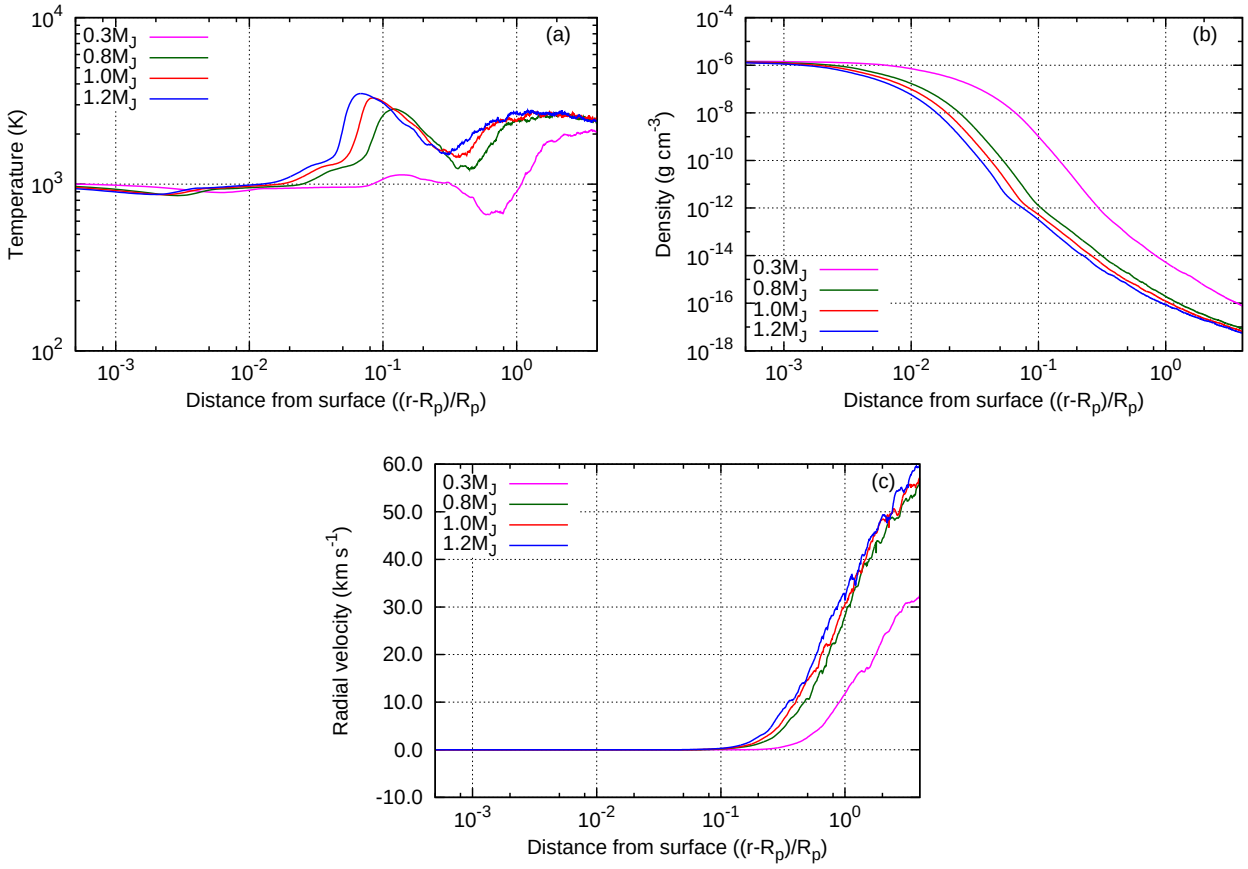

Figure 4.15: Planetary mass dependence of the atmospheric structures. (a) Temperature structure, (b) density profile, and (c) radial velocity profile. The horizontal axes denote the distance from the surface of the planet that is normalized by the radius of the planet. The magenta, green, red, and blue lines correspond to masses of planets, $0.3M_{\rm J}$, $0.8M_{\rm J}$, $1.0M_{\rm J}$, and $1.2M_{\rm J}$, respectively. The surface temperature is set to 1000 K, and the velocity dispersion is 20% of the sound speed.

atmosphere is high in the cases for $M_{\rm p} = 0.8M_{\rm J}$, $1.0M_{\rm J}$, and $1.2M_{\rm J}$, but in the case for $M_{\rm p} = 0.3M_{\rm J}$, the temperature does not rise as the other cases, and shows an almost isothermal profile. This trend can be explained by the same reason in Section 4.6.1; the scale height of the atmosphere causes this trend. When the mass of the planet is smaller, the scale height becomes larger (Figure 4.15(b)). The case for $M_{\rm p} = 0.3M_{\rm J}$, the larger scale height causes the larger gas density in the upper atmosphere. Thus, the upper atmosphere becomes difficult to heat up compared to the other cases. The radial velocity profile is also affected by the scale height; the velocity in the upper atmosphere is about half of the other cases because the gas is heavier than the other cases and becomes difficult to accelerate. However, the effect of uplifting of the atmospheric gas is efficient to enhance the atmospheric escape. Figure 4.16 shows the

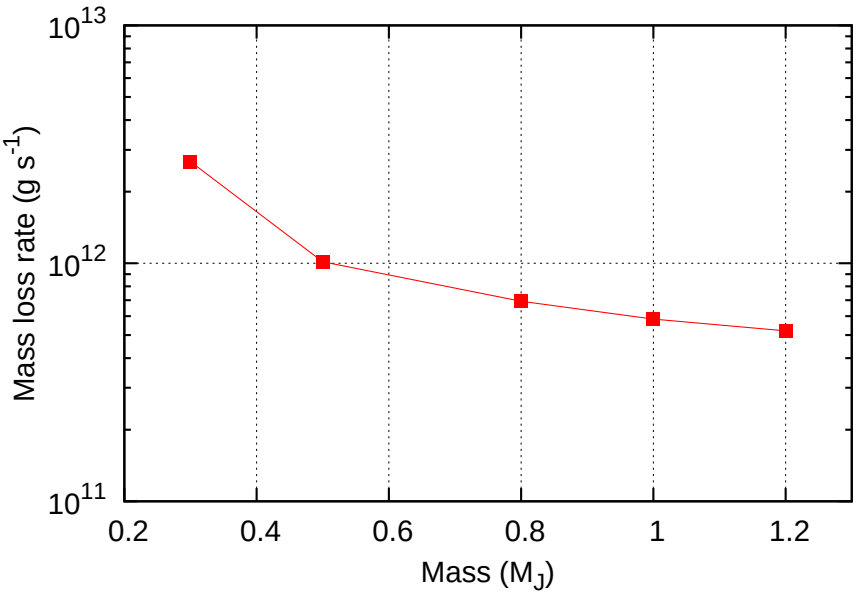

Figure 4.16: Relation between the mass of the planet and the mass-loss rate. The horizontal axis is the mass of the planet that is normalized by the mass of Jupiter, and the vertical axis is the mass-loss rate in units of $\mathrm{g\,s^{-1}}$.

dependence of the mass-loss rate on the planetary mass. As shown in the figure, the larger amount of mass loss is expected from lighter gaseous planets, because of the enhancement of the gas density in the upper atmosphere due to the larger scale height. For the heavier planets, the mass-loss rate decrease as the increase of the planetary mass, but the decrease rate is small, because the difference of the density profiles in the upper atmosphere is small (Figure 4.15(b)) and the radial velocity is almost same (c).

4.6.3 Dependence of the Mass-Loss Rate

Figure 4.17 shows the dependence of the mass-loss rate on the radius and mass of the planets. In this calculations, the surface temperature is fixed to 1000 K, and the velocity dispersion is 20% of the sound speed. The clear trend appears in the figure; the larger mass-loss rates from lighter and larger planets, and the smaller mass-loss rates from heavier and smaller planets. This trend is explained by the scale height of the planet that depends on the radius and mass

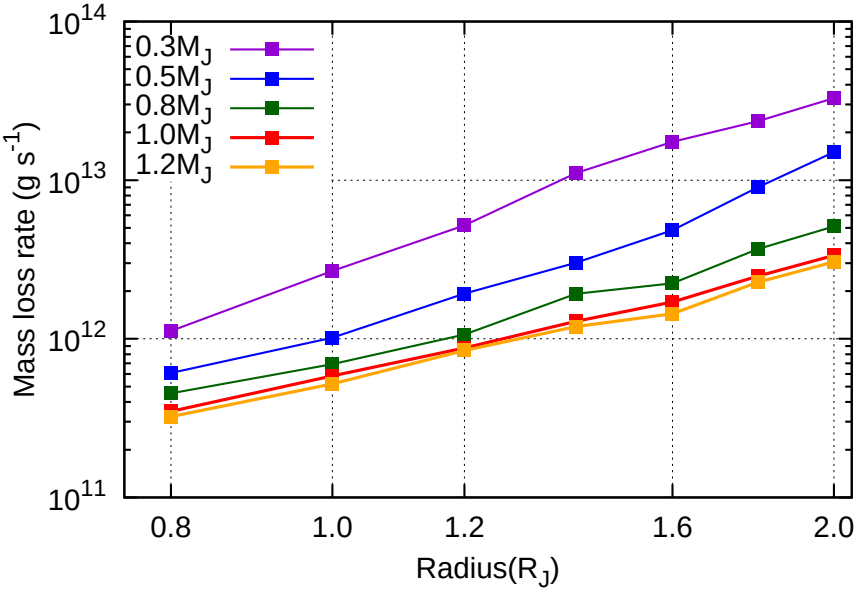

Figure 4.17: Relation between the radius and mass of the planets, and the mass-loss rate. The horizontal axis is the radius of the planets that is normalized by the radius of Jupiter, and the vertical axis is the mass-loss rate in units of $\mathrm{g\,s^{-1}}$. Note that both axes are logarithmic scale. The violet, blue, green, red, and orange lines correspond to the masses of the planets, $0.3M_\mathrm{J}$, $0.5M_\mathrm{J}$ $0.8M_\mathrm{J}$, $1.0M_\mathrm{J}$, and $1.2M_\mathrm{J}$, respectively. The surface temperature is set to 1000 K, and the velocity dispersion is 20% of the sound speed in all cases.

of the planet, as discussed in Section 2.3. In this range of the radius, the mass-loss rate changes around an order of magnitude in the all cases of the planetary mass.

4.7 Summary of This Chapter

As described above, we have improved the radiative cooling and heating in the atmosphere. In the previous calculations described in Chapter 2 and 3, the radiative cooling function for the solar coronal plasma (Landini and Monsignori Fossi, 1990; Sutherland and Dopita, 1993) and the empirical cooling function for the solar chromospheric gas (Anderson and Athay, 1989a)

are used for the radiative cooling term in the energy equation (Equation (2.6)). However, this treatment is too simplified for assumption of the radiative cooing in the planetary atmosphere, because the temperature of the atmosphere of typical hot Jupiters is much lower than the solar and stellar atmosphere. Therefore, we have applied the modified Unno-Kondo method (Unno and Kondo, 1976; Unno, 1989; Hashimoto, 1995) to calculate the radiative cooling and heating in the planetary atmosphere.

We have incorporated the modified Unno-Kondo method to calculate the radiation temperature and the radiative cooling and heating rate, and have shown that the radiative cooling in the previous calculation overestimated in the lower atmosphere, and underestimated in the upper atmosphere. This improvement of the radiative cooling result in the larger mass-loss rate compared with the previous simulations.

We have also shown that the dependence of the mass-loss rate on the parameters, and that shows similar trend with the previous calculations. Therefore we can say that the treatment of the radiative cooling and heating in the planetary atmosphere has the important effects to the structure of the atmosphere and the mass-loss rate, and the planetary pressure scale height also strongly affect to them.

Chapter 5

Radiative Transfer in the MHD Calculation for the Atmosphere of Gaseous Planets II

5.1 Possibly Problematic Points in the Modified Unno-Kondo Method

In the previous chapter, Chapter 4, we have improved the treatment of the radiative cooling and heating in the planetary atmosphere for the MHD calculation by applying the modified Unno-Kondo method (Unno and Kondo, 1976; Unno, 1989; Hashimoto, 1995; Winters et al., 1997; Schirrmacher et al., 2003). However, there are still problematic points in the current treatment by the modified Unno-Kondo method.

First, although the radiative temperature in the atmosphere is solved, the radiative transfer itself is not solved in this method. The original idea of the Unno-Kondo method is based on the two-stream approximation (Unno and Kondo, 1976), and modified version of it (Unno, 1989; Hashimoto, 1995). These methods are mainly applied for the calculations of the outer envelope of AGB stars, but in these applications, only the outward mean intensity is solved because of the simplification. In association with this point, the emission from the gas in each radius is also not included in this method. Therefore, this method only solves the mean intensity (and the resultant radiation temperature) that is derived from the emission from the surface of the object, and only the absorption of the outward intensity is included.

In addition to this, the irradiation from the outer boundary cannot be included in the current formulation because the inward flux or intensity is not solved in this method. The modified Unno-Kondo method is originally developed for the radiative transfer in hydrodynamical simu-

lations for the outer envelopes of the AGB stars (Unno, 1989; Hashimoto, 1995; Winters et al., 1997; Schirrmacher et al., 2003). In conditions of the envelopes of the AGB star, the points we recited above are not problematic, because the radiation is dominated by the emission from the surface from the AGB stars, and the incoming radiation from outer boundary can be ignored. For the conditions of exoplanets, however, the emission from the surface is much weaker due to the relatively lower surface temperature, and short-period planets are strongly irradiated by the central star. Therefore, the modified Unno-Kondo method that we have formalized in the previous chapter cannot be applied for further improvements, for example, including effects of the stellar irradiation, and including XUV irradiation to solve with the XUV-driven atmospheric escape with the magnetically driven wind. For these reasons, we should treat the radiative transfer properly for more realistic calculations and to test the validity of the modified Unno-Kondo method in the previous calculations.

5.2 Two-Stream Approximation

5.2.1 Concept of the Two-Stream Approximation

In order to further improve the treatment of the radiative cooling and heating in the planetary atmosphere, we introduce the two-stream approximation. The modified Unno-Kondo method is also based on the two-stream approximation, and takes the moments of the radiative transfer equation to derive the analytic formula of the mean intensity. Instead of taking the moments of the equation, we use the simple two-stream approximation to calculate the intensity of the radiation and derive the radiation temperature from the mean intensity in the atmosphere. Here we consider the plane-parallel atmosphere, and assume the grey atmosphere for simplicity, so the wavelength dependence of the quantities is ignored. Figure 5.1 is a schematic picture of the two-stream approximation. The left panel shows a single ray in the direction θ in some altitude in the atmosphere. The z direction corresponds to the radial direction in this plane-parallel condition. The intensity $I(z, \mu)$ is a function of the altitude z, and the angle θ between the direction of the ray and the z axis, where $\mu = \cos\theta$. The radiative transfer equation is written as follows;

$$\frac{dI}{ds} = -\alpha I + j, \tag{5.1}$$

where ds is a differential element of length along the ray, α is the absorption coefficient, and j is the emissivity. Here we ignore the effect of scattering. This equation can be rewritten by

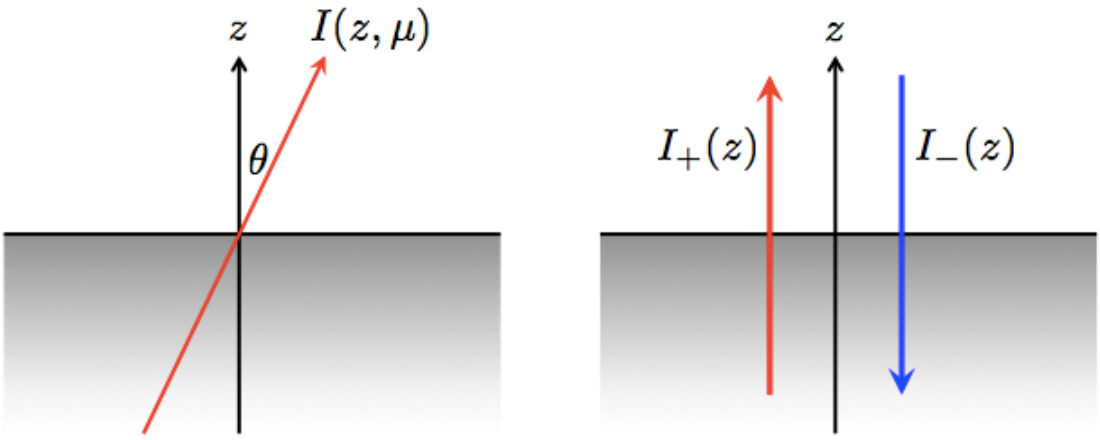

Figure 5.1: A schematic picture of the two-stream approximation. The left panel shows a single ray in the direction θ in some altitude in the atmosphere. The right panel is a conceptual rendering of the two-stream approximation.

using the direction z as follows,

$$\mu \frac{dI}{dz} = \alpha I + j. \tag{5.2}$$

Introducing the source function

$$S \equiv \frac{j}{\alpha}, \tag{5.3}$$

and the optical depth

$$d\tau = \alpha dz, \tag{5.4}$$

the equation becomes

$$\mu \frac{dI}{d\tau} = -I + S. \tag{5.5}$$

In order to derive many properties that related with the radiation such as the mean intensity or flux, we have to calculate the intensity in all directions, and integrate over all solid angles, but generally it is difficult to do so. Therefore, some kind of approximation is needed to solve the equation. One of the approximation is the two-stream approximation; dividing the intensity of the all direction into only two components, upward (outward) intensity and downward (inward) intensity as shown in the right panel of Figure 5.1. In this approximation, $\mu \geq 0$ correspond to the upward, and $\mu < 0$ correspond to the downward intensity. Now Equation (5.5) can be divided into two equations; for $\mu \geq 0$,

$$\mu \frac{dI_+}{d\tau} = -I_+ + S, \tag{5.6}$$

and for $\mu < 0$,

$$-\mu \frac{dI_-}{d\tau} = -I_- + S. \tag{5.7}$$

In this condition, the mean intensity J can be calculated by the following relation;

$$\begin{aligned} J &= \frac{1}{2}\int_{-1}^{1} I d\mu \\ &= \frac{1}{2}\left(\int_{-1}^{0} I_{-} d\mu + \int_{0}^{1} I_{+} d\mu\right) \\ &= \frac{1}{2}\left(I_{+} + I_{-}\right). \end{aligned} \tag{5.8}$$

Therefore we can calculate the mean intensity if we obtain both upward and downward intensity, then the radiation temperature can be calculated. When the temperature and density of each point are calculated, the upward and downward intensity can be calculated by solving Equation (5.6) and (5.7). Then the mean intensity is derived by Equation(5.8) and the radiation temperature is determined by

$$T_{\rm rad}^4(r) = \frac{\pi}{\sigma_{\rm SB}} J(r)\,, \tag{5.9}$$

and finally the radiative cooling or heating rate is obtained by

$$Q_{\rm rad} = 4\sigma_{\rm SB}\left(\kappa_J T_{\rm rad}^4 - \kappa_{\rm B} T_{\rm gas}^4\right). \tag{5.10}$$

5.2.2 Test Calculations

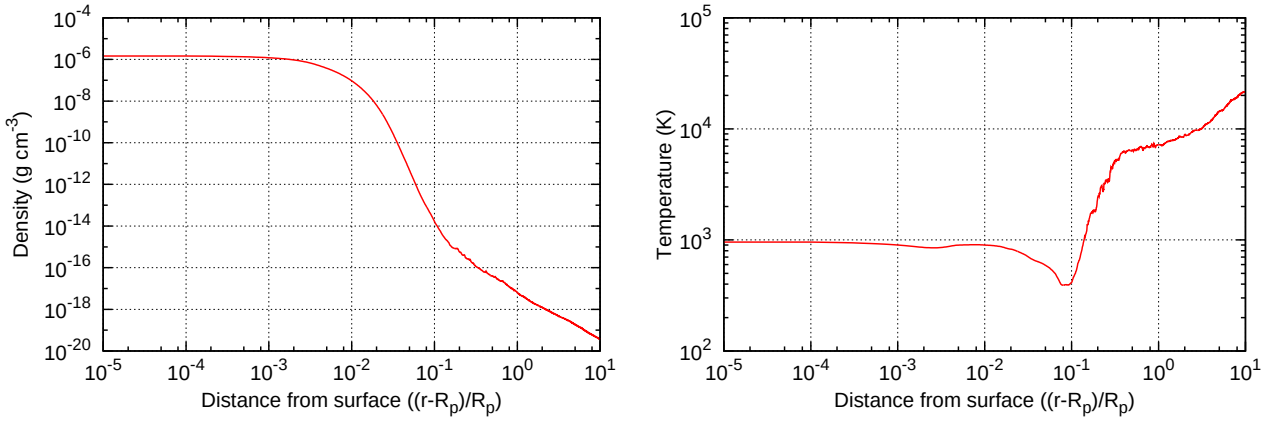

Figure 5.2: The model atmosphere for the test calculation of the radiation temperature. The left panel shows the time-averaged density structure, and the right panel shows the time-averaged temperature structure. The horizontal axis denotes the distance from the planetary surface that is normalized by the planetary radius.

Here we demonstrate test calculations of the derivation of the radiation temperature by the two-stream approximation. Similar to Section 4.3.5, first we solve the radiative transfer in the

model atmosphere that is a time-averaged density profile and temperature structure which is calculated by the ideal MHD simulation in Chapter 2. Figure 5.2 shows the model atmosphere we use for the test calculations. The parameters for the calculation are follows; the radius and mass are same as Jupiter, the surface temperature is 1000 K, and the velocity dispersion at the surface is 20% of the sound speed. We solve Equation (5.6) and (5.7) in this atmosphere.

First, we solve Equation (5.6) and (5.7) under the condition that the emission from the atmospheric gas is zero, and no incident flux from the outer boundary. In this condition, only the absorption takes place in the atmosphere, and the upward intensity monotonically decreases with the optical depth. In addition, downward intensity is zero in everywhere because no incident flux and no emission from the atmospheric gas are considered. An exact solution for the upward intensity can be derived in this assumption as follows;

$$I_+(\tau) = I_0 \exp(-\tau)\,, \tag{5.11}$$

where I_0 is the intensity at the surface of a planet. We use the Rosseland mean opacity (Helling and Lucas, 2009) to calculate the optical depth.

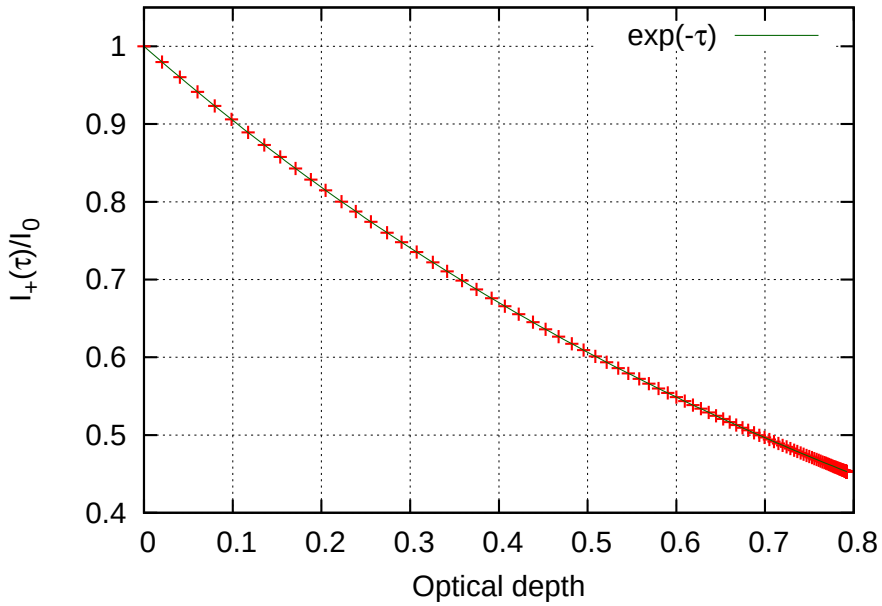

Figure 5.3: One of the results of the test calculations. This shows the upward intensity I_+ as a function of the optical depth τ with no emission from the atmospheric gas. The red points are the numerical results, and the green line is the exact solution, $I_+(\tau)/I_0 = \exp(-\tau)$. The horizontal axis is the optical depth measured from the surface of the planet to the upper atmosphere, and the vertical axis is the upward intensity that is normalized by the intensity at the surface, I_0.

Figure 5.3 shows one of the results of the test calculations and comparison with the exact solution. The numerical result is over-plotted the exact solution (Equation (5.11)) We note that the optical depth is measured from the surface of a planet to the upward direction, so the $\tau = 0$ correspond to the planetary surface, and larger τ correspond to the higher altitude in this plot. Since the density is large in the lower atmosphere, optical thickness of each numerical grid becomes relatively larger, but the density decreases rapidly in the upper atmosphere, the optical thickness of each grid becomes extremely small. Therefore, absorption takes place only in the lower atmospheric region. As shown in Figure 5.3, the numerical result (red points) reconstruct very well the exact solution (green solid line).

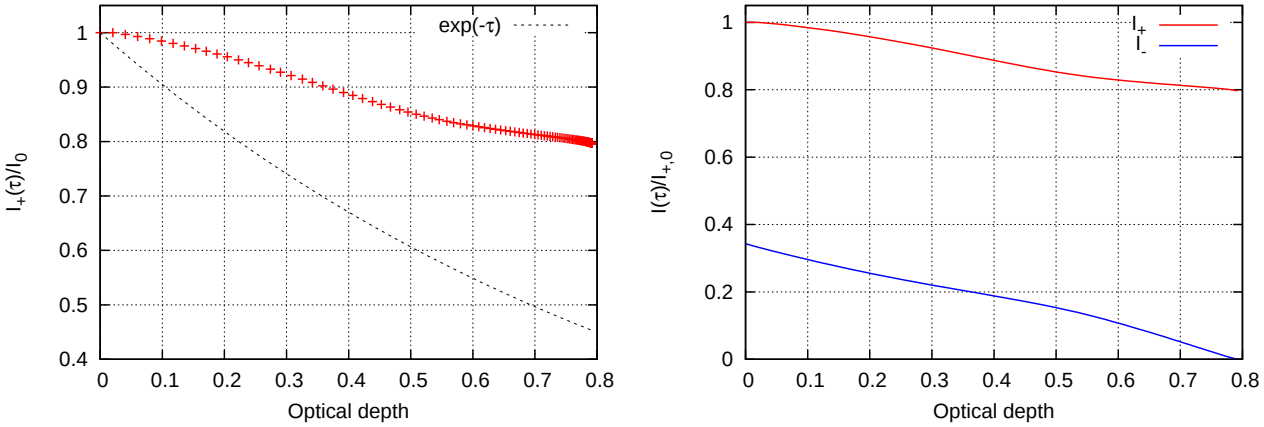

Figure 5.4: One of the results of the test calculations. The left panel show the upward intensity including the contribution from the emission from the atmospheric gas. The red points are the numerical results, and black dotted line is $I_+(\tau)/I_0 = \exp(-\tau)$, for comparison. The right panel shows the both upward (red) and downward (blue) intensity as a function of τ. The horizontal axis is the optical depth measured from the surface of the planet to the upper atmosphere, and the vertical axis is the intensity that is normalized by the intensity at the surface, I_0.

Next we include the emission from the atmospheric gas. Here we assumed the emission that is proportional to the fourth power of the gas temperature that is calculated in the ideal MHD calculation (Figure 5.2). The result is shown in the left panel of the Figure 5.4. In this condition both absorption and emission occur in the atmosphere, thus the upward intensity does not match with the line of $I_+(\tau)/I_0 = \exp(-\tau)$, which is shown in black dotted line in the figure. Because the emission from the atmospheric gas is considered, the upward intensity does not decrease with the exponential of the optical depth, but decreases much gradual.

Since the emission of the atmospheric gas is included, the downward intensity is generated. The right panel of Figure 5.4 shows both upward and downward intensity as a function of the

optical depth. As shown in the figure, the downward intensity I_- is generated because of the emission of the atmospheric gas. Although the temperature in the upper atmosphere is much higher due to the heating by the dissipation of the MHD wave energy, contribution to the emission is weak because the gas density is extremely small. Therefore, both absorption and emission is important in the lower atmosphere where the gas density is higher and the optical thickness is large.

Now we can calculate the mean intensity from the upward and downward intensities by Equation (5.8), and the radiation temperature by Equation (5.9). Figure 5.5 comperes the

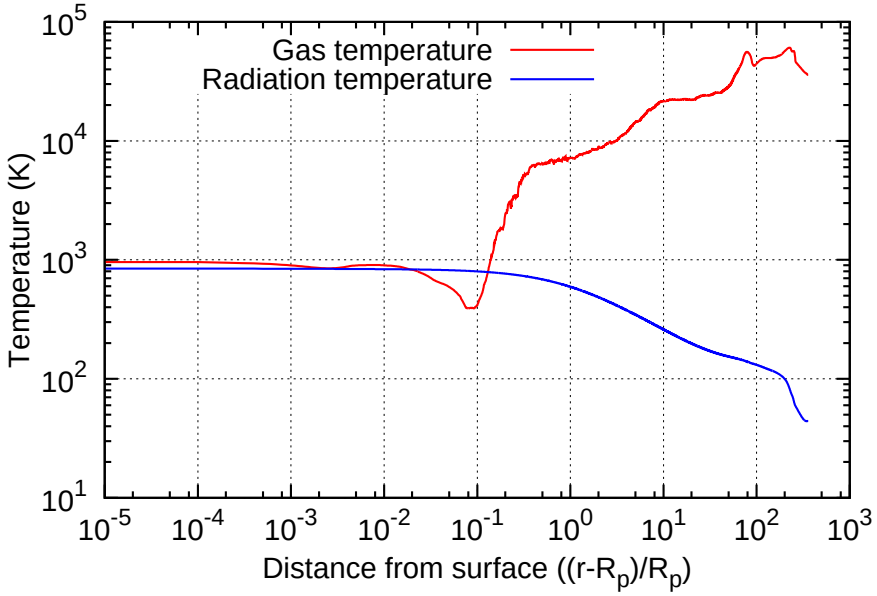

Figure 5.5: Comparison of the (time-averaged) gas temperature calculated by ideal MHD simulation and the radiation temperature calculated through the two-stream approximation. The red, and blue lines are the gas temperature, and radiation temperature, respectively, and the horizontal axis denotes the distance from the surface that is normalized by the planetary radius.

gas temperature of the model atmosphere and the radiation temperature calculated here. The radiation temperature almost same as the gas temperature in the lower atmosphere. However, while the gas temperature increases because of the heating by the MHD waves, the radiation temperature simply drops as the altitude, therefore difference becomes very large in the upper atmosphere. The radiation temperature exceeds the gas temperature around $(r - R_\mathrm{p})/R_\mathrm{p} \sim 10^{-1}$, because the gas temperature around there decreases due to the adiabatic expansion that is caused by the strong acceleration of the planetary wind at just above region. These trend is almost similar to the results that is derived by the modified Unno-Kondo method.

Finally we calculate the radiative cooling and heating rate in the model atmosphere. From the gas temperature and radiation temperature, we calculate the radiative cooling and heating rate in each numerical grid. The result is shown in Figure 5.6. The picture shows the radiative

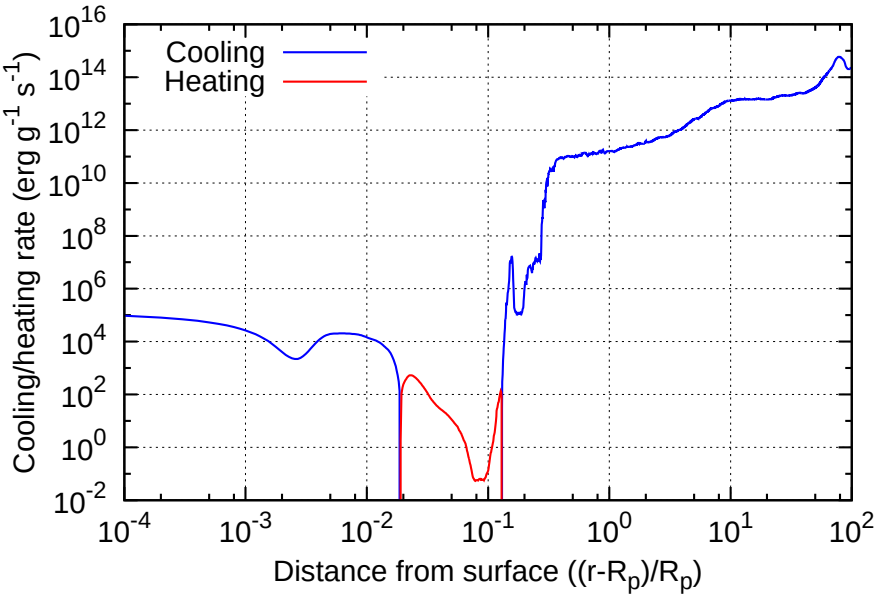

Figure 5.6: Cooling and heating rates in the atmosphere that is calculated by Equation (5.10). The blue and red lines are cooling rate, and heating rate per unit mass, respectively, and shown in the units of erg g^{-1} s^{-1}.

cooling and heating rate per unit mass. In the almost all region of the atmosphere, cooling takes place because the gas temperature is higher than the radiation temperature. In particular, since the deviation of both temperature is large in the upper atmosphere, the radiative cooling rate also becomes large. However, in the middle region of the atmosphere, $(r - R_{\rm p})/R_{\rm p} \sim 10^{-1}$, heating takes place because the radiation temperature is higher than the gas temperature in this region, whose reason is same as discussed in Section 4.3.5.

5.2.3 Incorporating into the MHD Simulations

Since we have derived the radiative cooling and heating rate by the new treatment of the radiative transfer, we next incorporate this method into the previous MHD simulation. The procedure is same as that denoted in Section 4.3.6. First, the MHD part is calculated to determine the temperature and density in each numerical grid. Then, by using the calculated atmospheric structure and mean opacity table (Helling and Lucas, 2009), radiative transfer is solved with the two-stream approximation. Subsequently the mean intensity and the radiation

temperature are calculated, and the radiative cooling or heating rate is obtained by Equation 5.10. Since $Q_{\rm rad}$ denotes the radiative cooling or heating rate per unit mass, we multiply the density of the gas to it and obtain the radiative cooling or heating rate per unit volume. Then we substitute it to the radiative cooling or heating term $q_{\rm R}$ in the energy equation, Equation (2.6). From the next time step, MHD part is solved with the new radiative cooling and heating rate.

5.3 Comparison of New Results with the Previous Results

Here we show results of the new calculations whose radiative cooling and heating function is updated by the two-stream approximation that described above. First we compare the new results and the previous results whose radiative cooling rate is calculated by the modified Unno-Kondo method (Unno and Kondo, 1976; Unno, 1989; Hashimoto, 1995). We also compare the results described in Chapter 2 that use the cooling function of the solar coronal plasma and that of the solar chromospheric gas, for comparison.

5.3.1 Atmospheric Structures and Mass-Loss Rate

First we compare the atmospheric structures. Figure 5.7 shows the temperature structures, density profiles, and radial velocity profiles in each cases. In these calculations, the parameters for the planet are follows; the radius and mass are same as Jupiter, the surface temperature is fixed to 1000 K, and the value of the velocity dispersion is 20% of the sound speed at the surface. Only the method to determine the radiative cooling or heating rate is changed in each cases. The red solid lines show the result with the new cooling function which based on the two-stream approximation described in Section 5.2, and the blue dashed lines show the result with the modified Unno-Kondo method described in Section 4.3, and the black dotted lines show the previous result that is same calculation in Section 2, whose cooling rate is based on the cooling function for the solar coronal plasma and the solar chromospheric gas. As shown in the figures, the atmospheric structures of the new calculation is almost same with the results with the modified Unno-Kondo method, therefore the red lines almost overlap the blue lines.

Compared with the previous result (black dotted lines), the temperature does not drop in the middle region of the atmosphere, and the upper atmosphere becomes cooler, because of change of the radiative cooling and heating rate. The decrease of the density becomes more

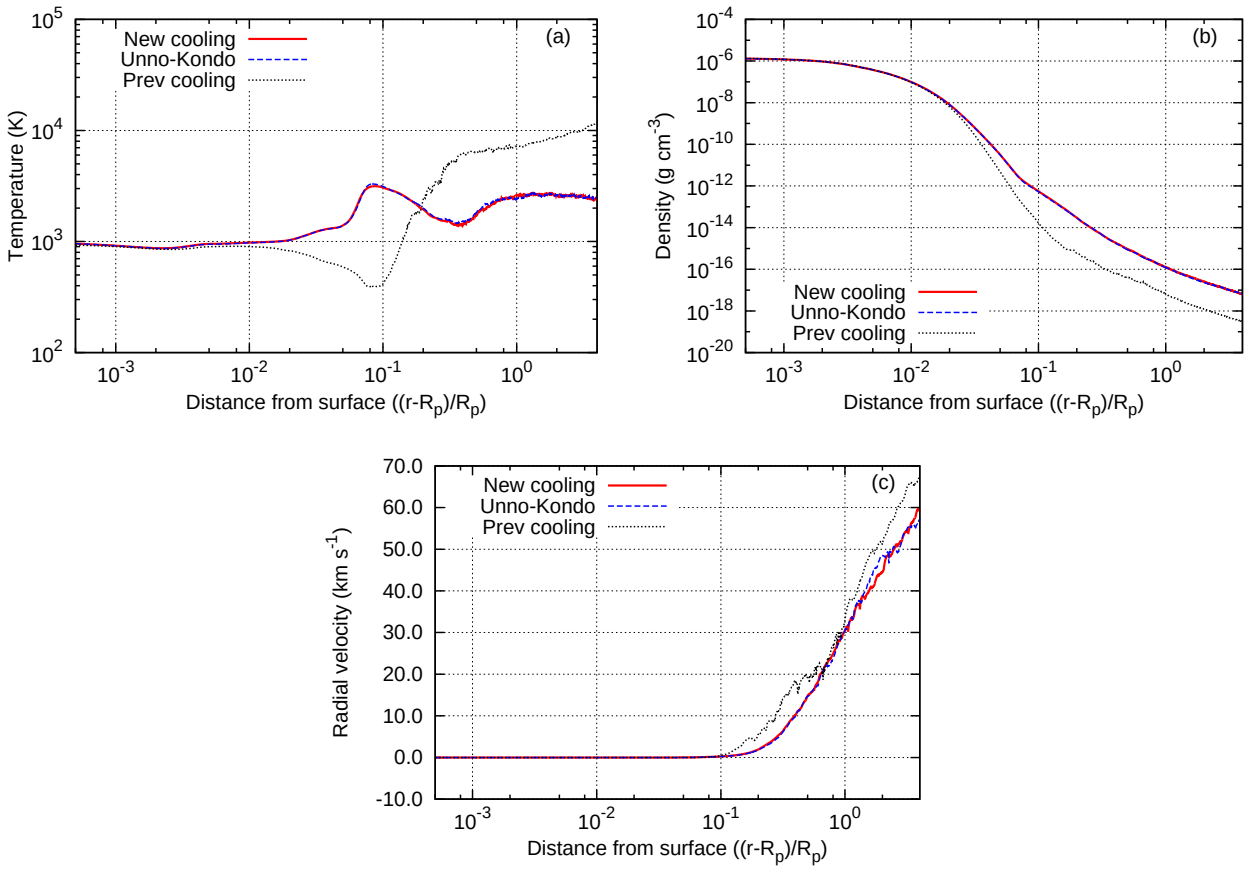

Figure 5.7: Comparison of the atmospheric structures between the previous and new calculations. (a) Temperature structure, (b) density profile, and (c) radial velocity profile. The red lines correspond to the new calculation, and the blue lines correspond to the result with the modified Unno-Kondo method, and the black dotted lines correspond to the result with the cooling function for the solar coronal plasma and solar chromospheric gas.

gradual than the previous calculation, so the dissipation of the MHD wave energy is efficiently uplifting the gas in the new calculation. The radial velocity profiles are similar in three cases; the atmospheric gas is strongly accelerated to exceed the sound speed in the upper atmosphere, therefore the supersonic outflow is achieved. The radial velocity of the escaping atmosphere is slightly slower than the result of the previous calculation, but almost same with the result that includes the modified Unno-Kondo method.

Since the calculated atmospheric structures are not much different between the two-stream approximation and the modified Unno-Kondo method, resultant mass-loss rates are close. According to the new calculation, the mass-loss rate for this parameters is $\dot{M} = 5.89 \times 10^{11}\,\mathrm{g\,s^{-1}}$, where it was $\dot{M} = 5.83 \times 10^{11}\,\mathrm{g\,s^{-1}}$ for the calculation including the modified Unno-Kondo method. This value is ~ 25 times larger than the result of previous calculation that is denoted

in Chapter 2.

5.3.2 Radiative Cooling Rate

Despite the method to calculate the radiative cooling and heating rate in the atmosphere is different, the atmospheric structures are almost same, and the mass-loss rates are also quite similar. In order to understand these results, here we compare the radiative cooling rate in each cases in Figure 5.8. In this figure, we show the time-averaged radiative cooling rate per unit

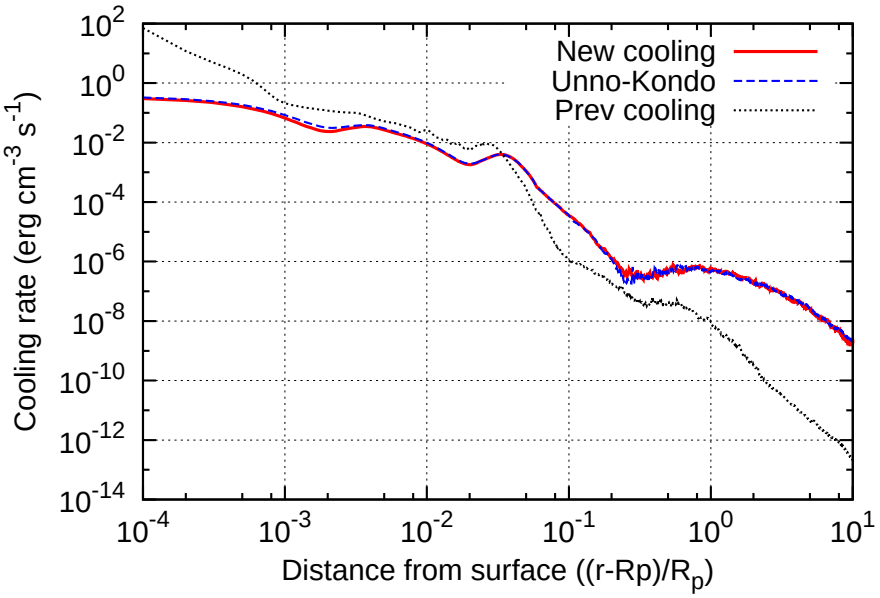

Figure 5.8: Comparison of the cooling rate in the planetary atmosphere. The red solid, blue dashed, and black dotted lines correspond to the radiative cooling rate obtained by the two-stream approximation, the modified Unno-Kondo method, and the cooling functions for solar coronal plasma and chromospheric gas, respectively. The horizontal axis denotes the distance from the surface that is normalized by the planetary radius, and the vertical axis denotes the radiative cooling rate per unit volume in the units of erg $\mathrm{cm}^{-3}\,\mathrm{s}^{-1}$.

volume as a function of the distance from the surface. The radiative cooling rates calculated by the two-stream approximation (red solid), the modified Unno-Kondo method (blue dashed), and cooling functions for the solar coronal plasma and chromospheric gas (black dotted) are shown. Compared to the previous calculation, the radiative cooling rate is about two orders of magnitude smaller in the bottom region of the atmosphere, and two to four orders of magnitude larger in the upper atmosphere. Therefore the atmospheric structures are different from the previous calculation; the uplifting of the atmospheric gas becomes more sufficient and the temperature of the upper atmosphere becomes lower.

At the same time, it is almost same with the radiative cooling rate by the modified Unno-Kondo method in all region in the atmosphere. The fact that the radiative cooling rates calculated by both two methods are almost same causes the remarkably similar atmospheric structures and mass-loss rate.

As we described in Section 5.1, the modified Unno-Kondo method we used for calculation does not include the contribution of the emission of the atmospheric gas and downward intensity. Although this point might be problematic in principle, but it can be said that the approximated treatments in the modified Unno-Kondo method do not affect results, at least in the condition we are considering in here. In the new method that the two-stream approximation is used includes both the contribution of the emission from the atmospheric gas to radiation and downward intensity, and the result does not change compare to the modified Unno-Kondo method. Consequently, the modified Unno-Kondo method in the planetary atmosphere is thought to be an available way to treat the radiative transfer in hydrodynamic simulations, at least within the parameters we used here.

5.4 Dependence on the Velocity Dispersion

As mentioned in Section 2.2 and 4.5, the value of the velocity dispersion at the planetary surface is one of the important parameter which determines the atmospheric structure and mass-loss rate. Therefore, similar to the previous chapters, we perform the MHD simulations in wide parameter space with the new radiative cooling rate that described above. From here we show the dependence of the atmospheric structure and mass-loss rates on the value of the velocity dispersion at the planetary surface.

5.4.1 Dependence of the Mass-Loss Rate

First we show mass-loss rate dependence on the velocity dispersion. Figure 5.9 is the mass-loss rates as a function of the velocity dispersion at the surface in the three cases. The new result whose radiative cooling and heating rates are calculated by the two-stream approximation is plotted by the red points ("New result"). We also show the dependence of the other cases for comparison. The result whose radiative cooling and heating rates are calculated by the modified Unno-Kondo method is shown in the blue points ("Unno-Kondo"), and the result of Tanaka et al. (2014) is shown in the grey points ("Prev result").

Since the radiative cooling rates and the atmospheric structures of the results of new cal-

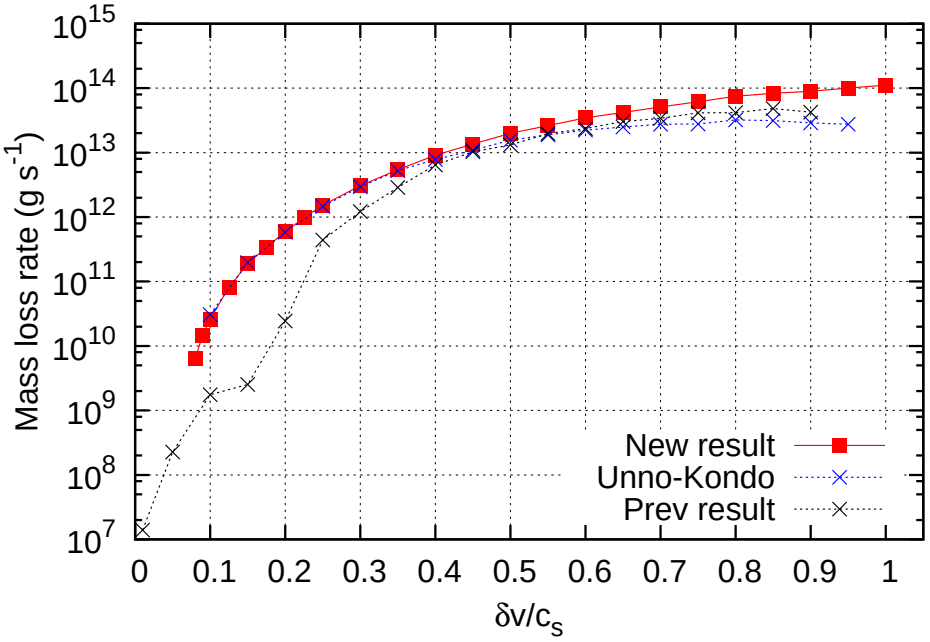

Figure 5.9: Relation between the value of the velocity dispersion at the surface of the planet and the mass-loss rate from the planet. The horizontal axis denotes the velocity dispersion that is normalized by the sound speed at the surface, and the vertical axis denotes the mass-loss rate in units of $\mathrm{g\,s^{-1}}$. In these calculations we assumed that the radius and mass of the planet are same as Jupiter, and the surface temperature is fixed to 1000 K. The mass-loss rate whose radiative cooling and heating rates are calculated by the modified Unno-Kondo method (same as red line in Figure 4.8 is shown in the blue dashed line, and the result of the previous calculations (same as in Figure 2.2) is also shown in the grey dotted line, for comparison.

culation and modified Unno-Kondo case are almost similar (see Figure 5.7 and 5.8), general trend of the dependence of the mass-loss rates are also quite similar. In particular, two results almost completely coincide when the velocity dispersion is $\lesssim 0.4c_{\mathrm{s}}$. Compared to the result of the previous calculation, the mass-loss rate becomes one to two orders of magnitude larger in the lower velocity dispersion cases, because of the overestimation of the radiative loss in the lower atmosphere in the previous calculations. Difference of the mass-loss rates between three cases is not significant when the velocity dispersion is larger.

In the higher velocity dispersion cases, an increase rate of the mass-loss rate seems to be small. In the previous calculations (blue and black points in Figure 5.9), the increase of the mass-loss rate saturates or slightly decreases in the higher velocity dispersion region. The new calculation, however, although the increase of the mass-loss rate seems to be small, but it is not clear that it saturates or not. In order to clarify this point, we show an another figure,

Figure 5.10. In this figure, the same plots shown in Figure 5.9 are presented, but the horizontal

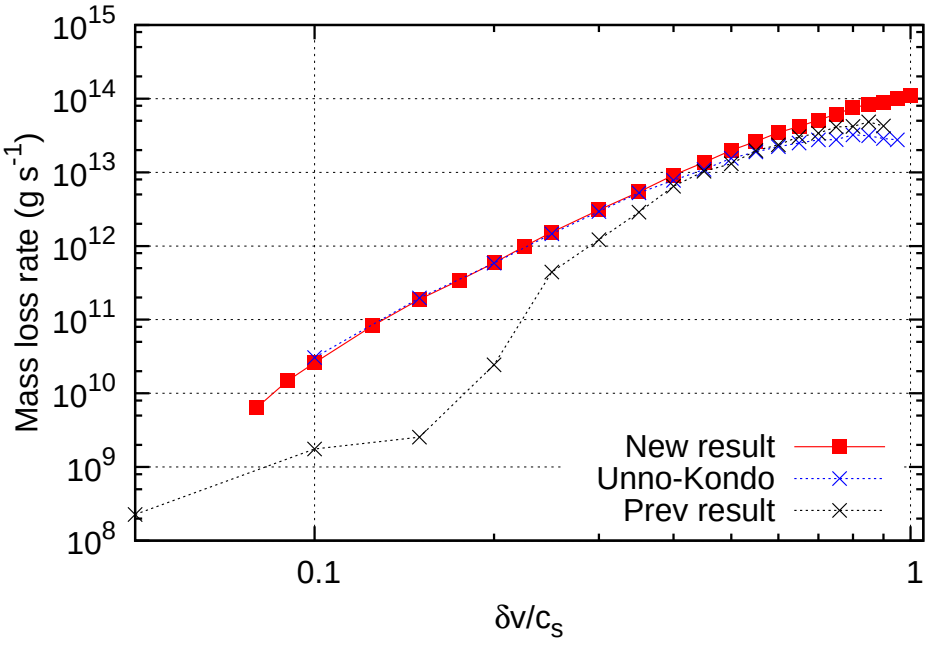

Figure 5.10: The velocity dispersion dependence of the mass-loss rate which is same data plots with Figure 5.9, but the horizontal axis is changed to logarithmic scale.

axis is changed to logarithmic scale. As shown in the figure, the blue points and black points clearly saturate when the velocity dispersion is large, but the new calculation (red points) is not saturated in the same range. Though the increase rate of the mass-loss rate is gradually decreasing as the velocity dispersion, the mass-loss rate is still increasing. The dependency of the new result and "Unno-Kondo" case are almost similar in the wide range, but the difference between two cases appears when the value of the velocity dispersion is extremely large.

5.4.2 Atmospheric Structure

Next we show the atmospheric structures. The dependence of the atmospheric structures on the value of the velocity dispersion at the planetary surface is shown in Figure 5.11 In these calculations, the parameters for the planet are follows; the radius and mass are same as Jupiter, and the surface temperature is 1000 K.

The whole trend of the atmospheric structures is similar to that described in Section 4.5.2. The upper atmosphere is heated up by the dissipation of the MHD wave energy, and larger amount of the atmospheric gas can be uplifted when the velocity dispersion is larger because

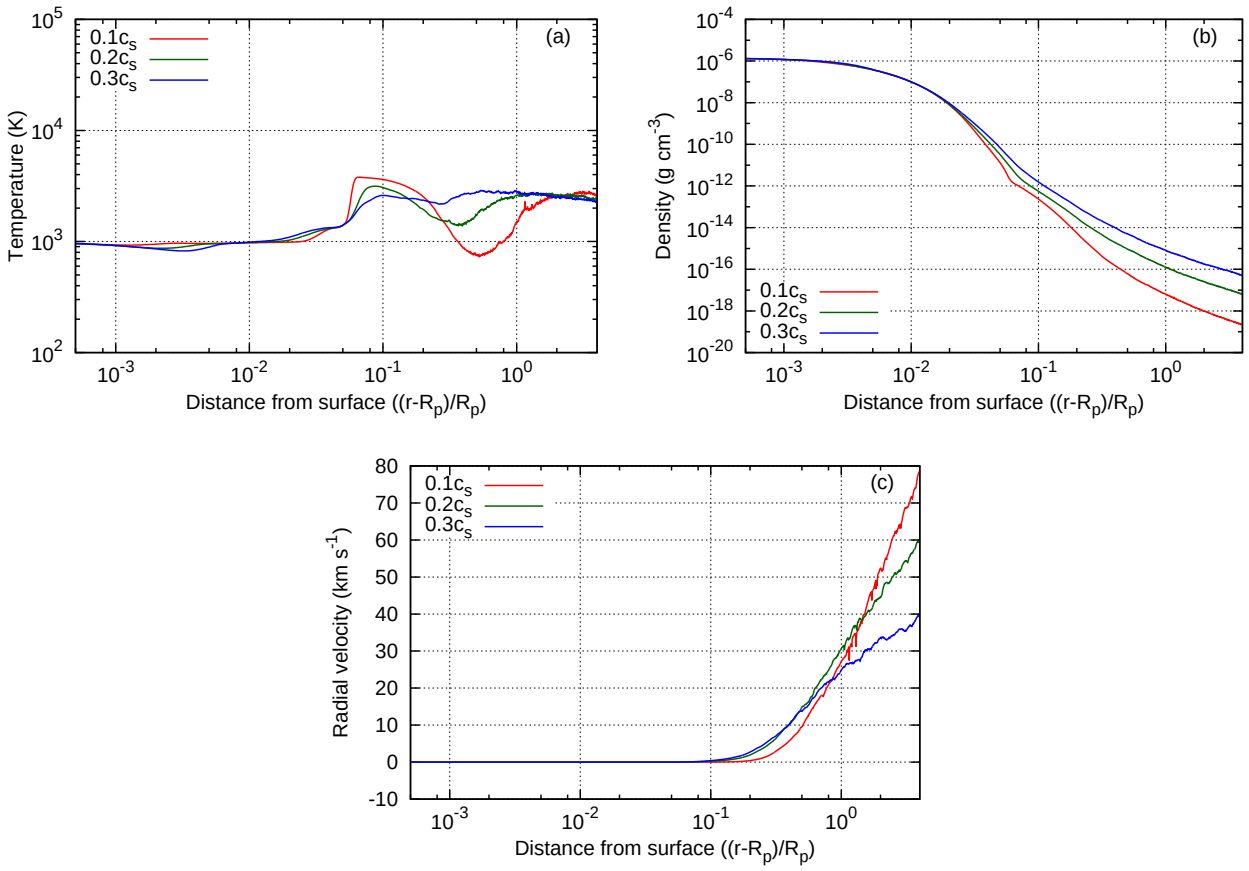

Figure 5.11: Velocity dispersion dependence of the atmospheric structures. (a) Temperature structure, (b) density profile, and (c) radial velocity profile. The horizontal axes denote the distance from the surface that is normalized by the planetary radius. The red, green, and blue lines correspond to the values of the velocity dispersion, $0.1c_{\rm s}$, $0.2c_{\rm s}$, and $0.3c_{\rm s}$, respectively.

the energy injected to the magnetic field is larger. The escaping atmosphere is strongly accelerated and exceed the sound speed, but the radial velocity becomes smaller when the velocity dispersion is large, because the upper atmosphere is heavier.

5.4.3 Radiative Cooling Rate

As described in Section 4.4.2 and 5.3.2, the difference of the radiative cooling rate in the atmosphere strongly affects the resultant atmospheric structure and the mass-loss rate. Here we show the dependence of the radiative cooling rate in the atmosphere on the velocity dispersion to understand the behavior of the atmospheric structure and the mass-loss rate dependence on the velocity dispersion. Figure 5.12 shows the dependence of the radiative cooling rate per unit volume as a function of the altitude. In the almost all regions in the atmosphere, the radiative

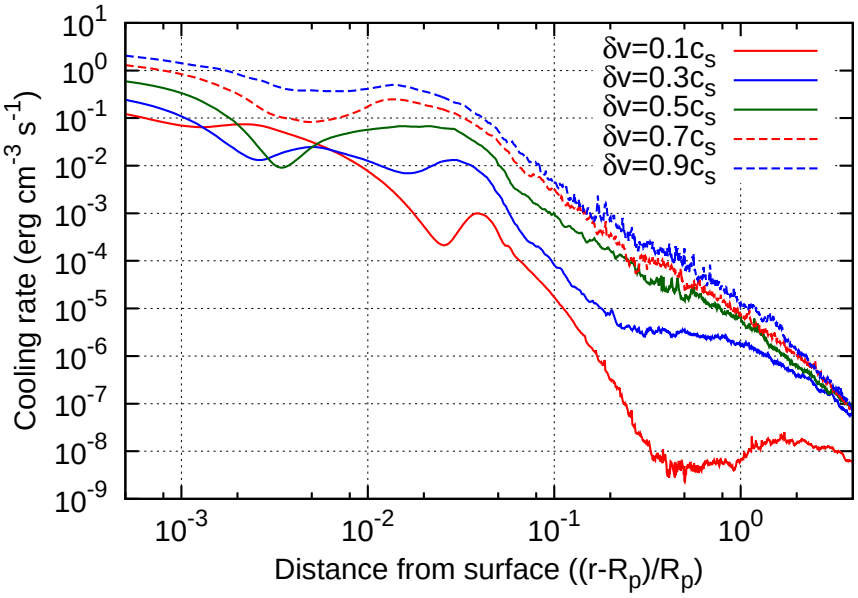

Figure 5.12: The radiative cooling rates in the atmosphere as a function of the altitude. The horizontal axis denotes the distance from the surface that is normalized by the planetary radius, and the vertical axis denotes the radiative cooling rate per unit volume in units of erg $\mathrm{cm}^{-3}\,\mathrm{s}^{-1}$. The red solid, blue solid, green solid, red dashed, and blue dashed lines correspond to the values of the velocity dispersion, $0.1c_\mathrm{s}$, $0.3c_\mathrm{s}$, $0.5c_\mathrm{s}$, $0.7c_\mathrm{s}$, and $0.9c_\mathrm{s}$, respectively.

cooling rate increases with the increase of the velocity dispersion, whose trend is almost same with the results that is denoted in Section 4.5.3. In particular, the radiative cooling rate differs largely in the upper atmosphere; it is up to three to four orders of magnitude larger in the upper atmosphere. The increase of the radiative cooling rate in the entire region of the atmosphere causes change of the atmospheric structures.

Figure 5.13 shows the density profile and radial velocity profile in several cases of the values of the velocity dispersion. The density in the upper atmosphere increases with the increase of the velocity dispersion, but the increase rate on the velocity dispersion become small when the velocity dispersion is larger. In addition, the radial velocity in the upper atmosphere significantly slows down in the larger velocity dispersion cases. These behavior is also similar to that of Figure 4.11, and can be understood as the same reason; it is caused by the enhancement of the radiative cooling rate due to the larger gas density in the upper atmosphere.

As shown in the right panel of the Figure 5.13, the radial velocities of the escaping atmosphere are quite slow when the velocity dispersion is larger. In fact, since the acceleration of the escaping atmosphere continues until distant region, the gas can be accelerated to supersonic at

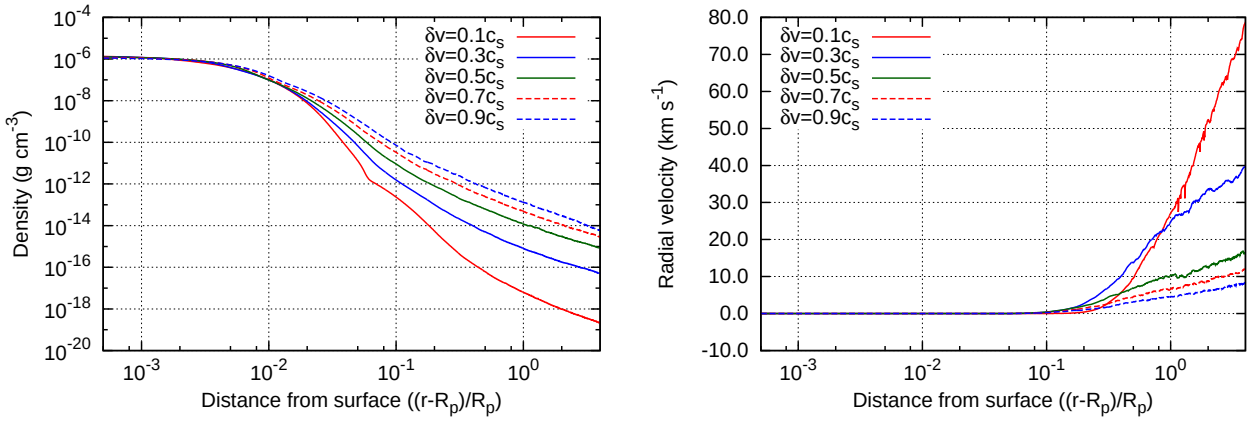

Figure 5.13: Velocity dispersion dependence of the density profile (left) and radial velocity profile (right) in several values of the velocity dispersion. The horizontal axes denote the distance from the surface that is normalized by the planetary radius. The red solid, blue solid, green solid, red dashed, and blue dashed lines correspond to the value of the velocity dispersion, $0.1c_{\rm s}$, $0.3c_{\rm s}$, $0.5c_{\rm s}$, $0.7c_{\rm s}$, and $0.9c_{\rm s}$, respectively.

the region far from the surface which is not shown in the figure. However, the Roche radius is several planetary radii for close-in exoplanets such as hot Jupiters, therefore the acceleration in the far region does not occur. For the condition of hot Jupiters, slow, subsonic and dense planetary wind is expected if the value of the velocity dispersion is extremely large. If gaseous planets are hot and isolated (or distant from the central star), such as young planets, acceleration of the escaping atmosphere in the region far from the surface can be valid.

5.4.4 Detailed Comparison

As described in Section 5.4.1, although the velocity dispersion dependence of the mass-loss rates of the new calculation and the "Unno-Kondo" case are almost similar, there are small difference when the velocity dispersion is large. The mass-loss rate saturates in the higher velocity dispersion region in the modified Unno-Kondo case, but is does not saturate in the new calculation, though the increase of the mass-loss rate seems to be getting smaller. In order to investigate it in detail, we compare the atmospheric structures and radiative cooling rates in several cases of the velocity dispersion.

Figure 5.14 - 5.19 show the comparison of the atmospheric structures and radiative cooling rates when the values of the velocity dispersion are 10% (Figure 5.14), 30% (Figure 5.15), 50% (Figure 5.16), 70% (Figure 5.17), 80% (Figure 5.18), and 90% (Figure 5.19). The red solid lines are the results of the new calculations that include the two-stream approximation for the

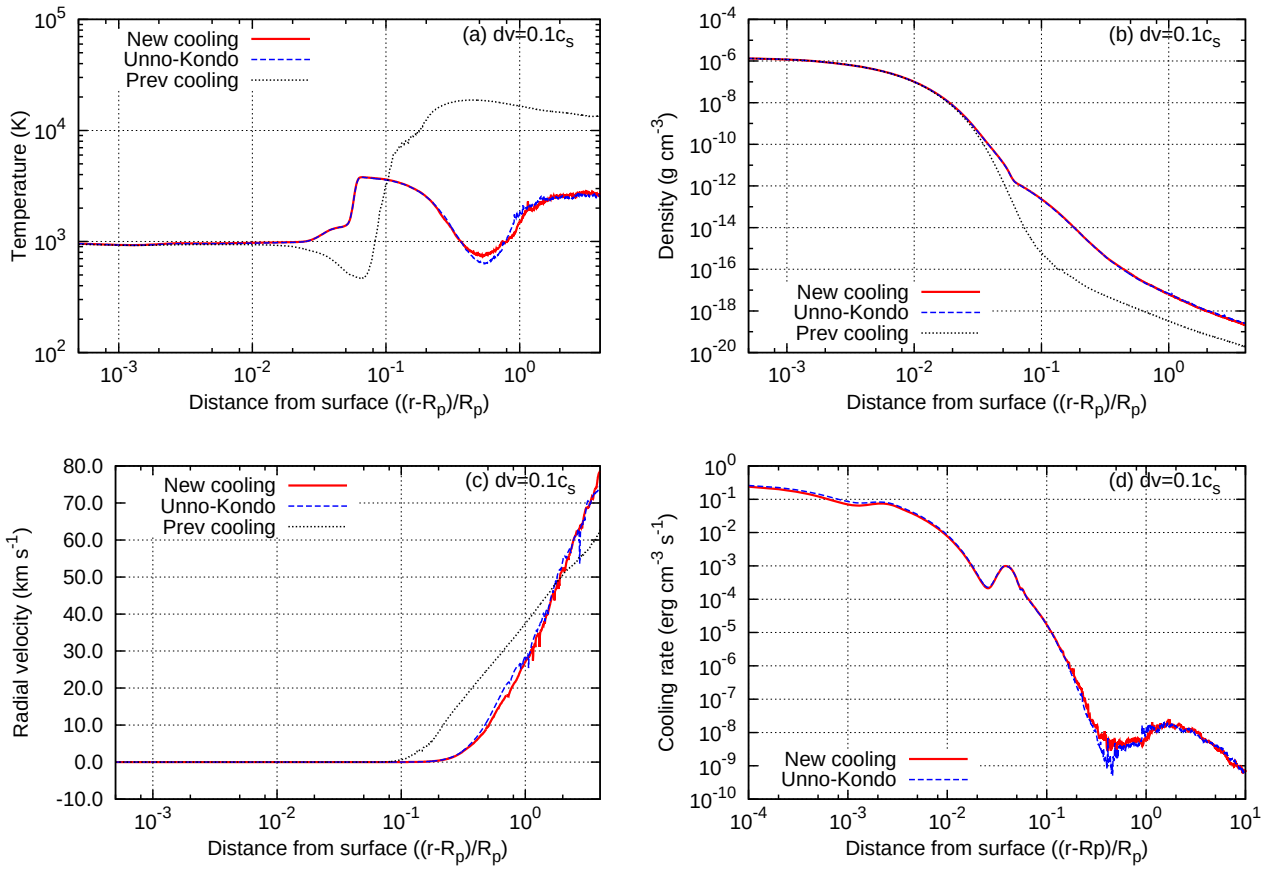

Figure 5.14: Comparison of the atmospheric structure and radiative cooling rate in the case of $dv = 0.1c_s$. (a) Temperature structure, (b) density profile, (c) radial velocity profile, and (d) radiative cooling rate, respectively. The red solid lines, blue dashed lines, and black dotted lines correspond to the results of the new calculation that includes the two-stream approximation, results that includes the modified Unno-Kondo method, and results with the cooling functions for solar coronal plasma and chromospheric gas, respectively.

radiative cooling rate, the blue dashed lines are the results of the calculation that include the modified Unno-Kondo method for the radiative cooling rate, and the black dotted lines are the results whose radiative cooling rate is obtained from the cooling functions for solar coronal plasma and chromospheric gas. As we described in Section 5.3, the cooling rates are quite similar, and the atmospheric structures are also similar when the velocity dispersion is small (Figure 5.14 and 5.15).

However, very small difference of the radiative cooling rate exists in the lower atmosphere when $dv = 0.5c_s$ (Figure 5.16(d)). The difference of the radiative cooling rate between the new calculation and the "Unno-Kondo" case becomes larger as the velocity dispersion (Figure 5.17, 5.18, and 5.19). For example, the radiative cooling rate in the lower atmosphere in

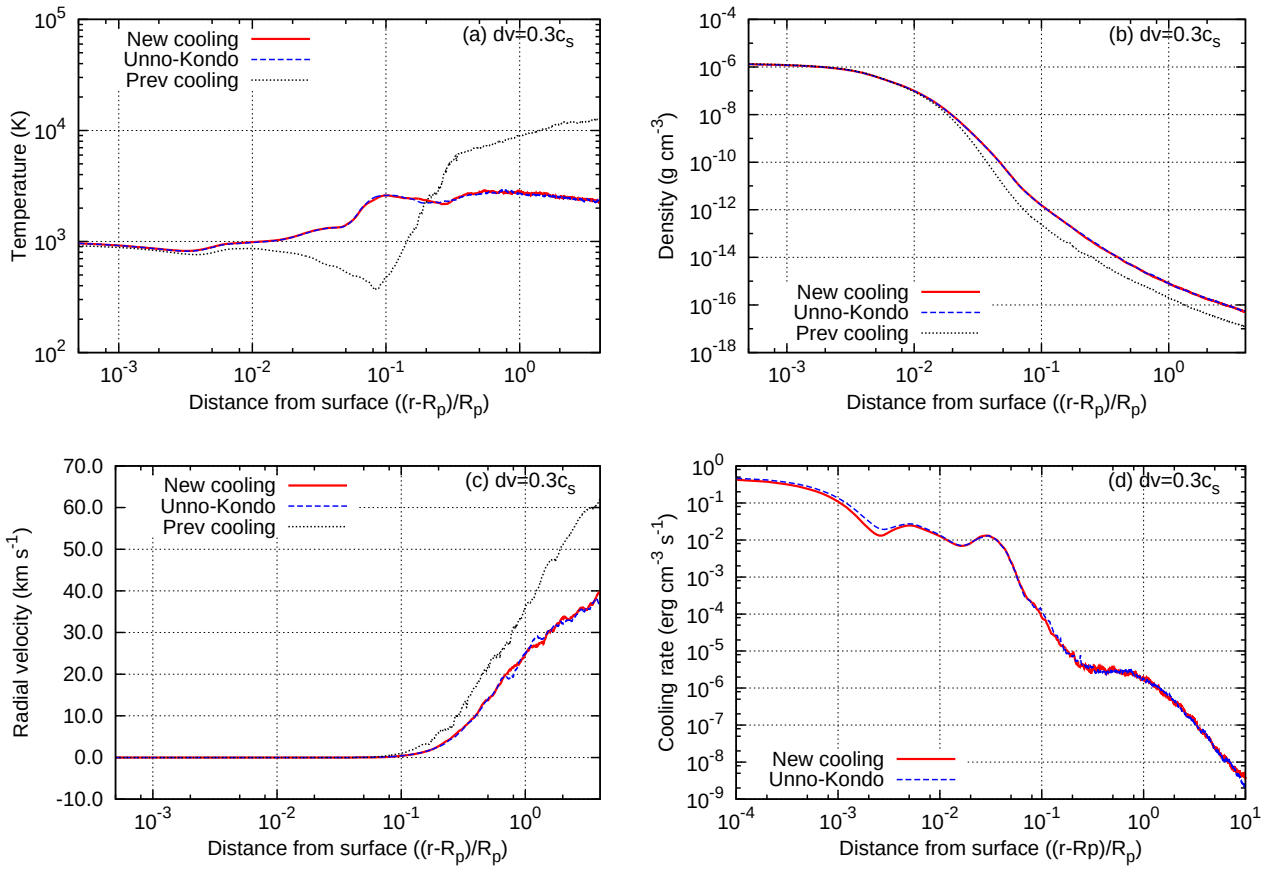

Figure 5.15: Comparison of the atmospheric structure and radiative cooling rate in the case of $dv = 0.3c_s$. (a) Temperature structure, (b) density profile, (c) radial velocity profile, and (d) radiative cooling rate, respectively. The red solid lines, blue dashed lines, and black dotted lines correspond to the results of the new calculation that includes the two-stream approximation, results that includes the modified Unno-Kondo method, and results with the cooling functions for solar coronal plasma and chromospheric gas, respectively.

the new calculation is two to three times smaller than that in the "Unno-Kondo" case when the velocity dispersion is 90% of the sound speed (Figure 5.19(d)). For the cases of the larger velocity dispersion, least enhancement of the density causes the increase of the absorption of the radiation in the lower atmosphere. Additionally, since the emission from the atmospheric gas is ignored in the modified Unno-Kondo method, the radiation temperature in the lowest region of the atmosphere is slightly underestimated. Therefore, the resultant radiative cooling rate is overestimated in the "Unnno-Kondo" case, and the overestimation of the radiative cooling rate causes the small decrease of the mass-loss rate in the higher velocity dispersion cases.

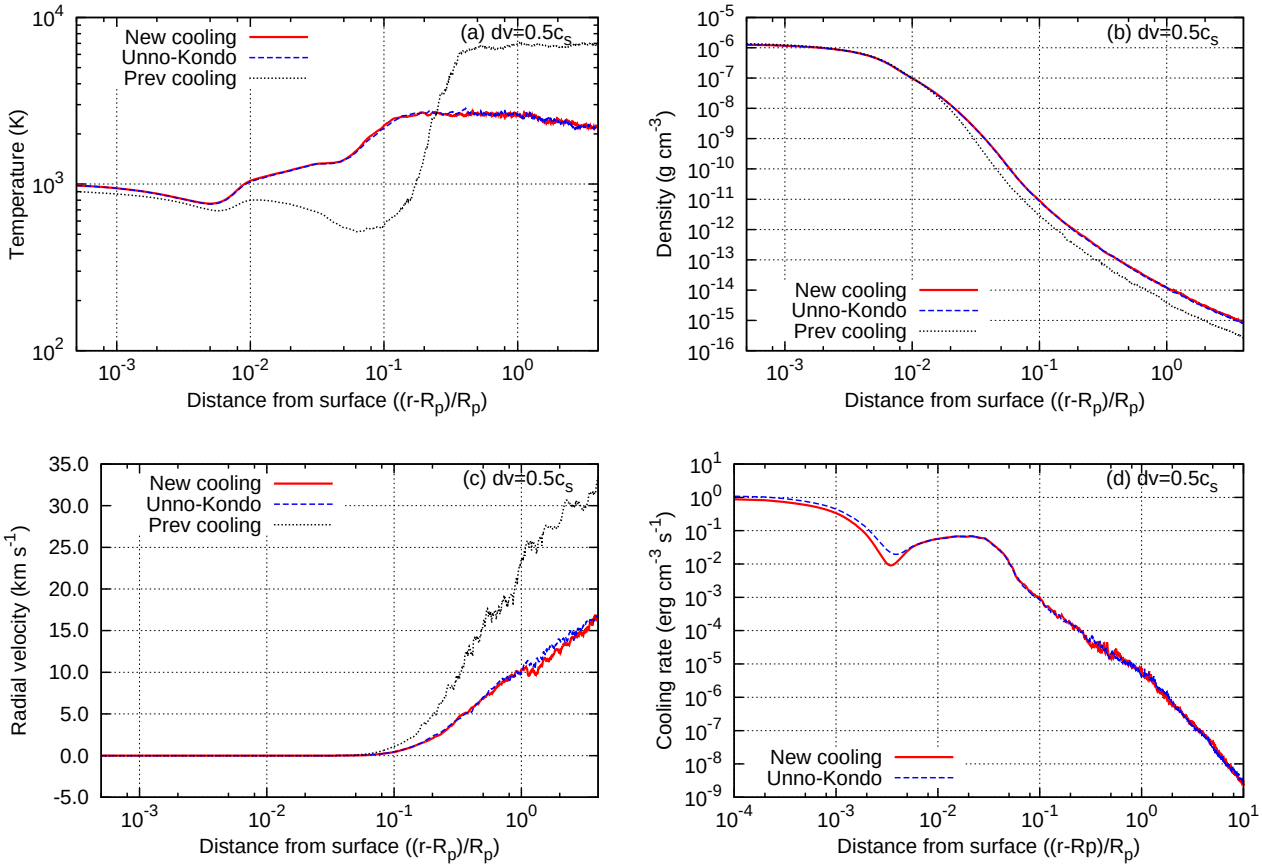

Figure 5.16: Comparison of the atmospheric structure and radiative cooling rate in the case of $dv = 0.5c_{\rm s}$. (a) Temperature structure, (b) density profile, (c) radial velocity profile, and (d) radiative cooling rate, respectively. The red solid lines, blue dashed lines, and black dotted lines correspond to the results of the new calculation that includes the two-stream approximation, results that includes the modified Unno-Kondo method, and results with the cooling functions for solar coronal plasma and chromospheric gas, respectively.

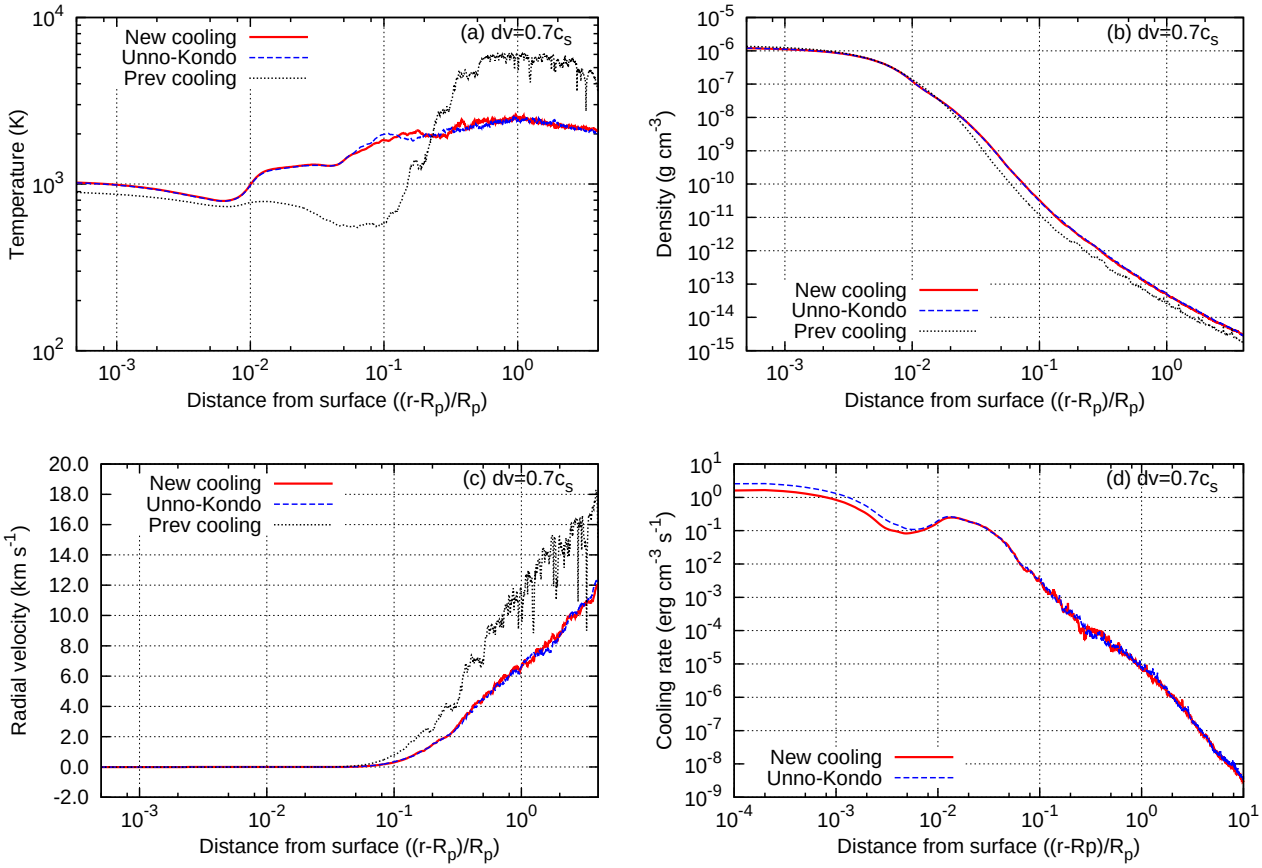

Figure 5.17: Comparison of the atmospheric structure and radiative cooling rate in the case of $dv = 0.7c_{\rm s}$. (a) Temperature structure, (b) density profile, (c) radial velocity profile, and (d) radiative cooling rate, respectively. The red solid lines, blue dashed lines, and black dotted lines correspond to the results of the new calculation that includes the two-stream approximation, results that includes the modified Unno-Kondo method, and results with the cooling functions for solar coronal plasma and chromospheric gas, respectively.

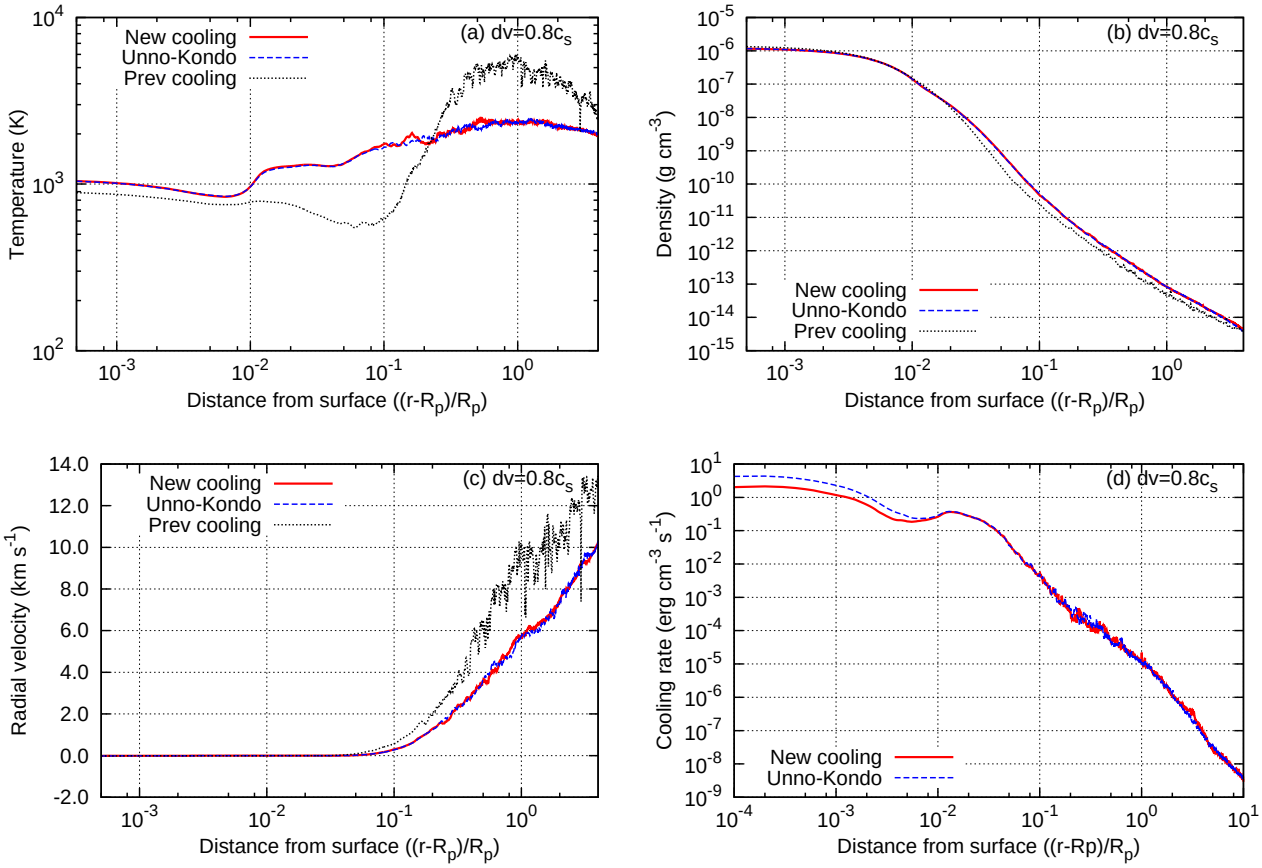

Figure 5.18: Comparison of the atmospheric structure and radiative cooling rate in the case of $dv = 0.8c_{\rm s}$. (a) Temperature structure, (b) density profile, (c) radial velocity profile, and (d) radiative cooling rate, respectively. The red solid lines, blue dashed lines, and black dotted lines correspond to the results of the new calculation that includes the two-stream approximation, results that includes the modified Unno-Kondo method, and results with the cooling functions for solar coronal plasma and chromospheric gas, respectively.

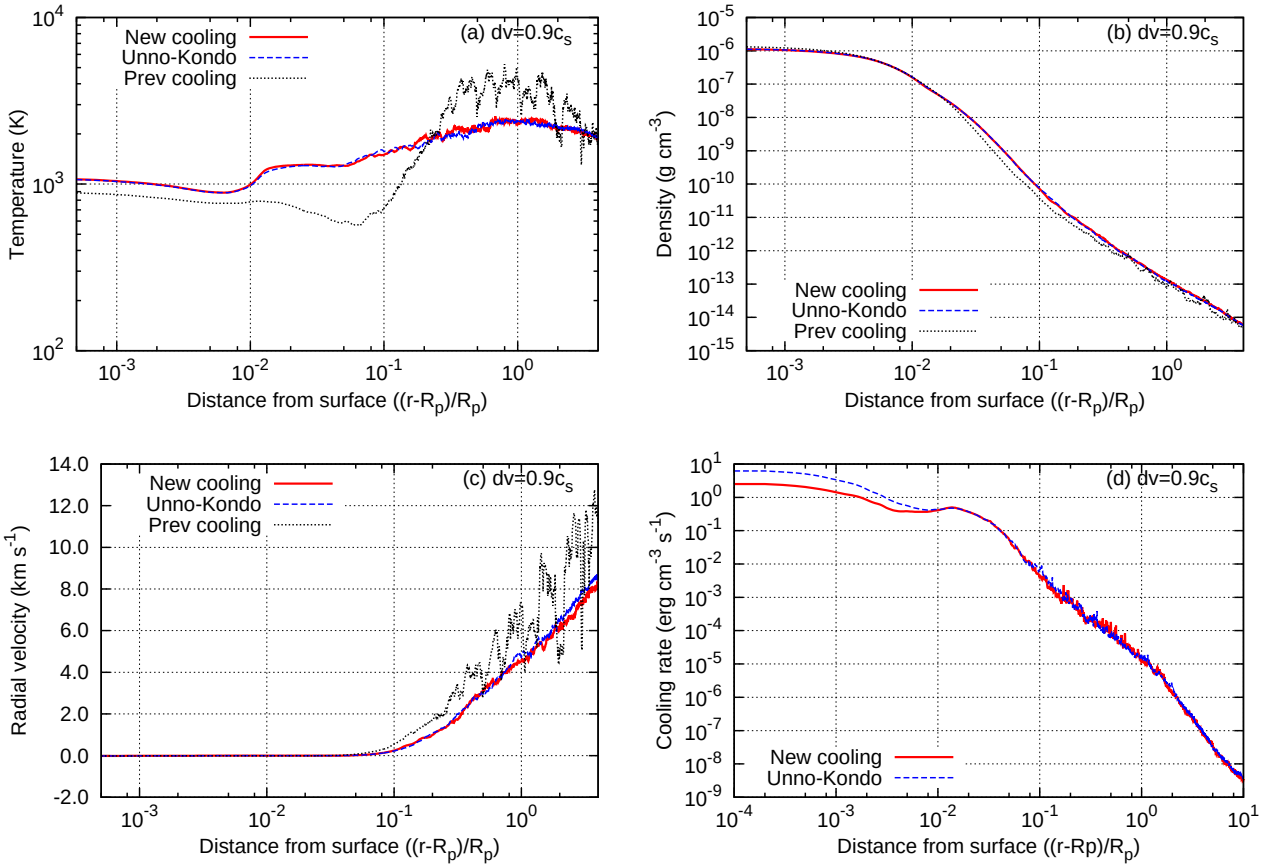

Figure 5.19: Comparison of the atmospheric structure and radiative cooling rate in the case of $dv = 0.9c_{\rm s}$. (a) Temperature structure, (b) density profile, (c) radial velocity profile, and (d) radiative cooling rate, respectively. The red solid lines, blue dashed lines, and black dotted lines correspond to the results of the new calculation that includes the two-stream approximation, results that includes the modified Unno-Kondo method, and results with the cooling functions for solar coronal plasma and chromospheric gas, respectively.

5.4.5 Time Variability of the Mass-Loss Rate and Atmospheric Structure

In the all cases, there are large time-variability in the upper atmosphere. In particular, fluctuation of the density and radial velocity in the upper atmosphere cause the time-variation of the mass-loss rate. Here we show how the mass-loss rates vary with the time.

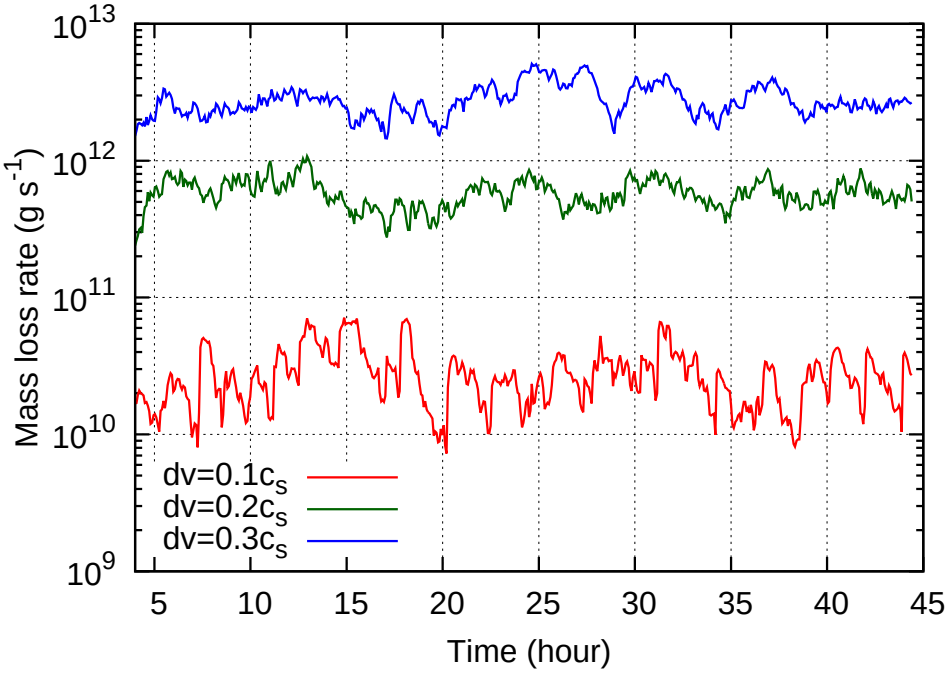

Figure 5.20: Time variability of the mass-loss rate. The horizontal axis is time in the units of hour, and the vertical axis is the mass-loss rate in units of $\mathrm{g\,s^{-1}}$. The red, blue, and green lines correspond to the value of the velocity dispersion, $0.1c_\mathrm{s}$, $0.2c_\mathrm{s}$, and $0.3c_\mathrm{s}$, respectively. For all cases, the radius and mass are set to the value same as Jupiter, and the surface temperature is set to 1000 K.

Figure 5.20 and 5.21 show the time variability of the mass-loss rate in several cases of the velocity dispersion. When the velocity dispersion is 10% of the sound speed (red line in Figure 5.20), the mass-loss rate has variations with the period that is about several hours, and its amplitude sometimes reaches about an order of magnitude. For the larger velocity dispersion cases, the mass-loss rates becomes larger, but the time-variation becomes smaller. The time-variation of the mass-loss rate also appears in the larger velocity dispersion cases (Figure 5.21), and the amplitude of the change is an order of the magnitude.

Figure 5.22 shows the snapshots of the atmospheric structure. The temperature structure, density profile, and radial velocity profile have large fluctuation in the upper atmosphere, where

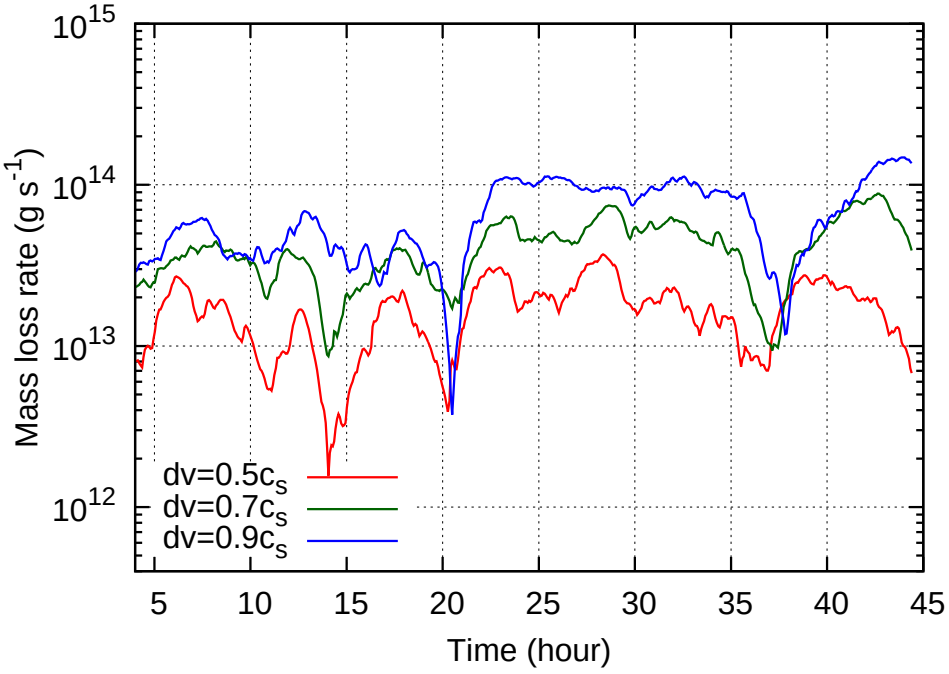

Figure 5.21: Time variability of the mass-loss rate. The horizontal axis is time in the units of hour, and the vertical axis is the mass-loss rate in units of $\mathrm{g\,s^{-1}}$. The red, blue, and green lines correspond to the value of the velocity dispersion, $0.5c_{\rm s}$, $0.7c_{\rm s}$, and $0.9c_{\rm s}$, respectively. For all cases, the radius and mass are set to the value same as Jupiter, and the surface temperature is set to 1000 K. Note that the range of the vertical axis is different from Figure 5.20.

the dissipation of the MHD waves occurs. Each line corresponds to the elapsed time from the beginning of the calculation, that is normalized by the crossing time of the planet that is expressed as $t_{\rm cross} = R_{\rm p}/c_s$, where $c_{\rm s}$ is the value at the surface. In the current setup for this calculation, $t = 1.00$ is equivalent to ~ 7.4 hours, thus the red solid, green dashed, blue dotted, and violet dot-dashed lines mean the elapsed time 22.2 hours, 25.9 hours, 29.6 hours, and 33.3 hours from the start of the calculation, respectively.

The temperature in the upper atmosphere ranges from ~ 1000 K to ~ 7000 K, but sometimes it drops down to several hundred kelvin because of the strong adiabatic expansion of the atmospheric gas. The time-averaged temperature profile (Green line in Figure 5.11(a)) is less than or comparable to only ~ 3000 K, but if we see snapshots of the time evolution, the upper atmosphere is partially heated up to higher temperature. In the density profile, the amplitude of the fluctuation in the upper atmosphere becomes around two orders of magnitude. This result shows that the outflow driven by the dissipation of the MHD waves does not occur as a statical outflow, but as a clumpy and highly-variable outflow. The variation of the radial

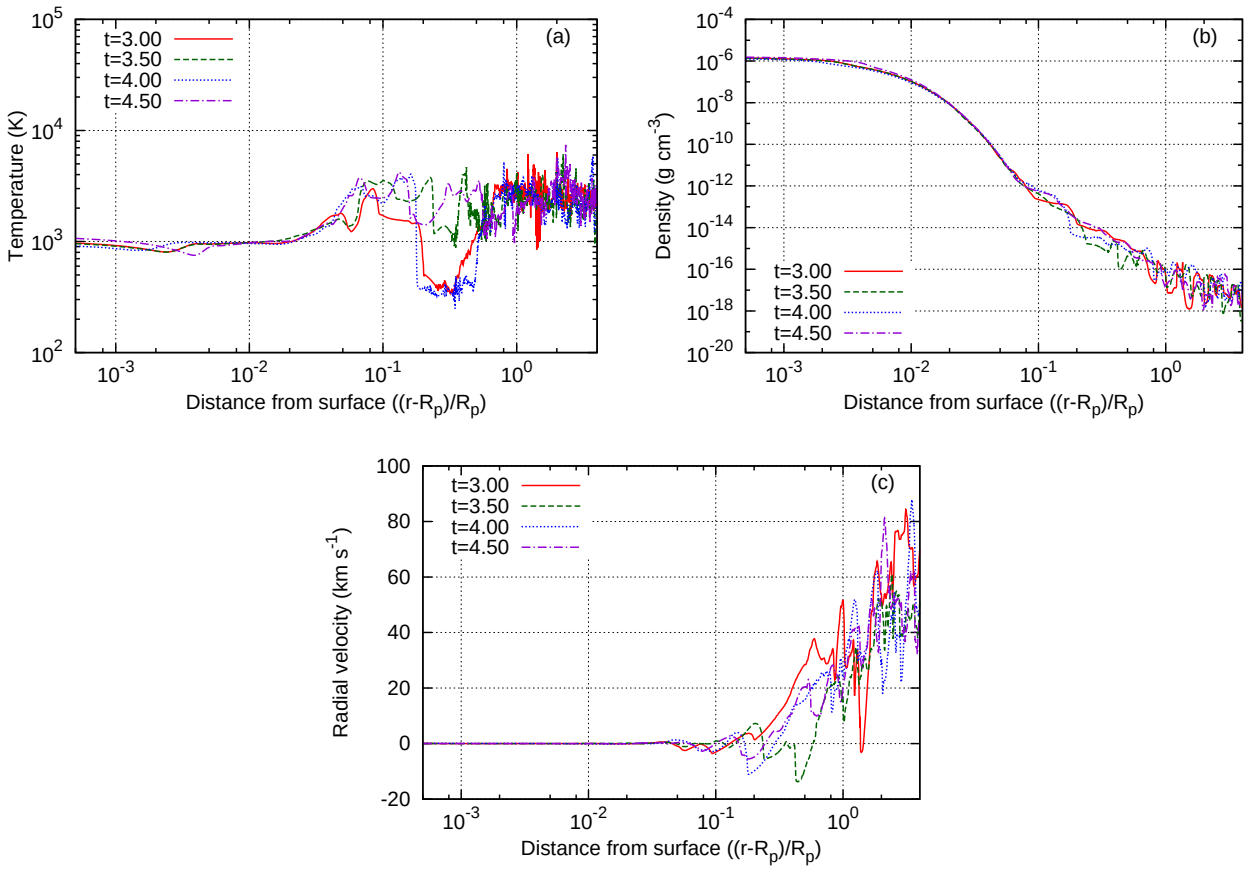

Figure 5.22: Snapshots of the time evolution of the atmospheric structures. (a) Temperature structure, (b) density profile, and (c) radial velocity profile, respectively. The radius and mass are set to the value same as Jupiter, the surface temperature is set to 1000 K, and the value of the velocity dispersion is fixed to 20% of the sound speed at the planetary surface. The red solid, green dashed, blue dotted, and violet dot-dashed lines correspond to the elapsed time from the beginning of the calculation, $t = 3.00$, 3.50, 4.00, and 4.50, respectively. The elapsed time t is normalized by the crossing time of the planet.

velocity of the escaping atmosphere is also large. The radial velocity increases with the altitude as a whole behavior, and the time-averaged profile also shows same trend (Green line in Figure 5.11(c)), but the snapshots show the highly variable profile. The radial velocity of the escaping atmosphere ranges from almost $0\,\mathrm{km\,s^{-1}}$ to $\sim 100\,\mathrm{km\,s^{-1}}$, and sometimes it can be negative value.

The high time-variability of the mass-loss rate and the atmospheric structure is quite characteristic of the atmospheric escape that is driven by the dissipation of the MHD wave energy in the atmosphere. We discuss the characteristics in a later section.

5.5 Dependence on the Radius and Mass

Next we show the dependence of the mass-loss rate and atmospheric structure on the radius and mass of the planets. We change the radius of hot Jupiters from $0.8R_{\rm J}$ to $2R_{\rm J}$, and the mass from $0.3M_{\rm J}$ to $1.5M_{\rm J}$.

5.5.1 Radius Dependence of the Atmospheric Structures

Figure 5.23 shows the relations between the atmospheric structures and the radius of the planets. As we described in the previous sections, the pressure scale height controls the whole

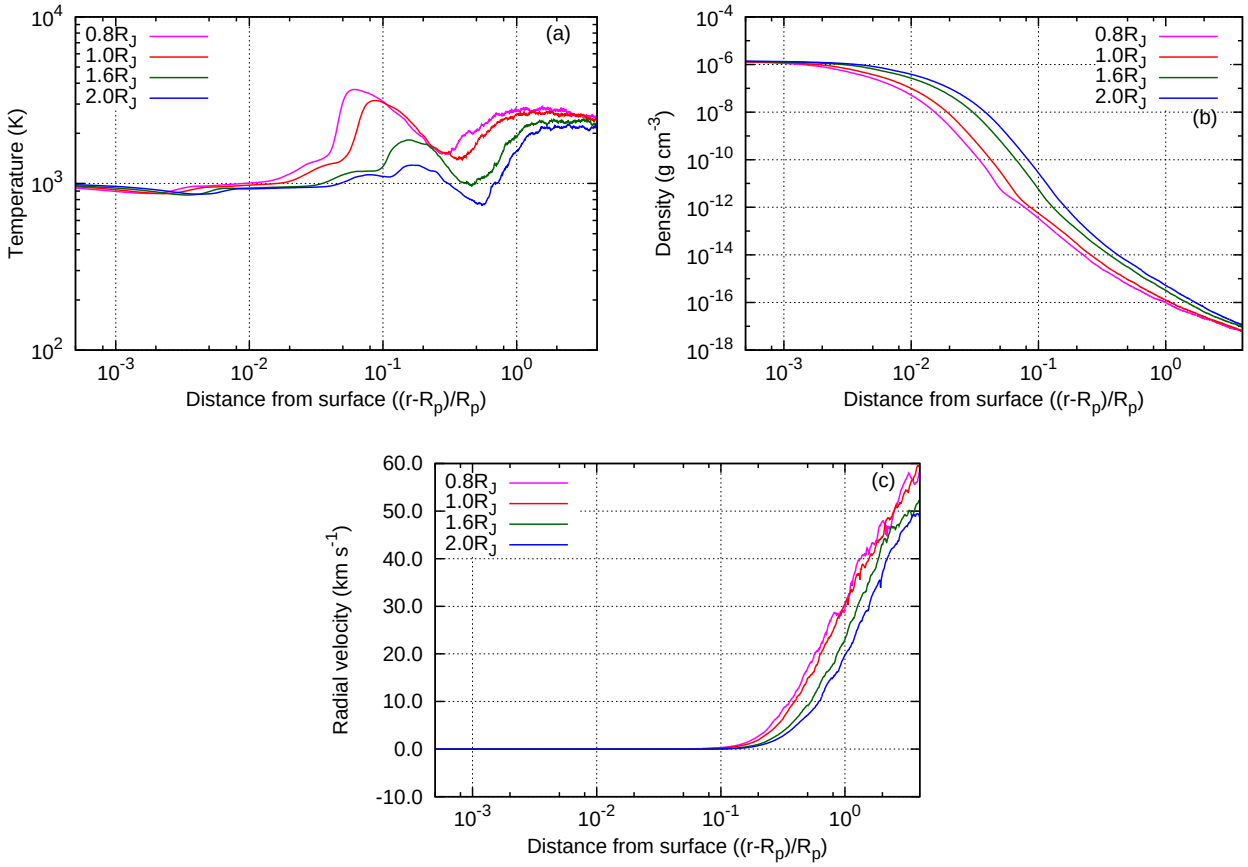

Figure 5.23: Planetary radius dependence of the atmospheric structures. (a) Temperature structure, (b) density profile, and (c) radial velocity profile. The horizontal axes denote the distance from the surface of the planet that is normalized by the radius of the planet. The magenta, red, green, and blue lines correspond to that radii of planets, $0.8R_{\rm J}$, $1R_{\rm J}$, $1.6R_{\rm J}$, and $2.0R_{\rm J}$, respectively. The surface temperature is set to 1000 K, and the velocity dispersion is 20% of the sound speed in the all cases.

behavior of the dependence of the atmospheric structure. The temperature is heated up by

the dissipation of the MHD wave energy in the upper atmosphere in the all cases, and the altitude where the temperature rises rapidly becomes higher as the increase of the radius of the planet. This is caused by the larger density in the upper atmosphere; the density of the upper atmosphere is much more enhanced in the larger radius cases because of the larger scale height, so the gas becomes difficult to heat up. By the same token, the denser upper atmosphere becomes hard to accelerate, and that results in the radial velocity profile that the slightly slower outflow from the larger planets.

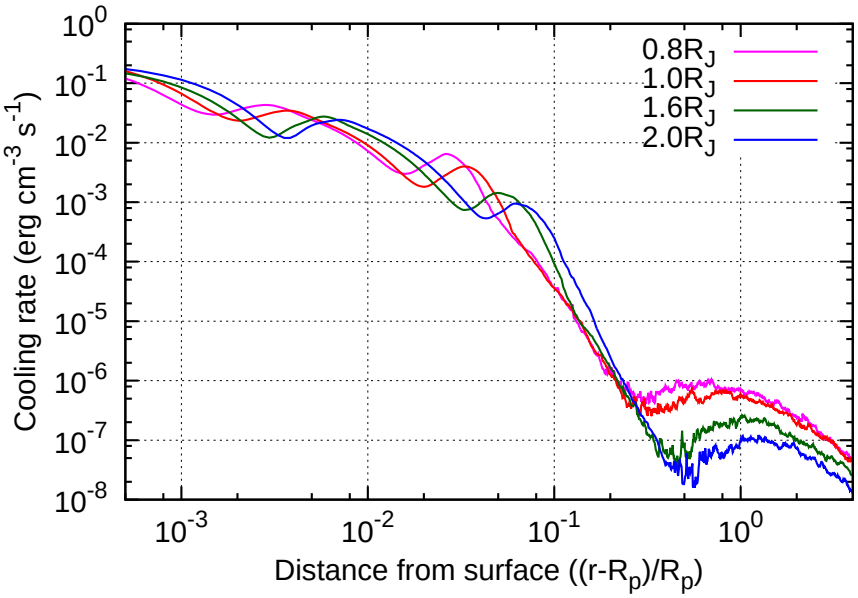

Figure 5.24: The radiative cooling rates in the atmosphere as a function of the altitude. The horizontal axis denotes the distance from the surface that is normalized by the planetary radius, and the vertical axis denotes the radiative cooling rate per unit volume in units of $\mathrm{erg\,cm^{-3}\,s^{-1}}$. The magenta, red, green, and blue lines correspond to that radii of planets, $0.8R_{\rm J}$, $1R_{\rm J}$, $1.6R_{\rm J}$, and $2.0R_{\rm J}$, respectively. The surface temperature is set to 1000 K, and the velocity dispersion is 20% of the sound speed in the all cases.

Figure 5.24 compares the radiative cooling rates of several cases of the radius of the planet. The radiative cooling rate per unit volume is $\sim 10^{-1}\,\mathrm{erg\,cm^{-3}\,s^{-1}}$ in the lower atmosphere in all cases, and general behavior of them are similar.

5.5.2 Mass Dependence of the Atmospheric Structures

Next we show the dependence of the atmospheric structures on the mass of the planet. Figure 5.25 is the relation between the atmospheric structures and the mass of the planets. In these calculations, the radius of the planet is fixed to Jupiter's radius, the surface temperature is

1000 K, and the velocity dispersion is 20% of the sound speed. In these calculations, since the

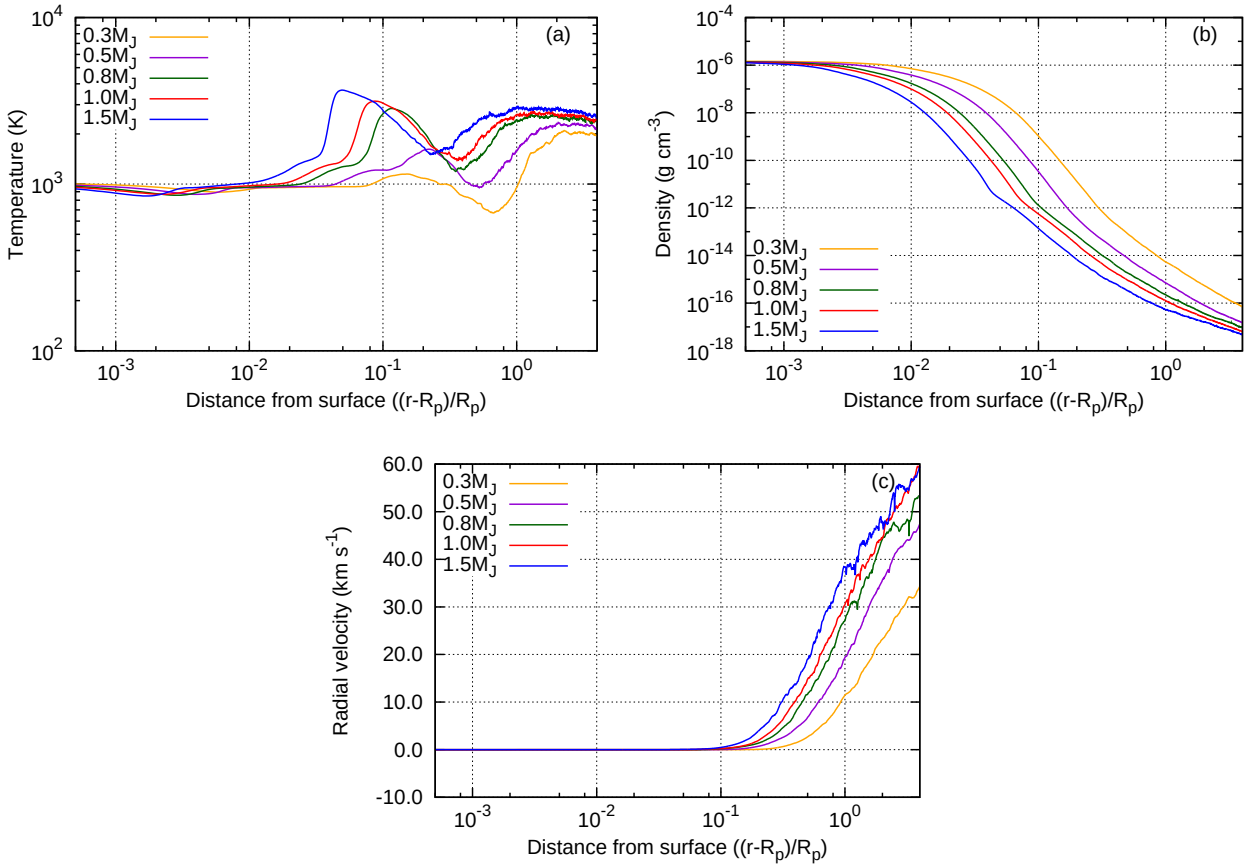

Figure 5.25: Planetary mass dependence of the atmospheric structures. (a) Temperature structure, (b) density profile, and (c) radial velocity profile. The horizontal axes denote the distance from the surface of the planet that is normalized by the radius of the planet. The orange, violet, green, red, and blue lines correspond to the masses of planets, $0.3M_{\rm J}$, $0.5M_{\rm J}$, $0.8M_{\rm J}$, $1.0M_{\rm J}$, and $1.5M_{\rm J}$, respectively. The surface temperature is set to 1000 K, and the velocity dispersion is 20% of the sound speed.

radius and surface temperature are fixed, the pressure scale height decreases with the increase of the mass of the planet. As shown in Section 5.5.1, the temperature in the upper atmosphere is relatively lower for the larger scale height, and that trend also appears here; the temperature of the upper atmosphere is relatively lower for the cases of lighter planets. When the mass of the planet is larger, the temperature in the middle region of the atmosphere rises drastically, due to the steep decrease of the density. The radial velocities of the escaping atmosphere are faster than sound speed in the all cases, but they are relatively slower when the planetary mass is smaller, because of the denser upper atmosphere.

Figure 5.26 compares the radiative cooling rates of several cases of the radius of the planet.

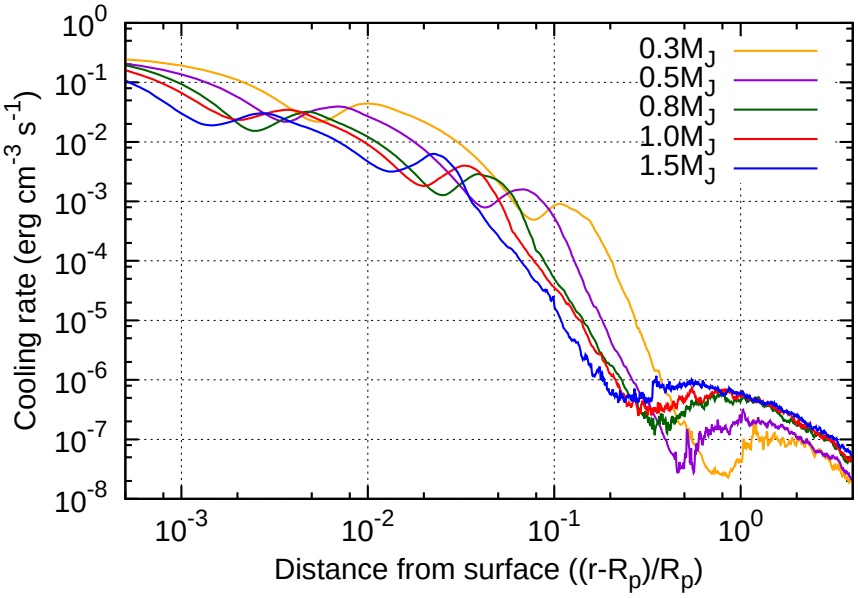

Figure 5.26: The radiative cooling rates in the atmosphere as a function of the altitude. The horizontal axis denotes the distance from the surface that is normalized by the planetary radius, and the vertical axis denotes the radiative cooling rate per unit volume in units of erg cm^{-3} s^{-1}. The orange, violet, green, red, and blue lines correspond to the masses of planets, $0.3M_{\rm J}$, $0.5M_{\rm J}$, $0.8M_{\rm J}$, $1.0M_{\rm J}$, and $1.5M_{\rm J}$, respectively. The surface temperature is set to 1000 K, and the velocity dispersion is 20% of the sound speed in the all cases.

The radiative cooling rates ver unit volume are $\sim 10^{-1}$ erg cm^{-3} s^{-1} in the lowest region of the atmosphere in all cases, but in the middle and upper region of the atmosphere, they differ several orders of magnitude because the difference of the temperature structure in each case.

Although the radial velocity of the escaping atmosphere is slower when the mass of the planet is smaller, the density in the upper atmosphere is several orders of magnitude larger. While the difference of the radial velocities are only several times at a maximum. Therefore, this dense and slow outflow enhances the mass-loss rate from lighter planets. Figure 5.27 shows the dependence of the mass-loss rate on the mass of the planet. The mass-loss rate decreases as the increase of the mass of the planet. We also show the dependence of the mass-loss rate on the planetary mass when the modified Unno-Kondo method is used to derive the radiative cooling function, which is shown in Figure 4.16, for comparison. Since the difference between two methods is quite small, the dependence of the mass-loss rates are also similar.

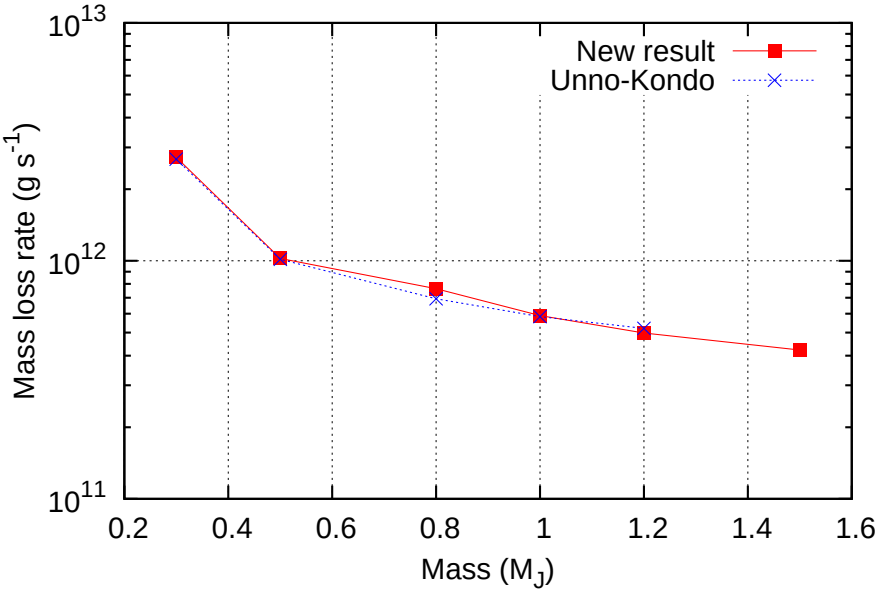

Figure 5.27: Relation between the mass of the planet and the mass-loss rate. The horizontal axis is the mass of the planet that is normalized by the mass of Jupiter, and the vertical axis is the mass-loss rate in units of $\mathrm{g\,s^{-1}}$. The red line and points are the results of the new calculation, and blue line and points are the result of "Unno-Kondo" cases.

5.5.3 Dependence of the Mass-Loss Rate

Figure 5.28 shows the dependence of the mass-loss rate on the radius and mass of the planets. In this calculations, the surface temperature is fixed to 1000 K, and the velocity dispersion is 20% of the sound speed. The clear trend appears in the figure; the larger mass-loss rate from lighter and larger planets, and smaller mass-loss rate from heavier and smaller planets, which are similar to the previous results.

As we mentioned in the introduction, the discovered exoplanets are very rich in diversity, that is to say, the pressure scale height of the planetary atmosphere ranges widely with the properties of each exoplanet. Therefore, amounts of the atmospheric escape that is driven by the dissipation of the MHD wave energy are expected to be different largely, depending on their physical properties. For example, highly irradiated gaseous planets tend to have larger radii, and the level of inflation of the radii is related to a level of the irradiation (Demory and Seager, 2011). This means that the highly irradiated gaseous planets generally have larger radii and high surface temperature, so the large amounts of atmospheric escape are expected. Of course the mass-loss rate and the atmospheric structure strongly depend on other features such as the velocity dispersion at the planetary surface and the strength of the magnetic fields

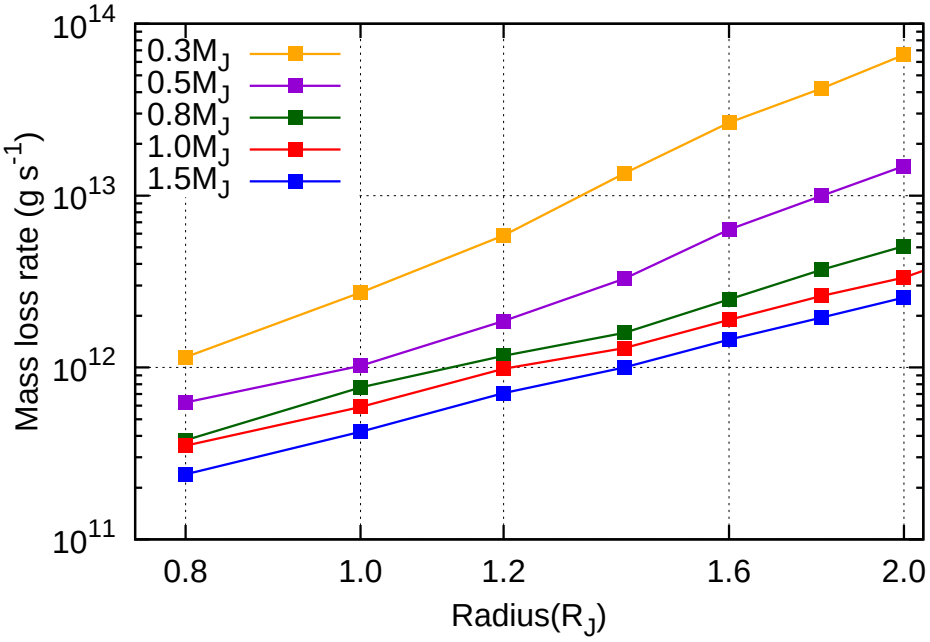

Figure 5.28: Relation between the radius and mass of the planets, and the mass-loss rate. The horizontal axis is the radius of the planets that is normalized by the radius of Jupiter, and the vertical axis is the mass-loss rate in the units of $\mathrm{g\,s^{-1}}$. Note that both axes are logarithmic scale. The orange, violet, green, red, and blue lines correspond to the masses of the planets, $0.3M_\mathrm{J}$, $0.5M_\mathrm{J}$ $0.8M_\mathrm{J}$, $1.0M_\mathrm{J}$, and $1.5M_\mathrm{J}$, respectively. The surface temperature is set to 1000 K, and the velocity dispersion is 20% of the sound speed in the all cases.

and its configurations, but in other words, if the atmospheric escape and structure are well characterized, it may be possible to estimate the velocity dispersion or features of the planetary magnetic fields.

5.5.4 Time Variability of the Mass-Loss Rate and Atmospheric Structures

Here we show the time variability of the mass-loss rate for several cases of the radius and mass of the planet. Figure 5.29 shows the temporal variation of the mass-loss rates when the radii of the planets are $1.0R_\mathrm{J}$, $1.6R_\mathrm{J}$, and $2.0R_\mathrm{J}$. In our simulations, calculation time is normalized by the crossing time of a planet, that is defined as $t_\mathrm{cross} = R_\mathrm{p}/c_\mathrm{s}$, where R_p is the radius of a planet, and c_s is the sound speed at the surface, and the duration of each calculation is $6.0t_\mathrm{cross}$. Therefore, the calculation time in the real unit is proportional to the planetary radii, when the other properties are same in each calculation. In these cases, the mass of the planet is fixed to Jupiter's mass, the surface temperature is 1000 K, and the value of the velocity dispersion

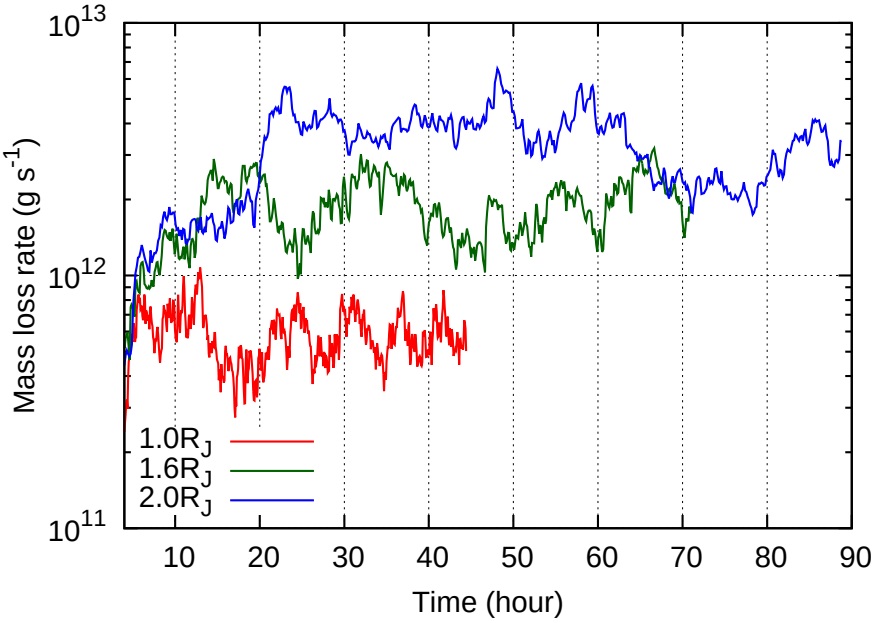

Figure 5.29: Time variability of the mass-loss rate. The horizontal axis is time in units of hour, and the vertical axis is the mass-loss rate in units of $\mathrm{g\,s^{-1}}$. The red, blue, and green lines correspond to the planetary radius, $1.0R_{\rm J}$, $1.6R_{\rm J}$, and $2.0R_{\rm J}$, respectively. For all cases, the mass is Jupiter's mass, the surface temperature is set to 1000 K, and the value of the velocity dispersion is 20% of the sound speed at the surface.

is 20% of the sound speed at the planetary surface. That is the reason why the green ($1.6R_{\rm J}$) and blue ($2.0R_{\rm J}$) lines last longer than the red line ($1.0R_{\rm J}$).

As shown in the figure, the mass-loss rates have large time-variability in each case. For the $1.0R_{\rm J}$ case, variations with a period of several hours appear, and small jitter with a shorter period also appears. For the larger radius cases, the variations with a period of several hours also appears, but another variations with a period of several tens of hours are seen. These results suggest that the long period of several tens of hours are expected from the larger inflated hot Jupiters, if the magnetically driven atmospheric escape exists.

Figure 5.30 shows the temporal variation of the mass-loss rate when the masses of the planets are $0.3M_{\rm J}$, $0.5M_{\rm J}$, $0.8M_{\rm J}$, $1.0M_{\rm J}$, and $1.5M_{\rm J}$. In these calculations, the radius of the planet is fix to Jupiter's radius, the surface temperature is 1000 K, and the value of the velocity dispersion is 20% of the sound speed at the planetary surface. For the lighter planets, while the mass-loss rate is larger, its ranges of the variations are relatively smaller. For the case of $0.3M_{\rm J}$, a very short period of about an hour with small variation appears. The fluctuation of the mass-loss rate seems to be large with the increase of the mass of the planet. In particular,

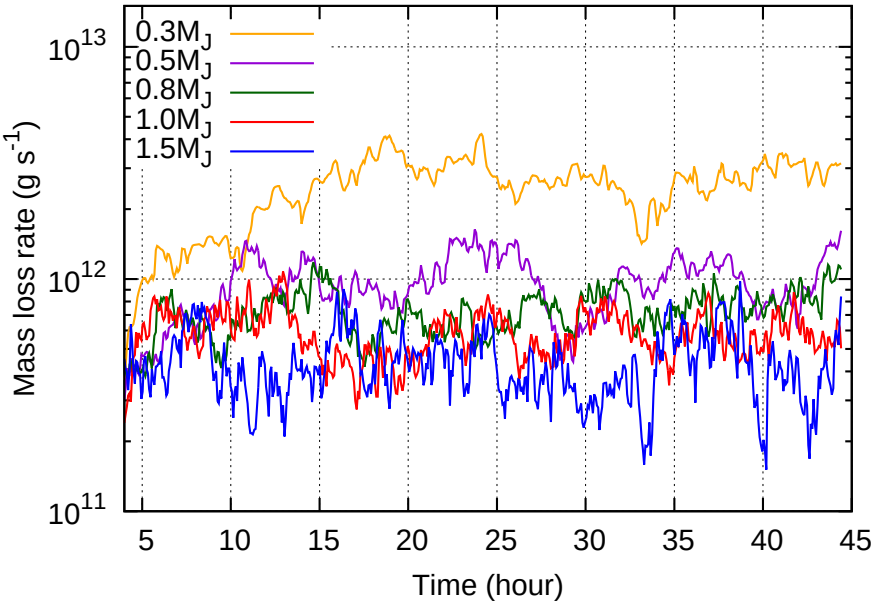

Figure 5.30: Time variability of the mass-loss rate. The horizontal axis is time in units of hour, and the vertical axis is the mass-loss rate in units of $\mathrm{g\,s^{-1}}$. The orange, violet, green, red, and blue lines correspond to the planetary mass, $0.3M_\mathrm{J}$, $0.5M_\mathrm{J}$, $0.8M_\mathrm{J}$, $1.0M_\mathrm{J}$, and $1.5M_\mathrm{J}$, respectively. For all cases, the radius is Jupiter's radius, the surface temperature is set to 1000 K, and the value of the velocity dispersion is 20% of the sound speed at the surface.

in the $1.5M_\mathrm{J}$ case, larger range of the variation with a short period of several hours can be seen. Thus the relatively smaller amount but highly variable mass-loss rate and atmospheric structures are expected to exist at heavier gaseous planets.

In our model of the atmospheric escape that is driven by the dissipation of the MHD wave energy, non-linear dissipation of the waves in the planetary atmosphere becomes important. Therefore, the time-variation of the mass-loss rate and the atmospheric structure appear in the results. This large time-variability can be one of the significant features of the magnetically driven atmospheric escape.

Figure 5.31 and 5.32 show the snapshots of the atmospheric structures of two cases of the planetary mass, $0.3M_\mathrm{J}$ and $1.5M_\mathrm{J}$, respectively. In the both cases, the radius is fixed to Jupiter's radius, the surface temperature is set to 1000 K, and the value of the velocity dispersion is 20% of the sound speed at the planetary surface. The temperature structures, density profiles, and radial velocity profiles are highly time-variable in both cases. Each line corresponds to the elapsed time from the beginning of the calculation, that is normalized by the crossing time of the planet. In the current setup for this calculation, $t = 1.00$ is equivalent

to $\sim$ 7.4 hours. In Figure 5.31, the red solid, green dashed, blue dotted, and violet dot-dashed lines mean the elapsed time 18.5 hours, 24.0 hours, 29.6 hours, and 32.9 hours from the start of the calculation, respectively. These elapsed times are corresponding to follows; $t = 2.50$

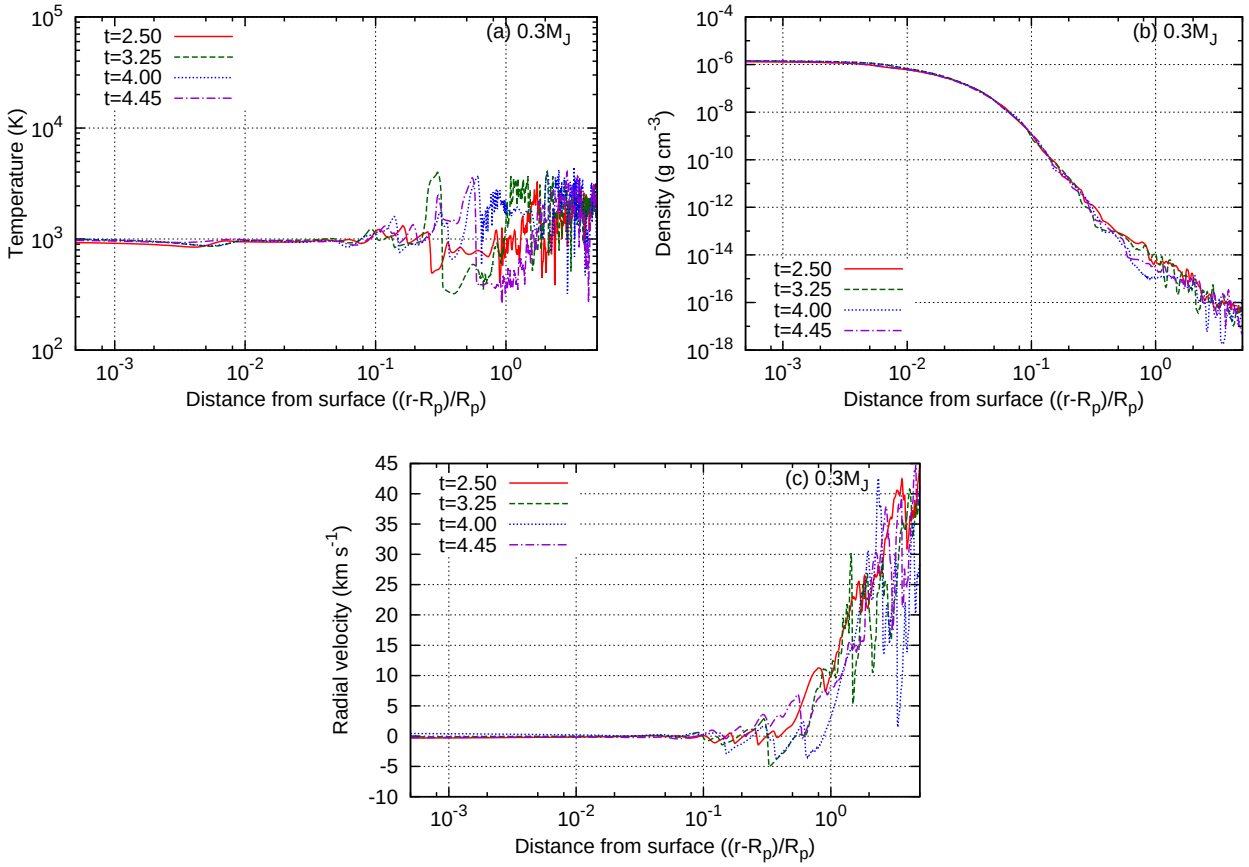

Figure 5.31: Snapshots of the time evolution of the atmospheric structures when the mass of the planet is $0.3M_{\rm J}$. (a) Temperature structure, (b) density profile, and (c) radial velocity profile, respectively. The radius is fixed to Jupiter's radius, the surface temperature is set to 1000 K, and the value of the velocity dispersion is fixed to 20% of the sound speed at the planetary surface. The red solid, green dashed, blue dotted, and violet dot-dashed lines correspond to the elapsed time from the beginning of the calculation, $t = 2.50$, 3.25, 4.00, and 4.45, respectively. The elapsed time t is normalized by the crossing time of the planet.

(18.5 hours) and $t = 3.25$ (24.0 hours) are the time when the mass-loss rate almost reach the maximum value that shown by the orange line in Figure 5.30, $t = 4.45$ (32.9 hours) is the time when the mass-loss rate almost reach the minimal value, and $t = 4.00$ (29.6 hours) is the time when the mass-loss rate is almost same with the time-averaged value, respectively. The mass flux from the planet is determined by the product of the density and radial velocity, thus the both values are important. In the snapshots of the atmospheric structures, the fluctuation of

the density in the upper atmosphere is as large as one to two orders of magnitude in units of $\mathrm{g\,cm^{-3}}$, and the radial velocity varies between almost zero to $\sim 50\ \mathrm{km\,s^{-1}}$.

In Figure 5.32, the red solid, green dashed, blue dotted, and violet dot-dashed lines mean the elapsed time 33.3 hours, 34.7 hours, 37.7 hours, and 40.2 hours from the start of the calculation, respectively. These elapsed times are corresponding to follows; $t = 4.69$ (34.7 hours) and $t = 5.10$ (37.7 hours) are the time when the mass-loss rate almost reach the maximum value that shown by the blue line in Figure 5.30, $t = 4.50$ (33.3 hours) and $t = 5.43$ (40.2 hours) are the time when the mass-loss rate almost reach the minimal value, respectively. Similar to

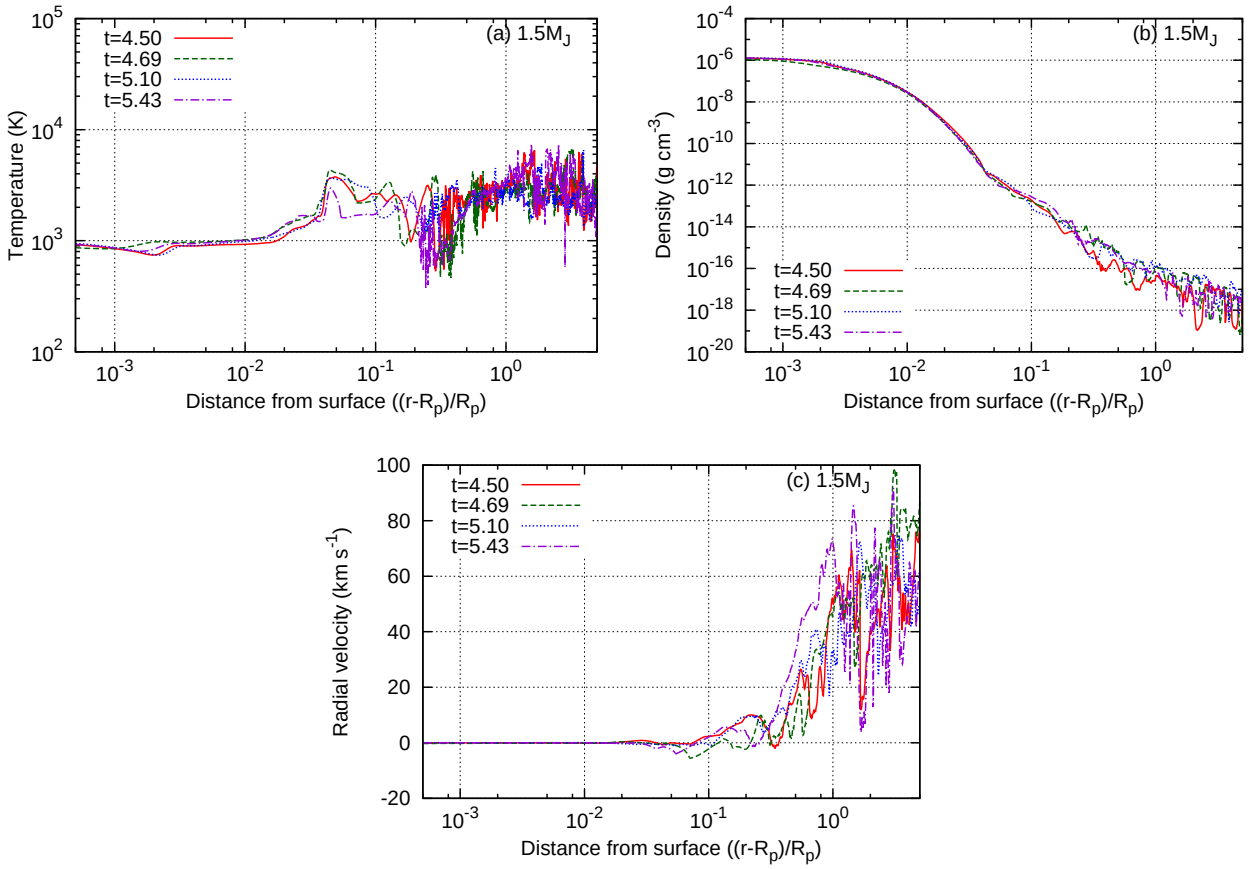

Figure 5.32: Snapshots of the time evolution of the atmospheric structures when the mass of the planet is $1.5M_{\mathrm{J}}$. (a) Temperature structure, (b) density profile, and (c) radial velocity profile, respectively. The radius is fixed to Jupiter's radius, the surface temperature is set to 1000 K, and the value of the velocity dispersion is fixed to 20% of the sound speed at the planetary surface. The red solid, green dashed, blue dotted, and violet dot-dashed lines correspond to the elapsed time from the beginning of the calculation, $t = 4.50$, 4.69, 5.10, and 5.43, respectively. The elapsed time t is normalized by the crossing time of the planet.

Figure 5.31, the atmospheric structures show the large time-variability. The fluctuation of the

density is the upper atmosphere is as large as one to two orders of magnitude in units of $\mathrm{g\,cm^{-3}}$, and the radial velocity dispersion ranges between almost zero to $\sim$ 50 $\mathrm{km\,s^{-1}}$. The maximal value of the radial velocity in the case of $1.5M_{\mathrm{J}}$ is larger than the case of $0.3M_{\mathrm{J}}$, because the escape velocity is larger than the former case due to the heavier mass of the planet. As shown in Figure 5.31 and 5.32, the outflow that is driven by the dissipation of the MHD wave energy does not occur statically, but it occurs clumpy and highly time-variable.

Chapter 6

Discussion

6.1 Application to a Hot Neptune GJ 436b

In the previous chapters, we have mainly focused on the atmospheric escape and structure of hot Jupiters. As mentioned in Chapter 1, the extended exospheres and signatures of the atmospheric escape from several hot Jupiters have been observed (e.g., Vidal-Madjar et al., 2003; Lecavelier des Etangs et al., 2010). Recently, however, the atmospheric escape from smaller planets also have been reported, as introduced in Section 1.3.3. A notable example of them is GJ 436b, which is a Neptune-sized exoplanet. In this section, we briefly introduce observed features of GJ 436b and interpretations of them, and then we apply our model to this exoplanet to explain the observed feature of it.

6.1.1 Atmospheric Escape from GJ 436b

GJ 436b is orbiting around nearby ($d = 10.3\,\mathrm{pc}$) M dwarf star, GJ 436. It is detected by the radial velocity method (Butler et al., 2004) first, then the transit of the planet is also observed later (Gillon et al., 2007), therefore both radius and mass are well characterized by the observations. The mass of GJ 436b is $23.1\,M_\oplus$ ($\simeq 1.35\,M_{\mathrm{Nep}}$) (Ehrenreich et al., 2015), and the radius is $\sim 4\,R_\oplus$ ($\simeq 1\,R_{\mathrm{Nep}}$) (Knutson et al., 2011), where $M_\oplus$ and $R_\oplus$ are the mass and radius of Earth, M_{Nep} and R_{Nep} are the mass and radius of Neptune, respectively, so the mass and radius are similar to Neptune. Since the semi-major axis is $0.029\,\mathrm{AU}$(Ehrenreich et al., 2015), this planet is a member of the close-in exoplanets. Although the extremely small distance from the host star, irradiation that the planet receives is not so strong but moderate, because the host star is a low-mass star. Thus, this Neptune-mass planet is sometimes called a hot Neptune, but also called a "warm" Neptune.

Recent observations have reported the existence of a huge amount of the atmospheric escape and its characteristic exosphere (Kulow et al., 2014; Ehrenreich et al., 2015). The transit depth of GJ 436b in the optical wavelength is only $\sim 0.69\%$ and this value corresponds to the radius of the planet in the optical. In the UV (H Lyα) band, however, transit depth is extremely deep $\sim 56.2\%$ in maximum (Ehrenreich et al., 2015). In addition, the ingress of the transit in the UV band is about two hours earlier than the optical wavelength, and the transit duration is much longer. Furthermore, the shape of the transit light curve in the UV band is highly asymmetric. This anomalous feature of the transit of GJ 436b in the UV band can be explained by the enlarged exosphere and escaping atmosphere; GJ 436b has a large exosphere and a cometary structure of the escaping atmosphere that is optically thick in the UV band, and they create the significantly deep transit depth and asymmetric shape of the transit light curve in the UV band (Ehrenreich et al., 2015).

Some external force is needed for the escaping atmosphere to shape the cometary-tail-like structure, such as the radiation pressure of the host star. Bourrier et al. (2015) performed simulations of the escaping atmosphere that take into account the effect of the radiation pressure, and successfully explained the formation of the huge cometary-tail-like escaping atmosphere and its observed feature. The estimated radial velocity of the escaping atmosphere of GJ 436b exceeds $\sim 100\,\mathrm{km\,s^{-1}}$ (Ehrenreich et al., 2015), and this large velocity can also be explained by the model (Bourrier et al., 2015).

In their model, however, a large radial velocity at the Roche radius of the planet is needed as an inner boundary condition to explain the observed features. They found that the radial velocity at the Roche radius to explain the observed features is needed to be about $30\,\mathrm{km\,s^{-1}}$ (Bourrier et al., 2015). This value is much faster than expected by several models of thermosphere of hot Jupiters, which predict around $1 - 10\,\mathrm{km\,s^{-1}}$ for the radial velocity at the Roche radius in the condition of the hot/warm Neptune GJ 436b (e.g., Murray-Clay et al., 2009; Koskinen et al., 2013). Furthermore, time-variable features are also found in the observation at different epochs, therefore they mentioned that additional physics may be needed to explain these features.

In this section, we perform the MHD simulations in the conditions of the atmosphere of GJ 436b to show the magnetically driven atmospheric escape can explain or contribute to the observed features or not. The radius and mass of the planet are fixed to the values of GJ 436b. The surface temperature is set to 800 K, which is expected value of the equilibrium temperature of GJ 436b that can be calculated from the luminosity of the host star GJ 436

and the semi-major axis of GJ 436b. Since the value of the velocity dispersion at the surface is unknown, we treat it as a parameter. Similar to hot Jupiters, multi-dimensional hydrodynamic simulations of the atmosphere suggest that hot Neptunes also have the strong atmospheric circulation regardless of their metallicity of the atmosphere (Lewis et al., 2010). Therefore, it can be thought that there is certain level of atmospheric turbulence that is generated by the strong atmospheric circulation, and the velocity dispersion due to the turbulence can also be created.

6.1.2 Time-Averaged Atmospheric Structures

Here we show results of the simulations. We change the value of the velocity dispersion at the surface from 5% to 30% of the sound speed at the planetary surface. Figure 6.1 and 6.2 show the dependence of the atmospheric structure on the value of the velocity dispersion. Figure 6.1 is the cases of $\delta v = 0.05 - 0.08 c_{\rm s}$, and Figure 6.2 is the cases of $\delta v = 0.1 - 0.3 c_{\rm s}$, respectively.

For the density profile, the density in the upper atmosphere increases as the increase of the

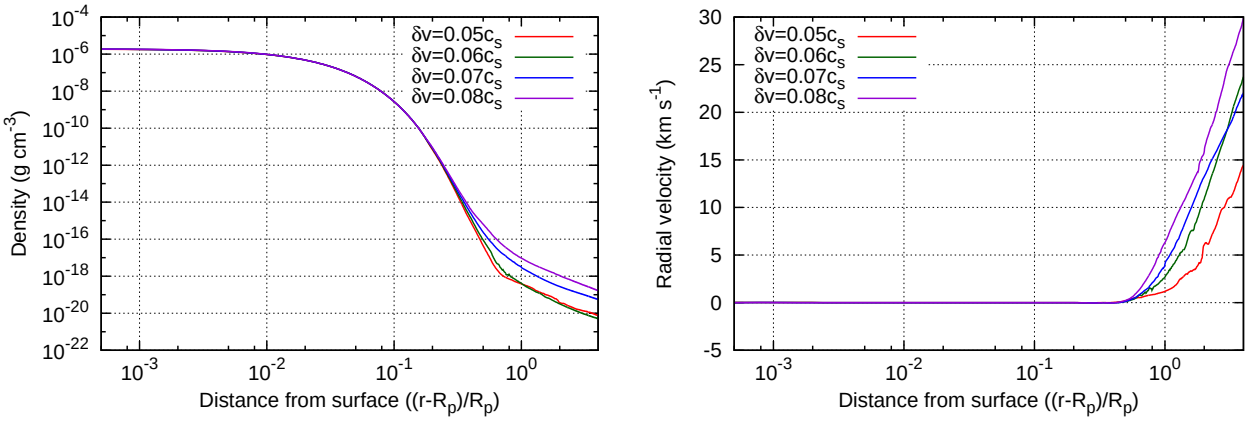

Figure 6.1: Velocity dispersion dependence of the atmospheric structure of GJ 436b. The left panel shows the density profile, and the right panel shows the radial velocity profile. The horizontal axes denote the distance from the surface that is normalized by the planetary radius. The red, green, blue, and violet lines correspond to the values of the velocity dispersion, $0.05 c_{\rm s}$, $0.06 c_{\rm s}$, $0.07 c_{\rm s}$, and $0.08 c_{\rm s}$, respectively.

velocity dispersion, except for the cases of $\delta v = 0.05 c_{\rm s}$ and $\delta v = 0.06 c_{\rm s}$, which show almost similar density profiles. In this range of the velocity dispersion, the energy injected to the magnetic field is too small to lift up the atmospheric gas efficiently, therefore the difference between two cases are very small.

However, the radial velocity profiles show the different and interesting trend. In the right

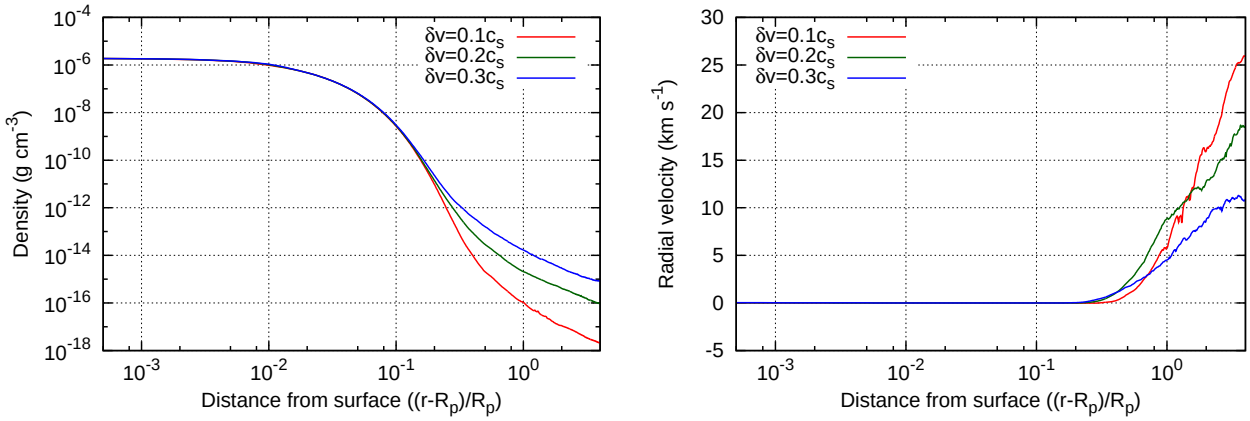

Figure 6.2: Velocity dispersion dependence of the atmospheric structure. The left panel shows the density profile, and the right panel shows the radial velocity profile. The horizontal axes denote the distance from the surface that is normalized by the planetary radius. The red, green, and blue lines correspond to the values of the velocity dispersion, $0.1c_{\rm s}$, $0.2c_{\rm s}$, and $0.3c_{\rm s}$, respectively.

panel of Figure 6.1, the radial velocity in the upper atmosphere increases with the increase of the velocity dispersion. The $0.05c_{\rm s}$ case shows the slowest profile, and the $0.08c_{\rm s}$ case shows the faster profile. On the other hand, in the right panel of Figure 6.2, the radial velocity in the upper atmosphere decreases with the increase of the velocity dispersion. Therefore, the trend of the radial velocity in the upper atmosphere behaves the other way; it becomes faster as the velocity dispersion when the velocity dispersion is smaller than $\sim 0.1c_{\rm s}$, and it becomes slower when the velocity dispersion is larger than $\sim 0.1c_{\rm s}$. The latter trend is explained by the same reason that is described in Section 4.5.2 and 5.4.2; since the upper atmosphere becomes heavier due to the efficient uplifting by the dissipation of the MHD wave energy, so the upper atmosphere becomes harder to accelerate faster. In addition to this, since the radiative cooling is enhanced by the denser atmospheric gas, more amount of energy is lost by radiative loss rather than converted to the kinetic energy of the escaping atmosphere.

The former trend seems, however, the opposite sense. In this range of the velocity dispersion, intrinsically injected energy of the MHD waves is small. As shown in Figure 3.5 in Section 3.4.2, almost all amount of the injected energy is reflected in the each altitude of the atmosphere, and only a tiny fraction of the energy of the MHD waves is converted to the heating and acceleration of the upper atmosphere. In this range of the velocity dispersion, the energy of the MHD waves that contribute to the uplifting of the atmosphere and acceleration is significantly small, therefore the radial velocity in the upper atmosphere becomes slower in spite of the

lighter upper atmosphere compared to the larger δv cases.

In terms of the radial velocity at the Roche radius, as shown in the figures, it seems possible to achieve the radial velocity of $30\,\mathrm{km\,s^{-1}}$ in the upper atmosphere. In the figures, the right-hand edge corresponds to the Roche radius of GJ 436b ($\sim 4R_\mathrm{p}$). For example, the radial velocity at the Roche radius reaches $\sim 30\,\mathrm{km\,s^{-1}}$ when the velocity dispersion is 8% of the sound speed. However, these are the time-averaged profiles, so it is important to see the time-variability of the atmospheric structure if we compare with the observations. We show the time-variation of the atmospheric structure later.

6.1.3 Dependence of the Mass-Loss Rate

Next we show the dependence of the mass-loss rate on the velocity dispersion at the surface. Figure 6.3 is the dependence of the mass-loss rate on the velocity dispersion. Similar to the

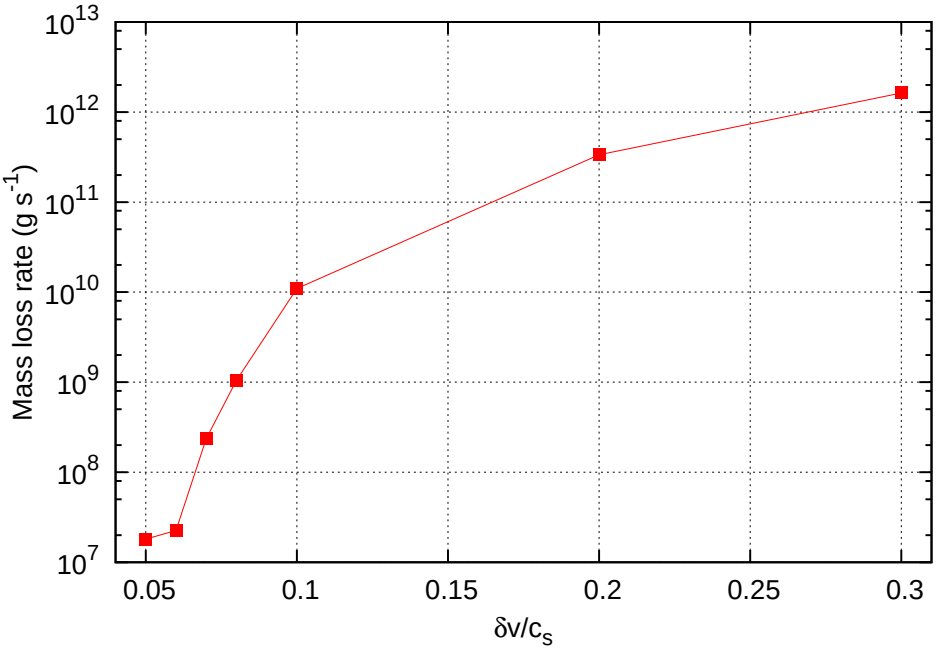

Figure 6.3: Relation between the value of the velocity dispersion at the surface of the planet and the mass-loss rate from the planet. The horizontal axis denotes the velocity dispersion that is normalized by the sound speed at the surface, and the vertical axis denotes the mass-loss rate in units of $\mathrm{g\,s^{-1}}$. In these calculations we assumed that the radius and mass of the planet is same as GJ 436b, and the surface temperature is fixed to 800 K.

previous behavior, the mass-loss rate increases with the increase of the velocity dispersion. When δv is larger than 10% of the sound speed, the radial velocity of the upper atmosphere

decreases as the velocity dispersion as shown in Figure 6.2, but the mass-loss rate increases because of the strong enhancement of the gas density in the upper atmosphere. But when the δv is smaller than 10% of the sound speed, both gas density and radial velocity in the upper atmosphere decrease with the decrease of the velocity dispersion. Therefore, the dependence of the mass-loss rate on the velocity dispersion becomes steeper. The observed mass-loss rate at GJ 436b is estimated to be $10^8 - 10^9\,\mathrm{g\,s^{-1}}$ (Ehrenreich et al., 2015), so the range of the value of the velocity dispersion $\delta v = 0.07c_\mathrm{s} - 0.08c_\mathrm{s}$ seems to be favorable for the explanation for the observed value.

6.1.4 Time-Variability of the Mass-Loss Rate

The dependence of the mass-loss rate on the velocity dispersion we showed in Figure 6.3 is time-averaged. Since the magnetically driven outflow has a large time variation in the mass-loss rate and atmospheric structures, here we represent the behavior of the mass-loss rate as a function of the elapsed time. The time variation of the mass-loss rates are shown in Figure 6.4. The

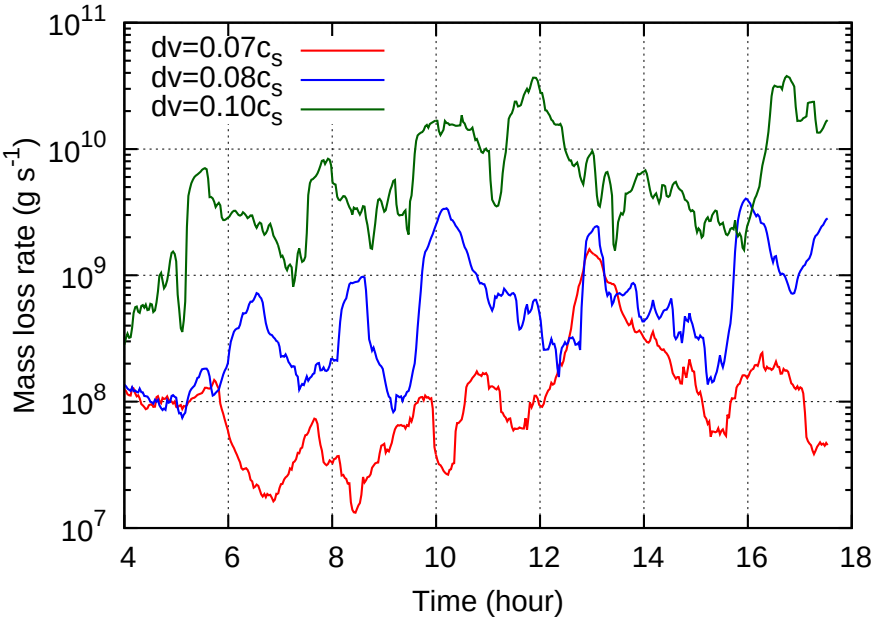

Figure 6.4: Relation between the value of the velocity dispersion at the planetary surface and the mass-loss rate from the planet, as a function of elapsed time from the beginning of the calculation. The horizontal axis denotes the elapsed time in units of hour, and the vertical axis denotes the mass-loss rate in units of $\mathrm{g\,s^{-1}}$. The red, blue, and green lines correspond to the each value of the velocity dispersion, $0.07c_\mathrm{s}$, $0.08c_\mathrm{s}$, and $0.1c_\mathrm{s}$, respectively. In these calculations we assumed that the radius and mass of the planet are same as GJ 436b, and the surface temperature is fixed to 800 K.

mass-loss rates have the large time-variability in each case. For the case of $0.07c_{\rm s}$, the mass-loss rate ranges between $\sim 10^7\,{\rm g\,s^{-1}}$ to $\sim 10^9\,{\rm g\,s^{-1}}$, with a period of about an hour to several hours. For the case of $0.08c_{\rm s}$, it ranges between $\sim 10^8\,{\rm g\,s^{-1}}$ to $\sim 4\times10^9\,{\rm g\,s^{-1}}$ with a period of similar length. Although the averaged mass-loss rates vary strongly depending on the velocity dispersion, they show the large time-variability in this range of the velocity dispersion. The change of the mass-loss rate sometimes very fast, and it can increase an orders of magnitude in around an hour. The transit duration, the time between the ingress and egress, is ~ 1 hour in the visible wavelength (e.g., Gillon et al., 2007). However, the transit duration in the UV wavelength is much longer (Ehrenreich et al., 2015) Therefore, this large time-variation in the mass-loss rate can be detectable.

6.1.5 Time-Variability of Radial Velocities

In Section 6.1.2, we showed the time-averaged atmospheric structures. As shown in Figure 6.1 and 6.2, for the radial velocity at the Roche radius, only the case of $\delta v = 0.08c_{\rm s}$ can reach $\sim 30\,{\rm km\,s^{-1}}$ which is estimated radial velocity at the Roche radius of GJ 436b by Bourrier et al. (2015). However, due to the large time-variability of our driving mechanism of atmospheric escape, the radial velocity at the Roche radius can be both faster and slower in any case of the velocity dispersion.

Figure 6.5 represents the snapshots of the radial velocity profiles in three cases of the velocity dispersion. In our simulation, the elapsed time from the beginning of the calculation is normalized by the crossing time of the planet, $t_{\rm cross} = R_{\rm p}/c_{\rm s}$. In this setup for GJ 436b, $t_{\rm cross} = 1.0$ corresponds to ~ 2.9 hours. The upper left panel shows the case of $\delta v = 0.07c_{\rm s}$. The red, green, and blue lines correspond to the elapsed times, $t = 3.24$ (9.5 hour), $t = 4.27$ (12.5 hours), and $t = 5.60$ (16.4 hours), respectively. The lower atmosphere is almost hydrostatic and the radial velocity is zero. The upper atmosphere is hydrodynamic because the dissipation of the MHD wave energy becomes important, and the radial velocity varies largely around the Roche radius of the planet. In the time-averaged profile, the radial velocity at the Roche radius is $\sim 24\,{\rm km\,s^{-1}}$ (see the blue line in Figure 6.1), but in the snapshots, it can easily exceed $30\,{\rm km\,s^{-1}}$ around the Roche radius, and sometimes reaches $\sim 50\,{\rm km\,s^{-1}}$. For this case, the radial velocity of the escaping atmosphere cannot reach or exceed $30\,{\rm km\,s^{-1}}$ averagely, but it can reach or exceed that velocity transiently.

The upper right panel is the case of $\delta v = 0.08c_{\rm s}$, The red, green, and blue lines correspond to the elapsed times, $t = 3.95$ (11.5 hour), $t = 4.49$ (13.1 hours), and $t = 5.38$ (15.7 hours),

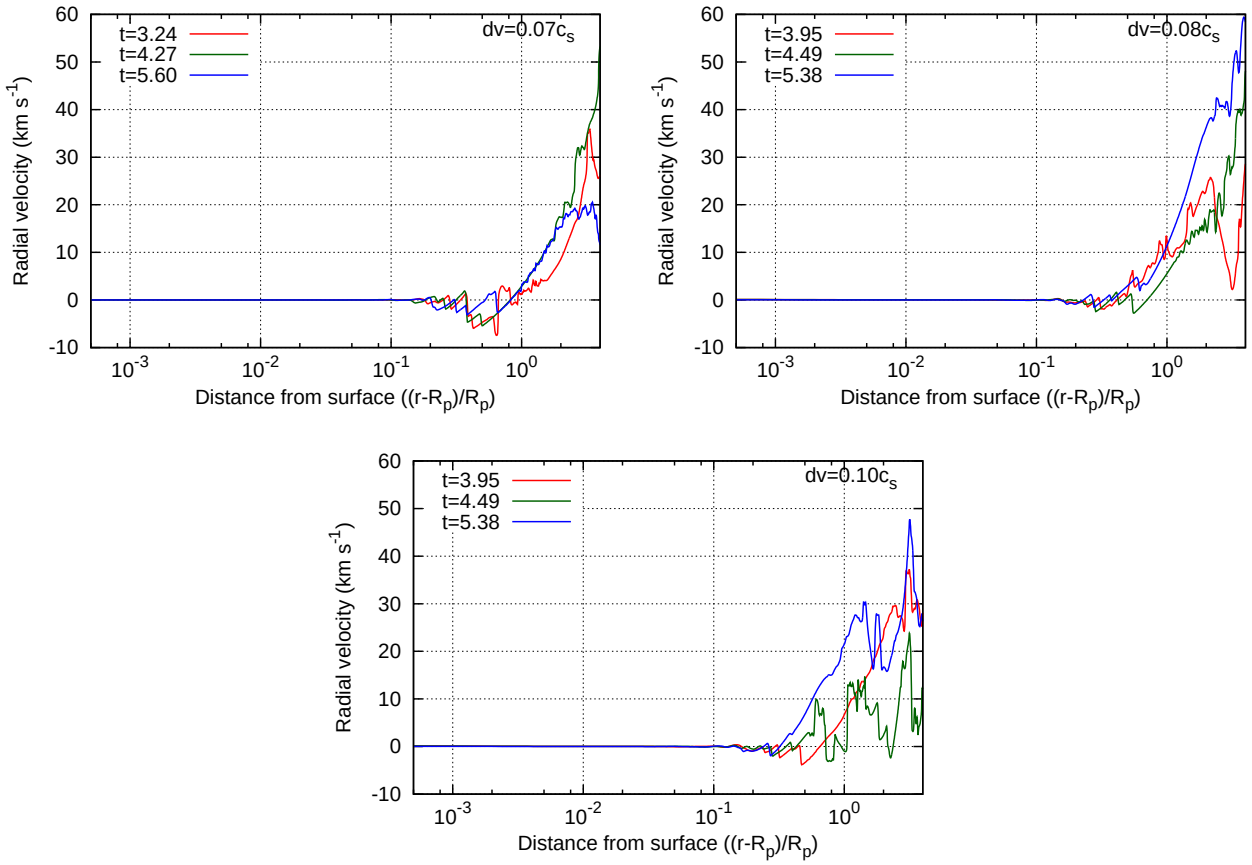

Figure 6.5: Snapshots of the radial velocity profiles. The upper left, upper right, and lower panels correspond to the cases of $\delta v = 0.07c_{\rm s}$, $0.08c_{\rm s}$, and $0.1c_{\rm s}$, respectively. The horizontal axes denote the distance from the surface that is normalized by the planetary radius. The red, green, and blue lines correspond to the elapsed times from the beginning of the calculation, and it is normalized by the crossing time of the planet. In these figures, the right-hand edges correspond to the Roche radius of the planet, $\sim 4R_{\rm p}$.

respectively. This case has the fastest radial velocity in the range of the velocity dispersion we calculated. The time-averaged radial velocity of the escaping gas at the Roche radius is $\sim 30\,{\rm km\,s^{-1}}$, which satisfies the estimated value by Bourrier et al. (2015). In the snapshots, it can be seen that the radial velocity can reach much faster value, $\sim 60\,{\rm km\,s^{-1}}$. However, the radial velocity in the upper atmosphere sometimes takes quite low value, only several ${\rm km\,s^{-1}}$ (red line). Therefore, it is expected that the feature of the escaping atmosphere may change in each observation and each transit event. The bottom panel is the case of $\delta v = 0.1c_{\rm s}$, The red, green, and blue lines correspond to the elapsed times, $t = 3.95$ (11.5 hour), $t = 4.49$ (13.1 hours), and $t = 5.38$ (15.7 hours), respectively. In this case, the mass-loss rate is around an order of magnitude larger than the other two cases, but the radial velocity at the Roche radius

is $\sim 25\,\mathrm{km\,s^{-1}}$ which is slightly slower then the estimated value, because the heavier upper atmosphere becomes hard to accelerate. But if we see the time-variation, the radial velocity of the escaping atmosphere can reach or exceed $\sim 30\,\mathrm{km\,s^{-1}}$, and sometimes reaches around $50\,\mathrm{km\,s^{-1}}$ as shown in Figure 6.5.

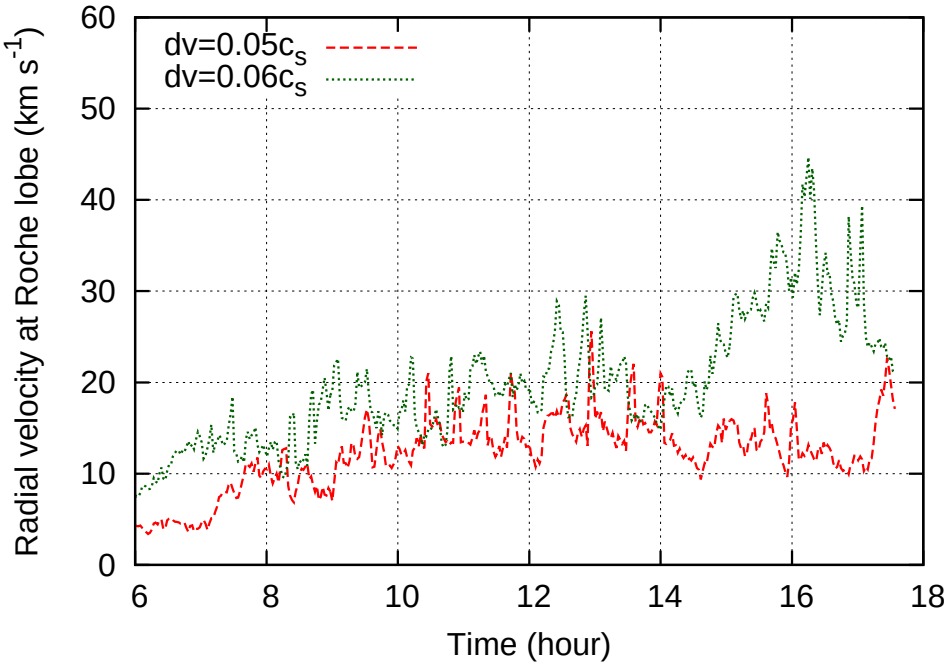

Figure 6.6: Time variation of the radial velocity of the escaping atmosphere at the Roche radius. The horizontal axis denotes the lapse time from the beginning of the simulation in units of hour, and the vertical axis denotes the radial velocity at the Roche radius in units of $\mathrm{km\,s^{-1}}$. The red dashed, and green dotted lines correspond to $\delta v = 0.05c_\mathrm{s}$, and $0.06c_\mathrm{s}$, respectively.

Figure 6.6, 6.7, and 6.8 show the time variation of the radial velocity of the escaping atmosphere at the Roche radius of the planet. The cases of $\delta v = 0.05c_\mathrm{s}$ and $0.06c_\mathrm{s}$ are shown in Figure 6.6. The case of $\delta v = 0.05c$ has the slowest time-averaged radial velocity profile. The time variation is also same, it rarely exceed $20\,\mathrm{km\,s^{-1}}$, because of the small injection energy to the magnetic field. The case of $\delta v = 0.06c_\mathrm{s}$ shows the same behavior, but slightly faster then the $\delta v = 0.05c_\mathrm{s}$ case. This case rarely exceed $30\,\mathrm{km\,s^{-1}}$, but sometimes can be faster than that velocity as a transient event. Therefore, these cases may be difficult to explain the estimated radial velocity at the Roche radius $\sim 30\,\mathrm{km\,s^{-1}}$.

The cases of $\delta v = 0.07c_\mathrm{s}$ and $0.08c_\mathrm{s}$ are shown in Figure 6.7. In these cases, since the uplifted gas in the upper atmosphere is not too dense, and the amount of the energy that is injected to the magnetic fields is larger enough, the atmosphere can be accelerated more efficiently

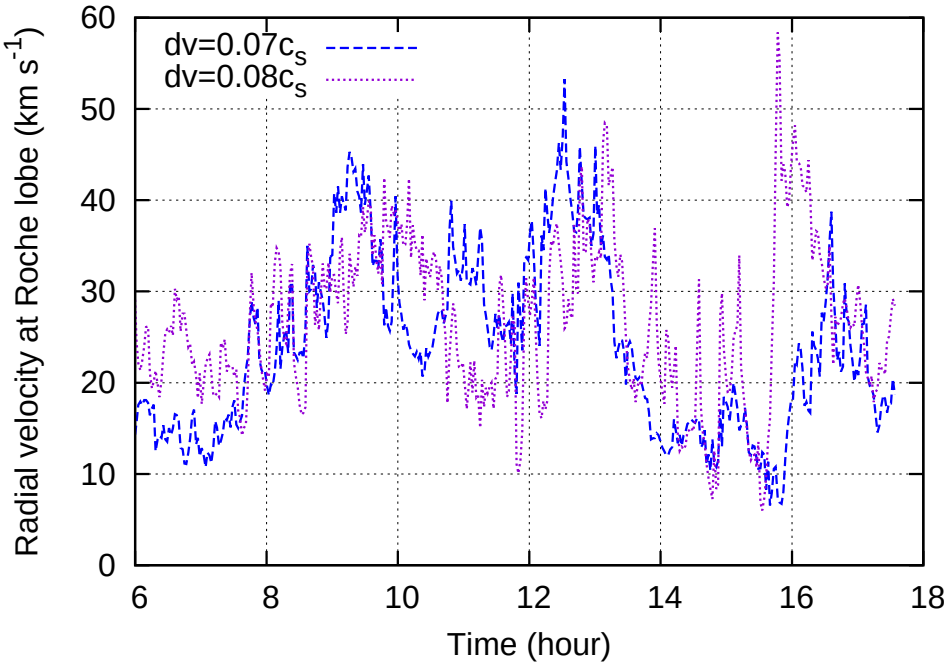

Figure 6.7: The axes are same as Figure 6.6. The blue dashed, and violet dotted lines correspond to $\delta v = 0.07 c_{\rm s}$, and $0.08 c_{\rm s}$, respectively.

than the other cases, and hence the radial velocity at the Roche radius can be faster. In the time-averaged radial velocity profiles, the radial velocity at the Roche radius in the $\delta v = 0.07 c_{\rm s}$ case exceed $\sim 20\,{\rm km\,s^{-1}}$, and that in the $\delta v = 0.08 c_{\rm s}$ almost reach $30\,{\rm km\,s^{-1}}$. In the time evolution of the radial velocity of these cases, they varies very actively. The radial velocity at the Roche radius ranges wide value, between $\sim 10\,{\rm km\,s^{-1}}$ to $\sim 50\,{\rm km\,s^{-1}}$, and sometimes reaches $\sim 60\,{\rm km\,s^{-1}}$ as a transient event in the $\delta v = 0.08 c_{\rm s}$ case. The radial velocity varies in very short period that is shorter than an hour, and also varies in much longer period, several hours. In this range of the value of the velocity dispersion, the radial velocity at the Roche radius fluctuates around $\sim 30\,{\rm km\,s^{-1}}$, thus it is more likely for the radial velocity to exceed that value when one observes the transit of the planet.

Figure 6.8 represents the cases of $\delta v = 0.1 c_{\rm s}$, $0.2 c_{\rm s}$, and $0.3 c_{\rm s}$. In these cases, the amount of the energy that is injected to the magnetic fields is large enough, so the more amount of the atmospheric gas can be uplifted to the upper atmosphere by the dissipation of the MHD wave energy, and the density of the upper atmosphere is enhanced, and then the resultant mass-loss rate becomes larger than the other cases. However, in spite of larger energy injection, the denser upper atmosphere and enhanced radiative loss from the upper atmosphere prevent the radial velocity from being accelerated efficiently. For example, the time-averaged radial velocity at

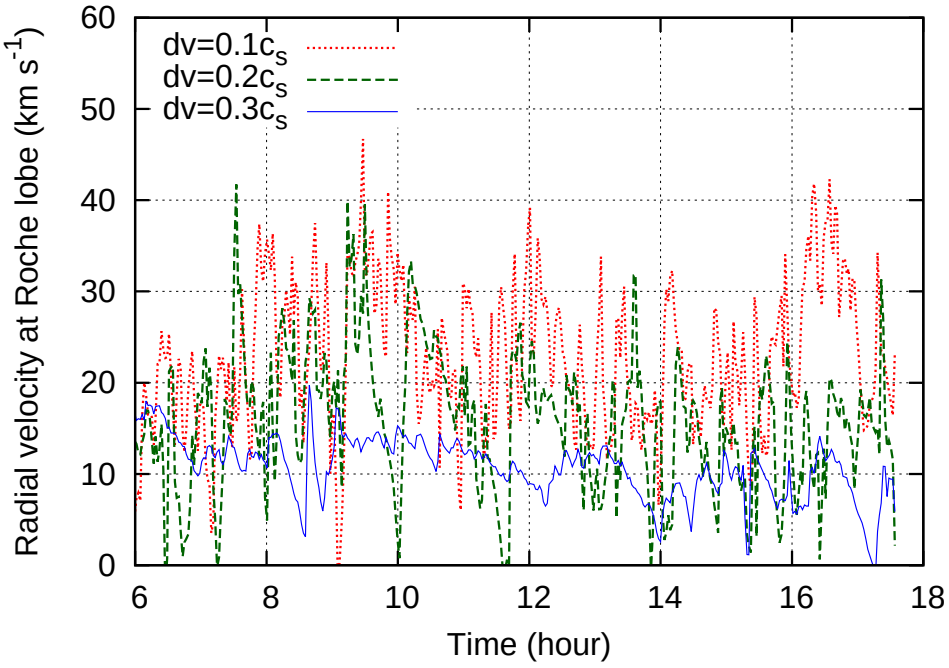

Figure 6.8: The axes are same as Figure 6.6 and 6.7. The red dotted, green dashed and blue solid lines correspond to $\delta v = 0.1c_{\rm s}$, $0.2c_{\rm s}$, and $0.3c_{\rm s}$, respectively.

the Roche radius is about $25\,{\rm km\,s^{-1}}$ when the velocity dispersion is 10% of the sound speed, and only $\sim 10\,{\rm km\,s^{-1}}$ when the 30% of the sound speed. These slower radial velocity can also be seen in Figure 6.8. The radial velocity at the Roche radius sometimes becomes faster than $30\,{\rm km\,s^{-1}}$ in the $\delta v = 0.1c_{\rm s}$ case, but it only happens as a quite short transient event in the $\delta v = 0.2c_{\rm s}$ case. In addition, the fluctuation of the radial velocity is very large in these two cases, and sometimes it become almost zero. In the $\delta v = 0.3c_{\rm s}$ case, the radial velocity is slower, and the range of the variation is also small. The fluctuation of the radial velocity is suppressed due to the denser upper atmosphere. when the value of the velocity dispersion at the surface is larger. In general, the radial velocity at the Roche radius becomes slow, and fluctuation of it also becomes small when the velocity dispersion increases in this range. Therefore, the larger value of the velocity dispersion at the planetary surface is not favorable to explain the feature that is estimated from the observations.

6.1.6 Comparison with the Observations

We represented the results of the simulations for GJ 436b in several cases of the velocity dispersion. Here we discuss the comparison between the results of the simulations and the features of the observations in the UV transit (Ehrenreich et al., 2015), and the detailed analyses

of the observations (Bourrier et al., 2015). Key points for comparison with the observations are the mass-loss rate and the estimated radial velocity at the Roche radius of the GJ 436b. Figure 6.9 represents the dependence of the mass-loss rates on the velocity dispersion. Since the

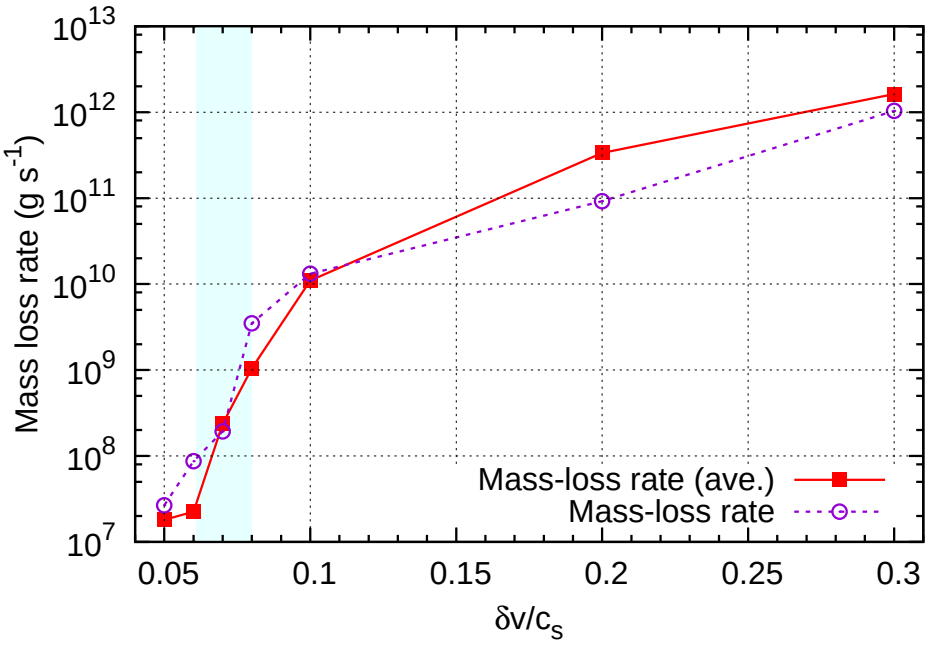

Figure 6.9: Dependence of the mass-loss rate on the value of the velocity dispersion at the surface. The horizontal axis is the velocity dispersion that is normalized by the sound speed at the surface, and the vertical axis is the mass-loss rate in units of $\mathrm{g\,s^{-1}}$. The red points and line denote the time-averaged mass-loss rate which is same as shown in Figure 6.3. The violet points and line denote the mass-loss rate when the radial velocity of the escaping atmosphere at the Roche radius of the planet becomes maximum value during the calculation time. The blue color-coded region corresponds to the range of the velocity dispersion that can obtain the consistent mass-loss rate with the observations.

mass-loss rates have the large time-variability as described in Section 6.1.4, we also show the mass-loss rate when the radial velocity at the Roche radius of the planet becomes the maximum value (violet points and line), for comparison.

According to Ehrenreich et al. (2015), the estimated value of the mass-loss rate of GJ 436b is $10^8 - 10^9\,\mathrm{g\,s^{-1}}$. The region highlighted by light blue is the range of the velocity dispersion that satisfies this estimated range of the mass-loss rate. In this region of the velocity dispersion, the mass-loss rate changes rapidly with the velocity dispersion, thus the allowed range of the velocity dispersion becomes narrow. As shown in the figure, the range of the velocity dispersion of $\sim 0.06 - 0.08 c_\mathrm{s}$ is favorable to explain the observed value of the mass-loss rate from GJ 436b.

Therefore, in terms of the mass-loss rate, it is expected that there is a certain level of the atmospheric turbulence at the surface that can generate the velocity dispersion of 6 - 8% of the sound speed. Hot Neptunes are thought to have strong atmospheric circulation (e.g., Lewis et al., 2010), therefore we believe that this strength of the turbulence can be generated.

Next we discuss the radial velocity of the escaping atmosphere. The radial velocity is observed directly through the blue shift of the absorption line of H Lyα during the transit in UV wavelength, and its value is $\gtrsim 100\,\mathrm{km\,s^{-1}}$ (Ehrenreich et al., 2015; Bourrier et al., 2015). This extremely fast escaping atmosphere in outer region of the exosphere might be explained by known acceleration mechanism such as charge exchange, but they also found that the fast radial velocity at the Roche radius of GJ 436b, $\sim 30\,\mathrm{km\,s^{-1}}$ is needed to explain the observed features (Bourrier et al., 2015). Additionally, they pointed out that such a fast radial velocity

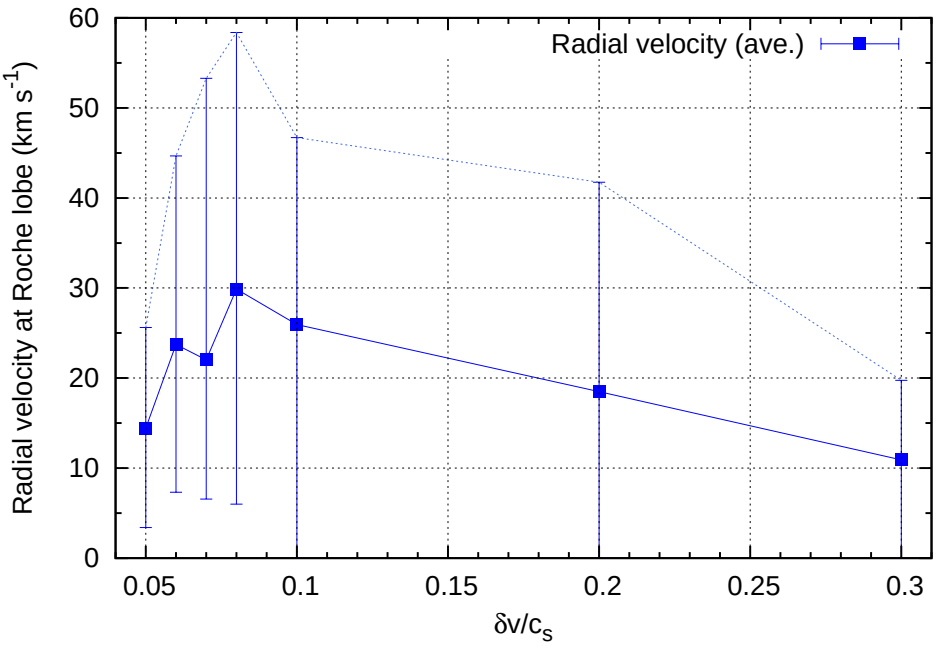

Figure 6.10: Dependence of the radial velocity at the Roche radius of the planet on the value of the velocity dispersion at the surface. The horizontal axis is the velocity dispersion that is normalized by the sound speed at the surface, and the vertical axis is the radial velocity at the Roche radius in units of $\mathrm{km\,s^{-1}}$. The blue points with error bars and line denote the time-averaged radial velocity. The error bars denotes the range of the radial velocity; the range between the minimum value and the maximum value during the simulation. The blue dotted line that connecting the upper ends of the error bars denotes the dependence of the maximum radial velocity at the Roche radius on the velocity dispersion at the planetary surface.

at the Roche radius cannot be explained by the existing models of thermosphere (Bourrier

et al., 2015). The magnetically driven mechanism we are proposing here can be a prospective mechanism for the acceleration of the escaping atmosphere. Figure 6.10 shows the dependence of the radial velocity at the Roche radius of the GJ 436b on the velocity dispersion. The blue square points correspond to the time-averaged radial velocity at the Roche radius as a function of the velocity dispersion. The error bars denote the range of the variation of the radial velocity during the simulations, and the blue dotted line corresponds to the maximum radial velocity at the Roche radius as a function of the velocity dispersion.

As mentioned in Section 6.1.2, the radial velocity at the Roche radius is an increasing function of the velocity dispersion when the velocity dispersion is small. When the velocity dispersion at the surface is too small, the amount of the energy injected to the magnetic field itself is small, so only the tiny amount of the energy can be converted to the kinetic energy of the gas. In addition, when the velocity dispersion is small, the gradient of the density profile becomes steep because the only small amount of the atmosphere can be uplifted, and thus the reflection of the MHD waves is enhanced. if the reflection of the MHD waves increases, the waves which can reach the upper atmosphere and contribute to the heating and acceleration of the atmosphere decrease, so the radial velocity is the increasing function of the velocity dispersion in this region. On the other hand, it becomes decreasing function of the velocity dispersion when the velocity dispersion is large. In this setup for GJ 436b, the radial velocity at the Roche radius has a maximum value $\sim 30\,\mathrm{km\,s^{-1}}$ at $\delta v \simeq 0.08 c_\mathrm{s}$. This is due to the denser upper atmosphere. When the velocity dispersion is larger and the amount of the energy injected to the magnetic fields is large enough, the uplifting of the upper atmosphere becomes efficient. It follows that the mass-loss rate increases with the velocity dispersion, but the denser upper atmosphere becomes hard to accelerate efficiently, thus the radial velocity decreases with the enhancement of the density of the upper atmosphere. The maximum radial velocity at the Roche radius also shares this feature. It is quite small (but exceeds the sound speed), and increases rapidly with the velocity dispersion at the surface when the velocity dispersion is small. Then it has a maximum value $\sim 60\,\mathrm{km\,s^{-1}}$ when $\delta v \simeq 0.08 c_\mathrm{s}$, and becomes decreasing function of the velocity dispersion.

In terms of the radial velocity at the Roche radius, only for the case of $\delta v = 0.08c$ can explain the fast radial velocity of $\sim 30\,\mathrm{km\,s^{-1}}$ when we consider the time-averaged radial velocity. However, as described in the previous sections, it has the large time-variability. According to Figure 6.10, the maximum velocity can exceed $30\,\mathrm{km\,s^{-1}}$ in the wide range of the velocity dispersion of $\sim 0.05 - 0.25 c_\mathrm{s}$. However, it is rare and only occurs as a short transient event

when the velocity dispersion is too small and large. For example, as shown in Figure 6.6, the radial velocity at the Roche radius do exceed $30\,\mathrm{km\,s^{-1}}$ when the case of $\delta v = 0.06 c_\mathrm{s}$, but the duration is short, and it rarely occurs. It is same for larger δv cases. As shown in Figure 6.8, the radial velocity can be faster then $30\,\mathrm{km\,s^{-1}}$ when $\delta v = 0.1 c_\mathrm{s}$ and $0.2 c_\mathrm{s}$, but the durations are also very short, and they occur rarely, in particular for the $\delta v = 0.2 c_\mathrm{s}$ case. Therefore, when the velocity dispersion is too small or large, the probability that the radial velocity at the Roche radius can be faster than $30\,\mathrm{km\,s^{-1}}$ is small. When the cases of $\delta v = 0.07 c_\mathrm{s}$ and $0.08 c_\mathrm{s}$, the durations of the radial velocity being faster than $30\,\mathrm{km\,s^{-1}}$ are long, and they occur frequently, that is shown in 6.7. Therefore, from the view point of the radial velocity at the Roche radius of GJ 436b, the favorable range of the velocity dispersion to explain the fast velocity that is estimated from the observations is $\sim 0.07 c_\mathrm{s}$ to $\sim 0.08 c_\mathrm{s}$. This range of the velocity dispersion is consistent with the constraint from the mass-loss rate of the GJ 436b.

For these reasons, it can be said that the magnetically driven atmospheric escape that we are proposing plays the important roles in the atmosphere of GJ 436b. We can explain both the observed mass-loss rate, and the radial velocity at the Roche radius of the planet which is estimated from the escaping model of the atmosphere (Bourrier et al., 2015). From these two aspects, we can constraint the value of the velocity dispersion at the planetary surface that is difficult to measure directly, and its range is around 7 - 8% of the sound speed at the surface. Furthermore, the time variation of the observed features that are reported by Bourrier et al. (2015) can also be explained by the large time-variability of the magnetically driven wind.

6.2 Observable Features of the Magnetically Driven Wind

The signatures of the atmospheric escape and extended upper atmosphere are observed through the transit in the UV wavelength in several exoplanets (e.g., Vidal-Madjar et al., 2003). Here we discuss the possibility to observe the outflow from exoplanets that is driven by the dissipation of the MHD waves and how to distinguish it from the other driving mechanisms of the atmospheric escape. It is thought that the most dominant mechanism of the atmospheric escape is the XUV-driven escape (e.g., Lammer et al., 2003). In the conditions of hot Jupiters, the mass-loss rate is expected to be comparable to $\sim 10^{10}\,\mathrm{g\,s^{-1}}$ or larger by the XUV-driven escape, and its value is consistent with the observations. However, the mass-loss rate by the magnetically driven outflow also can be the order of $\sim 10^{10}\,\mathrm{g\,s^{-1}}$ or larger, so it might be difficult to distinguish them by the mass-loss rate from hot Jupiters.

Other aspects, such as the time-variability might be possible to detect and can be a feature to distinguish the driving mechanisms of the atmospheric escape from hot Jupiters. The XUV-driven escape is limited by the XUV irradiation of the central star to the planet. If the XUV flux from host stars varies with time, the mass-loss rate driven by the stellar XUV should varies in response to it. For example, in the early stage of the stellar evolution, stars are generally active and emit strong X-ray, so the mass loss driven by the XUV irradiation is significantly large, and gaseous planets can lose their envelope in the early stage in some situations (e.g., Kurokawa and Nakamoto, 2014). In addition, not only the long term evolution of the XUV intensity, but also variation with short time-scale also exist, such as stellar flare, and stellar chromospheric and coronal activities. Therefore, if the variation of the mass-loss rate and/or the structure of the upper atmosphere are observed, and their variation is correlated with the stellar XUV activity, the variations should originate in the stellar XUV variation. However, if the central stars are quiet in XUV activity, and the variations of the mass-loss rate and/or the structure of the upper atmosphere do not correlate with the stellar activities, it is expected that the variations are caused by the magnetically driven outflow, and can be a collateral evidence of the magnetically driven atmospheric escape. Several observations of the transit in the UV band have been suggested that the existence of the time-variability of the transit depth in H Lyα (e.g., Lecavelier des Etangs et al., 2012). They reported that the detection of the transit of H Lyα was not detect in one observation, but it was detected in another timing of the transit. This difference suggests that the evaporation of the hydrogen has a large time-variability. Lecavelier des Etangs et al. (2012) argued the correlation between the variation of the mass-loss rate and activity of host star, but more detail observations and analyses might be needed.

In addition, our model predicts that a large amount of the mass-loss rate from exoplanets which are not irradiated strongly, such as warm Jupiters and warm Neptunes. The mass-loss rate by the XUV-driven escape strongly depends on the level of the XUV irradiation that the planet receives, thus the mass-loss rate from gaseous planets that are moderately irradiated is expected to be small in proportion to the XUV flux. Therefore, if gaseous planets that receive the moderate XUV irradiation have a large amount of the mass-loss rate, the magnetic activity in the planetary atmosphere may be playing the important role to drive the outflow from the planets. Furthermore, young gaseous planets, which have relatively high surface temperature and large radius, are candidate objects to apply our driving mechanism of the atmospheric escape. The young gaseous planets tend to have large entropy due to the accretion of the material during their formation stage. Although the detailed features of the

magnetic fields of the young gaseous planets such as the geometry and strength are unknown, the magnetically driven outflow can exist if the young gaseous planets have their own magnetic fields and certain level of the turbulence of the atmosphere. Recently these young gaseous planets have been discovered by the direct imaging in the optical and infrared wavelength. We hope that detailed observations of the young gaseous planets in a wide range of the wavelength will reveal the aspects of the atmospheric escape. In cool gaseous planets, such as Jupiter and Saturn, generation of the MHD waves and the heating and acceleration of the gas due to the dissipation of them occurs at least in principle. In this instance, our mechanism might be able to contribute as a heating mechanism in the upper atmosphere of cool gaseous planets, and can enhance the polar wind. However, more careful treatment of the radiative cooling and possibly strong non-ideal effects due to the quite low ionization degree are needed to apply our mechanism to the cool gaseous planets.

Of course the mass-loss rate and the atmospheric structure strongly depend on the value of the velocity dispersion at the planetary surface and the strength of the magnetic fields. The velocity dispersion will be generated by the atmospheric turbulence, and it will be caused by strong atmospheric circulation and/or the convection of the atmosphere. The strong atmospheric circulation is thought to be common for gaseous planets (e.g., Showman and Guillot, 2002; Cooper and Showman, 2005; Dobbs-Dixon and Lin, 2008; Lewis et al., 2010), so the turbulence should be excited at the surface. The strength of the magnetic fields depends on the internal structure and condition of planets, and weak constraints are obtained from observations (e.g., Kislyakova et al., 2014) As described in Section 6.1, it is possible to constrain the physical properties that are difficult to observe and measure directly, such as the value of the velocity dispersion, through the combination of the observations and theoretical assumption. Therefore, it is expected to predict unobservable physical properties through the features of the atmospheric escape and the upper atmospheric structure of exoplanets, by considering observed properties such as the radius, mass, semi-major axis and surface temperature. At any rate, the combinations of our model and other models for the atmosphere, and further observations are important for future investigations.

Additionally, observable features are affected by the geometry of the planetary magnetic fields. As described in Section 3.8, and Section 4.2 in Tanaka et al. (2015), bipolar outflows are expected from planets if the planets have a dipole magnetic field. In this condition, the heating and acceleration of the atmosphere only occur in the magnetic polar regions. Therefore, asymmetry of the geometry of the escaping atmosphere is expected depending on the

configuration of the magnetic fields and the line of sight of the system. This asymmetry will, in principle, appear as the asymmetry in the blueshift and redshift of the escaping atmosphere. Since the shift of the absorption lines is already observed (e.g., Vidal-Madjar et al., 2003), the asymmetry of them caused by the bipolar outflows can be detected in the future high precision observations.

6.3 Possible Impacts on the Current Properties and Long-Term Evolution of Exoplanets

6.3.1 Relations to Surface Environment and Internal Structures

Observations of the atmospheres are important ways to make diagnoses of the properties of exoplanets. One cannot observe directly the inside of exoplanets, but information of the atmosphere can be obtained from observation, such as transit spectroscopy in wide range of the wavelength, and direct imaging of exoplanets. Physical properties of the atmosphere which we can know from observations might be related with other properties which we cannot observe directly.

As we described in Section 6.1.6, for example, we can give a constraint on the range of the value of the velocity dispersion at the planetary surface through the comparison of the observed features of the atmospheric escape and theoretical assumption. The strong atmospheric circulation in hot Jupiters and hot Neptunes are theoretically predicted by a number of the multi-dimensional hydrodynamic simulations (e.g., Showman and Guillot, 2002). Recently several observations show the consistent results with the theoretical prediction that the existence of strong eastward equatorial jets in hot Jupiters (Snellen et al., 2010; Wyttenbach et al., 2015; Louden and Wheatley, 2015). These observed features should be strongly related with the velocity dispersion of the atmosphere, because it is expected that this strong equatorial circulation may generate the turbulence in the atmosphere. Our model suggests that there is the strong relation between the mass-loss rate and the value of the velocity dispersion at the surface (Tanaka et al., 2014, 2015). Therefore, we can constraint the surface environment such as the turbulence of the atmosphere, from the features of the atmospheric escape of the planet.

In addition, the properties of the atmospheric escape that is driven by the dissipation of the MHD waves depend on the strength of the magnetic field. We have shown that the mass-loss rate is the decreasing function of the strength of the planetary magnetic field in Section 2.5. Therefore, the properties of the atmospheric escape can be one of the tool to presume the

properties of the magnetic fields of exoplanets. The characteristics of the planetary magnetic fields are thought to be strongly related to the internal structure and activity of planets, thus we might be able to investigate the unseen properties of the inside of exoplanets through the features of the atmospheric escape.

6.3.2 Long-Term Evolution of Exoplanets and Systems

The mass of a planet decreases with the continual atmospheric escape. In the early stage of the stellar evolution, the XUV irradiation from host stars to close-in gaseous planets is several orders of magnitude larger than the later stage, so the huge amount of the atmospheric escape that is driven by the XUV is expected. Therefore, young and light gaseous planets can lose almost all of their gaseous envelope in the early stage of the evolution in some cases, and will disappear or remain only their solid cores (e.g., Kurokawa and Nakamoto, 2014). After the early stage, the XUV emission from central stars becomes weaker, so the resultant mass-loss rate by the XUV-driven escape also becomes smaller than the early stage. The amount of the mass-loss rate that is estimated from several observations, $\sim 10^{10}\,\mathrm{g\,s^{-1}}$ is quite large, but it is small compared with the mass of the planet itself. This value corresponds to $\sim 1.66 \times 10^{-13}\,M_{\mathrm{J}}$ per year, so only $\sim 0.166\%$ of its mass are lost during 10 Gyrs. This mass-loss rate is too small to lose the entire envelope of gaseous planets during the lifetime of the main-sequence of the host stars.

However, we have shown that the mass-loss rate strongly depends on the properties of gaseous planets. For example, if the value of the velocity dispersion at the planetary surface is large, the mass-loss rate becomes several orders of magnitude large. Also, the mass and radius are the important aspects to control the mass-loss rate. Therefore, a gaseous planet that has small mass and large radius, and a large value of the velocity dispersion, will have a significantly large mass-loss rate. In this case, the loss of the entire envelope of the gaseous planet can occur not only in the early stage when the XUV irradiation is strong enough, but also the later stage when the XUV irradiation becomes more moderate than the early stage. This kind of the long-term evolution of the gaseous planets can affect the population and size distribution of the detected exoplanets (e.g., Jin et al., 2014). In addition, the evolution of the radius of gaseous planets also strongly affects the atmospheric escape and the fate of gaseous planets. The radii of gaseous planets are large just after the formation because of the heating by the accretion of the material, and then shrink with the cooling. It is proposed that the radius of gaseous planets can be re-inflated when their host stars evolve into the post main-

sequence such as the sub-giant phase and red giant branch phase, because the irradiation that is received by gaseous planets increases with the expansion of the central stars (Lopez and Fortney, 2015). Lopez and Fortney (2015) pointed out that the re-inflation depends on the heating mechanism of the interior of the gaseous planet, and if the heating rate at the deep interior is large, gaseous planets can be re-inflated in shorter timescale than the lifetime of the sub-giant phase and the red giant branch phase. In this situation, the atmospheric escape from the planets will be enhanced due to the higher level of the irradiation than that of the period of the main-sequence, and low surface gravity caused by the large radius. Therefore, a huge amount of mass-loss rate that is driven by the magnetic activity in the planetary atmosphere can affect the evolution of the planet in the later stage of the systems.

The atmospheric escape also affects the orbital configuration and the status of the rotation of exoplanets. The large amount of the escaping atmosphere can remove the orbital angular momentum of the planet in some cases. The possibility of the migration of the orbit of close-in planets that is caused by the removal of the orbital angular momentum by the atmospheric escape is argued in several theoretical studies (Gu et al., 2003; Chang et al., 2010). The migration rate depends on the mass-loss rate and its geometry, so the detailed properties of the atmospheric escape can affect the migration of close-in planets. Additionally, the removal of the angular momentum of the rotation of a planet also occur by the escaping atmosphere. If these effects are significant, they also affect the population of the exoplanets in particular the distribution of the semi-major axis. Furthermore, they are also important for formation and evolution scenarios of planetary systems and exoplanets. The atmospheric escape not only affects the planet itself but also affects the properties of the host stars. Signatures of the accretion from a close-in gaseous planet to the host star is observed as a excess in far ultraviolet emission (Pillitteri et al., 2015), therefore the transport of the angular momentum can be done through the atmospheric escape from close-in planets and subsequent accretion onto the host stars. In order to investigate these effects, more detailed studies are needed to estimate these effect.

Chapter 7

Summary and Future Prospects

7.1 Summary

The atmospheric escape is one of the important observable features of exoplanets. Several observations in the UV band have been revealed that the signatures of the ongoing atmospheric escape from hot Jupiters and Neptunes, and their surprisingly large extended upper atmospheres. It is thought that the heating of the upper atmosphere by the X-ray and extreme ultraviolet irradiation from host stars is a promising driving mechanism of the atmospheric escape from close-in planets. However, the dissipation of the MHD waves in the upper atmosphere should be considered as a mechanism to drive the atmospheric escape from gaseous planets.

We have performed MHD simulations in the atmosphere of hot Jupiters to show the possibility of the magnetically driven outflow, and then developed our simulation in several ways. First, we performed the ideal MHD simulations in the atmosphere of hot Jupiters (Tanaka et al., 2014). If planets have magnetic fields, and there is turbulence at the surface, MHD waves can be excited. The MHD waves propagate upward along with the magnetic field lines, and dissipate in the upper atmosphere. Subsequently, the dissipation of the MHD wave energy causes the heating of the upper atmospheric gas and acceleration of the gas. Therefore, the temperature of the upper atmosphere becomes quite high, and supersonic outflows are driven from the upper atmosphere. When we assumed the parameters which are thought to be typical for hot Jupiters, the resultant mass-loss rate became $\sim 10^{10}\,\mathrm{g\,s^{-1}}$, which is consistent with the estimated value from the observations of hot Jupiters, such as HD 209458b and HD 189733b, and the value is comparable to that is expected by the XUV-driven escape.

We also did a parameter study of the mass-loss rate. We treated the value of the velocity

dispersion at the planetary surface, radius, and mass of planets as the free parameters to investigate how the mass-loss rate depends on these physical parameters. We showed that the mass-loss rate strongly depends on the velocity dispersion when the velocity dispersion is small, and the dependence becomes relatively weaker in higher velocity dispersion region. The mass-loss rate also strongly depends on the radius and mass of planets, and its dependence can be scaled by the pressure scale height of the atmosphere. In addition, we studied the time-variability of the mass-loss rate, and the dependence on the strength of the magnetic fields.

Second, we included effects of magnetic diffusion in our simulations. The atmosphere of hot Jupiters is expected to be weakly-ionized, and in a such conditions, non-ideal effects will play an important role in diffusion of the MHD waves. In order to examine this we performed non-ideal MHD simulations, and showed the magnetic diffusion strongly affects the atmospheric structure and the properties of the atmospheric escape. We evaluated the transport of the energy by the Alfvén waves in the weakly-ionized atmosphere and discovered the two regimes of the Poynting flux; the net outgoing energy decreases as the increase of the surface temperature until a certain critical temperature, and increases above the critical temperature. This strange trend is caused by the complicated behavior of the magnetic resistivity and the planetary scale height, and these two properties control the amount of the energy that diffuse out in the atmosphere. We also evaluated the effect of the ohmic heating in the atmosphere and showed the ohmic heating rate can be comparable to the ideal MHD heating in the lower atmosphere, but it barely affects the entire structure of the atmosphere and the mass-loss rate.

Next, we improved our treatment of the radiative cooling of the ideal MHD simulations by using radiative transfer. We used modified Unno-Kondo method (Unno and Kondo, 1976; Unno, 1989; Hashimoto, 1995) that is originally developed for the radiative transfer in the outer envelope of AGB stars. By the installation of the new cooling and heating rates of the atmosphere that are derived by the modified Unno-Kondo method, we showed that the previous cooling rate was about two orders of magnitude overestimated in the lowest region of the atmosphere, and about four orders of magnitude underestimated in the upper atmosphere. Because of this correction of the radiative cooling rate, the mass-loss rate became one to two orders of magnitude larger when the velocity dispersion at the surface is small.

We also investigated the parameter dependence of the mass-loss rate, and similar dependences was obtained. In addition, we studied the time-variability of the mass-loss rate. In these calculations, durations of the variation and the amplitude of the variation of the mass-

loss rates became smaller than the previous calculations, but they are still significant, and will be characteristics of the magnetically driven outflows.

Finally, we further improve the treatment of the radiative transfer in the atmosphere by using the two-stream approximation. In these calculations, behaviors of the dependence of the mass-loss rate and atmospheric structure are almost same with the results that the modified Unno-Kondo method is used. We showed that the radiative cooling rates in the new method and the modified Unno-Kondo method are almost same, but differs slightly in the lower atmosphere when the velocity dispersion at the planetary surface is large. Same as the previous analyses, we investigated in detail the parameter dependence of the mass-loss rate and atmospheric structures, and the time-variability of them.

The atmospheric escape is also important for small planets like hot and warm Neptunes. We applied our driving mechanism of atmospheric escape to the hot Neptune, GJ 436b, and we demonstrate that the acceleration of the escaping atmosphere by the dissipation of the MHD waves plays an important role in this planet. The magnetically driven outflow can explain the estimated radial velocity of the escaping atmosphere at the Roche radius of GJ 436b. In addition, we found that the velocity dispersion of 7 - 8% of the sound speed at the surface is a favorable value to explain the observed mass-loss rate and the radial velocity at the Roche radius. Therefore, we can constraint the unseen physical properties through the combination of the observation of the features of the atmospheric escape and theoretical assumption in this way.

In the condition of typical hot Jupiters, both the XUV-driven escape and magnetically driven escape will be important mechanism of the atmospheric escape. In order to distinguish them, observations of the time-variability of the mass-loss rate that is not correlated with the stellar XUV activity is expected to be a promising way. Furthermore, the magnetically driven wind can be valid in the condition where the XUV-driven is not expected due to the low level of the XUV irradiation, if the velocity dispersion is large enough to generate the MHD waves. Therefore, we emphasize that the roles of the dissipation of the MHD waves in the planetary atmosphere are considerably important, and it should be taken into account to treat the atmospheric escape ant structure of the upper atmosphere.

7.2 Future Prospects

7.2.1 Further Improvement of the Radiative Transfer

In Chapter 5, we performed the ideal MHD simulation with the new radiative cooling rate by using the two-stream approximation. In the calculations, we assumed the grey atmosphere that is no wavelength dependence of the emission and absorption for simplicity. In reality, wavelength dependence will be especially important for cooler atmosphere, because of the appearance of the line cooling by various kinds of molecules. The detailed treatment of the wavelength dependence of the radiative transfer to determine the radiative cooling and heating rates might be critically important when we extend our model to cooler gaseous planets. Therefore, wavelength-dependent treatment of the radiative transfer in the MHD simulations is one of the important future tasks. Also, irradiation from a host star is not included at the current stage for simplicity. The modified Unno-Kondo method cannot include the irradiation from the outer boundary because of the approximation in the formulation, but the two-stream approximation can include the incoming intensity from the outer boundary. Thus this point is also our future task to improve our calculations.

Additionally, increasing the number of the stream is a possible improvement of our calculations. The two-stream approximation is the method that the direction of the intensity is divided into only two directions, the upward and downward components. This approximation seems to be crude but works well, but more accurate approximation is possible to treat multi-stream of the radiation. If we divide the direction in several components, the improvement of the treatment of the radiative transfer will be achieved.

7.2.2 Combination with the XUV-driven Escape

As described in Section 1.3.2, it is thought that the heating of the upper atmosphere by the strong X-ray and extreme ultraviolet from the host star is the plausible mechanism of the atmospheric escape from close-in planets. However, we have showed that the mass-loss rate that is driven by the dissipation of the MHD waves in the upper atmosphere becomes comparable or larger than that driven by the XUV irradiation. Therefore, it is important to combine the effect of the XUV irradiation with our MHD simulations. Both the XUV irradiation and dissipation of the MHD waves strongly affect the structure of the upper atmosphere, and resultant mass-loss rate. By the combination of both driving mechanisms, we can evaluate the effects of both mechanisms and its parameter dependence. In addition, if there are variation of the XUV flux

caused by the stellar activity such as flare and chromospheric and coronal activity, it is expected that the mass-loss rate also varies with the XUV irradiation. By evaluating the difference of the variation of mass-loss rate caused by the XUV variation and the variation caused by the magnetically driven atmospheric escape, it may be possible to determine which mechanism is operating in real objects.

It will also be possible to investigate the change of the regime of the atmospheric escape in different stages of the stellar evolution. In the early stage of the stellar evolution, the XUV radiation of stars are several orders of magnitude larger than the later main-sequence stage. In that situation, the XUV-driven escape and in some cases the Roche lobe overflow of the envelope are important, and can dominate over the magnetically driven atmospheric escape. In the middle stage of the stellar evolution, the XUV radiation of stars becomes relatively moderate, and the atmospheric escape driven by the XUV heating and the dissipation of the MHD waves can become comparable, depending on the irradiation level of the XUV. In the later stage of the stellar evolution, the magnetically driven atmospheric escape can dominate over the XUV-driven escape, because evolved stars are weak in the XUV radiation, and the subsequent mass-loss rate driven by XUV heating will become small. Therefore, there can be several regimes of the atmospheric escape in which one driving mechanism dominates over another, and/or become comparable.

7.2.3 Non-Ideal MHD Calculation and Effects of Dust Grains

We performed the non-ideal MHD simulations and showed their results in Chapter 3. The non-ideal effect, the ohmic dissipation, is quite important for propagating, reflection, and diffusion of the MHD waves in the weakly-ionized atmosphere, and complicated behavior of the energy transport by Alfvén waves. In Chapter 4 and 5, we assumed the ideal MHD approximation, so the inclusion of the non-ideal effect into the new calculation is needed for more realistic calculations. Since both the non-ideal effect and improvement of the treatment of the radiative cooling and heating rates strongly affect the resultant characteristics of the atmospheric escape and atmospheric structure, combination of the non-ideal effect with our new calculation is needed.

In terms of the non-ideal calculations, the determination of the ionization state in the atmosphere is critically important. In the condition of the atmosphere of typical hot Jupiters, the thermal ionization of the alkali metals is a main source of the ions. In this condition, dust grains will play an important role to control the ionization degree, thus the calculation of

the ionization degree that takes into account the effects of dust grains is needed. Our model solves the time-dependent basic MHD equations, so less time-consuming methods to determine the ionization state are needed. One example is the method by Fujii et al. (2011), which was developed to calculate the ionization state fast in protoplanetary and circumplanetary disks. Therefore, adopting their method to our simulation will allow us to investigate the behavior of the MHD waves and resultant atmospheric escape and atmospheric structure in dusty conditions.

Also, the existence or absent of the many components of cloud have been investigated thought both the theoretically and observationally (e.g., Fortney et al., 2005). These clouds affect the atmospheric structure, and may also affect physical properties of the atmosphere such as ionization degree. Therefore, effects of the existence of the cloud might be also important.

7.2.4 Transport of Dust Grains by Planetary Winds

The atmospheric escape from close-in gaseous planets is the hydrodynamic escape, so not only the hydrogen but also heavier elements can escape with the hydrogen. As mentioned in the introduction section, these heavier species are detected in the escaping atmosphere thought the transit observation in the UV wavelength. In addition to these heavier elements, it may be possible that dust grains, if they exist around the acceleration altitude of the outflow, can also be transported by the strong atmospheric escape. Of course it strongly depends on the dragging force onto the dust grains, but it have been shown that, in protoplanetary disks, the dust grains can be transported to high altitude and fly away from the disks in some situations by the disk winds that is driven by the MHD waves (Miyake et al., 2015). The dust grains will settle to the lower altitude in the quiet atmosphere, but if the atmospheric motion is active, for example the existence of the strong atmospheric circulation and the convection, the dust grain can diffuse and spread to the higher altitude. If the dust grains get around to the acceleration region of the outflow, then they are blowed off by the fast radial flow of the atmosphere, depending on the dragging force onto the dust grains. This phenomena can occur regardless of the acceleration mechanisms of the atmospheric escape, but it is particularly interesting in the magnetically driven winds because the winds have the significantly large time-variation in the atmospheric structure, for example the variability of the radial velocity. Of course, the temperature of the upper atmosphere becomes quite high in the both driving mechanisms, thus the dust grains will melt away and evaporate in the upper atmosphere depending on conditions such as timescales of the evaporation of the dust and transport of the dust. Therefore, careful assumption of these

properties that may depends on the temperature, and density in the upper atmosphere, and the composition and physical properties of the dust grains.

If the amount of the transported dust grains is huge, it is interesting because the presence of the enough amount of the dust grains in the upper atmosphere or surrounding region of planets can affect the observational features in the optical and infrared wavelength. The features of the atmospheric escape and extended upper atmospheres have been investigated mainly by the observations in the UV wavelength, and sometimes in the X-ray. If the atmospheric escape and upper atmosphere affect the features in the optical and infrared, it will be interesting target to detect the time-variation of the transmission and reflection spectra of planetary atmospheres.

7.2.5 Application to Other Types of Planets

In terms of the magnetically driven outflows from the atmosphere, the presence of the planetary magnetic fields and the velocity dispersion caused by the atmospheric turbulence is important. Therefore, it can occur not only hot Jupiters but also at other types of planets. One example of possible applications is young terrestrial planets that have magma ocean and high-temperature atmosphere. At the present day of the Earth, atmospheric escape driven by the MHD waves does not occur because of the physical conditions, for example the low temperature and neutral atmosphere. However, in the early stage of the rocky planets during or just after the formation, the surface and atmospheric temperature are thought to be very high because of the accretion of a huge amount of planetesimals. In this condition, the planets are expected to have magma ocean on their surface. Because the surface temperature is significantly high, strong atmospheric convection may occur in the atmosphere. In addition, the high temperature will cause the ionization of the species that have relatively lower ionization energy, and they become ionization sources in the atmosphere. Therefore, if the planets have their own magnetic fields, the MHD waves are excited by the turbulence in the high-temperature atmosphere, and the magnetically driven outflows can take place (Figure 7.1).

There are several large uncertainties on this scenario. For example, it is unknown that the existence and properties of strong magnetic fields at young terrestrial planets. If the dynamo action in the interior of a young rocky planet does not develop yet, it is unclear that the planet has magnetic fields or not. The physical properties of the atmosphere of young terrestrial planets are also uncertain, but it is natural to assume the strong turbulence because the large thermal source, the magma ocean exists. The largest uncertainty would be the composition of the atmosphere and the validity of the MHD in that atmosphere. We assumed the composition

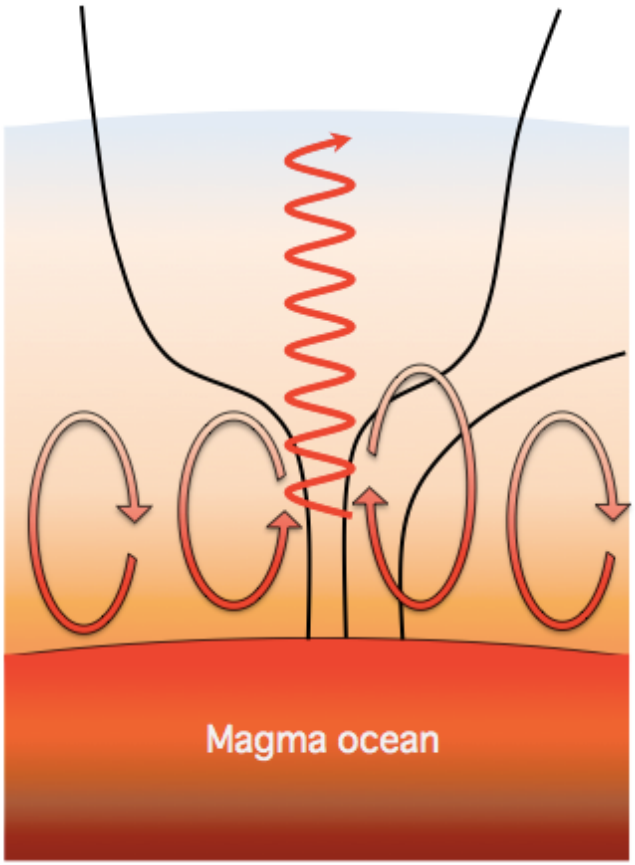

Figure 7.1: A schematic view of the magnetically driven atmospheric escape from a young terrestrial planet that has magma ocean. Black lines correspond to the planetary magnetic field lines.

that is thought to be typical for hot Jupiters. However, the atmospheres of young terrestrial planets contain much heavier elements, such as minerals in the vapor phase. The primordial atmospheres of the terrestrial planets are mixture of the light elements such as hydrogen and helium, and the heavier elements. Therefore, careful assumption of the composition of the atmosphere and the evaluation of the validity of the MHD in such atmospheres will be needed.

Although there are several uncertainty in the scenario, it will affect the evolution of the atmosphere in the early stage of the evolution, if the magnetically driven atmospheric escape is valid. The composition and the evolution of the primordial atmosphere of terrestrial planets, including the Earth, is one of interesting and important problems. The primordial atmosphere that contains a large amount of light species such as hydrogen and helium that came from the protoplanetary disk, is thought to be lost by the hydrodynamic escape. If the magnetically driven atmospheric escape enhance the hydrodynamic escape from the young Earth, the

assumption of the properties of the primordial atmosphere and its escape may be changed. Therefore, it is important for the current situation of the Earth, and also for other terrestrial planets.

In addition, rocky planets that have extremely small orbital separations have been detected recently, such as CoRoT-7b (Léger et al., 2009), and Kepler-10b (Batalha et al., 2011), and such kind of planets are thought to have a silicate atmosphere and magma ocean (Schaefer and Fegley, 2009). Same as the case for the primordial atmosphere of terrestrial planets, the metallicity of the atmosphere is significantly different from typical gaseous planets. It is interesting to apply our model to this type of planets and evaluate the mass loss of metal-rich atmospheres.

Acknowledgement

First, I would like to extend my deepest appreciation to my supervisor, Shu-ichiro Inutsuka, for giving me fruitful guidance for my research during the course of my study. Also I would like to express my appreciation to Takeru K. Suzuki, for providing me the numerical code and many comments and suggestions on the numerical simulations. I am grateful to Hiroshi Kobayashi for giving me beneficial comments and advice for my research activities. I would like to thank Christiane Helling, my supervisor in University of St Andrews, for giving me the opportunity to stay University of St Andrews as a visiting PhD student, and giving me fruitful advice to improve my research. I am really thankful to Jennifer M. Stone, Hiroyuki Kurokawa, Yuri I. Fujii, Sanemichi Z. Takahashi, and Masanobu Kunitomo, for valuable discussions, and helpings in various situations. I also thank Graham Harper for providing a useful code to calculate ionization degree in the atmospheric gas.

References

F. C. Adams. Magnetically Controlled Outflows from Hot Jupiters. *ApJ*, 730:27, March 2011. doi: 10.1088/0004-637X/730/1/27.

E. Anders and N. Grevesse. Abundances of the elements - Meteoritic and solar. *Geochimica et Cosmochimica Acta*, 53:197–214, January 1989. doi: 10.1016/0016-7037(89)90286-X.

L. S. Anderson and R. G. Athay. Chromospheric and coronal heating. *ApJ*, 336:1089–1091, January 1989a. doi: 10.1086/167078.

L. S. Anderson and R. G. Athay. Model solar chromosphere with prescribed heating. *ApJ*, 346: 1010–1018, November 1989b. doi: 10.1086/168083.

I. Baraffe, F. Selsis, G. Chabrier, T. S. Barman, F. Allard, P. H. Hauschildt, and H. Lammer. The effect of evaporation on the evolution of close-in giant planets. *A&A*, 419:L13–L16, May 2004. doi: 10.1051/0004-6361:20040129.

N. M. Batalha, W. J. Borucki, S. T. Bryson, L. A. Buchhave, D. A. Caldwell, J. Christensen-Dalsgaard, D. Ciardi, E. W. Dunham, F. Fressin, T. N. Gautier, III, R. L. Gilliland, M. R. Haas, S. B. Howell, J. M. Jenkins, H. Kjeldsen, D. G. Koch, D. W. Latham, J. J. Lissauer, G. W. Marcy, J. F. Rowe, D. D. Sasselov, S. Seager, J. H. Steffen, G. Torres, G. S. Basri, T. M. Brown, D. Charbonneau, J. Christiansen, B. Clarke, W. D. Cochran, A. Dupree, D. C. Fabrycky, D. Fischer, E. B. Ford, J. Fortney, F. R. Girouard, M. J. Holman, J. Johnson, H. Isaacson, T. C. Klaus, P. Machalek, A. V. Moorehead, R. C. Morehead, D. Ragozzine, P. Tenenbaum, J. Twicken, S. Quinn, J. VanCleve, L. M. Walkowicz, W. F. Welsh, E. Devore, and A. Gould. Kepler's First Rocky Planet: Kepler-10b. *ApJ*, 729:27, March 2011. doi: 10.1088/0004-637X/729/1/27.

K. Batygin, D. J. Stevenson, and P. H. Bodenheimer. Evolution of Ohmically Heated Hot Jupiters. *ApJ*, 738:1, September 2011. doi: 10.1088/0004-637X/738/1/1.

J. L. Bean, G. F. Benedict, D. Charbonneau, D. Homeier, D. C. Taylor, B. McArthur, A. Seifahrt, S. Dreizler, and A. Reiners. A Hubble Space Telescope transit light curve for GJ 436b. *A&A*, 486:1039–1046, August 2008. doi: 10.1051/0004-6361:200810013.

J. L. Bean, E. Miller-Ricci Kempton, and D. Homeier. A ground-based transmission spectrum of the super-Earth exoplanet GJ 1214b. *Nature*, 468:669–672, December 2010. doi: 10.1038/nature09596.

L. Ben-Jaffel and G. E. Ballester. Hubble Space Telescope detection of oxygen in the atmosphere of exoplanet HD 189733b. *A&A*, 553:A52, May 2013. doi: 10.1051/0004-6361/201221014.

L. Ben-Jaffel and S. Sona Hosseini. On the Existence of Energetic Atoms in the Upper Atmosphere of Exoplanet HD209458b. *ApJ*, 709:1284–1296, February 2010. doi: 10.1088/0004-637X/709/2/1284.

O. M. Blaes and S. A. Balbus. Local shear instabilities in weakly ionized, weakly magnetized disks. *ApJ*, 421:163–177, January 1994. doi: 10.1086/173634.

W. J. Borucki, D. Koch, G. Basri, N. Batalha, T. Brown, D. Caldwell, J. Caldwell, J. Christensen-Dalsgaard, W. D. Cochran, E. DeVore, E. W. Dunham, A. K. Dupree, T. N. Gautier, J. C. Geary, R. Gilliland, A. Gould, S. B. Howell, J. M. Jenkins, Y. Kondo, D. W. Latham, G. W. Marcy, S. Meibom, H. Kjeldsen, J. J. Lissauer, D. G. Monet, D. Morrison, D. Sasselov, J. Tarter, A. Boss, D. Brownlee, T. Owen, D. Buzasi, D. Charbonneau, L. Doyle, J. Fortney, E. B. Ford, M. J. Holman, S. Seager, J. H. Steffen, W. F. Welsh, J. Rowe, H. Anderson, L. Buchhave, D. Ciardi, L. Walkowicz, W. Sherry, E. Horch, H. Isaacson, M. E. Everett, D. Fischer, G. Torres, J. A. Johnson, M. Endl, P. MacQueen, S. T. Bryson, J. Dotson, M. Haas, J. Kolodziejczak, J. Van Cleve, H. Chandrasekaran, J. D. Twicken, E. V. Quintana, B. D. Clarke, C. Allen, J. Li, H. Wu, P. Tenenbaum, E. Verner, F. Bruhweiler, J. Barnes, and A. Prsa. Kepler Planet-Detection Mission: Introduction and First Results. *Science*, 327:977–, February 2010. doi: 10.1126/science.1185402.

V. Bourrier and A. Lecavelier des Etangs. 3D model of hydrogen atmospheric escape from HD 209458b and HD 189733b: radiative blow-out and stellar wind interactions. *A&A*, 557:A124, September 2013. doi: 10.1051/0004-6361/201321551.

V. Bourrier, A. Lecavelier des Etangs, and A. Vidal-Madjar. The Mg i line: a new probe of the

atmospheres of evaporating exoplanets. *A&A*, 573:A11, January 2015. doi: 10.1051/0004-6361/201323266.

J. Budaj. Light-curve analysis of KIC 12557548b: an extrasolar planet with a comet-like tail. *A&A*, 557:A72, September 2013. doi: 10.1051/0004-6361/201220260.

A. Burrows, D. Sudarsky, and W. B. Hubbard. A Theory for the Radius of the Transiting Giant Planet HD 209458b. *ApJ*, 594:545–551, September 2003. doi: 10.1086/376897.

A. Burrows, I. Hubeny, J. Budaj, H. A. Knutson, and D. Charbonneau. Theoretical Spectral Models of the Planet HD 209458b with a Thermal Inversion and Water Emission Bands. *ApJL*, 668:L171–L174, October 2007. doi: 10.1086/522834.

R. P. Butler, S. S. Vogt, G. W. Marcy, D. A. Fischer, J. T. Wright, G. W. Henry, G. Laughlin, and J. J. Lissauer. A Neptune-Mass Planet Orbiting the Nearby M Dwarf GJ 436. *ApJ*, 617: 580–588, December 2004. doi: 10.1086/425173.

J. M. Chadney, M. Galand, Y. C. Unruh, T. T. Koskinen, and J. Sanz-Forcada. XUV-driven mass loss from extrasolar giant planets orbiting active stars. *Icarus*, 250:357–367, April 2015. doi: 10.1016/j.icarus.2014.12.012.

S.-H. Chang, P.-G. Gu, and P. H. Bodenheimer. Tidal and Magnetic Interactions Between a Hot Jupiter and its Host Star in the Magnetospheric Cavity of a Protoplanetary Disk. *ApJ*, 708:1692–1702, January 2010. doi: 10.1088/0004-637X/708/2/1692.

D. Charbonneau, T. M. Brown, D. W. Latham, and M. Mayor. Detection of Planetary Transits Across a Sun-like Star. *ApJL*, 529:L45–L48, January 2000. doi: 10.1086/312457.

D. Charbonneau, T. M. Brown, R. W. Noyes, and R. L. Gilliland. Detection of an Extrasolar Planet Atmosphere. *ApJ*, 568:377–384, March 2002. doi: 10.1086/338770.

A. R. Choudhuri, M. Schussler, and M. Dikpati. The solar dynamo with meridional circulation. *A&A*, 303:L29, November 1995.

U. R. Christensen, V. Holzwarth, and A. Reiners. Energy flux determines magnetic field strength of planets and stars. *Nature*, 457:167–169, January 2009. doi: 10.1038/nature07626.

C. S. Cooper and A. P. Showman. Dynamic Meteorology at the Photosphere of HD 209458b. *ApJL*, 629:L45–L48, August 2005. doi: 10.1086/444354.

S. R. Cranmer and S. H. Saar. Testing a Predictive Theoretical Model for the Mass Loss Rates of Cool Stars. *ApJ*, 741:54, November 2011. doi: 10.1088/0004-637X/741/1/54.

S. R. Cranmer, A. A. van Ballegooijen, and R. J. Edgar. Self-consistent Coronal Heating and Solar Wind Acceleration from Anisotropic Magnetohydrodynamic Turbulence. *ApJS*, 171: 520–551, August 2007. doi: 10.1086/518001.

D. Deming, J. Harrington, G. Laughlin, S. Seager, S. B. Navarro, W. C. Bowman, and K. Horning. Spitzer Transit and Secondary Eclipse Photometry of GJ 436b. *ApJL*, 667:L199–L202, October 2007. doi: 10.1086/522496.

B.-O. Demory and S. Seager. Lack of Inflated Radii for Kepler Giant Planet Candidates Receiving Modest Stellar Irradiation. *ApJS*, 197:12, November 2011. doi: 10.1088/0067-0049/197/1/12.

J.-M. Désert, A. Lecavelier des Etangs, G. Hébrard, D. K. Sing, D. Ehrenreich, R. Ferlet, and A. Vidal-Madjar. Search for Carbon Monoxide in the Atmosphere of the Transiting Exoplanet HD 189733b. *ApJ*, 699:478–485, July 2009. doi: 10.1088/0004-637X/699/1/478.

J.-M. Désert, D. Sing, A. Vidal-Madjar, G. Hébrard, D. Ehrenreich, A. Lecavelier Des Etangs, V. Parmentier, R. Ferlet, and G. W. Henry. Transit spectrophotometry of the exoplanet HD 189733b. II. New Spitzer observations at 3.6 μm. *A&A*, 526:A12, February 2011. doi: 10.1051/0004-6361/200913093.

H. Diamond-Lowe, K. B. Stevenson, J. L. Bean, M. R. Line, and J. J. Fortney. New Analysis Indicates No Thermal Inversion in the Atmosphere of HD 209458b. *ApJ*, 796:66, November 2014. doi: 10.1088/0004-637X/796/1/66.

I. Dobbs-Dixon and D. N. C. Lin. Atmospheric Dynamics of Short-Period Extrasolar Gas Giant Planets. I. Dependence of Nightside Temperature on Opacity. *ApJ*, 673:513–525, January 2008. doi: 10.1086/523786.

H. J. Durand-Manterola. Dipolar magnetic moment of the bodies of the solar system and the Hot Jupiters. *P&SS*, 57:1405–1411, October 2009. doi: 10.1016/j.pss.2009.06.024.

D. Ehrenreich, V. Bourrier, X. Bonfils, A. Lecavelier des Etangs, G. Hébrard, D. K. Sing, P. J. Wheatley, A. Vidal-Madjar, X. Delfosse, S. Udry, T. Forveille, and C. Moutou. Hint

of a transiting extended atmosphere on 55 Cancri b. *A&A*, 547:A18, November 2012. doi: 10.1051/0004-6361/201219981.

D. Ehrenreich, V. Bourrier, P. J. Wheatley, A. L. Des Etangs, G. Hébrard, S. Udry, X. Bonfils, X. Delfosse, J.-M. Désert, D. K. Sing, and A. Vidal-Madjar. A giant comet-like cloud of hydrogen escaping the warm Neptune-mass exoplanet GJ 436b. *Nature*, 522:459–461, June 2015. doi: 10.1038/nature14501.

A. Ekenbäck, M. Holmström, P. Wurz, J.-M. Grießmeier, H. Lammer, F. Selsis, and T. Penz. Energetic Neutral Atoms Around HD 209458b: Estimations of Magnetospheric Properties. *ApJ*, 709:670–679, February 2010. doi: 10.1088/0004-637X/709/2/670.

N. V. Erkaev, Y. N. Kulikov, H. Lammer, F. Selsis, D. Langmayr, G. F. Jaritz, and H. K. Biernat. Roche lobe effects on the atmospheric loss from "Hot Jupiters". *A&A*, 472:329–334, September 2007. doi: 10.1051/0004-6361:20066929.

J. J. Fortney, M. S. Marley, K. Lodders, D. Saumon, and R. Freedman. Comparative Planetary Atmospheres: Models of TrES-1 and HD 209458b. *ApJL*, 627:L69–L72, July 2005. doi: 10.1086/431952.

J. J. Fortney, M. S. Marley, and J. W. Barnes. Planetary Radii across Five Orders of Magnitude in Mass and Stellar Insolation: Application to Transits. *ApJ*, 659:1661–1672, April 2007. doi: 10.1086/512120.

L. Fossati, S. Bagnulo, A. Elmasli, C. A. Haswell, S. Holmes, O. Kochukhov, E. L. Shkolnik, D. V. Shulyak, D. Bohlender, B. Albayrak, C. Froning, and L. Hebb. A Detailed Spectropolarimetric Analysis of the Planet-hosting Star WASP-12. *ApJ*, 720:872–886, September 2010a. doi: 10.1088/0004-637X/720/1/872.

L. Fossati, C. A. Haswell, C. S. Froning, L. Hebb, S. Holmes, U. Kolb, C. Helling, A. Carter, P. Wheatley, A. Collier Cameron, B. Loeillet, D. Pollacco, R. Street, H. C. Stempels, E. Simpson, S. Udry, Y. C. Joshi, R. G. West, I. Skillen, and D. Wilson. Metals in the Exosphere of the Highly Irradiated Planet WASP-12b. *ApJL*, 714:L222–L227, May 2010b. doi: 10.1088/2041-8205/714/2/L222.

Y. I. Fujii, S. Okuzumi, and S.-i. Inutsuka. A Fast and Accurate Calculation Scheme for

Ionization Degrees in Protoplanetary and Circumplanetary Disks with Charged Dust Grains. *ApJ*, 743:53, December 2011. doi: 10.1088/0004-637X/743/1/53.

A. García Muñoz. Physical and chemical aeronomy of HD 209458b. *P&SS*, 55:1426–1455, July 2007. doi: 10.1016/j.pss.2007.03.007.

M. Gillon, F. Pont, B.-O. Demory, F. Mallmann, M. Mayor, T. Mazeh, D. Queloz, A. Shporer, S. Udry, and C. Vuissoz. Detection of transits of the nearby hot Neptune GJ 436 b. *A&A*, 472:L13–L16, September 2007. doi: 10.1051/0004-6361:20077799.

M. L. Goldstein. An instability of finite amplitude circularly polarized Alfven waves. *ApJ*, 219: 700–704, January 1978. doi: 10.1086/155829.

J.-M. Grießmeier, A. Stadelmann, T. Penz, H. Lammer, F. Selsis, I. Ribas, E. F. Guinan, U. Motschmann, H. K. Biernat, and W. W. Weiss. The effect of tidal locking on the magnetospheric and atmospheric evolution of "Hot Jupiters". *A&A*, 425:753–762, October 2004. doi: 10.1051/0004-6361:20035684.

P.-G. Gu, D. N. C. Lin, and P. H. Bodenheimer. The Effect of Tidal Inflation Instability on the Mass and Dynamical Evolution of Extrasolar Planets with Ultrashort Periods. *ApJ*, 588: 509–534, May 2003. doi: 10.1086/373920.

R. Hanel, B. Conrath, L. Herath, V. Kunde, and J. Pirraglia. Albedo, internal heat, and energy balance of Jupiter - Preliminary results of the Voyager infrared investigation. *JGR*, 86:8705–8712, September 1981. doi: 10.1029/JA086iA10p08705.

G. M. Harper, M. J. Richter, N. Ryde, A. Brown, J. Brown, T. K. Greathouse, and S. Strong. Texes Observations of M Supergiants: Dynamics and Thermodynamics of Wind Acceleration. *ApJ*, 701:1464–1483, August 2009. doi: 10.1088/0004-637X/701/2/1464.

J. Harrington, S. Luszcz, S. Seager, D. Deming, and L. J. Richardson. The hottest planet. *Nature*, 447:691–693, June 2007. doi: 10.1038/nature05863.

L. Hartmann and E. H. Avrett. On the extended chromosphere of Alpha Orionis. *ApJ*, 284: 238–249, September 1984. doi: 10.1086/162402.

O. Hashimoto. Infrared properties of circumstellar dust envelopes of oxygen-rich asymptotic giant branch stars. *ApJ*, 442:286–295, March 1995. doi: 10.1086/175440.

C. A. Haswell, L. Fossati, T. Ayres, K. France, C. S. Froning, S. Holmes, U. C. Kolb, R. Busuttil, R. A. Street, L. Hebb, A. Collier Cameron, B. Enoch, V. Burwitz, J. Rodriguez, R. G. West, D. Pollacco, P. J. Wheatley, and A. Carter. Near-ultraviolet Absorption, Chromospheric Activity, and Star-Planet Interactions in the WASP-12 system. *ApJ*, 760:79, November 2012. doi: 10.1088/0004-637X/760/1/79.

C. Helling and W. Lucas. Gas-phase mean opacities for varying [M/H], N/O and C/O. *MNRAS*, 398:985–994, September 2009. doi: 10.1111/j.1365-2966.2009.15164.x.

G. W. Henry, G. W. Marcy, R. P. Butler, and S. S. Vogt. A Transiting "51 Peg-like" Planet. *ApJL*, 529:L41–L44, January 2000. doi: 10.1086/312458.

J. Heyvaerts and E. R. Priest. Coronal heating by phase-mixed shear Alfven waves. *A&A*, 117: 220–234, January 1983.

J. V. Hollweg. Heating of the corona and solar wind by switch-on shocks. *ApJ*, 254:806–813, March 1982. doi: 10.1086/159791.

M. Holmström, A. Ekenbäck, F. Selsis, T. Penz, H. Lammer, and P. Wurz. Energetic neutral atoms as the explanation for the high-velocity hydrogen around HD 209458b. *Nature*, 451: 970–972, February 2008. doi: 10.1038/nature06600.

X. Huang and A. Cumming. Ohmic Dissipation in the Interiors of Hot Jupiters. *ApJ*, 757:47, September 2012. doi: 10.1088/0004-637X/757/1/47.

I. Hubeny, A. Burrows, and D. Sudarsky. A Possible Bifurcation in Atmospheres of Strongly Irradiated Stars and Planets. *ApJ*, 594:1011–1018, September 2003. doi: 10.1086/377080.

H. Ito, S. Tsuneta, D. Shiota, M. Tokumaru, and K. Fujiki. Is the Polar Region Different from the Quiet Region of the Sun? *ApJ*, 719:131–142, August 2010. doi: 10.1088/0004-637X/719/1/131.

S. A. Jacques. Momentum and energy transport by waves in the solar atmosphere and solar wind. *ApJ*, 215:942–951, August 1977. doi: 10.1086/155430.

S. Jin, C. Mordasini, V. Parmentier, R. van Boekel, T. Henning, and J. Ji. Planetary Population Synthesis Coupled with Atmospheric Escape: A Statistical View of Evaporation. *ApJ*, 795: 65, November 2014. doi: 10.1088/0004-637X/795/1/65.

D. M. Kipping and D. S. Spiegel. Detection of visible light from the darkest world. *MNRAS*, 417:L88–L92, October 2011. doi: 10.1111/j.1745-3933.2011.01127.x.

K. G. Kislyakova, M. Holmström, H. Lammer, P. Odert, and M. L. Khodachenko. Magnetic moment and plasma environment of HD 209458b as determined from Lyα observations. *Science*, 346:981–984, November 2014. doi: 10.1126/science.1257829.

H. A. Knutson, D. Charbonneau, L. E. Allen, A. Burrows, and S. T. Megeath. The 3.6-8.0 μm Broadband Emission Spectrum of HD 209458b: Evidence for an Atmospheric Temperature Inversion. *ApJ*, 673:526–531, January 2008. doi: 10.1086/523894.

H. A. Knutson, N. Madhusudhan, N. B. Cowan, J. L. Christiansen, E. Agol, D. Deming, J.-M. Désert, D. Charbonneau, G. W. Henry, D. Homeier, J. Langton, G. Laughlin, and S. Seager. A Spitzer Transmission Spectrum for the Exoplanet GJ 436b, Evidence for Stellar Variability, and Constraints on Dayside Flux Variations. *ApJ*, 735:27, July 2011. doi: 10.1088/0004-637X/735/1/27.

R. A. Kopp and T. E. Holzer. Dynamics of coronal hole regions. I - Steady polytropic flows with multiple critical points. *Solar Physics*, 49:43–56, July 1976. doi: 10.1007/BF00221484.

T. T. Koskinen, R. V. Yelle, P. Lavvas, and N. K. Lewis. Characterizing the Thermosphere of HD209458b with UV Transit Observations. *ApJ*, 723:116–128, November 2010. doi: 10.1088/0004-637X/723/1/116.

T. T. Koskinen, M. J. Harris, R. V. Yelle, and P. Lavvas. The escape of heavy atoms from the ionosphere of HD209458b. I. A photochemical-dynamical model of the thermosphere. *Icarus*, 226:1678–1694, November 2013. doi: 10.1016/j.icarus.2012.09.027.

T. Kudoh and K. Shibata. Alfvén Wave Model of Spicules and Coronal Heating. *ApJ*, 514: 493–505, March 1999. doi: 10.1086/306930.

J. R. Kulow, K. France, J. Linsky, and R. O. P. Loyd. Lyα Transit Spectroscopy and the Neutral Hydrogen Tail of the Hot Neptune GJ 436b. *ApJ*, 786:132, May 2014. doi: 10.1088/0004-637X/786/2/132.

H. Kurokawa and T. Nakamoto. Mass-loss Evolution of Close-in Exoplanets: Evaporation of Hot Jupiters and the Effect on Population. *ApJ*, 783:54, March 2014. doi: 10.1088/0004-637X/783/1/54.

H. Lammer, F. Selsis, I. Ribas, E. F. Guinan, S. J. Bauer, and W. W. Weiss. Atmospheric Loss of Exoplanets Resulting from Stellar X-Ray and Extreme-Ultraviolet Heating. *ApJL*, 598: L121–L124, December 2003. doi: 10.1086/380815.

M. Landini and B. C. Monsignori Fossi. The X-UV spectrum of thin plasmas. *A&AS*, 82: 229–260, February 1990.

A. Lecavelier des Etangs, A. Vidal-Madjar, J. C. McConnell, and G. Hébrard. Atmospheric escape from hot Jupiters. *A&A*, 418:L1–L4, April 2004. doi: 10.1051/0004-6361:20040106.

A. Lecavelier des Etangs, D. Ehrenreich, A. Vidal-Madjar, G. E. Ballester, J.-M. Désert, R. Ferlet, G. Hébrard, D. K. Sing, K.-O. Tchakoumegni, and S. Udry. Evaporation of the planet HD 189733b observed in H I Lyman-α. *A&A*, 514:A72, May 2010. doi: 10.1051/0004-6361/200913347.

A. Lecavelier Des Etangs, S. K. Sirothia, Gopal-Krishna, and P. Zarka. GMRT search for 150 MHz radio emission from the transiting extrasolar planets HD 189733 b and HD 209458 b. *A&A*, 533:A50, September 2011. doi: 10.1051/0004-6361/201117330.

A. Lecavelier des Etangs, V. Bourrier, P. J. Wheatley, H. Dupuy, D. Ehrenreich, A. Vidal-Madjar, G. Hébrard, G. E. Ballester, J.-M. Désert, R. Ferlet, and D. K. Sing. Temporal variations in the evaporating atmosphere of the exoplanet HD 189733b. *A&A*, 543:L4, July 2012. doi: 10.1051/0004-6361/201219363.

A. Léger, D. Rouan, J. Schneider, P. Barge, M. Fridlund, B. Samuel, M. Ollivier, E. Guenther, M. Deleuil, H. J. Deeg, M. Auvergne, R. Alonso, S. Aigrain, A. Alapini, J. M. Almenara, A. Baglin, M. Barbieri, H. Bruntt, P. Bordé, F. Bouchy, J. Cabrera, C. Catala, L. Carone, S. Carpano, S. Csizmadia, R. Dvorak, A. Erikson, S. Ferraz-Mello, B. Foing, F. Fressin, D. Gandolfi, M. Gillon, P. Gondoin, O. Grasset, T. Guillot, A. Hatzes, G. Hébrard, L. Jorda, H. Lammer, A. Llebaria, B. Loeillet, M. Mayor, T. Mazeh, C. Moutou, M. Pätzold, F. Pont, D. Queloz, H. Rauer, S. Renner, R. Samadi, A. Shporer, C. Sotin, B. Tingley, G. Wuchterl, M. Adda, P. Agogu, T. Appourchaux, H. Ballans, P. Baron, T. Beaufort, R. Bellenger, R. Berlin, P. Bernardi, D. Blouin, F. Baudin, P. Bodin, L. Boisnard, L. Boit, F. Bonneau, S. Borzeix, R. Briet, J.-T. Buey, B. Butler, D. Cailleau, R. Cautain, P.-Y. Chabaud, S. Chaintreuil, F. Chiavassa, V. Costes, V. Cuna Parrho, F. de Oliveira Fialho, M. Decaudin, J.-M.

Defise, S. Djalal, G. Epstein, G.-E. Exil, C. Fauré, T. Fenouillet, A. Gaboriaud, A. Gallic, P. Gamet, P. Gavalda, E. Grolleau, R. Gruneisen, L. Gueguen, V. Guis, V. Guivarc'h, P. Guterman, D. Hallouard, J. Hasiba, F. Heuripeau, G. Huntzinger, H. Hustaix, C. Imad, C. Imbert, B. Johlander, M. Jouret, P. Journoud, F. Karioty, L. Kerjean, V. Lafaille, L. Lafond, T. Lam-Trong, P. Landiech, V. Lapeyrere, T. Larqué, P. Laudet, N. Lautier, H. Lecann, L. Lefevre, B. Leruyet, P. Levacher, A. Magnan, E. Mazy, F. Mertens, J.-M. Mesnager, J.-C. Meunier, J.-P. Michel, W. Monjoin, D. Naudet, K. Nguyen-Kim, J.-L. Orcesi, H. Ottacher, R. Perez, G. Peter, P. Plasson, J.-Y. Plesseria, B. Pontet, A. Pradines, C. Quentin, J.-L. Reynaud, G. Rolland, F. Rollenhagen, R. Romagnan, N. Russ, R. Schmidt, N. Schwartz, I. Sebbag, G. Sedes, H. Smit, M. B. Steller, W. Sunter, C. Surace, M. Tello, D. Tiphène, P. Toulouse, B. Ulmer, O. Vandermarcq, E. Vergnault, A. Vuillemin, and P. Zanatta. Transiting exoplanets from the CoRoT space mission. VIII. CoRoT-7b: the first super-Earth with measured radius. *A&A*, 506:287–302, October 2009. doi: 10.1051/0004-6361/200911933.

N. K. Lewis, A. P. Showman, J. J. Fortney, M. S. Marley, R. S. Freedman, and K. Lodders. Atmospheric Circulation of Eccentric Hot Neptune GJ436b. *ApJ*, 720:344–356, September 2010. doi: 10.1088/0004-637X/720/1/344.

J. L. Linsky, H. Yang, K. France, C. S. Froning, J. C. Green, J. T. Stocke, and S. N. Osterman. Observations of Mass Loss from the Transiting Exoplanet HD 209458b. *ApJ*, 717:1291–1299, July 2010. doi: 10.1088/0004-637X/717/2/1291.

E. D. Lopez and J. J. Fortney. Re-inflated Warm Jupiters Around Red Giants. *ArXiv e-prints*, September 2015.

E. D. Lopez, J. J. Fortney, and N. Miller. How Thermal Evolution and Mass-loss Sculpt Populations of Super-Earths and Sub-Neptunes: Application to the Kepler-11 System and Beyond. *ApJ*, 761:59, December 2012. doi: 10.1088/0004-637X/761/1/59.

T. Louden and P. J. Wheatley. Spatially resolved eastward winds and rotation of HD 189733b. *ArXiv e-prints*, November 2015.

R. Luger, R. Barnes, E. Lopez, J. Fortney, B. Jackson, and V. Meadows. Habitable Evaporated Cores: Transforming Mini-Neptunes into Super-Earths in the Habitable Zones of M Dwarfs. *Astrobiology*, 15:57–88, January 2015. doi: 10.1089/ast.2014.1215.

P. Machalek, P. R. McCullough, C. J. Burke, J. A. Valenti, A. Burrows, and J. L. Hora. Thermal Emission of Exoplanet XO-1b. *ApJ*, 684:1427–1432, September 2008. doi: 10.1086/590140.

T. Matsumoto and R. Kitai. Temporal Power Spectra of the Horizontal Velocity of the Solar Photosphere. *ApJL*, 716:L19–L22, June 2010. doi: 10.1088/2041-8205/716/1/L19.

T. Matsumoto and T. K. Suzuki. Connecting the Sun and the Solar Wind: The First 2.5-dimensional Self-consistent MHD Simulation under the Alfvén Wave Scenario. *ApJ*, 749:8, April 2012. doi: 10.1088/0004-637X/749/1/8.

T. Matsumoto and T. K. Suzuki. Connecting the Sun and the solar wind: the self-consistent transition of heating mechanisms. *MNRAS*, 440:971–986, May 2014. doi: 10.1093/mnras/stu310.

W. H. Matthaeus, G. P. Zank, S. Oughton, D. J. Mullan, and P. Dmitruk. Coronal Heating by Magnetohydrodynamic Turbulence Driven by Reflected Low-Frequency Waves. *ApJL*, 523: L93–L96, September 1999. doi: 10.1086/312259.

M. Mayor and D. Queloz. A Jupiter-mass companion to a solar-type star. *Nature*, 378:355–359, November 1995. doi: 10.1038/378355a0.

K. Menou. Magnetic Scaling Laws for the Atmospheres of Hot Giant Exoplanets. *ApJ*, 745: 138, February 2012. doi: 10.1088/0004-637X/745/2/138.

T. Miyake, T. K. Suzuki, and S.-i. Inutsuka. Dust Dynamics in Protoplanetary Disk Winds Driven by Magneto-Rotational Turbulence: A Mechanism for Floating Dust Grains with Characteristic Sizes. *ArXiv e-prints*, May 2015.

M. Miyamoto, T. Imamura, M. Tokumaru, H. Ando, H. Isobe, A. Asai, D. Shiota, T. Toda, B. Häusler, M. Pätzold, A. Nabatov, and M. Nakamura. Radial Distribution of Compressive Waves in the Solar Corona Revealed by Akatsuki Radio Occultation Observations. *ApJ*, 797: 51, December 2014. doi: 10.1088/0004-637X/797/1/51.

D. O. Muchmore, J. A. Nuth, III, and R. E. Stencel. SiO cooling instability in the envelopes of cool giant stars. *ApJL*, 315:L141–L146, April 1987. doi: 10.1086/184876.

R. A. Murray-Clay, E. I. Chiang, and N. Murray. Atmospheric Escape From Hot Jupiters. *ApJ*, 693:23–42, March 2009. doi: 10.1088/0004-637X/693/1/23.

J. E. Owen and F. C. Adams. Magnetically controlled mass-loss from extrasolar planets in close orbits. *MNRAS*, 444:3761–3779, November 2014. doi: 10.1093/mnras/stu1684.

R. Perna, K. Menou, and E. Rauscher. Ohmic Dissipation in the Atmospheres of Hot Jupiters. *ApJ*, 724:313–317, November 2010. doi: 10.1088/0004-637X/724/1/313.

I. Pillitteri, A. Maggio, G. Micela, S. Sciortino, S. J. Wolk, and T. Matsakos. FUV Variability of HD 189733. Is the Star Accreting Material From Its Hot Jupiter? *ApJ*, 805:52, May 2015. doi: 10.1088/0004-637X/805/1/52.

F. Pont, R. L. Gilliland, C. Moutou, D. Charbonneau, F. Bouchy, T. M. Brown, M. Mayor, D. Queloz, N. Santos, and S. Udry. Hubble Space Telescope time-series photometry of the planetary transit of HD 189733: no moon, no rings, starspots. *A&A*, 476:1347–1355, December 2007. doi: 10.1051/0004-6361:20078269.

K. Poppenhaeger, J. H. M. M. Schmitt, and S. J. Wolk. Transit Observations of the Hot Jupiter HD 189733b at X-Ray Wavelengths. *ApJ*, 773:62, August 2013. doi: 10.1088/0004-637X/773/1/62.

S. Rappaport, A. Levine, E. Chiang, I. El Mellah, J. Jenkins, B. Kalomeni, E. S. Kite, M. Kotson, L. Nelson, L. Rousseau-Nepton, and K. Tran. Possible Disintegrating Short-period Super-Mercury Orbiting KIC 12557548. *ApJ*, 752:1, June 2012. doi: 10.1088/0004-637X/752/1/1.

A. Reiners and U. R. Christensen. A magnetic field evolution scenario for brown dwarfs and giant planets. *A&A*, 522:A13, November 2010. doi: 10.1051/0004-6361/201014251.

L. A. Rogers, P. Bodenheimer, J. J. Lissauer, and S. Seager. Formation and Structure of Low-density exo-Neptunes. *ApJ*, 738:59, September 2011. doi: 10.1088/0004-637X/738/1/59.

T. M. Rogers and A. P. Showman. Magnetohydrodynamic Simulations of the Atmosphere of HD 209458b. *ApJL*, 782:L4, February 2014. doi: 10.1088/2041-8205/782/1/L4.

A. Sánchez-Lavega. The Magnetic Field in Giant Extrasolar Planets. *ApJL*, 609:L87–L90, July 2004. doi: 10.1086/422840.

T. Sano, S. Inutsuka, and S. M. Miyama. A Higher-Order Godunov Scheme for Non-Ideal Magnetohydrodynamics^{CD}. In S. M. Miyama, K. Tomisaka, and T. Hanawa, editors, *Numerical Astrophysics*, volume 240 of *Astrophysics and Space Science Library*, page 383, 1999.

L. Schaefer and B. Fegley. Chemistry of Silicate Atmospheres of Evaporating Super-Earths. *ApJL*, 703:L113–L117, October 2009. doi: 10.1088/0004-637X/703/2/L113.

V. Schirrmacher, P. Woitke, and E. Sedlmayr. On the gas temperature in the shocked circumstellar envelopes of pulsating stars. III. Dynamical models for AGB star winds including time-dependent dust formation and non-LTE cooling. *A&A*, 404:267–282, June 2003. doi: 10.1051/0004-6361:20030444.

E. Schlawin, E. Agol, L. M. Walkowicz, K. Covey, and J. P. Lloyd. Exoplanetary Transits of Limb-brightened Lines: Tentative Si IV Absorption by HD 209458b. *ApJL*, 722:L75–L79, October 2010. doi: 10.1088/2041-8205/722/1/L75.

J. Schneider, H. Rauer, J. P. Lasota, S. Bonazzola, and E. Chassefiere. The Cometary Tail of Giant Extrasolar Planets at Small Orbital Distance. In R. Rebolo, E. L. Martin, and M. R. Zapatero Osorio, editors, *Brown Dwarfs and Extrasolar Planets*, volume 134 of *Astronomical Society of the Pacific Conference Series*, page 241, 1998.

H. Schwarz, M. Brogi, R. de Kok, J. Birkby, and I. Snellen. Evidence against a strong thermal inversion in HD 209458b from high-dispersion spectroscopy. *A&A*, 576:A111, April 2015. doi: 10.1051/0004-6361/201425170.

V. I. Shematovich, D. E. Ionov, and H. Lammer. Heating efficiency in hydrogen-dominated upper atmospheres. *A&A*, 571:A94, November 2014. doi: 10.1051/0004-6361/201423573.

D. Shiota, S. Tsuneta, M. Shimojo, N. Sako, D. Orozco Suárez, and R. Ishikawa. Polar Field Reversal Observations with Hinode. *ApJ*, 753:157, July 2012. doi: 10.1088/0004-637X/753/2/157.

A. P. Showman and T. Guillot. Atmospheric circulation and tides of "51 Pegasus b-like" planets. *A&A*, 385:166–180, April 2002. doi: 10.1051/0004-6361:20020101.

A. P. Showman, C. S. Cooper, J. J. Fortney, and M. S. Marley. Atmospheric Circulation of Hot Jupiters: Three-dimensional Circulation Models of HD 209458b and HD 189733b with Simplified Forcing. *ApJ*, 682:559–576, July 2008. doi: 10.1086/589325.

D. K. Sing, F. Pont, S. Aigrain, D. Charbonneau, J.-M. Désert, N. Gibson, R. Gilliland, W. Hayek, G. Henry, H. Knutson, A. Lecavelier Des Etangs, T. Mazeh, and A. Shporer. Hubble Space Telescope transmission spectroscopy of the exoplanet HD 189733b: high-altitude

atmospheric haze in the optical and near-ultraviolet with STIS. *MNRAS*, 416:1443–1455, September 2011. doi: 10.1111/j.1365-2966.2011.19142.x.

S. K. Sirothia, A. Lecavelier des Etangs, Gopal-Krishna, N. G. Kantharia, and C. H. Ishwar-Chandra. Search for 150 MHz radio emission from extrasolar planets in the TIFR GMRT Sky Survey. *A&A*, 562:A108, February 2014. doi: 10.1051/0004-6361/201321571.

I. A. G. Snellen, S. Albrecht, E. J. W. de Mooij, and R. S. Le Poole. Ground-based detection of sodium in the transmission spectrum of exoplanet HD 209458b. *A&A*, 487:357–362, August 2008. doi: 10.1051/0004-6361:200809762.

I. A. G. Snellen, R. J. de Kok, E. J. W. de Mooij, and S. Albrecht. The orbital motion, absolute mass and high-altitude winds of exoplanet HD209458b. *Nature*, 465:1049–1051, June 2010. doi: 10.1038/nature09111.

K. B. Stevenson, J. Harrington, J. J. Fortney, T. J. Loredo, R. A. Hardy, S. Nymeyer, W. C. Bowman, P. Cubillos, M. O. Bowman, and M. Hardin. Transit and Eclipse Analyses of the Exoplanet HD 149026b Using BLISS Mapping. *ApJ*, 754:136, August 2012. doi: 10.1088/0004-637X/754/2/136.

D. Sudarsky, A. Burrows, and P. Pinto. Albedo and Reflection Spectra of Extrasolar Giant Planets. *ApJ*, 538:885–903, August 2000. doi: 10.1086/309160.

R. S. Sutherland and M. A. Dopita. Cooling functions for low-density astrophysical plasmas. *ApJS*, 88:253–327, September 1993. doi: 10.1086/191823.

T. K. Suzuki. Structured Red Giant Winds with Magnetized Hot Bubbles and the Corona/Cool Wind Dividing Line. *ApJ*, 659:1592–1610, April 2007. doi: 10.1086/512600.

T. K. Suzuki and S.-i. Inutsuka. Making the Corona and the Fast Solar Wind: A Self-consistent Simulation for the Low-Frequency Alfvén Waves from the Photosphere to 0.3 AU. *ApJL*, 632:L49–L52, October 2005. doi: 10.1086/497536.

T. K. Suzuki and S.-I. Inutsuka. Solar winds driven by nonlinear low-frequency Alfvén waves from the photosphere: Parametric study for fast/slow winds and disappearance of solar winds. *Journal of Geophysical Research (Space Physics)*, 111:A06101, June 2006. doi: 10.1029/2005JA011502.

T. K. Suzuki, S. Imada, R. Kataoka, Y. Kato, T. Matsumoto, H. Miyahara, and S. Tsuneta. Saturation of Stellar Winds from Young Suns. *PASJ*, 65:98, October 2013. doi: 10.1093/pasj/65.5.98.

M. R. Swain, G. Vasisht, and G. Tinetti. The presence of methane in the atmosphere of an extrasolar planet. *Nature*, 452:329–331, March 2008. doi: 10.1038/nature06823.

M. R. Swain, G. Tinetti, G. Vasisht, P. Deroo, C. Griffith, J. Bouwman, P. Chen, Y. Yung, A. Burrows, L. R. Brown, J. Matthews, J. F. Rowe, R. Kuschnig, and D. Angerhausen. Water, Methane, and Carbon Dioxide Present in the Dayside Spectrum of the Exoplanet HD 209458b. *ApJ*, 704:1616–1621, October 2009. doi: 10.1088/0004-637X/704/2/1616.

Y. A. Tanaka, T. K. Suzuki, and S.-i. Inutsuka. Atmospheric Escape by Magnetically Driven Wind from Gaseous Planets. *ApJ*, 792:18, September 2014. doi: 10.1088/0004-637X/792/1/18.

Y. A. Tanaka, T. K. Suzuki, and S.-i. Inutsuka. Atmospheric Escape by Magnetically Driven Wind from Gaseous Planets. II. Effects of Magnetic Diffusion. *ApJ*, 809:125, August 2015. doi: 10.1088/0004-637X/809/2/125.

T. Terasawa, M. Hoshino, J.-I. Sakai, and T. Hada. Decay instability of finite-amplitude circularly polarized Alfven waves - A numerical simulation of stimulated Brillouin scattering. *JGR*, 91:4171–4187, April 1986. doi: 10.1029/JA091iA04p04171.

F. Tian, O. B. Toon, A. A. Pavlov, and H. De Sterck. Transonic Hydrodynamic Escape of Hydrogen from Extrasolar Planetary Atmospheres. *ApJ*, 621:1049–1060, March 2005. doi: 10.1086/427204.

G. Tinetti, A. Vidal-Madjar, M.-C. Liang, J.-P. Beaulieu, Y. Yung, S. Carey, R. J. Barber, J. Tennyson, I. Ribas, N. Allard, G. E. Ballester, D. K. Sing, and F. Selsis. Water vapour in the atmosphere of a transiting extrasolar planet. *Nature*, 448:169–171, July 2007. doi: 10.1038/nature06002.

G. B. Trammell, P. Arras, and Z.-Y. Li. Hot Jupiter Magnetospheres. *ApJ*, 728:152, February 2011. doi: 10.1088/0004-637X/728/2/152.

G. B. Trammell, Z.-Y. Li, and P. Arras. Magnetohydrodynamic Simulations of Hot Jupiter Upper Atmospheres. *ApJ*, 788:161, June 2014. doi: 10.1088/0004-637X/788/2/161.

P. Tremblin and E. Chiang. Colliding planetary and stellar winds: charge exchange and transit spectroscopy in neutral hydrogen. *MNRAS*, 428:2565–2576, January 2013. doi: 10.1093/mnras/sts212.

T. Tsuji. Model atmosphere approach in late-type stars. In M. Hack, editor, *Late-Type Stars*, page 260, 1967.

T. Tsuji. Molecular abundances in stellar atmospheres. II. *A&A*, 23:411–431, March 1973.

S. Tsuneta, K. Ichimoto, Y. Katsukawa, B. W. Lites, K. Matsuzaki, S. Nagata, D. Orozco Suárez, T. Shimizu, M. Shimojo, R. A. Shine, Y. Suematsu, T. K. Suzuki, T. D. Tarbell, and A. M. Title. The Magnetic Landscape of the Sun's Polar Region. *ApJ*, 688:1374–1381, December 2008. doi: 10.1086/592226.

W. Unno. Radiative transfer in spherical geometry. *PASJ*, 41:211–215, 1989.

W. Unno and M. Kondo. The Eddington approximation generalized by radiative transfer in spherically symmetric systems. I. *PASJ*, 28:347–354, 1976.

J. E. Vernazza, E. H. Avrett, and R. Loeser. Structure of the solar chromosphere. III - Models of the EUV brightness components of the quiet-sun. *ApJS*, 45:635–725, April 1981. doi: 10.1086/190731.

A. Vidal-Madjar, A. Lecavelier des Etangs, J.-M. Désert, G. E. Ballester, R. Ferlet, G. Hébrard, and M. Mayor. An extended upper atmosphere around the extrasolar planet HD209458b. *Nature*, 422:143–146, March 2003. doi: 10.1038/nature01448.

A. Vidal-Madjar, J.-M. Désert, A. Lecavelier des Etangs, G. Hébrard, G. E. Ballester, D. Ehrenreich, R. Ferlet, J. C. McConnell, M. Mayor, and C. D. Parkinson. Detection of Oxygen and Carbon in the Hydrodynamically Escaping Atmosphere of the Extrasolar Planet HD 209458b. *ApJL*, 604:L69–L72, March 2004. doi: 10.1086/383347.

A. Vidal-Madjar, C. M. Huitson, V. Bourrier, J.-M. Désert, G. Ballester, A. Lecavelier des Etangs, D. K. Sing, D. Ehrenreich, R. Ferlet, G. Hébrard, and J. C. McConnell. Magnesium in the atmosphere of the planet HD 209458 b: observations of the thermosphere-exosphere transition region. *A&A*, 560:A54, December 2013. doi: 10.1051/0004-6361/201322234.

A. A. Vidotto, M. Jardine, and C. Helling. Early UV Ingress in WASP-12b: Measuring Planetary Magnetic Fields. *ApJL*, 722:L168–L172, October 2010. doi: 10.1088/2041-8205/722/2/L168.

J. M. Winters, A. J. Fleischer, T. Le Bertre, and E. Sedlmayr. Circumstellar dust shells around long-period variables. V. A consistent time-dependent model for the extreme carbon star AFGL 3068. *A&A*, 326:305–317, October 1997.

J. T. Wright, O. Fakhouri, G. W. Marcy, E. Han, Y. Feng, J. A. Johnson, A. W. Howard, D. A. Fischer, J. A. Valenti, J. Anderson, and N. Piskunov. The Exoplanet Orbit Database. *PASP*, 123:412–422, April 2011. doi: 10.1086/659427.

Y. Wu and Y. Lithwick. Ohmic Heating Suspends, Not Reverses, the Cooling Contraction of Hot Jupiters. *ApJ*, 763:13, January 2013. doi: 10.1088/0004-637X/763/1/13.

A. Wyttenbach, D. Ehrenreich, C. Lovis, S. Udry, and F. Pepe. Spectrally resolved detection of sodium in the atmosphere of HD 189733b with the HARPS spectrograph. *A&A*, 577:A62, May 2015. doi: 10.1051/0004-6361/201525729.

R. V. Yelle. Aeronomy of extra-solar giant planets at small orbital distances. *Icarus*, 170: 167–179, July 2004. doi: 10.1016/j.icarus.2004.02.008.

R. V. Yelle. Corrigendum to "Aeronomy of extra-solar giant planets at small orbital distances" [Icarus 170 (2004) 167 179]. *Icarus*, 183:508–508, August 2006. doi: 10.1016/j.icarus.2006.05.001.